Radar-rain gauge merging and discharge data assimilation for flood forecasting in Alpine catchments

Thèse N° 9777

Présentée le 11 décembre 2019

à la Faculté de l'environnement naturel, architectural et construit
Laboratoire d'écohydrologie - Plateforme de construction hydrauliques
Programme doctoral en génie civil et environnement

pour l'obtention du grade de Docteur ès Sciences

par

Alain Tommy FOEHN

Acceptée sur proposition du jury

Prof. Ph. Thalmann, président du jury
Prof. A. Rinaldo, Dr G. De Cesare, directeurs de thèse
Dr M. Gabella, rapporteur
Dr M. Zappa, rapporteur
Dr H. Huwald, rapporteur

2019

ÉCOLE POLYTECHNIQUE
FÉDÉRALE DE LAUSANNE

Birds are indicators of the environment.
If they are in trouble, we know we'll soon be in trouble.
— Roger Tory Peterson

A mes parents, à ma grand-mère, à mon frère,
A toi Camille et à notre bébé à venir...

Acknowledgements

This research is co-funded by the Centre de recherche sur l'environnement alpin (CREALP), located in Sion (Switzerland), and the Swiss Federal Office of Energy. I express my sincere thanks for this support. I also express my gratitude to all stakeholders involved in the project, namely the Canton of Valais, the Swiss Federal Office for Meteorology and Climatology (MeteoSwiss) and the engineering office HydroCosmos SA.

I would like to express my deep sense of thankfulness to Prof. Anton J. Schleiss, who directed the thesis during the first three years until his retirement, for having given me the fantastic opportunity to conduct this doctoral thesis at LCH. My sincere thanks also go to Prof. Andrea Rinaldo, who accepted to overtake the direction for the last year of the thesis. Your valuable guidance helped me in all the time of research and writing of this thesis.

I would like to thank also Dr. Giovanni De Cesare, co-director of the thesis. His valuable guidance, support and encouragements all along the project were highly appreciated. My research has been quite demanding in IT resources and I am very thankful for the computing capacity you allocated to my project. Merci beaucoup !

I would also like to express my sincere gratitude to Dr. Javier García Hernández, director of the CREALP, for having given me the chance to achieve this thesis by initiating the project and financing a large part of it. I thank you for all the discussions we have had together about the project, for your availability, for your positive attitude and your shared energy.

My thanks also go to Prof. Bettina Schaefli, from University of Lausanne, for her inputs about the methodology as well as in the redaction process of the published paper and the submitted one. Thanks also to Dr. Damiano Pasetto for his valuable inputs and contributions for the data assimilation part of the project.

Further, I wish to express my thanks to Dr. Hendrik Huwald (EPFL), Dr. Marco Gabella (MeteoSwiss) and Dr. Massimiliano Zappa (WSL) for being part of the jury and Prof. Philippe Thalmann (EPFL) for having accepted to preside the jury.

A thesis is an individual work. However, my thesis was part of a larger project, the operational flood forecasting system of the Canton of Valais, hosted by the CREALP. In that context, I had

the chance to collaborate with the wonderful CREALP team. Ma reconnaissance va notamment à toute les personnes ayant constitué l'équipe IT durant mes années de thèse, pour votre disponibilité et votre efficacité : Barnabé, Dany, Gilles et Stéphane ! Merci à toutes les autres personnes que j'ai pu côtoyé au CREALP durant ces années : Aurélie, Bastien (merci pour toutes les versions de RS MINERVE et le travail derrière !), Benjamin, Chloé, Eric B., Eric T. (merci pour les nombreuses discussions), Ivann, Javi (merci pour ton aide !), Jean-Yves, Guillaume, Marie-Hélène, Pascal M., Pascal O., Romain, Sabiré, Samuel, Thierry et Tristan.

J'en profite également pour remercier tou.te.s les collègues qui ont constitué le LCH, notamment Anne, Aldo, Alexandre, Azin, Carmelo, Cédric, Charles, Christian, Davide, Elena, Fränz, Irene, Ivan, Jessica, Nicolas, Paloma, Pedram, Pedro, Pierre, Ricardo, Romain, Sabine, Samuel, Sara, Sebastian, Severin, Séverine, Stéphane and Zé. Je tiens également à remercier l'équipe de la librairie de l'EPFL pour leurs excellentes formations et leur disponibilité. Merci notamment à Raphaël et Noémie pour votre aide sur les preprints, les styles CSS et mes autres questions !

The project has been intensely using data from MeteoSwiss, including station and spatial data. This brought me to have contacts with many people. A particular thanks to Ioannis Sideris, Yves-Alain Roulet, Didier Ulrich, Lorenzo Clementi, Martin Brändli, Mikhaël Schwander, Gergely Rigo, Joël Fisler, Tanja Weusthoff and Jacques Ambühl for your help.

Le travail qu'implique une thèse ne serait pas possible sans les moments de détente avec les amis et la famille. Merci à vous Dana, Nicolas et Yvan pour votre amitié de longue date ! Merci à l'équipe Guillaume, Mélanie, Michaël et Stéphanie pour les week-ends passés ensemble ici et là, ainsi que le triathlon fait en équipes ! Merci à Fabrice, Tristan et Raphaël pour les sorties course à pieds et montagne. Et merci à tou.te.s les autres ami.e.s d'ici et d'ailleurs.

Durant mes années en Valais, j'ai aussi eu la chance de faire partie de deux clubs magnifiques et plein de dynamisme ! Le premier est le Triathlon Club du Valais. Merci pour tous les entraînements du mardi soir, les combinés du jeudi et les autres activités ! Le second est la section Sion du Club Alpin Suisse. De magnifiques sorties et de superbes formations qui m'ont permis de prendre l'air le week-end avec des personnes formidables. Une pensée émue à vous trois, Adrien, Cédric et Raphaël, qui nous avez quitté subitement ce 12 mars 2019 en Ecosse.

Je terminerai ces remerciements en remerciant ma famille. Merci à vous, maman et papa, pour tout ce que vous m'avez apporté toutes ces années et votre soutien inconditionnel. Merci aussi à mon frère Cédric.

Finalement, un immense merci à toi, Camille, pour ton soutien, ta compréhension, ton réconfort, ton énergie. On forme une équipe magnifique et je me réjouis que celle-ci s'agrandisse tout prochainement !

Lausanne, juillet 2019 A. F.

Abstract

Floods are responsible for one third of the economic losses induced by natural hazards throughout the world. To better protect the population and infrastructures, flood forecasting systems make us of weather forecasts to foresee floods several days in advance, providing more lead time for preventive measures. In the canton of Valais (Switzerland), an operational flood forecasting and management system is operational since 2013, as a result of the MINERVE project initiated in 1999. The present thesis aims at answering some of the challenges faced by this system.

First, a new methodology for spatial interpolation of precipitation is implemented based on regression co-kriging using rain gauge and weather radar data. Two rain gauge networks equipped with instruments of different quality are considered. Compared to other precipitation interpolation methods, the quantitative precipitation estimates (QPE) obtained from the regression co-kriging provides the best performance over the studied area using cross-validation. The analysis highlights the need for further pre-processing of radar data, in particular to account for beam shielding by the complex topography.

Integration of the above-mentioned QPE product in a snow model revealed a clear precipitation underestimation. A methodology to account for solid precipitation undercatch in QPE computation is therefore proposed. Four different QPE products are compared: the operational QPE product *CombiPrecip* of MeteoSwiss, the regression co-kriging QPE and two variants of it considering a correction factor for solid precipitation undercatch of 1.2 and 1.3, applied before the interpolation. The snow model is calibrated using satellite-based data from the MODIS spectroradiometer and validated using snow water equivalent measurements 11 snow monitoring sites. The best performance is obtained using the QPE product including a correction factor of 1.2.

To evaluate the performance of the developed QPE products from a hydrological perspective, three sub-catchments of the MINERVE system were calibrated considering 5 different input. The GSM and SOCONT hydrological models are used to model respectively the glacial and non-glacial parts. A two-phase calibration of the model is explored, applying the MODIS-based calibration of snow-melt degree-day factors, before calibrating the other parameters using discharge data. Results suggest that the developed QPE product accounting for solid

precipitation undercatch (factor 1.2) leads to the best performance over the catchment with a good radar visibility. In case of lower radar visibility, using station data provides equal or better performances. With the current implementation, the two-phase calibration did not allow to outperform the conventional calibration.

Finally, an ensemble Kalman filter (EnKF) is implemented to improve initial conditions used for hydrological forecasts. Results are compared, for two high flow events, to the scenario without assimilation and to the simple assimilation scheme currently implemented in the MINERVE system, updating the soil saturation based on a discharge volume comparison over the preceding 24 hours. The Ensemble Kalman filter (EnKF) shows good performance during these events but also highlights difficulties over base flow, strengthened in presence of hydropower perturbations.

Keywords: *flood forecasting, rain gauge-radar merging, quantitative precipitation estimate, regression co-kriging, rain gauge undercatch, snow cover, hydrological modelling, semi-distributed model, data assimilation, ensemble Kalman filter.*

Résumé

Les crues génèrent un tiers des coûts liés aux dommages naturels au niveau mondial. Afin de protéger la population et les infrastructures, des systèmes de prévisions de crues utilisent les prévisions météorologiques pour anticiper avec plusieurs jours les crues, offrant plus de temps pour se préparer. Dans le canton du Valais (Suisse), un système de prévision et de gestion des crues est opérationnel depuis 2013, résultat du projet MINERVE initié en 1999. La présente thèse a pour objectif de répondre à certains défis posés par ce système.

Une nouvelle méthode de spatialisation des précipitations basée sur un co-krigeage avec régression de données de pluviomètres et de radar météorologique est présentée. Deux réseaux de mesure équipés de pluviomètres de qualité différente sont considérés. En comparant les précipitations estimées avec d'autres méthodes d'interpolation, l'évaluation quantitative des précipitations (EQP) obtenue avec le co-krigeage avec régression fournit la meilleure performance sur le bassin d'étude. L'analyse suggère le besoin de plus de prétraitement de la donnée radar, notamment en lien avec les zones d'ombre dû à la topographie complexe.

L'intégration du nouveau produit d'EQP dans un modèle de neige a révélé une claire sous-estimation des précipitations. Une méthodologie est proposée afin de corriger la sous-estimation des précipitations solides dans le calcul de produits d'EQP. Quatre produits différents sont considérés : le produit d'EQP opérationnel *CombiPrecip* de MétéoSuisse, le co-krigeage avec régression et deux variantes de ce dernier incluant un facteur correcteur pour la sous-estimation des précipitations solides de 1.2 et 1.3. Le modèle de neige est calé avec des données satellitaires du spectroradiomètre MODIS et validé avec l'équivalent en eau de la neige à 11 stations de mesure. La meilleure performance est obtenue avec le produit d'EQP incluant un facteur correcteur de 1.2.

Pour évaluer d'un point de vue hydrologique la performance de ces produits d'EQP, trois sous-bassins du système MINERVE sont calés avec 5 jeux de données de précipitation différents en entrée. Les modèles hydrologiques GSM et SOCONT sont utilisés pour les parties glaciaires et non-glaciaires. Un calage du modèle en deux phases est exploré, en appliquant la méthode de calage des facteurs degré-jour de fonte nivale basée sur MODIS, avant de caler les autres paramètres à l'aide des données de débit. Les résultats suggèrent qu'en présence d'une bonne visibilité du radar, le produit d'EQP intégrant un facteur correcteur de 1.2 fournit les meilleurs

résultats. Pour les deux bassins avec une moins bonne visibilité, l'utilisation de données de pluviomètres mène à des résultats équivalents ou meilleurs. Avec l'implémentation actuelle, le calage en deux phases n'a pas permis de surpasser le calage conventionnel.

Finalement, un filtre de Kalman d'ensemble (EnKF) est implémenté pour améliorer les conditions initiales utilisées pour les prévisions hydrologiques. Les résultats sont comparés, pour deux événements de fortes précipitations, au scénario sans mise à jour et à l'assimilation de données actuelle du système MINERVE, mettant à jour la saturation du sol sur la base d'une comparaison des volumes de débit sur les 24 dernières heures. Le filtre de Kalman d'ensemble (EnKF) montre de bonnes performances sur les 2 événements mais également des difficultés lors des faibles débits, notamment en présence de perturbations hydroélectriques.

Mots-clés : *prévision de crue, couplage pluviomètres-radar, évaluation quantitative des précipitations, co-krigeage avec régression, sous-estimation de pluie, couverture neigeuse, modélisation hydrologique, modèle semi-distribué, assimilation de données, filtre de Kalman d'ensemble.*

Contents

Abbreviations

CED	Co-kriging with external drift
CHF	Swiss francs
COSMO-1	Consortium for Small-scale Modeling deterministic forecast with a 1.1 km grid box size
COSMO-7	Consortium for Small-scale Modeling deterministic forecast with a 6.6 km grid box size
COSMO-E	Consortium for Small-scale Modeling ensemble forecast with 2.2 km grid box size
DA	Data assimilation
DDF	Degree-day factor
DHM	Digital height model
EKF	Extended Kalman filter
EnKF	Ensemble Kalman filter
EPFL	Ecole polytechnique Fédérale de Lausanne
FOEN	Swiss Federal Office for the environment
GR4J	Modèle du Génie Rural à 4 paramètres Journalier
GSM	Glacier and SnowMelt model
HBV	Hydrologiska Byrans Vattenbalansavdelning
IDW	Inverse Distance weighting
KED	Kriging with External drift
KF	Kalman filter
KGE	Kling-Gupta efficiency
LCH	Laboratory of Hydraulic Constructions
MAD	Median absolute deviation
MeteoSwiss	Swiss Federal Office of Meteorology and Climatology
MG	MeteoGroup Switzerland AG
MINERVE	Modélisation des Intempéries de Nature Extrême du Rhône Valaisan et de leur Effets
MODIS	Moderate-Resolution Imaging Spectroradiometer
MRTE	Mean-root-transformed error
NDSI	Normalized Difference Snow Index
NS	Nash-Sutcliffe model efficiency coefficient
NS-ln	Nash-Sutcliffe model efficiency coefficient for log values
OA	Overal accuracy
OK	Ordinary kriging
PF	Particle filter
PPM	Pointe de la Plaine Morte (weather radar)
QPE	Quantitative precipitation estimate
RIDW	Regression inverse distance weighting
RCK	Regression co-kriging
REnKF	Recursive ensemble Kalman filter
RMSE	Root mean square error
RK	Regression kriging

RVB	Relative volume bias
SAC-SMA	Sacramento Soil Moisture Accounting
SCA	Snow-covered area
SFOE	Swiss Federal Office of Energy
SMN	SwissMetNet - Swiss automatic ground meteorological network
Snow-SD	Snow model with a Seasonal Degree-day factor
SOCONT	Soil CONTribution model
SPICE	Solid Precipitation Intercomparison Experiment
SWE	Snow Water Equivalent
URR	Upper Rhône River basin
VBScripts	Visual Basic Scripts
VBU	Volume-based update
WMO	World Meteorological Organization

1 Introduction

Without water, life on earth would not exist. Source of life, water is also source of energy, with hydropower representing 60% of the electricity production in Switzerland. Rivers and lakes are appreciated areas for recreation and can be used as means of transportation. However, water can also be source of fear, death and destruction. When severe precipitation hits a region, soils, rivers and lakes might not be able to store and evacuate the large volume of water, resulting in floods. These natural phenomena shaped the landscape in which we are living today and deposited nutrient-rich sediments that enriched the soil for agriculture. But floods also result in life losses and damages to infrastructures. Flood damage thus represents about one third of the economic losses induced by natural hazards worldwide [Bosello et al., 2018].

In Switzerland, 124 people died due to floods over the period 1946–2015, representing 12% of deaths linked to natural hazards in the country, whereas 37% died in avalanches and 16% due to lightning [Andres et al., 2017]. In terms of damage, floods represent 88% of the damage resulting from natural hazards when considering flood, landslide, debris flows and rockfall over the period 1972-2018 [WSL, 2019]. The yearly average damage linked to flood is estimated to CHF 306 million over the last four decades (Figure 1.1) [Andres and Badoux, 2019b]. Most of this damage is associated to particular events. Among them, it is worth mentioning two events. In October 2000, heavy precipitation coming from the South affected Switzerland. The Canton of Valais was particularly impacted, with 16 fatalities and a damage cost estimated to CHF 470 million in the Canton (CHF 670 million for the entire Switzerland) [OFEG, 2002]. In August 2005, another high flow event affected central Switzerland and resulted in damage estimated to CHF 2 billion, thereby the most expensive flood Switzerland has experienced [OFEG, 2005].

With climate change, the socio-economic impacts of river floods are expected to increase considerably [Alfieri et al., 2015]. Castellarin and Pistocchi [2012] already showed evidence of variations in the frequency regime of annual maximum floods in the last five decades in the Swiss Alps.

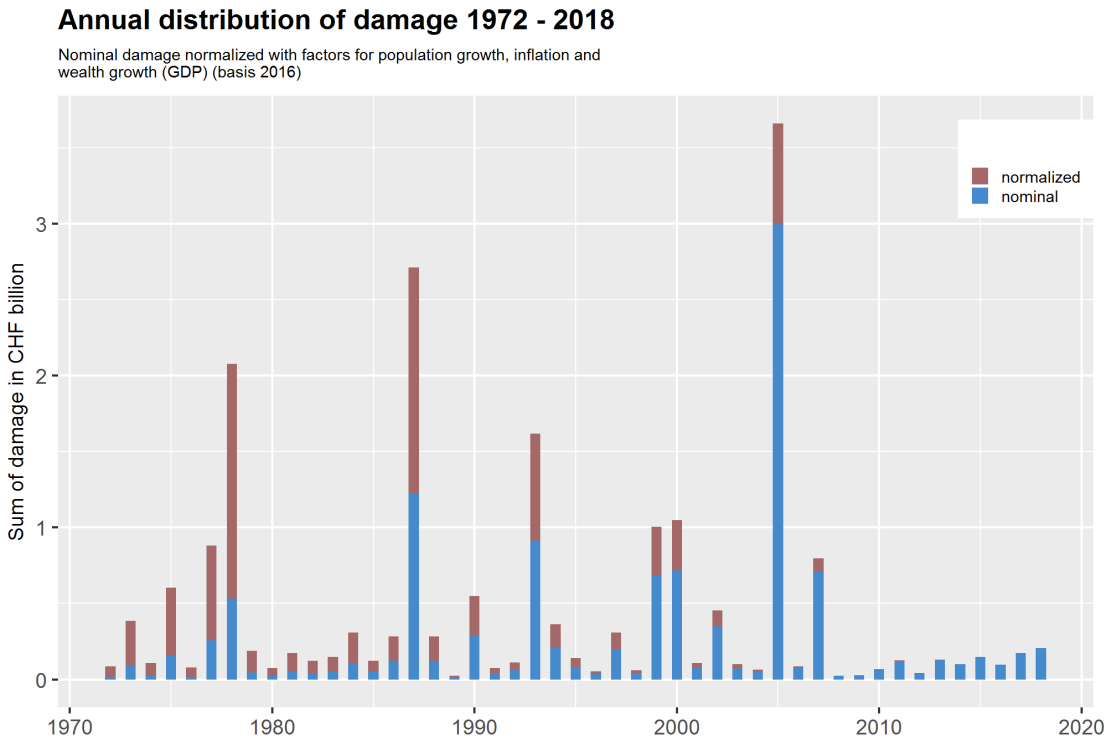

Figure 1.1 – Annual distribution of damage due to floods in Switzerland over the period 1972-2018. Source: Andres and Badoux [2019a]. Image courtesy: WSL.

To protect themselves against floods, humans have developed different strategies. One of them has been the construction of river embankments, to better control rivers. By limiting the extent of river channels, large surfaces have also been gained for agriculture and construction. In the case of the Upper Rhône River upstream of Lake Geneva in Switzerland, two important correction projects have been achieved, the first one over the period 1863-1894 and the second one over the period 1930-1960. The second correction mainly aimed at reinforcing the structures built during the first one. Unfortunately, floods continued to affect the Upper Rhône River basin and hydrological studies have shown that the current capacity is insufficient and has to be increased. This undercapacity motivated the Canton of Valais to start a third correction of the Rhône River, based mainly on an enlargement of the river bed and further reinforcement of the embankments.

1.1 Need for reliable hydrological forecasts

Another protection method against flood has been the development of flood forecasting systems. By foreseeing major flood events up to several days in advance, emergency measures can be taken with more lead time to protect the population and to reduce economic losses. This is particularly true in catchments like the Upper Rhône River basin, with large hydropower

reservoirs that can be operated to efficiently control the downstream discharges. To do so, operational flood forecasting systems have been implemented in many parts of the world. Adams and Pagano [2016] enumerates current flood forecast systems and operations around the world.

In 1999, the research project MINERVE (acronym in French of "*Modélisation des Intempéries de Nature Extrême du Rhône Valaisan et de leurs Effets*" [Jordan et al., 2008], meaning "*Modelling of extreme events in the Rhône of Valais and their effects*") was initiated by the Swiss cantons of Valais and Vaud with the objective of developing such a flood forecasting and management system for the Upper Rhône River basin upstream of Lake Geneva. After the major flood of October 2000 in the Canton of Valais, the need for such a system became even more evident.

1.2 The Upper Rhône River basin

The studied area corresponds to the Upper Rhône River (URR) basin, defined as the hydrological basin between the Rhône Glacier (on the east) and Lake Geneva (on the west). The catchment area is 5'351 km^2 (Figure 1.2) and the elevation range goes from 372 m a.s.l. at the outlet to 4'634 m a.s.l. on the top of the Dufourspitze, with a mean elevation of 2'158 m a.s.l. (Figure 1.3 shows the hypsometric curve (i.e. the cumulative distribution function) and the histogram of elevations in the basin). The area above 3'000 m a.s.l. represents 13.0% of the total area, whereas the part above 4000 m a.s.l. only covers 0.3% of the total area. The glacierized area has been estimated to 569.2 km^2 in 2010 [Fischer et al., 2015], which corresponds to about 10.6% of the total area.

Precipitation is spatially variable over the basin. The yearly average over the period 1981-2010 is 603 mm for the station Sion (SIO in Figure 1.2), at 482 m a.s.l. and located near the centre of the basin, whereas the station at Col du Grand St-Bernard (GSB), on the south-western border and situated at 2'472 m a.s.l., reported an average of 2'368 mm per year over the same period [MeteoSwiss, 2017]. Precipitation is observed all year long, with a monthly average minimum/maximum of 35 mm (April) and 64 mm (December) for SIO and 135 mm (July) respectively 248 mm (November) for GSB. Depending on the elevation, the solid precipitation fraction can represent a significant proportion of the annual precipitation. The available precipitation monitoring networks are presented in detail in Chapter 2.

Looking at the station Porte du Scex (abbreviated PDS in Figure 1.2), located 6 km upstream of Lake Geneva, the Upper Rhône River yearly average discharge is 182 m^3/s and the average yearly peak discharge is 645 m^3/s. The highest measured discharge occurred during the flood of October 2000 with 1363 m^3/s, representing a return period higher than 150 years [FOEN, 2017b].

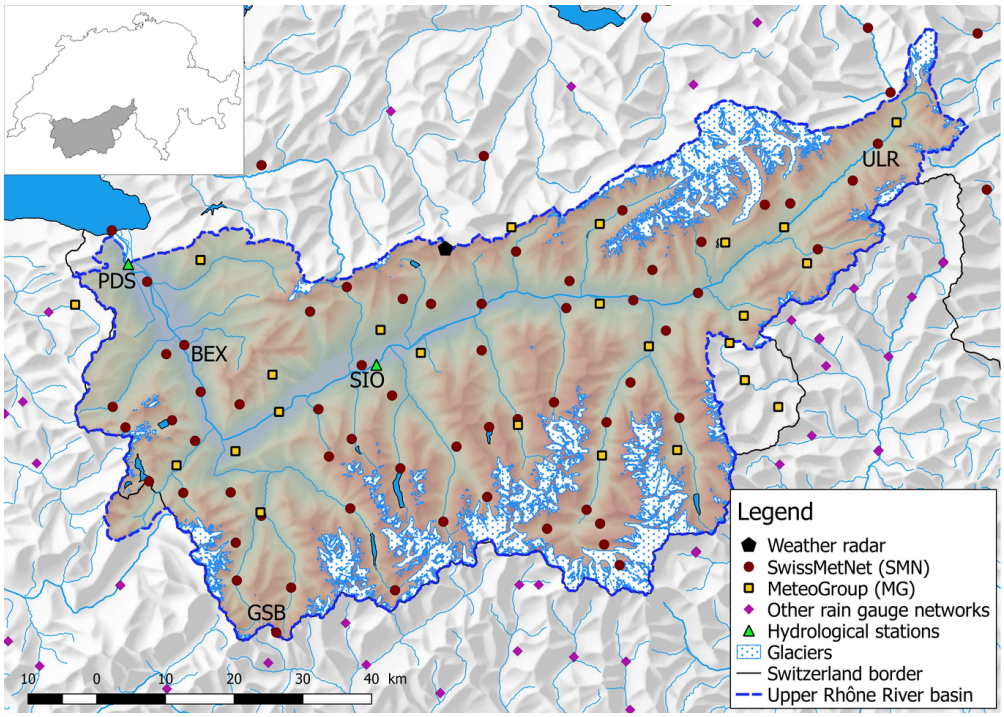

Figure 1.2 – Map of the Upper Rhône River basin with location of the MeteoSwiss, MeteoGroup and surrounding meteorological networks, as well as the Pointe de la Plaine Morte weather radar and a selection of hydrological stations. Abbreviations indicate the MeteoSwiss stations Sion (SIO), Col du Grand St-Bernard (GSB), Bex (BEX) and Ulrichen (ULR), later used in Chapter 2, as well as the hydrological stations Sion (SIO) and Porte du Scex (PDS). Glaciers and major rivers are also shown. (Topographic data source: Swisstopo [2017b] for rivers and lakes, Swisstopo [2013] for the glaciers (with modifications), Swisstopo [2005] for the digital height model (DHM), Swisstopo [2012] for the relief and Swisstopo [2017a] for the national boundary line).

The hydrology of the URR basin is strongly altered by many hydropower schemes. The cumulative operational discharge capacity is more than 500 m^3/s and the total storage capacity of the reservoirs is estimated to 1'195 million m^3 [García Hernández et al., 2014].

1.3 The MINERVE operational forecasting system

One of the primary objective of the MINERVE project (1999-2011) was to develop a hydrological-hydraulic model for the entire catchment [Jordan, 2007a,b, Hingray et al., 2010, Jordan et al., 2010, 2012, Tobin, 2012]. The model has been implemented in the Routing System modelling tool (RS II) developed within the MINERVE project by the Laboratory of Hydraulic Constructions (LCH) of the Ecole Polytechnique Fédérale de Lausanne (EPFL) [García Hernández et al., 2007, Bérod, 2013]. A decision-support system has also been developed to simulate different management scenarios [García Hernández et al., 2009a,b, García Hernández, 2011a,b].

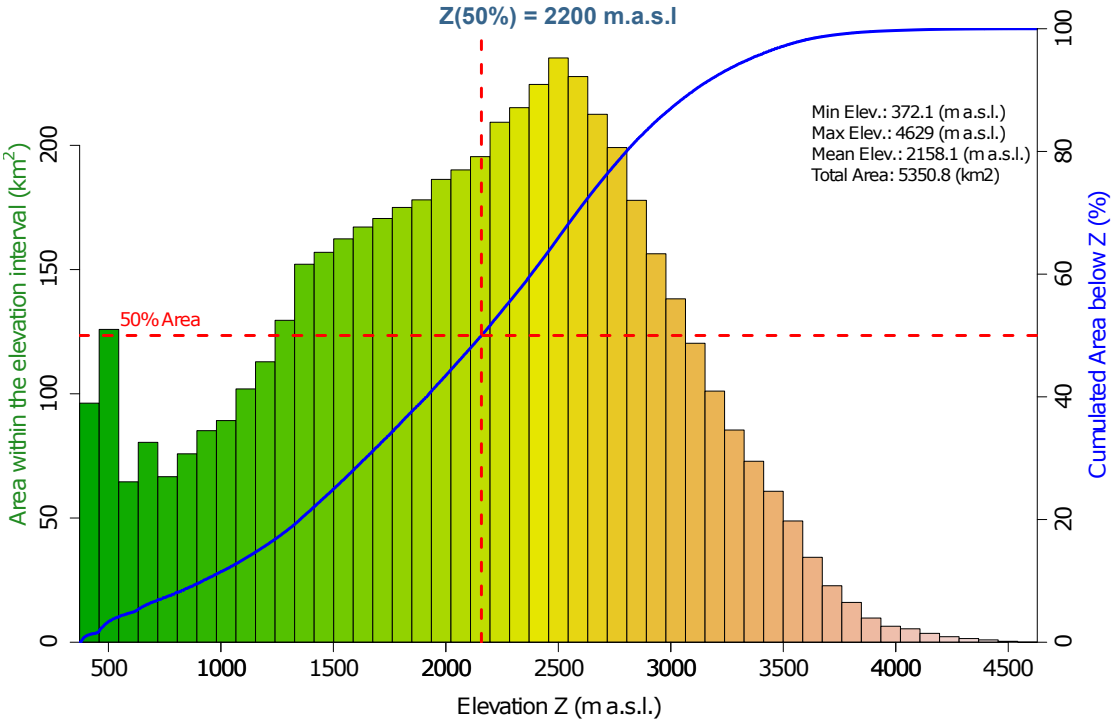

Figure 1.3 – Hypsometric curve (left axis) and histogram of elevations (right axis) of the URR basin. DHM data (spatial resolution of 25 m) are taken from Swisstopo [2005].

The hydrological model is based on a semi-distributed approach, which implies a division of the basin into sub-basins. During this step, hydraulic components such as reservoirs, gauging stations and hydropower plants are considered in addition to the hydrographic network. To account for meteorological processes induced by topography (e.g. temperature lapse-rate, rain-snow transition, orographic precipitation, etc.), the sub-basins are further divided into smaller entities, called elevation bands, each of them covering an elevation range of 300 to 400 m. Over the entire MINERVE basin, this leads to 269 sub-basins further divided into more than 1400 elevation bands.

In 2011, the Canton of Valais has given the mandate of developing and maintaining the MINERVE operational system to the Centre de recherche sur l'environnement alpin (CREALP), located in Sion. In that frame, the Routing System modelling tool has been further developed and completely recoded in C# to give place to the RS MINERVE software [García Hernández et al., 2019, Foehn et al., 2019a]. All the functionalities of the RS MINERVE software can be executed through Visual Basic Scripts (VBScripts), enabling complete automatization of the computation. Five different conceptual hydrological models, based on a simplified description of the physical components of a catchment, are implemented in RS MINERVE: GSM (Glacier and SnowMelt) and SOCONT (Soil CONTribution) [Schaefli et al., 2005, Hamdi et al., 2005],

HBV (Hydrologiska Byråns Vattenbalansavdelning) [Bergström, 1976], GR4J (Modèle du Génie Rural à 4 paramètres Journalier) [Perrin et al., 2003] and SAC-SMA (Sacramento Soil Moisture Accounting) [Burnash et al., 1973].

Since 2013, the forecasting system is operational for the entire URR basin and used as a tool for decision-making support [García Hernández et al., 2014]. To generate hydrological forecasts, the system uses the temperature and precipitation forecasts provided by the Swiss Federal Office of Meteorology and Climatology (MeteoSwiss). Two different forecast products are used operationally : COSMO-1 and COSMO-E. The COSMO-1 deterministic product, with a spatial resolution of 1.1 km, provides a short range weather forecast every three hours with a lead time of 33 hours (except one of 45 hours). The COSMO-E probabilistic product, with a spatial resolution of 2.2 km, provides a forecast with a horizon of 5 days and is generated twice a day.

The operational system is composed of three main components. First, two databases store all the required meteorological and hydrological input data. One database stores all the data from the ground stations. The second database has been set up to store the increasing number of spatial products used in the system, going from weather radar data to weather forecast and satellite images. Since 2018, a new database has been created to combine all these data in a unique database. The second component of the system is the computation process. The entire computation chain including data acquisition, management of RS MINERVE computations and storing results in the database is coded with the R language and environment for statistical computing [R Core Team, 2018]. Third, all the results including meteorological and hydrological observations and forecast are displayed on a web platform available to the stakeholders. Automatic email alerts and text messages are also sent in case of thresholds exceedance.

1.4 Research questions and organization of the thesis

The goal of this dissertation is to propose methodological improvements applicable to the above mentioned flood forecasting system in combination with a better representation of the meteorological data [Foehn et al., 2016a]. The thesis addresses three main scientific questions:

- How can precipitation data from different sources and of different types (from stations and weather radar) be combined to generate quantitative precipitation estimates for hydrological modelling ?
- How, and how much, can snow modelling in a hydrological model be improved by integrating snow-related data ?
- How can observed hydro-meteorological data be assimilated in real-time to increase the hydrological forecast performance in Alpine catchments ?

The present thesis addresses these questions in four chapters and is organized as follows:

- **Chapter 2** explores the combination of rain gauge data with weather radar data to propose an improved product of precipitation over the Upper Rhône River basin. The installation of the new weather radar of Pointe de la Plaine Morte, in June 2014, half a year before the start of the present project, represents an excellent new source of information and offers a terrain for exploration. The developed solution differs in several aspects from the operational methodology implemented by MeteoSwiss, described in Sideris et al. [2014a]. First, it considers not only the automatic monitoring network (SwissMetNet) of MeteoSwiss for the rain gauges data, but also the data from the private company MeteoGroup Switzerland AG. Thereby, the number of ground stations is increased. However, differences in terms of quality between the two networks imply a number of challenges discussed and illustrated in this chapter. Second, the methodology is not applied over entire Switzerland but only over the studied basin. This implies a more local computation but also brings new challenges such as having sufficient data for the interpolation methodology.

- **Chapter 3** proposes a methodology to define a global correction factor to be applied to hourly solid precipitation values before computing quantitative precipitation estimates (QPE). It builds on the previous chapter and exploits data of ground-based Snow Water Equivalent (SWE) to investigate measurement undercatch by rain gauges during winter. Using a temperature-index model, snow accumulation and melting is simulated at 11 SWE observation sites. The model is calibrated using snow-covered area fraction provided by satellite-based data from the Moderate-Resolution Imaging Spectroradiometer (MODIS). The performance is then evaluated by comparing the simulated SWE with the ground SWE measurements.

- In **Chapter 4**, the performance of the model considering different inputs and different calibration approaches is assessed from a hydrological point of view. The different products of precipitation presented in Chapters 2 and 3 are used as input data and performances are compared. In terms of calibration, two approaches are explored. First, a conventional calibration of all model parameters based exclusively on discharge data is performed. Second, a decoupling of the calibration is tested, with first a calibration of the degree-day factors based on MODIS data using the methodology developed at the pixel scale in Chapter 3 and second the other parameters are adjusted based on discharge data.

- **Chapter 5** presents the implementation of an Ensemble Kalman filter (EnKF) to improve the initial conditions of the state variables of the RS MINERVE model using observed discharge data. The proposed data assimilation scheme is based on an ensemble of model trajectories analysed to update the initial conditions before each hydrological forecast. The performance is compared to a scenario without data assimilation and to a simple data assimilation approach used operationally since 2017 in the MINERVE

system, based on a volume comparison over the last 24 hours preceding the forecast. The application is done over two sub-catchments of the URR basin.

- Finally, the **Conclusions** summarize the main findings of the thesis and present some outlook for future research in the different investigated fields.

2 Radar-rain gauge merging for spatial interpolation of precipitation

2.1 Introduction

Since the beginning of the forecasting system development (Section 1.3), enhancing the estimation of the spatial precipitation distribution has been identified as essential [Jordan, 2007a, García Hernández, 2011b, Tobin, 2012]. Indeed, to accurately predict flooding induced by heavy precipitation, it is crucial to estimate with good accuracy the causative precipitation [Sikorska and Seibert, 2018]. Two main data sources are usually considered: rain gauges (point observations) and weather radars (spatial information). Combining these two data types has been shown to produce improved precipitation estimates [Foehn et al., 2016b, Sideris et al., 2014a, Goudenhoofdt and Delobbe, 2009, Jewell and Gaussiat, 2015] for flood forecasting and hydrological modelling in general.

Rain gauges provide direct precipitation measurements which can be fairly accurate; but point observations are heterogeneously distributed over the domain and typically do not cover the entire elevation range of Alpine basins. They are also subject to various sources of error and uncertainty [Villarini and Krajewski, 2010, Cecinati et al., 2017a], such as wind-induced measurement errors [Nešpor and Sevruk, 1999], evaporation and wetting errors [Upton and Rahimi, 2003] or heating-related losses for heated tipping-buckets [Savina et al., 2012]. In addition, rain gauge values have to be considered to be spatially representative of their surrounding area, which is a strong hypothesis, in particular for short-time scales [Ciach and Krajewski, 1999, Villarini et al., 2008].

Weather radars, alternatively, provide a better spatial coverage but require a relatively sophisticated post-treatment of the signal back-scattered by the precipitation particles and are subject to significant bias and many sources of error [Germann et al., 2006, 2009, Berne and Krajewski,

This chapter is based on the scientific article "Spatial interpolation of precipitation from multiple rain gauge networks and weather radar data for operational applications in Alpine catchments" by Foehn A., García Hernández J., Schaefli B., De Cesare G. (2018). *Journal of Hydrology*. DOI: 10.1016/j.jhydrol.2018.05.027.

2013]. Radar estimates are in general well correlated both in space and time with rain gauge data, particularly for long accumulation periods but this correlation tends to decrease for sub-hourly accumulation periods [Sideris et al., 2014a].

A wide range of precipitation interpolation methods has been proposed in the literature for rain gauge data interpolation or radar-gauge combination, from rather simplistic methods such as Thiessen polygons [Thiessen, 1911] or Inverse distance weighting [Shepard, 1968] to more sophisticated methods such as simple and multiple linear regressions [Di Piazza et al., 2011], copulas [Vogl et al., 2012], ensemble spatial analysis [Frei and Isotta, 2019] and the wide range of geostatistical methods [Creutin et al., 1988]. Univariate geostatistical methods (e.g. simple or ordinary kriging) generally tend to smooth the interpolated variable and therefore struggle to accurately reproduce spatial variability. Multivariate geostatistical methods use additional spatial information from either static (e.g. elevation) or dynamic (e.g. weather radar) covariates to improve the interpolation performance [Wagner et al., 2012]. Different approaches of multivariate geostatistics applied to precipitations have been explored in the literature, including Kriging with external drift (KED) [Cantet, 2017], Co-kriging [Goovaerts, 2000], Conditional merging [Ehret, 2003] or Bayesian kriging [Verdin et al., 2015]. Ly et al. [2013] propose a methods review for spatial interpolation of daily rainfall data for hydrological modelling at the catchment scale.

Regarding possible covariates (additional information), only few studies focused on multivariate interpolation of hourly precipitation over Alpine catchments. Schiemann et al. [2011] showed that applying KED to hourly rain gauges and radar data over entire Switzerland performs better than interpolated rain gauge data or radar data alone. For flatter areas, Haberlandt [2007] has shown over the Elbe basin, in Germany, that for hourly precipitation, the most important additional information was the radar, followed by daily precipitation observations of a denser network with lower temporal resolution, and finally the elevation, which was considered “to play only a secondary role” in the studied case. Goovaerts [2000] reported that incorporating elevation can improve spatial interpolation of monthly and yearly rainfall when applied to a basin in Southern Portugal. Ly et al. [2011] analysed the integration of elevation in KED and Ordinary Co-kriging and concluded that it did not improve the interpolation accuracy for daily rainfall over a basin in Belgium. These observations tend to agree with Bárdossy and Pegram [2013], who found over three regions in Germany that “correlation between precipitation and topography increases with the length of time interval”. Sikorska and Seibert [2018] showed that radar-based daily precipitation estimates, adjusted to precipitation rates from ground stations, provided better flood predictions as compared to using only rain gauges observations.

Sideris et al. [2014a] proposed a methodology applied in Switzerland in which rain gauges were combined with weather radar data using data from the time step of interpolation as well as from the preceding time step (as secondary co-kriged variable) in a co-kriging with external drift (CED) approach. Comparing their spatio-temporal method with a classical KED approach, they concluded that the skill scores were similar when considering an aggregation

time of 60 min. However, for shorter aggregation periods (10-30 min.), CED resulted in higher performance values than KED. This methodology is used for the computation of the *CombiPrecip* product [MeteoSwiss, 2014b], the operational hourly spatialized precipitation product of the Swiss Federal Office of Meteorology and Climatology (MeteoSwiss).

Numerical weather forecasts can also represent an alternative covariate. Tobin et al. [2011] have applied KED for interpolation of precipitation and temperature in Switzerland using (i) elevation and (ii) the COSMO-7 weather forecast product of MeteoSwiss [MeteoSwiss, 2017]. Whereas temperature measurements were found to be "strongly correlated with the closest COSMO-7 grid point" at an hourly time step, good correlation between measurements and COSMO-7 estimates was observed for precipitation only for "cumulative data over the event". Tobin et al. [2011] thus proposed to use an event averaged linear drift for precipitation interpolation. Compared to Inverse distance weighting (IDW) and Ordinary kriging (OK), KED with elevation tended to produce the least biased estimation in their study. In terms of error, OK and both KED methods using elevation and the COSMO-7 data had similar scores and outperformed IDW. However, when looking only at stations above 1500 m a.s.l., KED with COSMO-7 showed the highest error for their case study in Switzerland.

Covariates can also be processed before being used in combination with rain gauge data. Berndt et al. [2014] showed that smoothing radar data both spatially with the adjacent cells or/and temporally over several time steps improved the performance of merging rain gauges and radar data. Instead of always using the radar pixel containing a rain gauge, Sideris et al. [2014b] incorporated in the *CombiPrecip* product a convection control routine, in which the coefficient of dispersion over the 25 pixels around the rain gauge pixel is computed. When a certain threshold is exceeded, the value of the pixel with the closest value to the rain gauge within the 25 pixels is used for the merging.

Commercial microwave link networks have also been explored over the last decade as a supplementary source of data [Messer et al., 2006]. Hydrological applications show a great potential of this approach, in particular in poorly equipped areas [Smiatek et al., 2017].

Besides providing a reliable radar-rain gauge combination for the target region, the objective of this chapter is to assess in detail what gain can be expected from combining the most recent radar data for precipitation interpolation with rain gauge data from two ground-based networks of different data quality. This includes a comparison to the commonly used deterministic Inverse distance weighting method applied to rain gauge data as baseline scenario. Another key question is the quality of the radar-gauge combination methodology if applied to the data situation prevailing before the installation of a new weather radar covering the studied basin in 2014. Using the data from the already existing other Swiss weather radars, such an application allows computing series over a longer time period which is required for hydrological modelling purposes. Finally, the chapter also aims at analysing the effect of incorporating additional station networks located within and around the target region in the interpolation computation.

2.2 Input data and events description

2.2.1 Rain gauges data within the basin

Several networks of rain gauges are available within the studied basin, but only the two networks with heated rain gauges have been considered for this study, in order to make the methodology applicable all year round. The first one is the SwissMetNet [MeteoSwiss, 2016a] network of MeteoSwiss, hereafter refereed as SMN. The SMN data are based on reliable equipment and subject to a serious quality control [Musa et al., 2003]. On July 1^{st}, 2013, 40 SMN stations were operational within the basin. This number had increased to 58 on March 1^{st}, 2017, which represents an average area per station of 92 km^2, which makes it a particularly dense network. As a comparison, on the same date, the Swiss average was 168 km^2 per station and values reported by other authors tend to be higher: about 571 km^2 per station in Germany [Berndt et al., 2014] or 135 km^2 in the Wallon region, where Goudenhoofdt and Delobbe [2009] described the network as "dense". A complete list of used SMN stations is given in Appendix B, Tables B.1 and B.2.

For the analysis, all available stations have been considered in each event, regardless whether the station was available or not for the other events. This implies that the number of stations considered for the computation increases over the events between 2012 and 2017. Table 2.1 lists the equipment used in the different networks [MeteoSwiss, 2015] and the number of stations.

The second network is composed of 23 stations of the private company MeteoGroup Switzerland AG, hereafter refereed as MG. More stations of this network are available within the basin, but data from only 23 stations were available for the present study, which have been selected to supplement SMN stations over uncovered areas. A complete list of used MG stations is given in Table B.3.

Combined with the SMN stations, the average area per station over the basin drops to 66 km^2. The elevation range is 381 to 2472 m a.s.l. for the SMN stations and 460 to 2347 m a.s.l for the MG stations, with median elevations of respectively 1537 and 1365 m a.s.l. The analysis of the data has shown a tendency of MG stations to report less precipitation than the SMN stations, with differences largely exceeding 20% for some hourly time steps. Similar observations had been made by MeteoSwiss when comparing their manual daily precipitation measurements with automatic observations from MeteoGroup stations (J. Fisler, MeteoSwiss, personal communication, January 9, 2017). In the field intercomparison of rain intensity gauges realized by Vuerich et al. [2009] for the account of the World Meteorological Organization (WMO), all three concerned station types, or their predecessor (for the OTT equipment), had been tested [Lanza and Vuerich, 2009]. The stations used by MeteoSwiss were evaluated as "satisfactory" (Lambrecht) and "very good" (OTT), whereas the stations installed by MeteoGroup (Davis) were evaluated as "insufficient". Based on these conclusions, the SMN stations have been defined for this study as being the "primary" network and the MG stations as the "secondary"

network. This distinction will be considered when using data from both networks. It is worth mentioning here that neither the MeteoSwiss nor the MeteoGroup station data are corrected for undercatch of solid precipitation, which is known to have an effect on solid precipitation intensity estimation in mountainous regions [Egli et al., 2009].

2.2.2 Rain gauges data around the basin

In addition to the presented two networks located within the basin (81 stations) and their 12 stations located around the basin (Table 2.1), 62 stations of networks located around the basin and equipped with heated rain gauges have been considered (Table 2.1). This additional information is expected to allow a better estimation at the border of the basin as well as a more correct estimation of the precipitation fields for example in the southern neighbouring area. This is important as more than half of the meteorological situations having produced more than 110 mm/d of precipitation over 3 days in the Upper Valais since 1975 have originated from south according to Attinger and Fallot [2003], as cited in Tobin et al. [2011].

Table 2.1 – List of considered rain gauge networks and respective characteristics. Number of stations for MeteoSwiss refers to March 1^{st}, 2017.

Network	**Number of stations**	**Location**	**Sensor model**	**Period**
SwissMetNet (SMN)	17 (+9)	Basin (+ neighbouring cantons)	*1518 H3* and *15188* by Lambrecht (tipping bucket)	2012-2017
SwissMetNet (SMN)	41 (+2)	Basin (+ neighbouring cantons)	*Pluvio*^{2} by Ott (weighing principle)	2012-2017
MeteoGroup (MG)	23 (+1)	Basin (+ France)	*Rain Collector II* by Davis (tipping bucket)	2012-2017
Kanton Bern	11	Bern (Switzerland)	Unknown (heated)	2012-2017
MeteoFrance	5	France	Unknown (heated)	2012-2017
EDF	10	France	Unknown (heated)	2012-2016
Regione Aosta	25	Italy	Unknown (heated)	2012-2017
ARPA Piemonte	11	Italy	Unknown (heated)	2012-2015

2.2.3 Weather radar data

MeteoSwiss has operated since 1995 three weather radars (La Dôle, Albis, Monte Lema) covering the entire national territory of Switzerland [MeteoSwiss, 2016c], modernized in 2011 and 2012 with new technologies [MeteoSwiss, 2012]. In May 2014, a fourth installation has been inaugurated at the Pointe de la Plaine Morte (see Figure 2.1), within the basin studied in here [MeteoSwiss, 2014a], followed two years later by a fifth radar (Weissfluhgipfel) in the Eastern part of Switzerland [MeteoSwiss, 2016] (Figure 2.1). The radar of Pointe de la Plaine Morte is officially operational since June 2014. The two additional radars contributed to a better radar

coverage of Alpine regions [Germann et al., 2015]. The back-scattered signal measured by the five dual-polarization Doppler C-band radars [Gabella et al., 2017] is transformed into rain rate estimates through several procedures, described in Germann et al. [2006]. Radar precipitation estimates are generated every 5 minutes over a 1-km resolution raster based on a combination of the data of the available radars over Switzerland. For the present study, the hourly aggregated radar precipitation estimates product of MeteoSwiss is used, classified into 256 rain estimates categories. The computation routine of the product had been optimized by MeteoSwiss for the configuration with 3 weather radars in Switzerland. A new radar precipitation estimates product is generated by MeteoSwiss since February 2018, but no historical data are yet available (MeteoSwiss, personal communication, March 7, 2018).

Figure 2.1 – Location of the five weather radars of MeteoSwiss. Image reproduced with permission of the rights holder, MeteoSwiss. (Background: Swisstopo)

It is worth pointing out that the highly mountainous aspect of the studied basin implies an accuracy loss of the radar estimate as compared to flatlands [Erdin et al., 2012]. Beam shielding by mountain ranges is certainly one of the major issues, as discussed later in Section 2.5. To reduce this effect, a fixed adjustment map computed based on a long term comparison between weather radar estimation and rain gauge measurements is used by MeteoSwiss in the computation of their radar precipitation estimates product [Germann et al., 2006]. However, this long-term comparison-based correction does not consider the data of the two newly installed radars. Positive effect on the basin of interest is therefore probably lower than for some other regions of Switzerland. Ground echoes elimination also requires a proper pre-treatment of the data. In addition, radar data suffer of bias issue, by over- or under-shooting the precipitation. This is why they are combined with rain gauges to properly

adjust the precipitation field. In addition, solid precipitation estimation is known to be more challenging than the liquid phase, resulting in better detection performance in summer than in winter [Speirs et al., 2017], whereas melting snow tends to enhance the back-scattered signal [Germann et al., 2006].

2.2.4 Events description

The main analysis is carried out on four events (identified as 1 to 4) that occurred over the period of data availability for the meteorological radar of Pointe de la Plaine Morte (2014-2017). Additionally, two events identified as A and B in 2012 and 2013, corresponding to the highest peak flow in the basin over the 2008-2017 period, as well as an event identified as C in July 2014 during which the radar of Pointe de la Plaine Morte was temporary not operating, are also considered to discuss the performance of the methodology before the installation of the radar of Pointe de la Plaine Morte. This is important as data over several years are necessary when using the interpolated data for hydrological model calibration.

The four events considered for the main analysis cover different seasons and were chosen for their high precipitation accumulation over the events. The period for each event has been defined such as to start two hours before the first hour with at least four SMN stations reporting at least 1.5 mm/h, and to stop two hours after the last hour respecting this condition; interruptions of less than 12 h of the above mentioned condition were considered to be part of the same event.

The characteristics of the events are given in Table 2.2 and presented hereafter, listed in chronological order. The median and maximum accumulation values are computed from the rain gauge values. The snow line elevation has been estimated from archives of short term weather forecasts of MeteoSwiss. In fact, even if recent developments enable hydrometeor type analysis from radar data [Grazioli et al., 2015], snow line elevations cannot yet be estimated directly from the radar data. Return periods are provided by MeteoSwiss [2016b] from which only statistically robust results were considered. Peak discharges (Qmax) and corresponding return periods of the events at the hydrometric stations [FOEN, 2017a] in Sion and in Porte du Scex, at the outlet of the basin (Figure 1.2), are also indicated in Table 2.2 and discussed hereafter where relevant. All times are given in UTC+1.

Table 2.2 – Characteristics of the seven analysed events.

Event identifier	**A**	**B**	**C**	**1**	**2**	**3**	**4**
Year	2012	2013	2014	2014	2015	2016	2017
Start [day.month Time]	1.7 12:00	28.7 21:00	28.7 11:00	4.11 08:00	30.4 22:00	10.1 07:00	5.3 15:00
End [day.month Time]	2.7 16:00	29.7 17:00	29.7 15:00	6.11 04:00	4.5 10:00	13.1 04:00	7.3 13:00
Duration [h]	28	20	28	44	84	69	46
Season	Summer	Summer	Summer	Fall	Spring	Winter	Winter
Approx. snow line elevation [m a.s.l.]	3200-3400	2600	2500-3100	800-2000	1800-2600	800-1400	700-1400
Plaine Morte radar data	No	No	No	Yes	Yes	Yes	Yes
Median accumulation at stations [mm]	24.3	39.3	45.5	37.5	96.2	41.2	34
Maximum accumulation at a station [mm]	65.3	69.7	62.7	179.5	375.7	158	150.7
SMN stations (number)	28	40	52	52	52	55	58
MG stations (number)	20	22	23	23	23	23	23
Qmax at Sion [m^3/s]	703	708	394	146	231	64	53
Qmax at Porte du Scex [m^3/s]	864	901	537	272	606	191	139

Events without Pointe de la Plaine Morte data

Event A: 1.7.2012 12:00 to 2.7.2012 16:00
The event of July 2012 mostly concerned the eastern part of the basin. The overall precipitation was not particularly intense, with a median accumulation over all the stations of 24.3 mm, but with a snow line elevation reaching 3400 m a.s.l., most of the precipitation fell as rain. This resulted in a peak discharge in the Rhône at Sion of 703 m^3/s on 2 July [FOEN, 2017a], corresponding to an estimated return period of 20 years according to FOEN [2017b].

Event B: 28.7.2013 21:00 to 29.7.2013 17:00
The event of July 2013 touched the entire basin with locally intense storms (median accumulation of 39.3 mm). The high snow line elevation, situated at about 2600 m a.s.l., resulted in a high proportion of rainfall, which led to a peak discharges of 708 m^3/s in Sion and 901 m^3/s in Porte du Scex on 29 July [FOEN, 2017a]. The return period of the discharge in Sion was estimated to 21 years [FOEN, 2017b].

Event C: 28.7.2014 11:00 to 29.7.2014 15:00
A westerly depression affected the entire basin and particularly its western part. The median accumulation reached 45.5 mm over the event. The snow line elevation varied between around 2500 and 3100 m a.s.l. Compared to the events in 2012 and 2013, the intense precipitation was less concentrated in time, probably partially explaining why the resulting flow in downstream rivers did not reach values as high as in 2012 and 2013 (see Table 2.2). The event has the particularity of having taken place after the entry into service of the radar of Pointe de la Plaine Morte, but with the mentioned radar not being in operation over the event (temporary interruption). This offers a station density close to the maximum density of 2017 with a radar data configuration corresponding to the one of before 2014 (without the radar of Pointe de la Plaine Morte), which is interesting for analysis purposes.

Events including Pointe de la Plaine Morte data

Event 1: 4.11.2014 08:00 to 6.11.2014 04:00
An active westerly disturbance with polar air resulted in heavy precipitation mostly in the Eastern part of the basin. The median accumulation over the 44 hours was 37.5 mm but station Ulrichen (Figure 1.2) reported for example 96.2 mm over 16 hours, corresponding to a return period of 18 years according to MeteoSwiss [2016b]. The snow limit varied between 800 and 2000 m a.s.l.

Event 2: 30.04.2015 22:00 to 4.5.2015 10:00
A heavy precipitation event coming from the west with air relatively mild and very humid reached Switzerland, with successive precipitation episodes. The snow limit varied between 1800 and 2600 m a.s.l. The median accumulation was 96.2 mm for a maximum accumulation over the 84 hours of 375.7 mm (in station Clusanfe). In terms of return period, the station Bex (Figure 1.2), in the western part of the basin, reported a rainfall accumulation of 100.9

mm over 3 days, corresponding to a return period of 58 years. Other stations within the basin reported accumulation with return periods exceeding 10 years.

Event 3: 10.1.2016 07:00 to 13.1.2016 04:00
A series of disturbances reached Switzerland from the west with heavy snowfalls on the Alps, exceeding in some places 100 cm of fresh snow over the 3 days. The snow limit varied between 800 and 1400 m a.s.l. and the median liquid-equivalent precipitation was 41.2 mm.

Event 4: 5.3.2017 15:00 to 7.3.2017 13:00
Strong westerly winds resulted in successive rainy episodes towards the Swiss Alps, with a median precipitation of 34 mm. The snow limit varied between 700 and 1400 m a.s.l. over the event, thus a large fraction of the precipitation fell as snow.

2.3 Methodology

The high spatial variability of precipitation implies the use of methods capable of analysing and reproducing as reliably as possible the spatial pattern of the precipitation fields. On one side, the interpolation method should be efficient in combining the available rain gauge and radar data, considering different networks of ground stations. On the other side, for being used operationally, it should not imply long computational time and must work on an automatic basis.

2.3.1 Estimation methods

Five different estimation methods are compared within this work, ranging from commonly used methods to the newly proposed one handling with two non-collocated rain gauge networks of different quality. The first method is the so-called Inverse distance weighting method [Shepard, 1968], hereafter referred to as IDW, currently used within the MINERVE forecasting system and therefore considered as the baseline scenario. This method only uses the rain gauge data. The second method considers directly the radar value over the entire basin. The three other methods combine rain gauge and radar data by applying a multiplying coefficient to the radar raster, based on a linear regression of the radar data on the rain gauge data, to obtain a trend ("corrected radar"). Residuals, defined as the difference between the value observed at a rain gauge and the value of the containing pixel of the trend, are then computed at each gauge location before being interpolated. The way this interpolation is carried out differentiates the three last methods. The first one is applying IDW to the residuals, whereas the two others are based on a kriging approach [Webster and Oliver, 2007, Delhomme, 1978]. Finally, interpolated residuals are added to the trend to get the final product. Table 2.3 summarizes the five methods.

Table 2.3 – Estimation methods.

Name	Short name	Rain gauges	Radar	Remark
Inverse distance weighting	IDW	Yes	No	Reference
Radar value	Radar	No	Yes	Radar data
Regression inverse distance weighting	RIDW	Yes	Yes	IDW on residuals
Regression kriging	RK	Yes	Yes	Simple kriging on residuals
Regression co-kriging	RCK	Yes	Yes	Co-kriging on residuals

The implementation has been done on the R language and environment for statistical computing [R Core Team, 2018]. For the three regression methods, the methodology and nomenclature is partly based on Sideris et al. [2014a].

Inverse distance weighting (IDW)

The Inverse distance weighting method [Shepard, 1968] is a deterministic interpolation method [Ly et al., 2013], in the sense that it does not exploit the statistical properties of the observations sample, thus not providing a prediction errors assessment. In general, the aim of interpolation is to estimate the precipitation depth p at an unsampled spatial location s_0 with coordinates (x_0, y_0) using the available observation data at rain gauges (see Table 2.7 for all variables of the chapter). IDW applies a linear combination of the observations within a research radius ρ, with a decreasing influence with increasing distance. The rain gauge measurements vector over a period t is given by:

$$\boldsymbol{g}(t) = [g(s_1, t), g(s_2, t), ..., g(s_N, t)] \tag{2.1}$$

where N is the number of available rain gauge measurements over the period t and $s = (x, y)$ the spatial-coordinate vector of a given point.

The estimated precipitation $\hat{p}(s_0, t)$, at a given location s_0, is then given by:

$$\hat{p}(s_0, t) = \begin{cases} g(s_i, t) & \text{if } \exists\, i : d(s_0, s_i) = 0 \\ \frac{\sum_{i=1}^{N} \lambda_i g(s_i, t)}{\sum_{i=1}^{N} \lambda_i} & \text{else } \forall\ i\ : 0 > d(s_0, s_i) \leqslant \rho \end{cases} \qquad \forall\, s_0 \epsilon D \subseteq \mathbb{R}^2 \tag{2.2}$$

where

$$\lambda_i = \frac{1}{d(s_0, s_i)^\beta} \tag{2.3}$$

with d being the distance between the location of interpolation and the location of observation i, β a power coefficient, ρ the research radius and D the spatial domain ; $\mathbb{R}$ is the set of real numbers. The normalization allows the sum of the weights to equal 1.

Radar value (Radar)

The Radar value method consists in using directly the radar data provided by MeteoSwiss as the precipitation estimation over the basin. The quality of the radar product can thereby be investigated.

Regression inverse distance weighting (RIDW)

In the three remaining methods, the radar information is used to compute a trend of the precipitation field with a multiplicative coefficient. It is worth noting here that merging rain gauge and radar data implies several hypotheses [Sideris et al., 2014a]. Firstly, it is assumed that for both the rain gauges and the radar estimates, the measured physical quantity is the precipitation depth over spatial blocks of a size equal to the spatial resolution of the radar (1 km^2). This ignores the difference in spatial resolution. In complex topographies like in the context of this study, this can have implications due to the limited spatial representativeness of rain gauges. Secondly, the precipitation estimates of the radar over a spatial block of 1 km^2 is assumed to reflect the precipitation depth falling on the surface of the same block. This presumes perfect vertical precipitation fluxes and no exchange with adjacent blocks, which is not the case in reality. In addition, it must be noted that the precipitation depth estimates given by the radar can be affected by areas of invisibility due to shielding of the radar beam by mountain ranges. This obviously also impacts the performance of the interpolation.

In addition to the rain gauge measurements vector $\boldsymbol{g}(t)$ defined in the IDW method, the radar precipitation estimates at rain gauge locations over the period t are considered:

$$\boldsymbol{r}(t) = [r(s_1, t), r(s_2, t), ..., r(s_N, t)] \tag{2.4}$$

During the interpolation, radar precipitation estimates at each interpolation point are also used.

In geostatistics, a random process $Z(s,t)$ can be modelled as the sum of a deterministic part $m_Z(s,t)$, corresponding to the average or trend component, and a stochastic residual

component $\epsilon(s,t)$, which corresponds to local fluctuations of the trend, so that:

$$Z(s,t) = m_z(s,t) + \epsilon(s,t) \quad \forall\, s\,\epsilon\, D \subseteq \mathbb{R}^2; t\,\epsilon\, T \subseteq \mathbb{R} \tag{2.5}$$

where s is the vector of spatial coordinates of a given point and T the temporal domain.

In the context of the present work, Eq.(2.5) can be rewritten for the precipitation depth p over the entire domain as:

$$p(s,t) = m_p(s,t) + \epsilon(s,t) \tag{2.6}$$

The trend $m_p(\boldsymbol{s},t)$ for a spatial coordinates vector $\boldsymbol{s}$ is commonly modelled as a linear function of a smoothly varying external variable [Goovaerts, 1997] . In our case, this external variable is the radar $r(\boldsymbol{s},t)$:

$$m_p(\boldsymbol{s},t) = a(t)r(\boldsymbol{s},t) \tag{2.7}$$

where $a(t)$ is a regression coefficient and $r(\boldsymbol{s},t)$ is the radar values vector at time t. The coefficient $a(t)$ is computed as the slope of a linear regression of all pairs of points composed of the gauge values on the y-axis and the values of the containing radar pixel on the x-axis. $a(t)$ is assumed to be constant spatially in the interest of robustness.

In other methods, such as Kriging with external drift (KED), the trend is computed using two regression parameters (thereby adding also an intercept) and often evaluated within the kriging estimation process itself (e.g. in KED). The choice of a unique parameter has been motivated by the wish of maintaining zero precipitation in the trend where there was no precipitation reported by the radar estimates.

To compute the residuals $\epsilon(\boldsymbol{s},t)$, the trend $m_p(\boldsymbol{s},t)$ is subtracted from the observed value at the station locations:

$$\epsilon(\boldsymbol{s},t) = g(\boldsymbol{s},t) - m_p(\boldsymbol{s},t) = g(\boldsymbol{s},t) - a(t)r(\boldsymbol{s},t) \tag{2.8}$$

The residuals $\epsilon(\boldsymbol{s},t)$ are then interpolated using the inverse distance weighting method to obtain the interpolated residuals $\hat{\epsilon}_{\mathrm{RIDW}}(s_0,t)$ at location s_0. The final estimate is obtained by adding the trend $m_p(s_0,t)$ to the interpolated residual :

$$\hat{p}_{\mathrm{RIDW}}(s_0,t) = m_p(s_0,t) + \hat{\epsilon}_{\mathrm{RIDW}}(s_0,t) \qquad \forall\, s_0 \epsilon D \subseteq \mathbb{R}^2 \tag{2.9}$$

Figure 2.2 illustrates the different steps of the RIDW method.

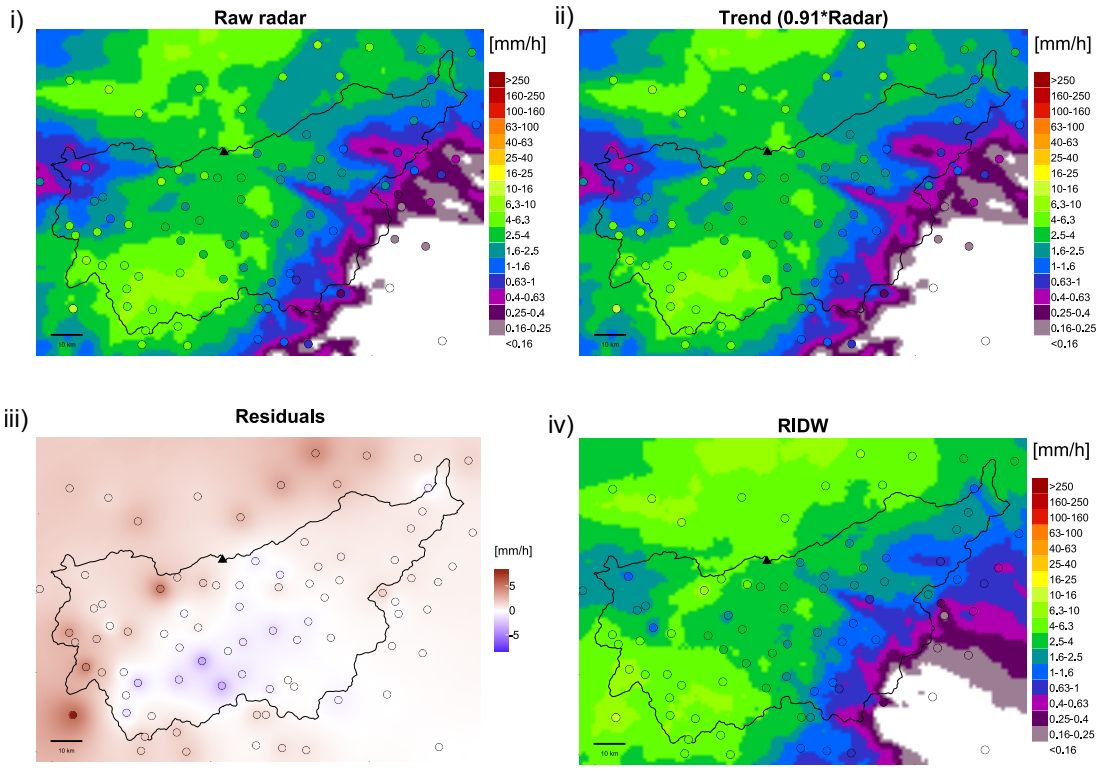

Figure 2.2 – Illustration of the different steps in RIDW: i) Radar data ; ii) Trend obtained by multiplying the radar data by the regression coefficient (Eq.2.7); iii) Residuals computed for each station and interpolated ; iv) Final product obtained by adding the trend (ii) and the interpolated residuals (iii). Circles represent rain gauge locations and filling colour the precipitation intensity observed at the station. Note that the colour classes division is not linear. The black triangle represents the radar of Pointe de la Plaine Morte. (Time step: 01-05-2015 2200 GMT+1).

Regression kriging (RK)

Kriging is a family of interpolation methods in which the covariance between observations is used to define a linear combination of the observations for interpolation. Practically, kriging methods consider the increasing dissimilarity between observations to characterize the spatial structure of the data. One of the conditions to apply the elementary methods of kriging, Simple and Ordinary kriging, is to assume the random variable to be first-order stationary: the expected value is constant over the domain of interpolation. This condition is hardly satisfied when working directly with rain gauge data, as it might rain for example only in one part of the basin. This non-stationarity of the precipitation fields is here addressed by removing the same trend based on the radar data as in RIDW so that Simple or Ordinary kriging can be applied to the computed residuals. This is however an approximation as the non-stationarity of the precipitation statistical properties cannot be fully captured by the radar data.

This approach is called Regression kriging (RK) in the present study, according to the nomenclature in Odeh et al. [1995]. Other names have been proposed for similar approaches in the literature: *kriging combined with linear regression* [Ahmed and De Marsily, 1987], *kriging detrended data* [Phillips et al., 1992], *kriging with a trend model* [Goovaerts, 1997] or *residual kriging* [Alsamamra et al., 2009]. Hengl et al. [2007] discussed the characteristics of *regression-kriging* and applied the approach to three case studies. RK is somewhat similar to Kriging with external drift (KED), the difference being that the linear regression and the kriging interpolation is done in successive steps in RK and all-at-once in KED. This choice of successive steps allows us to define different subsets of stations for (a) the linear regression step, (b) the variogram computation for the spatial interpolation of the residuals and (c) the interpolation of the residuals, to explore for example a larger number of stations in the last step.

Equations 2.5 to 2.8 about trend and residuals computation remain valid for RK. The covariance of the residuals at the locations of observation is given by the NxN covariance matrix $\boldsymbol{C_{aa}}$:

$$\mathbf{C_{aa}} = \begin{pmatrix} \sigma_Z^2 & C_{12} & \cdots & C_{1N} \\ C_{21} & \sigma_Z^2 & \cdots & C_{2N} \\ \vdots & \vdots & \ddots & \vdots \\ C_{N2} & C_{N2} & \cdots & \sigma_Z^2 \end{pmatrix} \tag{2.10}$$

where each element $C_{i,j}$ of the matrix is given by the covariance between the observation locations i and j and σ_Z^2 is the variance of the observations. Assuming a gaussian distribution of the residuals (discussed later in Subsection 2.3.3) and considering a constant zero mean and known variance, Simple kriging is used to spatialize the residuals. Considering the two conditions imposed by the kriging approach which are (i) an unbiased estimator and (ii) a minimal estimation variance, the following equation is obtained [Webster and Oliver, 2007]:

$$\mathbf{C}_{aa}\lambda = \mathbf{c_a} \tag{2.11}$$

where $\mathbf{c_a}$ is the covariance vector between the locations of interpolation and the observation locations.

Resolution of the system given in Eq.(2.11) provides the weights for the linear kriging predictor used to compute residual values at the interpolation location s_0, given by the linear combination of the observations:

$$\hat{\epsilon}_{\mathrm{RK}}(s_0, t) = \sum_{i=1}^{N} \lambda_i \epsilon(\mathbf{s}, t) \tag{2.12}$$

which is then added to the trend $m_p(s_0, t)$ to get the expected value of the precipitation depth:

$$\hat{p}_{\mathrm{RK}}(s_0, t) = m_p(s_0, t) + \hat{\epsilon}_{\mathrm{RK}}(s_0, t) \qquad \forall s_0 \epsilon D \subseteq \mathbb{R}^2 \tag{2.13}$$

Interpolation of the residual is done using a global neighbourhood, that means all the points are used for the interpolation.

Regression co-kriging (RCK)

Based on the comparative analysis between the MeteoSwiss and MeteoGroup networks (see Subsection 2.2.1), the choice was made to explore a variant of Regression-kriging using co-kriging and hereafter referred to as Regression co-kriging (RCK). Co-kriging has the advantage of offering the possibility of considering more than one variable in the kriging interpolation.

Thus, the multivariate RCK variant allows considering different vectors of rain gauges. Instead of having only one vector of observations, vector $\boldsymbol{g}(t)$ of Eq.(2.1) is replaced by two vectors:

$$\boldsymbol{g_a}(t) = [g(s_{a,1}, t), g(s_{a,2}, t), ..., g(s_{a,N_a}, t)] \tag{2.14}$$

$$\boldsymbol{g_b}(t) = [g(s_{b,1}, t), g(s_{b,2}, t), ..., g(s_{b,N_b}, t)] \tag{2.15}$$

where the subscripts a and b refer to the primary (a) and secondary (b) networks and N_a and N_b are the number of available rain gauges in the primary and in the secondary network over the period t.

Similarly, the radar precipitation estimates' vector of Eq.(2.4) is replaced by two vectors:

$$\boldsymbol{r_a}(t) = [r(s_{a,1}, t), r(s_{a,2}, t), ..., r(s_{a,N_a}, t)] \tag{2.16}$$

$$\boldsymbol{r_b}(t) = [r(s_{b,1}, t), r(s_{b,2}, t), ..., r(s_{b,N_b}, t)] \tag{2.17}$$

Statements about the trend (based on radar data with a regression on station data) and residuals computation of Equations 2.5 to 2.8 remain valid. The residuals are computed with the two equations:

$$\epsilon_a(\boldsymbol{s_a}, t) = g_a(\boldsymbol{s_a}, t) - a_a r_a(\boldsymbol{s_a}, t) \tag{2.18}$$

$$\epsilon_b(\boldsymbol{s_b}, t) = g_b(\boldsymbol{s_b}, t) - a_b r_b(\boldsymbol{s_b}, t) \tag{2.19}$$

where a_a and a_b are the multiplicative coefficients for the primary and secondary variables computed with a linear regression of the radar data on the rain gauge data. These two terms are the result of a linear regression computed for each of the corresponding subsets of data with respect to the corresponding radar data.

The consideration of two variables in RCK instead of one modifies Eq.(2.11) as follows [Myers, 1982]:

$$\begin{pmatrix} \mathbf{C_{aa}} & \mathbf{C_{ab}} \\ \mathbf{C_{ba}} & \mathbf{C_{bb}} \end{pmatrix} \begin{pmatrix} \lambda_a \\ \lambda_b \end{pmatrix} = \begin{pmatrix} \mathbf{c_a} \\ \mathbf{c_b} \end{pmatrix} \tag{2.20}$$

where $\mathbf{c_a}$ and $\mathbf{c_b}$ are the covariance vectors of residuals between the unmonitored locations and the locations with observations and $\mathbf{C_{ab}}$ (respectively $\mathbf{C_{ba}}$) the cross-covariance matrix between the primary and secondary variable (respectively the secondary and primary variable). Consequently, the estimator equation is given by:

$$\hat{\epsilon}_{\mathrm{RCK}}(s_0, t) = \sum_{i=1}^{N_a} \lambda_{a,i} \epsilon_a(\boldsymbol{s_a}, t) + \sum_{i=1}^{N_b} \lambda_{b,i} \epsilon_b(\boldsymbol{s_b}, t) \tag{2.21}$$

before being added to the trend $m_p(s_0, t)$:

$$\hat{p}_{\mathrm{RCK}}(s_0, t) = m_p(s_0, t) + \hat{\epsilon}_{\mathrm{RCK}}(s_0, t) \qquad \forall s_0 \epsilon D \subseteq \mathbb{R}^2 \tag{2.22}$$

2.3.2 Variogram fitting for non-collocated networks

Computation of the weights vector λ of Eq.(2.11) and λ_a and λ_b of Eq.(2.20) requires an estimate of the covariance matrices. Instead of computing the covariance, which is sensitive to sampling effects, kriging generally uses the concept of semivariogram [Matheron, 1971], which represents how the dissimilarity between pairs of points increases with increasing separation distance. The semivariogram, or simply variogram as called from now, is defined for the univariate case and expressed in terms of precipitation residuals by:

$$\gamma_a(h) = \frac{1}{2N(h)} \sum_{i=1}^{N(h)} (\epsilon(s_i) - \epsilon(s_i + h_i))^2 \tag{2.23}$$

$$\forall (s_i, s_i + h_i) \epsilon D \subseteq \mathbb{R}^2 \quad | \quad h_i \epsilon [h - b/2, h + b/2],$$

where h is the distance lag between pairs of locations, $\gamma_a(h)$ the variogram value for distance

lag h, b the bin size (the width of the distance interval up to which point pairs are grouped for variogram computation), h_i the distance separating a given pair of points, $N(h)$ the number of considered pairs of observations separated by distance h, $\epsilon_a(s_i)$ the residual value at location s_i and $\epsilon(s_i + h_i)$ the residual value at location $s_i + h_i$ [Pebesma, 2014].

In the case of Regression kriging, one variogram is computed with Eq.(2.23) for each time step of computation. For the Regression co-kriging, two direct variogams (one for each variable) and one cross-variogram must be computed to define the so-called linear model of coregionalization [Webster and Oliver, 2007]. For the computation of the cross-variogram, Eq.(2.23) must be generalized to two variables, identified by the subscripts a and b:

$$\gamma_{ab}(h) = \frac{1}{2N(h)} \sum_{i=1}^{N(h)} \big(\epsilon_a(s_i) - \epsilon_a(s_i + h_i)\big)\big(\epsilon_b(s_i) - \epsilon_b(s_i + h_i)\big) \tag{2.24}$$

$$\forall (s_i, s_i + h_i) \epsilon D \subseteq \mathbb{R}^2 \quad | \quad h_i \epsilon [h - b/2, h + b/2]$$

where $\epsilon_b(s_i)$ is the residual value at location s_i and $\epsilon_b(s_i + h_i)$ the residual value at location $s_i + h_i$.

However, Eq.(2.24) can be used only in case of collocated variables (i.e. observations are available for both variables in sufficient locations). This is not the case for SMN and MG stations since they are situated in different locations. Accordingly, one needs to work with so-called pseudo cross-variograms in which pairs of both variables are considered, as proposed by Pebesma [2014]:

$$\gamma_{ab}{}^{*}(h) = \frac{1}{2N(h)} \sum_{i=1}^{N(h)} (\epsilon_a(s_i) - \epsilon_b(s_i + h_i))^2 \tag{2.25}$$

$$\forall (s_i, s_i + h_i) \epsilon D \subseteq \mathbb{R}^2 \quad | \quad h_i \epsilon [h - b/2, h + b/2]$$

where $\gamma^*_{ab}(h)$ is the pseudo cross-variogram value for distance lag h considering variables a and b.

The equivalence between variogram and covariance is defined for second-order stationary processes (for which the variogram is always bounded), as follows [Webster and Oliver, 2007]:

$$\gamma(h) = C(0) - C(h) \tag{2.26}$$

where $\gamma(h)$ is the variogram value for a distance h, *C(0)* is the covariance at h=0 and *C(h)* the covariance at distance h. If the variogram is bounded by a sill, the value of $C(0)$ is equal to the total sill value.

In the present study, the variogram models have been fitted using the package 'gstat' [Pebesma and Graeler, 2017], within the R language and environment for statistical computing [R Core

Team, 2018]. The empirical variogram has been fitted with a spherical variogram model [Schuurmans et al., 2007]:

$$\gamma(h) = \begin{cases} 0 & \text{if } h = 0\,, \\ K_0 + K\left(\frac{3h}{2\alpha} - \frac{h^3}{2\alpha^3}\right) & \text{if } 0 < h \leq \alpha\,, \\ K_0 + K & \text{if } h > \alpha\,. \end{cases} \tag{2.27}$$

in which K_0 is the nugget value, K the partial sill, α the range (distance within which measurements are considered correlated).

The implemented code explores different values of bin size until a valid variogram model can be fitted. The routine also tries to obtain a low nugget-to-sill ratio by gradually increasing a success threshold: 100 iterations are first attempted with a threshold value of 0.1. If none of the obtained valid models has a nugget-to-sill ratio lower than the threshold, the threshold is increased by 0.1 until 0.9 with each time 100 iterations. In case of failure with the highest threshold value, the last valid variogram of previous time steps is considered.

Anisotropy of the variogram (different spatial variability in different directions) has not been explored in this work. This choice is justified by the use of the radar data, in which spatial variability of the precipitation fields is assumed to be contained and therefore considered in the interpolation process.

2.3.3 Transformation

Precipitation is inherently heteroscedastic (the variance is not constant over the domain) and has a skewed distribution, which is in contradiction with basic assumptions of classical geostatistics which assumes a gaussian distribution and stationarity of the mean and spatial covariance [Erdin et al., 2012]. Therefore, several methods have been explored in the literature to transform the data before their interpolation [Sideris et al., 2014a, Erdin et al., 2012, Schuurmans et al., 2007] and it has been shown that quantitative improvement is dependent on temporal and spatial variability [Cecinati et al., 2017b]. The process of applying kriging to data transformed into a more gaussian distribution is generally called trans-gaussian kriging.

In the case of the two methods employing kriging in this chapter, namely regression kriging (RK) and regression co-kriging (RCK), interpolation is not done directly on the precipitation observations but on the residuals (see Subsection 2.3.1), to which the gaussianity issue therefore applies. A transformation is applied to both the rain gauge and the radar data to translate them into a more gaussian distribution, with the objective of getting better gaussianity in the residuals. In this chapter, a square-root transformation of the data [Sideris et al., 2014a] is used for both RK and RCK methods (Subsection 2.3.1). Analysis of the residuals distribution has shown that this transformation tends to increase overall the gaussianity of the residuals, even though the effect is somewhat limited and for few time steps even negative. In analysing the

effect of such data transformation on precipitation interpolation, Erdin et al. [2012] reported "only small effects of transformation for the point estimates" but mentioned that "transformation improved the reliability of the probabilistic estimates substantially". The corresponding gain of introducing such transformation scheme is discussed in Subsection 2.4.2.

The advantage of the square-root transformation is the possibility of analytical back-transformation of the mean and the variance [Sideris et al., 2014a], given by:

$$\mathrm{E}[Y^2] = \mu_Y^2 + \sigma_Y^2 \tag{2.28}$$

and,

$$\mathrm{Var}[Y^2] = 4\mu_Y^2\sigma_Y^2 + 2\sigma_Y^4 \tag{2.29}$$

where μ_Y is the mean and σ_Y the standard deviation of the square-root-transformed kriging prediction at a certain location, whereas $\mathrm{E}[Y^2]$ represents the expected value of the back-transformed random variable, or, in other words, the final prediction, and $\mathrm{Var}[Y^2]$ the related variance. However, Eq.(2.28) is composed of two positive terms (both are squared values) with the variance (σ_Y^2) being positive and reaching the sample variance of the (transformed) residuals at estimation locations situated at a distance from the nearest observation higher than the variogram model range (Eq.2.27). Thereby, the back-transformed estimation would never provide zero precipitation estimates apart from rain gauge locations (where estimation variance is minimum). In the work of Sideris et al. [2014a], this problem is addressed by correcting the interpolated field and assigning zero precipitation to locations where the radar does not show any precipitation (I. Sideris, personal communication, May 30, 2017). The methodology proposed here overcomes this issue by weighting the variance term of Eq.(2.28) with the predicted precipitation:

$$\sigma_Y^{*\,2} = \frac{\mu_Y^2}{\tau}\sigma_Y^2 \tag{2.30}$$

where τ is a precipitation intensity threshold below which the variance is weighted and $\sigma_Y^{*\,2}$ is the variance effectively added in Eq.(2.28) instead of σ_Y^2, which gives:

$$\mathrm{E}[Y^2]^* = \mu_Y^2 + \sigma_Y^{*\,2} \tag{2.31}$$

where $\mathrm{E}[Y^2]^*$ represents the expected value of the back-transformed random variable considering the modified estimation variance. The value for τ has been fixed to 0.5 mm/h after initial tests. The impact of applying the transformation or not is discussed in Subsection 2.4.2.

2.3.4 Skill scores and cross-validation

The performance analysis is based on the leave-one-out approach: the precipitation is estimated at a rain gauge location using all observations except the one corresponding to the interpolation location. The procedure is undertaken on an hourly basis for each location and for each of the methods. The quality of the point estimates is then assessed over all locations for each time step using the following skill scores:

1. The Bias is used to assess systematic errors:

$$\text{Bias}(t) := 10\log_{10}\frac{\sum_{i=1}^{N}\hat{g}_i(t)}{\sum_{i=1}^{N}g_i(t)} \tag{2.32}$$

   where $\hat{g}_i(t)$ refers to the estimated value for a given location and a given time step, $g_i(t)$ to the observed value and N to the number of considered locations. As a result of the logarithmic scale used in Eq.2.32, the bias is expressed in decibel (dB). For each event, the overall bias is averaged over the entire period and the entire spatial extent. The bias has been computed only for hourly time steps during which the mean precipitation over the SMN stations was higher than 0.5 mm/h. This avoids values at the denominator close to 0, resulting in exaggeratedly high bias values.

2. The median absolute deviation (MAD) provides the median of the absolute value of the difference between estimated and observed values [Sideris et al., 2014a]:

$$\text{MAD}(t) := \text{median}(|\hat{g}_i(t) - g_i(t)|) \tag{2.33}$$

3. The Root mean square error (RMSE) is the most common parameter used in verification [Goudenhoofdt and Delobbe, 2009]. It represents the standard deviation of the differences between predicted and observed values:

$$\text{RMSE}(t) := \sqrt{\frac{\sum_{i=1}^{N}(\hat{g}_i(t) - g_i(t))^2}{N}} \tag{2.34}$$

4. The mean-root-transformed error (MRTE, Erdin et al. [2012]), mitigates the dominant influence of errors at large precipitation amounts as compared to RMSE:

$$\text{MRTE}(t) := \frac{1}{N}\sum_{i=1}^{N}\left(\sqrt{\hat{g}_i(t)} - \sqrt{g_i(t)}\right)^2 \tag{2.35}$$

5. The scatter is a measure of the spread of the ratio between estimated and measured values. It is based on the cumulative error distribution function of these ratios, expressed in decibel [Germann et al., 2006, Schiemann et al., 2011]:

$$\text{Scatter} := \frac{1}{2}(\xi_{84} - \xi_{16}) \tag{2.36}$$

where ξ_{16} and ξ_{84} represent the 16% and the 84% percentiles of the cumulative error distribution function. Only pairs of points for which both estimated and observed values where higher than 0.5 mm/h were considered for the computation of the scatter.

Table 2.4 – Summary of the performance indicators

Indicator	Min. value	Max. value	Optimal value
Bias	$-\infty$	∞	0
MAD	0	∞	0
RMSE	0	∞	0
MRTE	0	∞	0
Scatter	0	∞	0

2.3.5 Methodology application

For the IDW method, a value of 2 (common default value) is given to the power coefficient β (Eq.2.3) and the research radius fixed to 50 km. For the methods including a regression of the radar data, the regression has been computed only on stations located within the basin.

For the methods considering a single rain gauge network (IDW, RIDW and RK), the primary variable data (SMN) are considered. For the RCK method, both primary (SMN) and secondary (MG) variables data are used.

Variogram fitting with an insufficient number of points can lead to ill-defined variograms. For the RK method, a minimum of 5 stations with a precipitation of at least 0.5 mm/h is set as condition. For the RCK method, the condition is set to 5 stations exceeding the same precipitation threshold value for each variable. When the condition is not satisfied, the last previously computed valid variogram is used. The condition being generally not satisfied at the beginning of an event, an initial variogram must preliminarily be computed over a time step during the event with sufficient stations exceeding the threshold.

In addition, for both the RK and RCK methods, the model fitting has been constrained to a maximum range of 50 km. This value has been defined based on visual variogram analysis and allows to constrain the model for experimental variograms that do not show a clear upper bound.

2.4 Results

The five methods presented in Section 2.3 and listed in Table 2.5 have been applied to the four events including the Pointe de la Plaine Morte radar data (Subsection 2.2.4). For all the five methods, the interpolation has been computed over a grid with a resolution corresponding to the one of the radar data (1 km^2 per pixel).

Table 2.5 – Analysed methods and corresponding used data. For methods abbreviations, see Table 2.3.

Application	Radar	Primary variable	Secondary variable
Radar	Yes	-	-
IDW(SMN)	No	SMN	-
RIDW(SMN)	Yes	SMN	-
RK(SMN)	Yes	SMN	-
RCK(SMN,MG)	Yes	SMN	MG

For the cross-validation, the computation was based on the locations of the SMN rain gauges within the basin, even if more stations such as MG stations were used for the interpolation, to ensure a constant comparison basis for all methods. It is worth noting here that no direct comparison has been possible within this study with the *CombiPrecip* product of MeteoSwiss, as no leave-one-out computation was possible on the delivered *CombiPrecip* product.

The performance of the different methods is first discussed based on the cross-validation approach, including a discussion of the performance before the installation of the new weather radar in 2014. Results of the variogram fitting and the effect of data transformation are then presented. The last section discusses the effect of additional networks.

2.4.1 Methods performance analysis

In order to assess the performance of the different methods, the presented performance indicators have been computed for the main analysis over the four events 1 to 4 (Table 2.2). For each performance indicator (Table 2.4), hourly values were averaged over each event. Results are given in Figure 2.3. The cumulative volume over the events, considering all the pixels located within the basin, is also presented (dashed line border).

The estimation method considering only radar data (Radar) clearly shows the weakest performance. Particularly in terms of bias, which confirms the need of bias correction of the radar data with a regression using rain gauges. This observation is strengthened by the total volume that differs substantially from the other methods for part of the events. Overall, the RCK method provides the best performance. This is the case for the MRTE indicator for which the RCK method provides the best value over all four events. In terms of absolute bias, RCK outperforms for all the events the RK method but for some events, other methods such as IDW perform better than RCK. Furthermore, the results are not clear for all the indicators. For example for event 1, RMSE and Scatter values are comparable for RCK and IDW. It is worth to recall here that the station density within the basin is particularly high, which allows IDW to reach already good performances. It must also be pointed out that IDW has been applied with the default value of 2 for the exponent β of Eq.(2.2). Adjustment of this parameter could improve the performance of the IDW method.

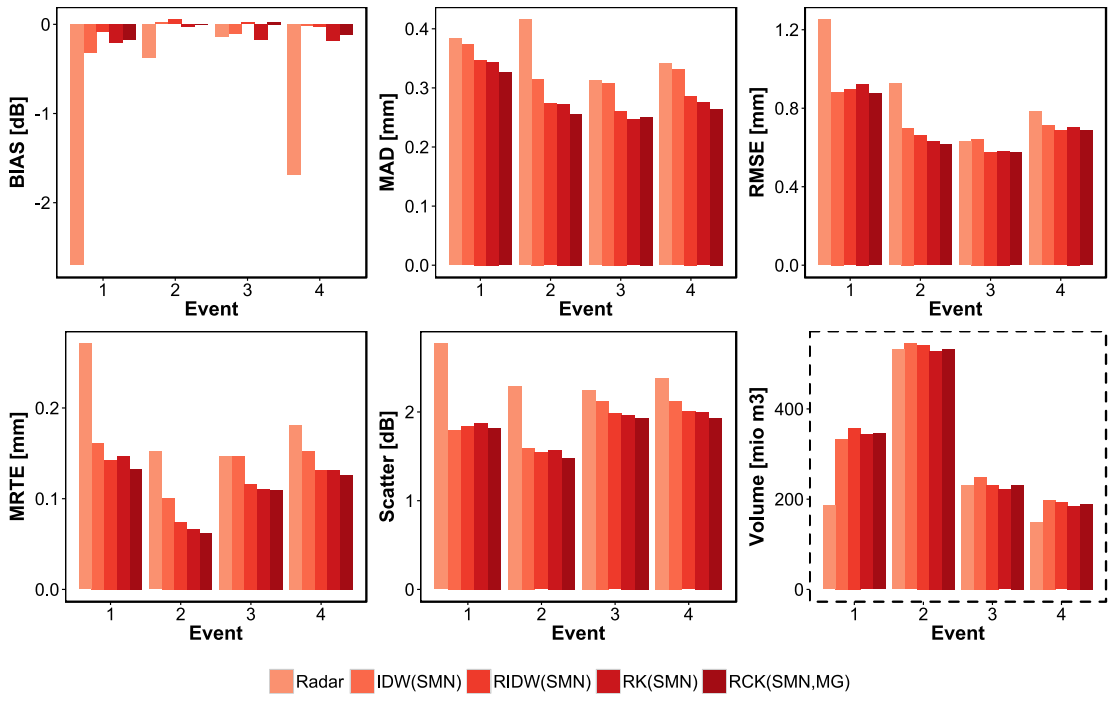

Figure 2.3 – Event-averaged performance indicator values and cumulative volume over the entire basin (dashed line border) over the 4 events.

For a finer analysis, Figure 2.4 presents hourly values for the four performance indicators computed at each time step, for the reference IDW method and the RCK method. Scatter is not shown in Figure 2.4 as it has been computed only over each event. Results for the bias show how reactive the indicator can be, with a strong negative value for the RCK method on 2 May 2015 at 16:00. However, this corresponds to the beginning of the second episode and only few stations already observed precipitation, in which case one single large cross-validation error can strongly affect the hourly indicator value. It must also be noted that such single negative (respectively positive) values can compensate for an overall positive (respectively negative) bias value and lead to an improvement in the overall value. This is one of the limitation of the bias indicator.

Regarding the three other indicators, all strictly positive by definition, it is interesting to note the varying difference between the two methods over the three episodes: whereas there is only a small gain of RCK over IDW over the first episode, it increases over the second and third episodes, in particular for the MRTE indicator. When analysing the different episodes, it appears that over the third one, only the north-western part of the basin is covered by the precipitation (Figure 2.5). The gain of integrating the radar information is here clearly visible, with the IDW method being not able to reproduce the sharp gradient cutting the basin in two parts. Figures C.1 to C.6 in Appendix C show the same indicators for the 6 other events.

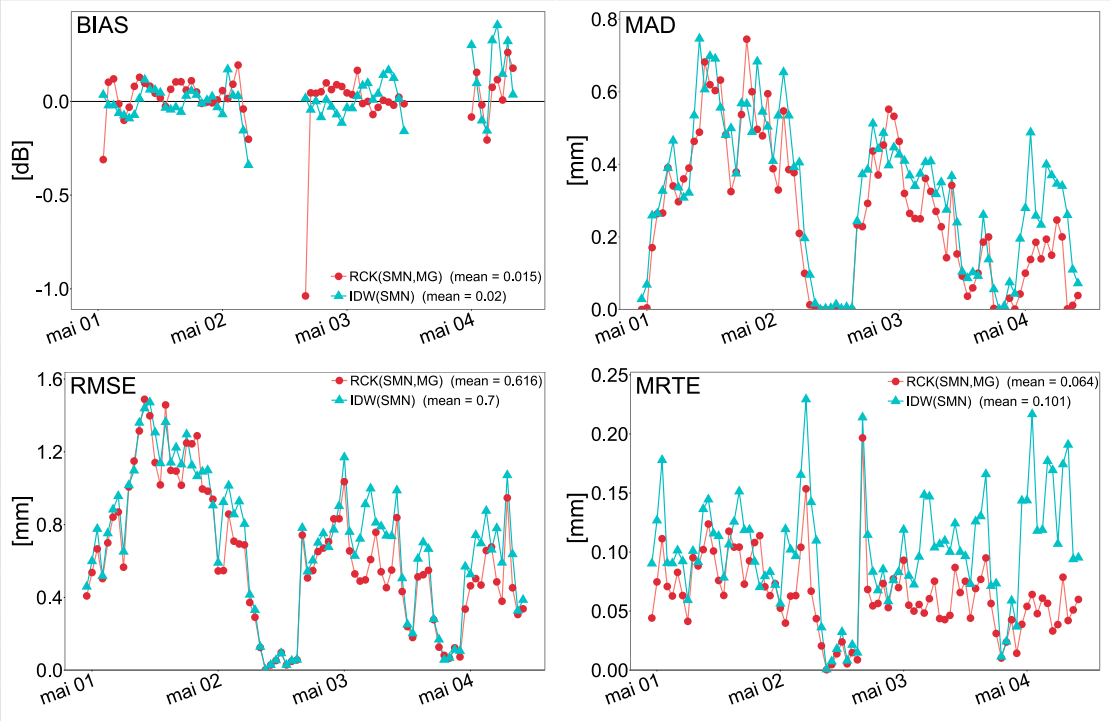

Figure 2.4 – Hourly values of performance indicators for IDW(SMN) and RCK(SMN,MG) over event 2 (May 2015).

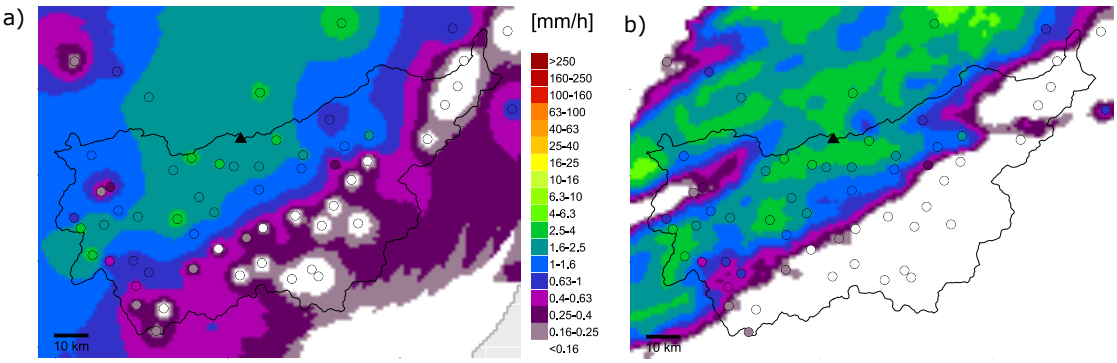

Figure 2.5 – Hourly interpolated precipitation using a) IDW(SMN) and b) RCK(SMN,MG) on 04-05-2015 0100 GMT+1. Circles represent rain gauges' locations and filling colour the intensity observed at the station. The black triangle represents the radar of Pointe de la Plaine Morte.

When analysing the cross-validation errors of event 1, it appeared that the station Col du Grand St-Bernard (GSB) resulted almost systematically (over the entire event) in high cross-validation errors, with both IDW and RCK methods not being able to correctly reproduce the observed precipitation, despite using the radar information in the RCK method. When looking at the total precipitation over the event for both methods, the GSB station is also very well visible at the south-western corner of the basin (Figure 2.6). The high difference between the rain gauge

values and the bias-corrected radar data only at this station suggested to further investigate this particularity. Interestingly, this station, located at an elevation of 2472 m a.s.l., had already been pointed out in precedent analyses [Gabella et al., 2011b, Erdin et al., 2012], in which the station was reported to suffer of "several known measurement problems (shielding, wind exposure, and drifting snow)" [Erdin et al., 2012]. And with a snow limit varying between 1000 and 2000 m a.s.l. over the event, the GSB station only measured solid precipitation.

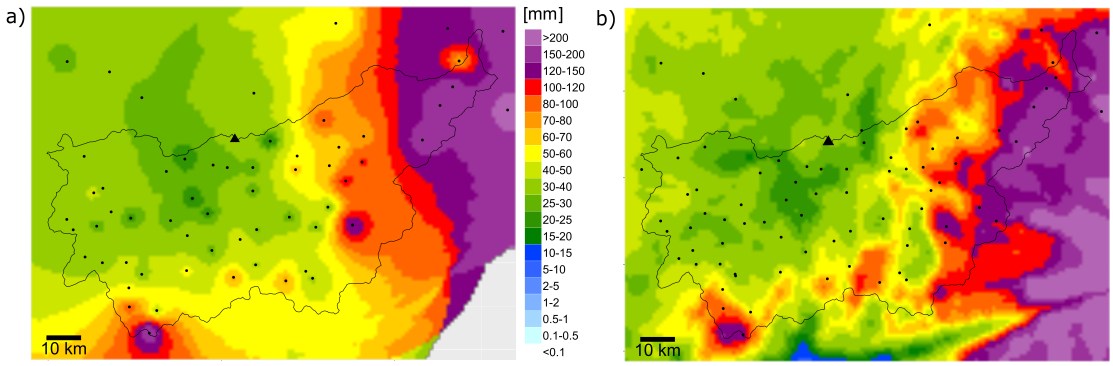

Figure 2.6 – Comparison of total precipitation over event 1 (04-11-2014 0800 to 06-11-2014 0400 GMT+1) for a) IDW(SMN) and b) RCK(SMN,MG). Note that the colour classes division is not linear. The black points represent the locations of the considered rain gauges. The black triangle represents the radar of Pointe de la Plaine Morte. The grey back-ground on the bottom-right corner of a) results from the absence of data within the research radius (50 km) of these pixels.

To investigate the impact of the station over the global performance over the event, the interpolation has been recomputed by totally excluding the GSB station. Figure 2.7 shows the result for the two methods, both with and without considering the GSB station. Results show that all indicators are improved when removing the station. In particular for RMSE and MRTE, the difference is non-negligible. This example shows well how considering as truth the data from the rain gauges can lead to incoherence or errors in the interpolation result.

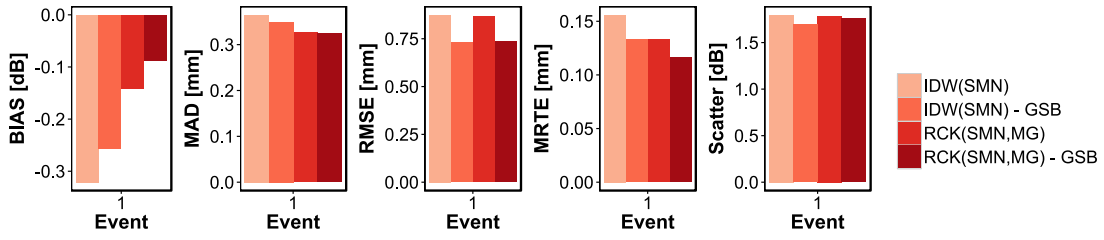

Figure 2.7 – Performance indicators over event 1 with exclusion of Col du Grand St-Bernard (GSB) station.

The analysis carried out over events 1 to 4 considered radar data including the new radar of Pointe de la Plaine Morte. In order to assess the quality of the Swiss-wide radar product over the studied basin before the installation of this new radar, performances over the three events A, B and C are presented in Figure 2.8. The performance gain of RCK over IDW for the three events is higher than for events 1 to 4. This is probably partly explained by the number of rain gauges available over the three events: only 28 and 40 SMN stations for 2012 (event A) and 2013 (event B) whereas at least 52 stations were available for the events 1 to 4. The lower station density reduces the performance of IDW and thereby increases the relative gain of RCK over IDW. The performance of the RCK method over the three analysed events excluding

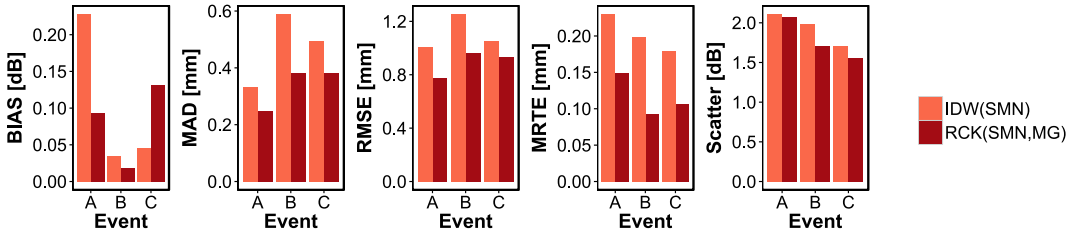

Figure 2.8 – Performance indicators for the method IDW using SMN data and the RCK method using SMN(primary) and MG (secondary) data over the 3 events without data of the radar of Pointe de la Plaine Morte.

Pointe de la Plaine Morte radar data suggests that this method provides clearly better results than IDW for the studied basin even before the installation of the new weather radar. This is an important result in the perspective of computing precipitation fields for hydrological modelling with data requirement over relatively long time periods, as it shows that even with an Alpine topography like the one in the studied basin, radar data seem to be usable even without a weather radar located within the basin.

2.4.2 Variogram and data transformation analysis

Performance of the variogram model fitting for the results presented in Subsection 2.4.1 are presented hereafter, before analysing the effect of data transformation looking at the RCK method.

Variogram fitting results

Good fitting of the variogram is essential to obtain a reliable interpolation. The implemented solution resulted in few time steps (0.5%) without valid variogram fitting. This considers only the time steps with enough stations reporting sufficient precipitation as defined in Subsection 2.3.5. The percentage of time steps with insufficient stations is considerably high: 7.4% for the RK method and 31.7% for the RCK method of the time steps over the four events 1 to 4. These time steps generally correspond to the lower intensity phase of the events. For all

these time steps (both failure and insufficient stations), the previously computed last valid variogram was used instead.

Figure 2.9 shows four direct variograms for the RK method over event 3. The differences in bin size are well visible: the fewer points are visible on the sample variogram, the more points were grouped together and averaged to compute each point of the experimental variogram. Figure 2.10 gives an example of the linear model of coregionalization, composed of two direct variograms (SMN and MG) and one pseudo cross-variogram (SMN vs. MG), all three fitted simultaneously. The higher variability observed in the MG direct variogram tends to be a common behaviour within this study. This difference cannot be directly attributed to a difference in the quality of the MG sensors, as these stations are also much less numerous, with only 23 MG stations for 52 SMN stations over the chosen event, enhancing the issue of limited number of wet stations for the MG network.

In addition, if most of the fitted models describe well the experimental variogram, for some time steps, a manual fitting would probably have led to more appropriate fittings.

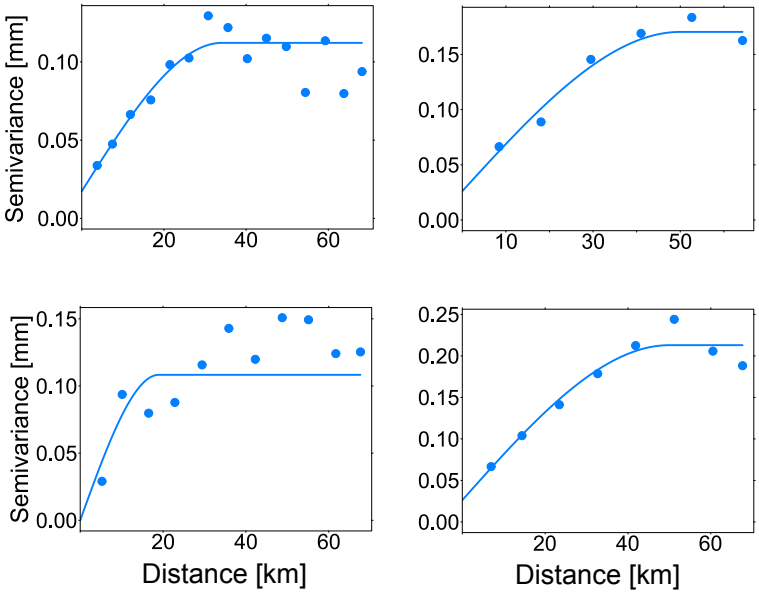

Figure 2.9 – Sample of the variogram and automatically fitted models for the first four hours of event 3 (January 2016).

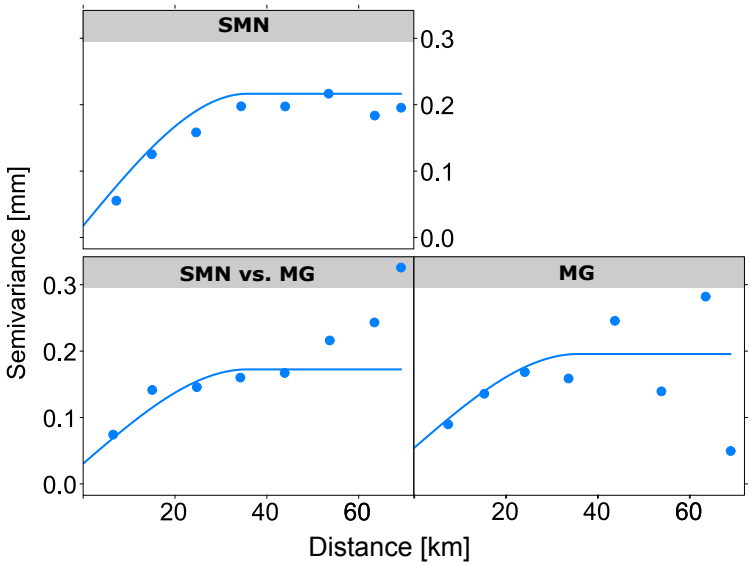

Figure 2.10 – Example of linear model of coregionalization composed of two direct variograms and one pseudo cross-variogram (bottom left) using SMN as primary variable and MG as secondary variable (01-05-2015 2200 GMT+1).

Effect of data transformation

The RCK method has been applied to events 1 to 4, both with and without transformation (Figure 2.11). The bias is considerably improved for two of the four considered events when applying the discussed square-root transformation (Eq.2.31). For the MRTE, a gain is observed for all events. For the other indicators, the difference is less important and more variable, for example for the MAD, for which loss and gain are observed; for the Scatter, the tendency is slightly negative, probably due to the back-transformation process. These results are coherent with the conclusions of Erdin et al. [2012], who reported only "small effects of the transformation" on the point estimates, but reported a higher reliability of the estimates when comparing "each gauge measurement against the probability function of the corresponding cross-validation probabilistic estimate". Further improvements in the transformation could be explored, not only on the power coefficient of the transformation, but also on the back-transformation process. Based on the obtained results, applying the proposed transformation is recommended.

2.4.3 Effect of additional networks

In the results presented in Subsection 2.4.1, the MG data have been used only in the RCK method as secondary variable. Combination of SMN and MG data as a unique set of data is discussed hereafter. Figure 2.12 presents the performance indicators for the IDW, RIDW and RK methods, each time considering first SMN data only and then combining SMN and MG

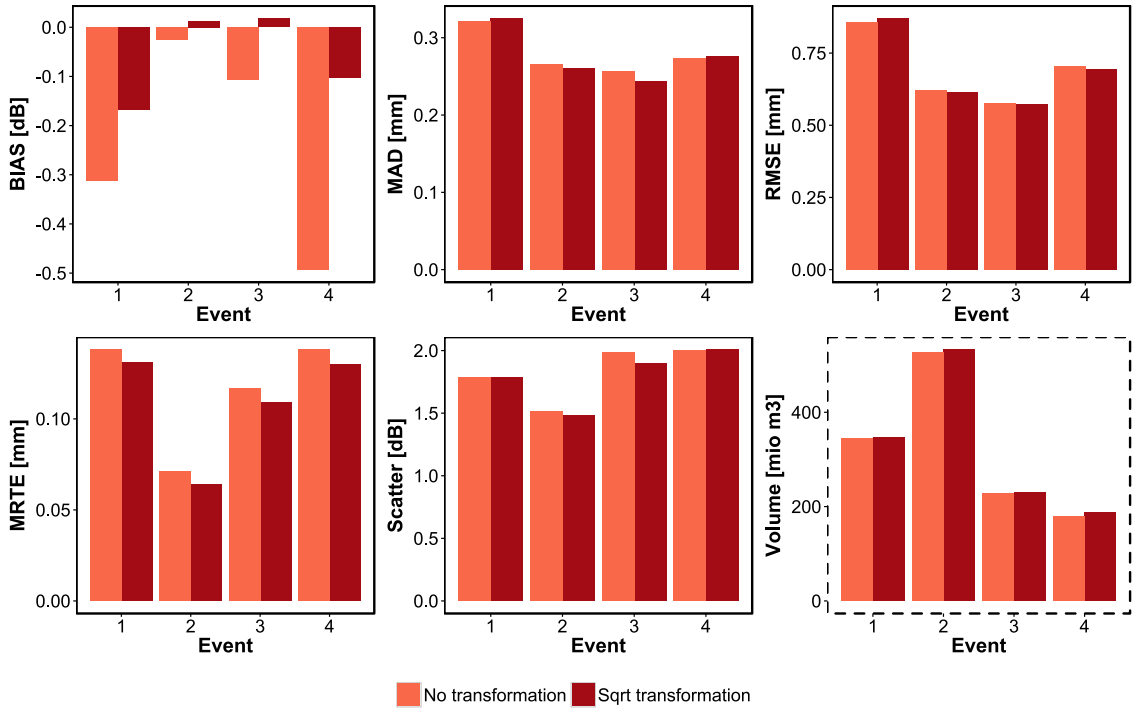

Figure 2.11 – Assessment of transforming or not the data when using the RCK(SMN,MG) method.

Table 2.6 – List of methods and data used for analysing the combination of SMN and MG data as a unique variable. For methods abbreviations, see Table 2.3.

Application	Radar	Primary variable	Secondary variable
IDW(SMN)	No	SMN	-
IDW(SMN&MG)	No	SMN+MG	-
RIDW(SMN)	Yes	SMN	-
RIDW(SMN&MG)	Yes	SMN+MG	-
RK(SMN)	Yes	SMN	-
RK(SMN&MG)	Yes	SMN+MG	-
RCK(SMN,MG)	Yes	SMN	MG

data, considering them together as one single variable (Table 2.6). Results of RCK using SMN data as primary variable and MG as secondary variable are also presented. For all indicators except the bias, considering MG data directly with SMN data as one single variable tended to improve the performance of the methods as compared to use only SMN data, which can be explained by the additional local information introduced by the MG stations. Performances were in some cases even slightly better than for RCK in which both variables are considered separately. However, and as expected from the data analysis presented in Section 2.2 (Data and events description), this joint use of SMN and MG data resulted in negative biases. This

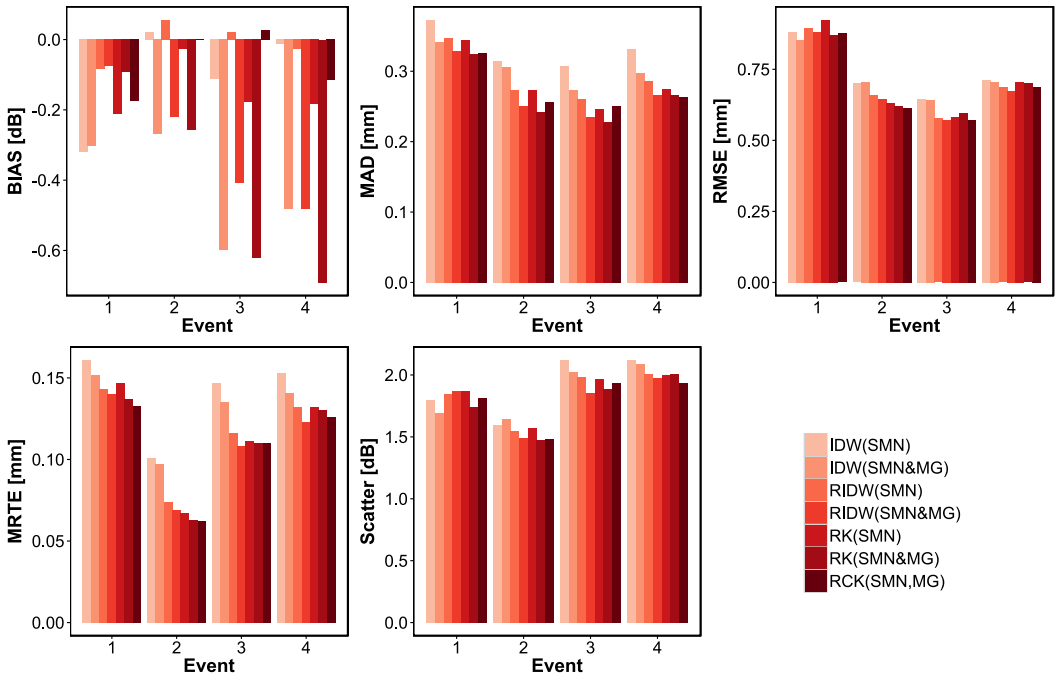

Figure 2.12 – Performance indicators over the 4 events, exploring combination of SMN and MG as primary variable for IDW, RIDW and RK methods.

effect is well visible in particular for events 3 and 4 (Figure 2.12), where values exceeded -0.6 dB corresponding to a negative bias of about -13%. Consequently, this bias issue suggests to consider both variables only with methods accounting for this deviation, that means in the present case the RCK method.

The present study also aimed at providing a preliminary analysis of integrating stations from surrounding areas. This is justified by the need for accurate information in terms of precipitation estimates for real-time hydro-meteorological monitoring and forecasting. Figure 2.13 shows for a time step of event 2 the interpolation results of RCK, using only SMN and MG data compared to the results obtained with integrating the data from all surroundings additional networks. With the additional stations, precipitation estimates are for example increased over the Aosta region south of the studied basin (see Figure 2.13c).

For a more quantitative assessment, Figure 2.14 gives the corresponding performance indicators, including different combinations of primary and secondary variables for the precipitation interpolation. The additional data have however not been used for the linear regression computation nor for the variogram fitting. This was motivated respectively to ensure an optimal radar regression over the studied basin and to reduce the risk of inconsistencies in the variogram model fitting, sensitive to discrepancies in even only one or two stations, potentially affecting the entire interpolation of a given time step.

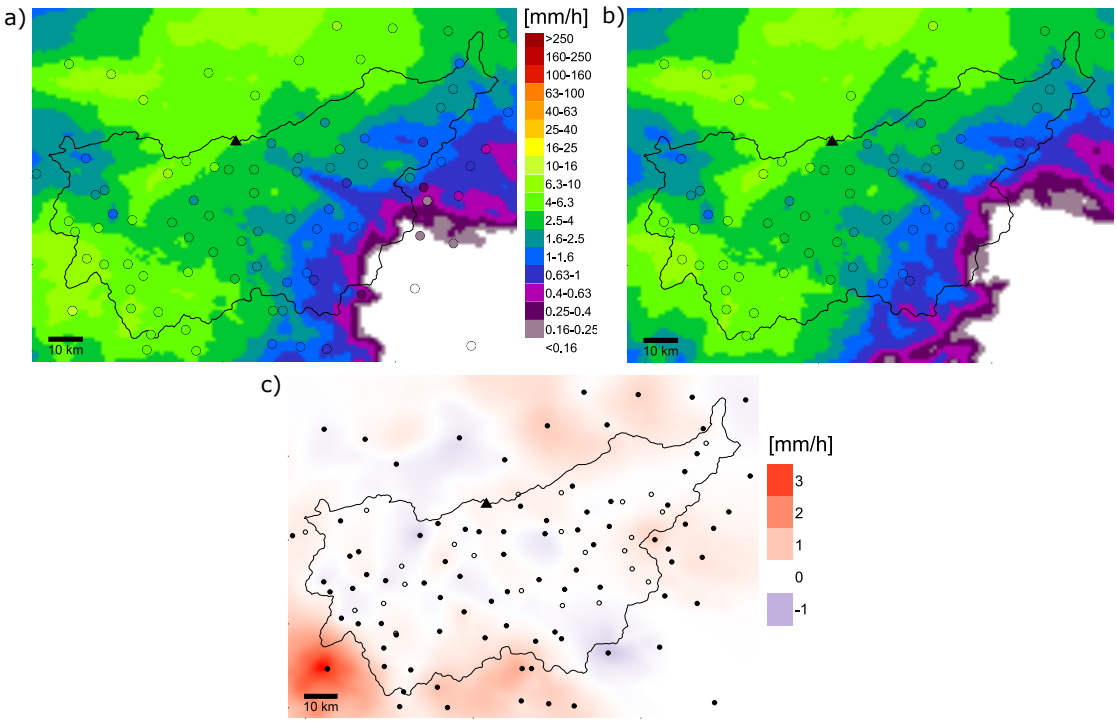

Figure 2.13 – Hourly precipitation interpolated using RCK(SMN,MG) a) considering all station networks around the basin (see Table 2.1) together with the SMN stations as a single (primary) variable (time step: 01-05-2015 2200 GMT+1) ; b) as a) but without surroundings station networks ; c) difference between a) and b). On a) and b), the circles represent the primary stations. On c), the filled circles represent primary stations, the empty circles the secondary stations. The triangle represents the location of the radar of Pointe de la Plaine Morte.

The results show that adding additional networks has a limited effect. Bias tends to be the most reactive indicator, even though differences are small. For the other indicators, as well as for the total precipitated volume, differences can be considered as limited, and it is difficult to define if it is rather a gain or a loss in terms of performance.

For some time steps, some stations of the additional networks reported no precipitation whereas the radar reported heavy precipitation, suggesting some possible quality issues. For operational purposes, the quality of these additional networks should be further investigated.

2.5 Discussion

The performance analysis used in this chapter, based on leave-one-out cross-validation, did not allow a direct comparison with outputs of previous works, for example with the *CombiPrecip* product as described in Sideris et al. [2014a]. In fact, the stations used in the cross-validation evaluation are used in the computation of the product, thus no comparison was possible. However, visual analysis of the interpolated precipitation fields revealed that

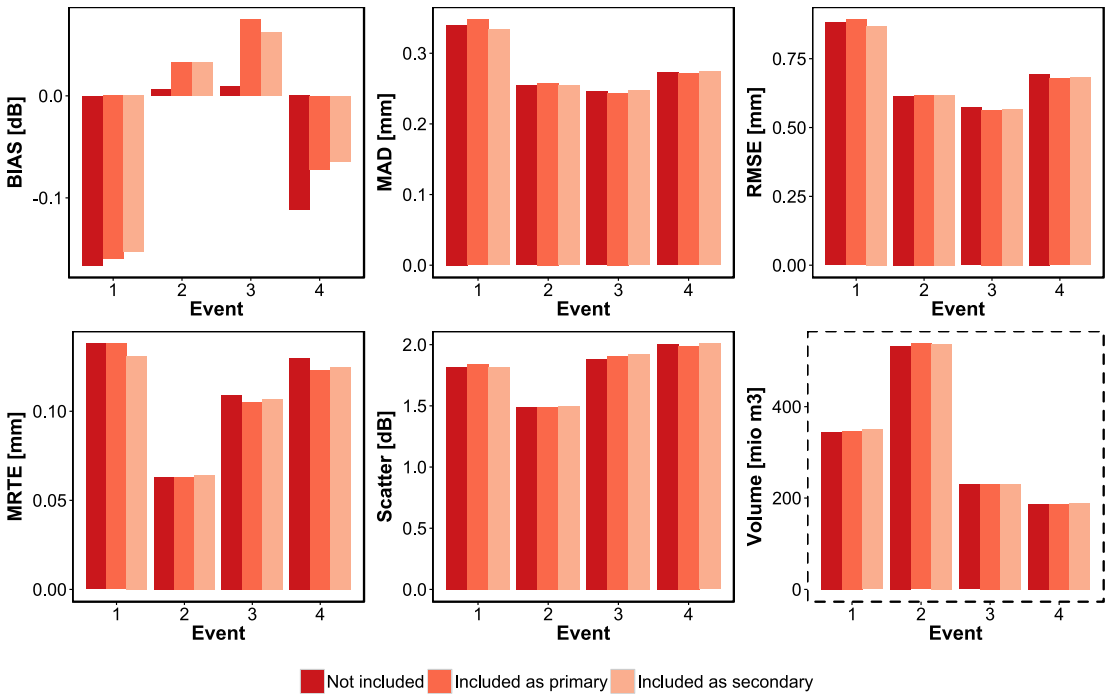

Figure 2.14 – Performance indicators comparison for RCK(SMN,MG) including or not the neighbouring networks, and using them as primary, respectively secondary network.

the spatial patterns were very similar for a very large fraction of the time steps. Integration of the discussed interpolated precipitation fields into a hydrological model could allow a quantitative comparison between the products from a hydrological point of view. This will be explored in Chapter 4. Furthermore, the analysis was carried out over the set of recent most heavy precipitation events, which were not evenly spread through all seasons, with events 1 to 4 (period 2014-2017) occurring from fall to spring and with events A to C (period 2012-2014) only in summer. This could have an impact on the analysis but should not modify the general conclusions from the comparison between methods.

The choice of performance indicators can also slightly modify the results of the analysis. For example, a bias indicator based on a ratio between estimated and observed values [Germann et al., 2006, Gabella et al., 2011a] is used here, indicator also used by several other authors [Sideris et al., 2014a, Goudenhoofdt and Delobbe, 2009]. However, alternative versions exist, based for example on a differential bias [Cecinati et al., 2017b], less sensitive to small denominators.

Two aspects of the presented precipitation interpolation deserve further discussion, namely the integration of different rain gauge networks and remaining challenges, due mainly to radar visibility.

Regarding the integration of the data from the private MeteoGroup (MG) rain gauges, it is important to point out here that their added value is probably somewhat underestimated in the presented results. In fact, their contribution to the overall interpolation quality is analysed only via cross-validation applied to the MeteoSwiss (SMN) stations. This cross-validation does probably not show a complete picture of the contribution brought by the MG stations as (i) the MG stations have been selected to complete the SMN network in areas without SMN stations and (ii) the MG stations contribute to the final interpolated precipitation field mostly in their immediate vicinity.

As expected, including the radar data as external drift improved the precipitation interpolation considerably for all tested methods. However, any radar data set in a comparably complex area is highly likely to suffer from several quality issues such as radar beam shielding by mountain peaks located in close vicinity of the radars. For our case study, the Mont Bonvin (2994 m a.s.l.), located two kilometres south-east of the radar of Pointe de la Plaine Morte (2926 m a.s.l.), creates such a blind zone due to radar shielding in south-eastern direction from the radar location (visible in Figure 2.15). In this area, precipitation is highly likely to be underestimated by the radar. This effect remains visible in the final estimation method retained here (RCK on the radar residuals with SMN as primary and MG as secondary variable) and is also well visible on Figure 2.13. A similar effect can be seen on Figure 2.6 (b) for a second radar, the Monte Lema radar (south-east of the case study basin, see Figure 2.1). In fact, before the installation of the new radar at Pointe de la Plaine Morte, such shielding beams were already common as illustrated in Figures 2.16 and 2.17.

The radar network configuration in terms of installed devices is supposed to not evolve in the near future. The most promising directions to further improve precipitation interpolation under the current configuration are, thus, the following:
i) Better accounting for radar shielding effects; the replacement by MeteoSwiss of their radar precipitation estimates product, used for the present study, by a new version, optimized for the new network configuration with 5 weather radars, will certainly contribute positively to this issue. Further investigations could e.g. consist in developing a raster of radar data quality based on the visibility of the weather radars or by analysing the annual radar precipitation estimates. Such a method to account for radar quality should also consider temporal variations of the radar network configuration resulting from temporary inactivity of individual weather radars (due e.g. to technical failures or scheduled maintenance);
ii) Improvement of the regression of the radar data on the rain gauge data, e.g. by including a second coefficient in the linear regression (Eq.2.7), by developing a more local regression method that could account explicitly for summer convective precipitation or by integrating other covariates (e.g. topography).

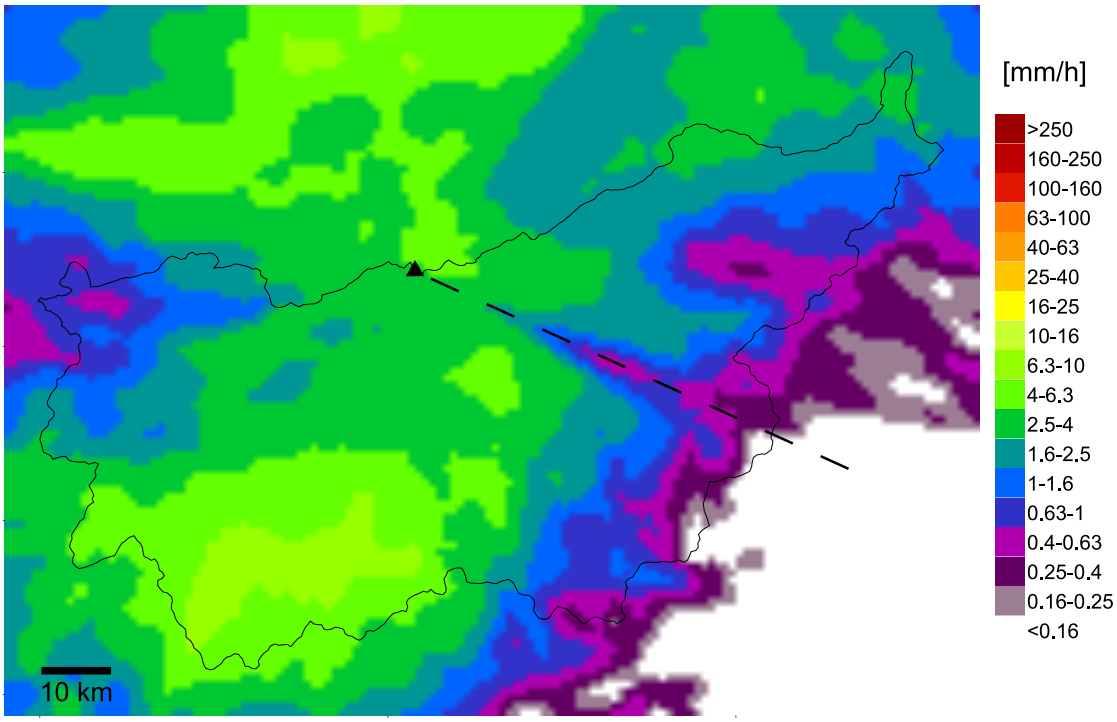

Figure 2.15 – Example of radar data with the blind zone in south-east direction of the radar of Pointe de la Plaine Morte (time step: 01-05-2015 2200 GMT+1). The black triangle represents the weather radar. The dashed-line indicates the blind zone direction.

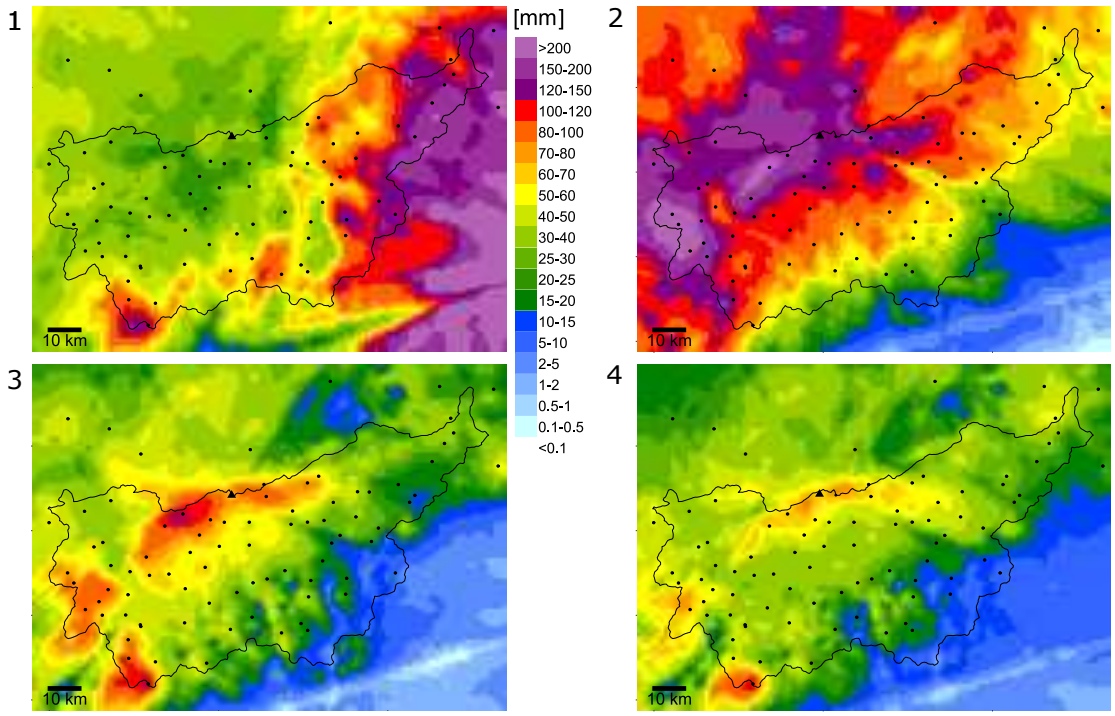

Figure 2.16 – Total precipitation accumulation over the four events: 1 (November 2014), 2 (May 2015), 3 (January 2016) and 4 (March 2017), based on the SMN(MCH,MG) method. Points indicate SMN and MG stations within and around the basin. The triangle indicates the location of the radar of Pointe de La Plaine Morte.

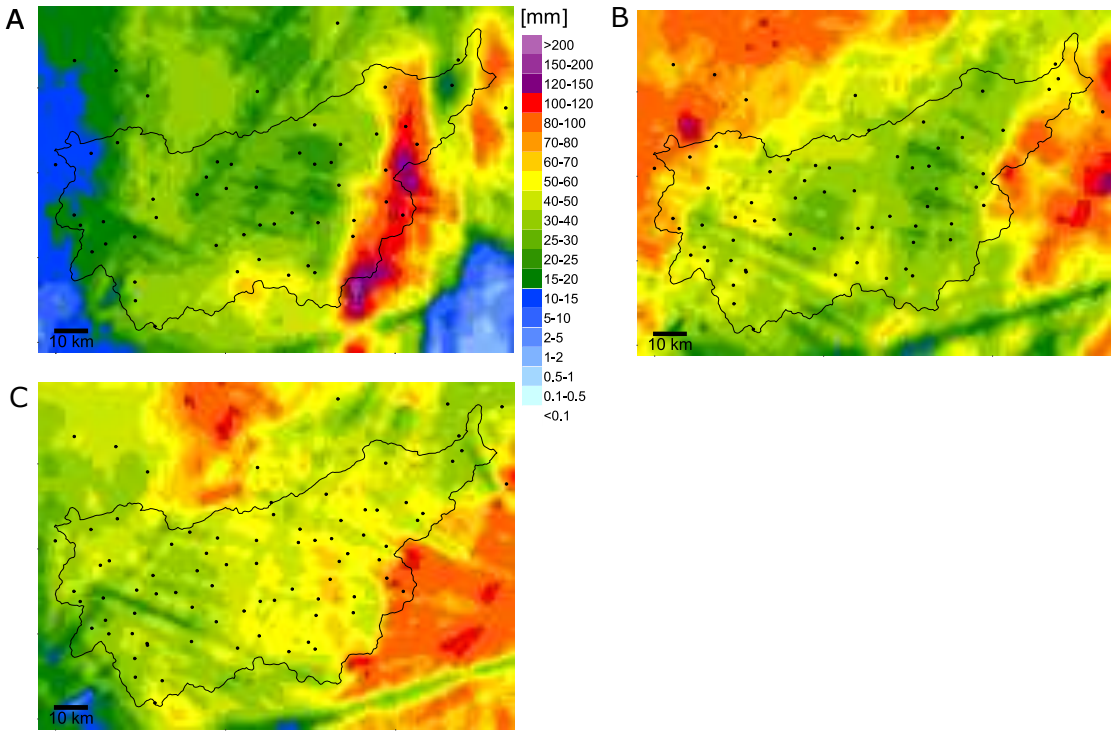

Figure 2.17 – Total precipitation accumulation over the three events A (July 2012), B (July 2013) and C (July 2014), based on the SMN(MCH,MG) method. Points indicate SMN and MG stations within and around the basin. Shielding beams corresponding to areas of low visibility for the two nearest weather radars (Monte Lema and La Dôle) and which were common before the installation of the new radar at Pointe de la Plaine Morte are well visible for the three events.

In addition, latest developments in the field of hydrometeor type classification from radar data [Grazioli et al., 2015], might open up new perspectives on precipitation-radar data integration for mixed snow and rain events in the near future, as well as higher quality radar precipitation estimates during snow fall.

A final point worth mentioning is the potential integration of secondary rain gauge networks composed of non-heated stations that can only observe liquid precipitation, such as the Agrometeo network [Agroscope, 2017] or the IMIS network [SLF, 2017] to further increase the density of rain observation stations. This is readily possible with the retained interpolation methodology and could potentially reduce the precipitation estimation error during rainfall events. However, 75.1 percent of the studied area lies above 1500 m a.s.l., where precipitation occurs regularly in the form of snow between November and March [Marty, 2008]. In addition, with the high density of higher quality data already available, it is not sure that this would improve the performance.

2.6 Conclusion

This chapter proposes a new method named Regression co-kriging for spatial interpolation of observed precipitation from two non-collocated rain gauge networks of different quality with radar data. Compared to the precipitation fields routinely produced in real-time by the Swiss national meteorological service MeteoSwiss [Sideris et al., 2014a] based on the observed precipitation data from their SwissMetNet (SMN) network, the final interpolation method retained here, additionally integrates data from the network of the private company MeteoGroup Switzerland AG (MG).

The performance of the interpolated precipitation fields is assessed for four events over a Swiss Alpine region, the Upper Rhône River basin, using inverse distance weighting applied directly to the rain gauge observations as baseline scenario. A series of well-established precipitation interpolation methods are tested, including methods that use (i) the radar data as an external drift to compute an overall precipitation trend and (ii) the rain gauge data to form local residuals that are spatially interpolated and added to the trend. Since the locations of the two network stations do not coincide, the concept of pseudo cross-variogram is employed to compute the linear model of coregionalization used for the co-kriging interpolation.

The completed detailed tests demonstrated that regression co-kriging using the SMN data as primary variable and MG data as secondary variable to interpolate the local precipitation residuals provides the best performance for the study area. The method even proved to outperform clearly the Inverse distance weighting method for historical data availability scenarios, before the radar network was completed and with lower rain gauge station density. This result is important for hydrological applications where data over many years are required. The gain introduced by the co-kriging approach is demonstrated by showing a bias issue when considering both networks jointly linked to a difference in the networks quality. Regardless of the spatial scale, data combination must therefore consider with care the quality of the sensors providing the data when elaborating a combination methodology. The results of the analysis also showed that even with up-to-date modern weather radar equipment, radar-gauge combination in a complex topography such as the Swiss Alps requires a high-level treatment of the data. This is particularly true for reducing the artefacts due to beam shielding by the topography.

An interesting side-result of this study is the fact that if a single rain gauge network (SMN stations) is combined with radar data, a kriging-based residual interpolation does not clearly outperform a simple inverse distance weighting of the residuals. This is probably explained, at least partly, by the relatively low number of rain gauges that report precipitation for some time steps over the considered domain, which is often near the limit or even below the minimum required number to obtain robust variograms (which is particularly limiting for RCK where two variables need to meet this criterion).

Overall, the presented results underline the importance of analysing in detail the evolving data situation to propose robust precipitation interpolation methods. This not only holds

for regions where the rain gauge and radar network is evolving; any existing network might indeed suffer from device failures and ensuing missing data.

In general, the detailed analysis of different rain gauge networks provided here (including networks of neighbouring regions, networks of different quality), illustrates that integration of several networks for operational interpolation purposes is not straightforward. Since the available meteorological data (quantity and quality) is permanently increasing, there is ample room for further studies on improving quantitative precipitation estimates for complex Alpine environments. Based on our analysis, the most promising research direction is certainly the pre-processing of the radar data in particular to account for known beam shielding effects and to take advantage of recent progress in the field of hydrometeor type classification for radar data.

Acknowledgments

Prof. Alexis Berne from the Environmental Remote Sensing Laboratory at EPFL and Dr. Ioannis Sideris from MeteoSwiss are acknowledged for their inputs and feedbacks on the manuscript.

Table of variables

Table 2.7 – Table of variables for Chapter 2.

Variable	Description
a	Regression coefficient for trend computation
b	Bin size for variogram computation
$\mathbf{c_a}$	Covariance vector between the location of interpolation and the monitored locations
$\mathbf{C_{aa}}$	Covariance matrix between the residuals of variable A
$\mathbf{C_{bb}}$	Covariance matrix between the residuals of variable B
$\mathbf{C_{ab}}$	Cross-covariance matrix between the residuals of variable A to the residuals of variable B
$\mathbf{C_{ba}}$	Cross-covariance matrix between the residuals of variable B to the residuals of variable A
C_{ij}	Covariance between the residuals at locations i and j
d	Distance separating two locations
D	Spatial domain
g	Rain gauge observation
h	Distance lag between pairs of locations
K_0	Nugget value
K	Partial sill
m	Trend component
N	Number of available rain gauge measurements
p	Precipitation depth
r	Radar estimate
s	Spatial coordinates
$\mathbf{s}$	Spatial coordinates vector
s_0	Spatial coordinates of interpolation location
t	Period of time
T	Temporal domain
x	x coordinate
y	y coordinate
Y	Square-root-transformed random variable
Y^2	Back-transformed random variable
Z	Random variable
α	Variogram model range
β	Power coefficient for the IDW method
$\delta_k(h)$	Kronecker delta function
ϵ	Residual component: observation - trend component
$\gamma(h)$	Variogram model
$\gamma_a(h)$	Univariate variogram

$\gamma_{ab}(h)$	Cross-variogram
$\gamma_{ab}{}^{*}(h)$	Pseudo cross-variogram
λ	Interpolation weights
μ_Y	Mean of the square-root-transformed kriging prediction
ρ	Research radius
σ_Y	Standard deviation of the square-root-transformed kriging prediction
${\sigma_Z}^2$	Variance of the observations
τ	Precipitation intensity threshold for computation of variance to add in the back-transformation

3 Solid precipitation undercatch correction and snow modelling

3.1 Introduction

The Snow Water Equivalent (SWE), defined as the depth of the layer of liquid water that would be produced if all the solid water in the snow pack was melted [Rees, 2006], is a major contribution to the hydrological cycle during the melting season in Alpine catchments [e.g. Jörg-Hess et al., 2015]. Proper modelling of the processes leading to the relative transformations between snow- and rainfall-originated drivers of the hydrologic response is therefore important for flood forecasting, water supply assessment or optimization of hydropower production [Barnett et al., 2005].

The temporal evolution of SWE is the combined outcome of a wide range of processes that affect snow accumulation and redistribution, snow melt and sublimation. Accordingly, estimating accurately SWE over large and complex mountainous terrain can be complex, in particular when the modelling is applied at catchment scale due, on the one hand, to the topographic and land use characteristics of the catchment [Engel et al., 2017] and, on the other, to the high spatial variability of meteorological conditions. In this context, a wide range of snow-hydrological literature has focused on the question of how to improve SWE simulation with the help of observed data and improved model parametrization [Clark et al., 2006, Parajka and Blöschl, 2008b, Clark et al., 2011]. The role of the precipitation input field that enters the SWE simulation has received much less attention and is the focus of the present chapter.

Most snow models used for hydrological applications use in general very similar methods to simulate the snow accumulation phase, essentially based on air temperature thresholds [Jennings et al., 2018]. Few models include explicitly snow redistribution [Schulla and Jasper, 2007]. For the snow ablation part (sum of melt and sublimation), there are two fundamentally

This chapter is based on the scientific article "Accounting for solid precipitation gauge undercatch in quantitative precipitation estimates for snow modelling in Alpine catchments" by Foehn A., García Hernández J., Schaefli B., De Cesare G., Rinaldo A., under review in *Journal of Hydrometeorology*.

different categories of models: energy balance models and temperature-index models [Rango and Martinec, 1979, 1995, Kane et al., 1997, Fierz et al., 2003, Hock, 2003]. Temperature-index models, also referred to as degree-day models, are based on an assumed relationship between snow melt and air temperature [Ohmura, 2001]. The snowmelt depth over a period is calculated by multiplying degree-day factors (DDF) with the difference between the air temperature and a melt threshold, usually set to 0° C.

In this chapter, the role of precipitation estimates for SWE simulation is investigated using such a temperature-index model, which are widely used at the catchment-scale due to four main reasons [Hock, 2003]: (1) wide availability of air temperature data, (2) relatively easy interpolation and forecasting possibilities of air temperature, (3) generally good model performance despite its simplicity and (4) computational ease, which is key for real-time forecasting.

The key parameter of most melt models is the DDF parameter, which is commonly calibrated simultaneously with all other parameters of the hydrological model based on streamflow data [Klok et al., 2001, Jordan, 2007b, Luo et al., 2013, Tobin et al., 2013]. However, efforts tend to increasingly integrate SWE-related data to calibrate snow models [Xu et al., 2014]. Point-measured SWE data can either be used alone [Kane et al., 1997] or in combination with snow depth data combined with empirical relationships between DDF and snow density developed by Rango and Martinec [1995] and later used for example by Bormann et al. [2014]. Such data-based methods to identify DDFs, however, require SWE observations with good spatial and temporal coverage, limiting their use at large scales.

In absence of detailed SWE observations, so-called Snow-Covered Area (SCA) curves are often used for parameter calibration. Such curves relate the area temporarily covered by snow to the average catchment-scale SWE; they were initially developed as statistically distributed snow simulation routines [Bergström, 1986] but can now be seen as transfer functions between (e.g. remotely sensed) snow covered area and catchment-scale SWE. SCA curves are typically used for model performance evaluation in combination with point-measured SWE data [Daly et al., 2000], with ground-based snow depth data [He et al., 2014] or alone [Besic et al., 2014, Pistocchi et al., 2017, Sohrabi et al., 2018]. Considering the hysteresis that exists between SCA and the SWE during the accumulation and melt phases has shown to further improve SCA simulation [Riboust et al., 2019].

The snow-covered area products of the Moderate-Resolution Imaging Spectroradiometer (MODIS) [Hall et al., 2002] are widely used in snow hydrological modelling [Klein and Barnett, 2003, Andreadis and Lettenmaier, 2006] and for snowmelt models calibration and validation [Déry et al., 2005, He et al., 2014, Parajka and Blöschl, 2008b]. The spatial resolution of the MODIS SCA products is 500 m, but higher resolution products have been developed, for example by Notarnicola et al. [2013a,b], who generated a SCA product of 250 m spatial resolution based on 250 m resolution MODIS bands.

In climates fostering seasonal snowpacks (i.e. snowpacks that last several weeks to months), reliable simulation of temporal SWE evolution during the melt phase is strongly dependent on a

correct estimation of the SWE during the accumulation phase. Quantifying solid precipitation, however, is known to be notoriously difficult due to gauge undercatch by precipitation gauges in snowy, windy conditions [Pollock et al., 2018]; in the frame of the World Meteorological Organization (WMO) Solid Precipitation Intercomparison Experiment (SPICE), the average undercatch for eight study sites across the globe with unshielded gauges was estimated to 34% [Kochendorfer et al., 2017] in comparison to the values reported by an automated weighing gauge within a Double Fence Intercomparison Reference (DFIR) shield.

Accordingly, without a correction of the solid precipitation input, simulations tend to underestimate observed SWE. Magnusson et al. [2014] reported that the snowfall amounts computed from 29 snow depth observation stations in Switzerland were approximatively 20% higher than the corresponding simulation results. Besic et al. [2014] reported correction factors ranging from 0.96 to 1.43 when calibrating accumulation correction factors for a distributed SWE model using in situ SWE measurements at four locations in a study case in France. Engel et al. [2017] fixed the best snow correction factor for the GEOtop2.0 model in the Eastern Italian Alps to 1.4 and identified this factor as a key parameter over the accumulation period.

To better understand the relationship between precipitation input and SWE simulation, a modelling framework for the Swiss Alps is developed to compare different quantitative precipitation estimates (QPE) obtained from radar data and meteorological station data. The aim is hereby to define a data- and simulation-based, transferable method to correct rain gauge undercatch for solid precipitation. Four different QPEs are injected in a snow temperature-index model and the simulations are compared to SWE data observed at snow monitoring stations. Two of the QPEs are obtained by applying a multiplicative correction factor to solid observed precipitation before computing the spatial interpolation. Thereby, the undercatch is corrected at the gauge level and not when precipitation is already interpolated.

The hydrological model developed in the MINERVE project is known to underestimate the discharge during the melting season for snow-dominated catchments with no or low glacier cover [Jordan, 2007a], which is most likely due to a lack in the received snow quantity. The objective of this chapter is thus to propose a methodology to define the best correction factor for solid precipitation from a snow hydrological modelling perspective.

3.2 Input data

The study is carried out over the Upper Rhône River (URR), as defined in Chapter 1 (Figure 3.1). The different sources of data used in the present chapter are presented hereafter.

3.2.1 Precipitation data

The QPEs used in this chapter are based on a combination of composite radar images provided by the Swiss Federal Office of meteorology and climatology (MeteoSwiss) and data from rain

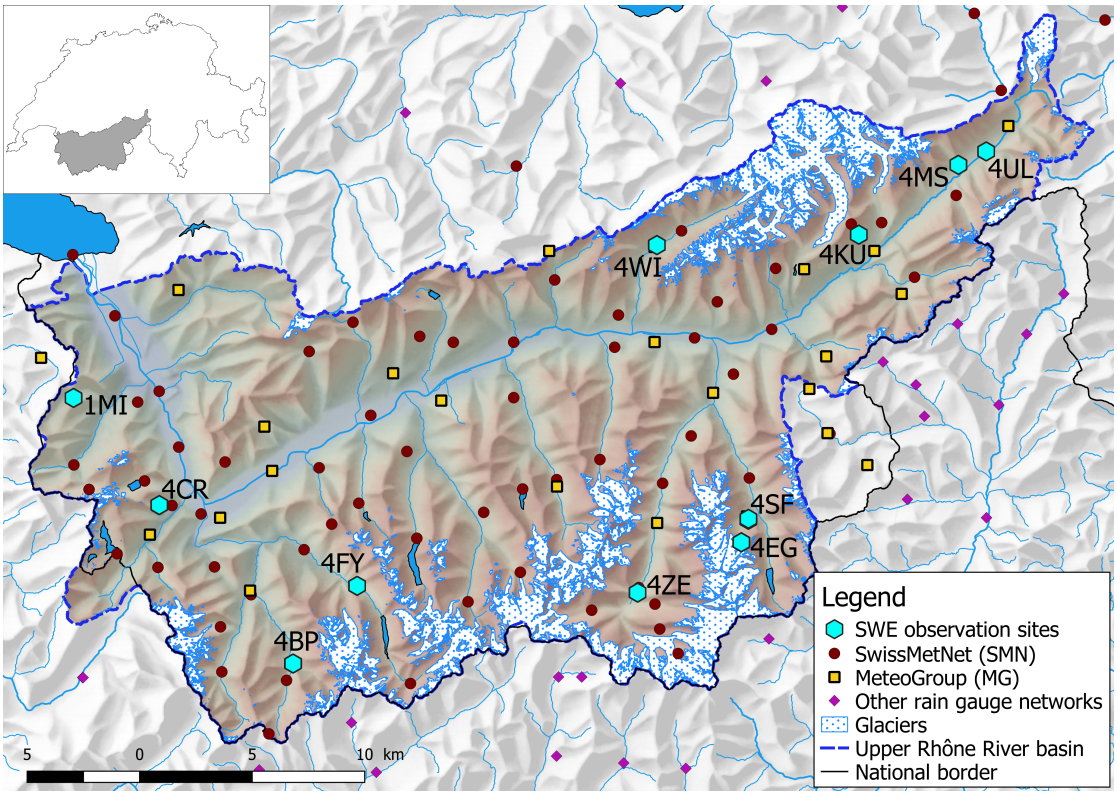

Figure 3.1 – Location of the SWE observation sites (with their short names) and the rain gauge stations (SwissMetNet, MeteoGroup and other networks). (Topographic data source: Swisstopo [2017b] for rivers and lakes, Swisstopo [2013] for the glaciers (with modifications), Swisstopo [2005] for the DEM, Swisstopo [2012] for the relief and Swisstopo [2017a] for the national boundary line).

gauges (see Subsection 3.3.3). The radar precipitation estimates are computed by MeteoSwiss at a 1-km spatial resolution and a 5 minutes temporal resolution. The back-scattered signal measured by the dual-polarization Doppler C-band weather radars in Switzerland is transformed into rain estimates, hereafter referred to as radar data, through several adjustment procedures [Germann and Joss, 2002, Germann et al., 2006, Gabella et al., 2017]. Initially composed of 3 installations, the Swiss weather radar network has been modernized and enriched with two new installations in 2014 and 2016 [MeteoSwiss, 2016]. The one installed in 2014, at Pointe de la Plaine Morte (PPM), is located within the studied basin and is operational since June 2014.

The radar precipitation estimates have been provided since November 2011; the analysis is thus carried out over the six hydrological years covering the period from 1 October 2012 to 30 September 2018.

3.2.2 Temperature data

Hourly temperature data from stations are interpolated at a 1 km grid resolution by applying a kriging with external drift (KED) using elevation [Hudson and Wackernagel, 1994]. Elevation data are aggregated from the digital height model (DHM) DHM25 [Swisstopo, 2005] from the Swiss Federal Office of Topography (Swisstopo). A temperature vs. elevation relation (red lines in Figure 3.2) is computed each hour with a moving window of 150 m elevation range and applying a two passes, forward and reverse signal filter using Butterworth filter polynomial coefficients. For elevation higher than 2500 m a.s.l., a linear interpolation of the available measurements is considered, as no temperature measurements are available in the highest elevation range of the basin (highest station at 3345 m a.s.l.). The temperature-elevation relation is used to adjust the elevation of temperature stations to the elevation of the DHM before residual computation in the kriging process.

The vertical gradient of temperature is generally well observable when displaying temperature vs elevation (Figure 3.2(i)). However, during some meteorological conditions, the relation between temperature and elevation is much less evident, such as on Figure 3.2(ii), where the lapse rate is visible only at highest elevation. The kriging with external drift applying a linear regression between elevation and temperature to compute the temperature trend (the grid of temperature used for residuals computation), conditions like the ones on Figure 3.2(ii) inevitably result in less accurate interpolated temperature fields.

Temperature data used for the interpolation are taken from 161 stations located within the URR basin and provided by 4 different networks. Table 3.1 provides the list of networks with the number of stations and the corresponding elevation range. The stations have different periods of data availability; in general, the coverage is increasing after 2012. There are only very few stations above 3000 m a.s.l. (corresponding to 13.0% of the catchment area); correspondingly, a higher uncertainty is associated to interpolated temperature at high elevation.

Table 3.1 – List of temperature station networks used for the interpolation.

Network name	**Number of stations**	**Elevation range [m a.s.l.]**
SwissMetNet	57	374-3129
MeteoGroup	24	460-2850
IMIS	56	950-3345
Agrometeo	24	376-1085

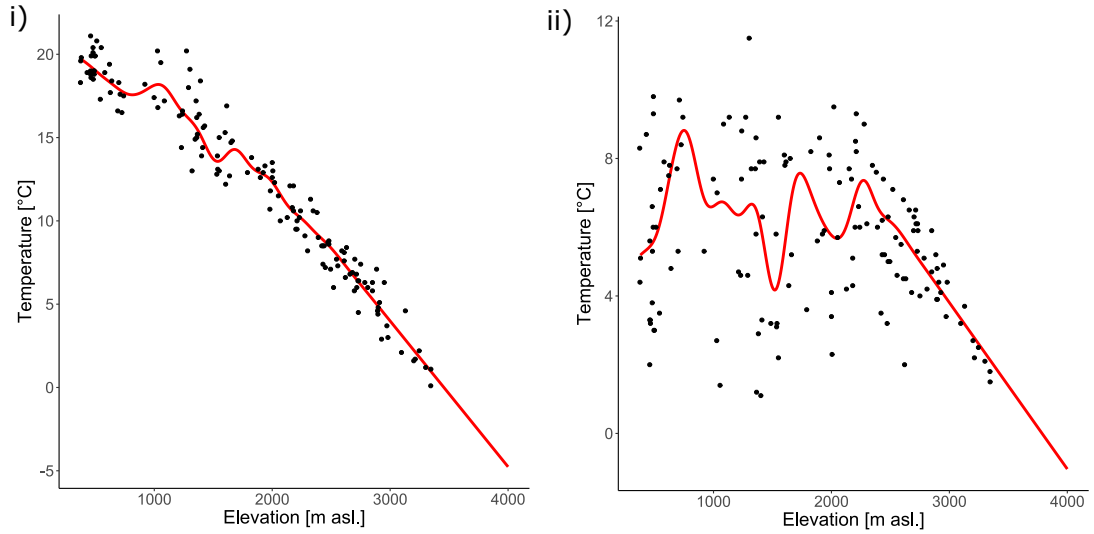

Figure 3.2 – Example of two hourly temperature vs. elevation relations, each point corresponding to a station: (i) one with a clear lapse rate of temperature (2013-09-26T10:00Z) and (ii) one with a less evident temperature-elevation relation (2013-10-19T05:00Z). The red line corresponds to the temperature-elevation relation computed on an hourly basis and used for elevation correction in the KED computation.

3.2.3 Snow-covered area

Two snow-covered area products from the Moderate-Resolution Imaging Spectroradiometer (MODIS) are used: MYD10A1 and MOD10A1 (version 6), respectively produced by the satellites Aqua and Terra [Hall et al., 2016a,b]. The data has been downloaded from the website of the National Snow and Ice Center (NSIDC, www.nsidc.org).

The two products have a spatial resolution of 500 m and provide a daily value of the Normalized Difference Snow Index (NDSI), related to the presence of snow in a pixel [Hall et al., 2002]. The index varies from 0 (no snow) to 100 (complete snow cover).

The original Aqua and Terra data were merged on a daily basis to handle cloud cover. On cloud-free days, the average of both satellite products is considered. On days with cloud cover in one product, the other value is retained. For days without data over a pixel, the daily value of the pixel is tagged as "NoData" (see Figure 3.3, in Appendix D). The merged data set is hereafter referred to as NDSI data. The daily computed values are attributed to 12:00 (UTC).

3.2.4 SWE data

Ground-based SWE observations are provided by the Institute for Snow and Avalanche research (SLF), Davos, at 11 observation sites located within the URR basin [SLF, 2019]. Coordi-

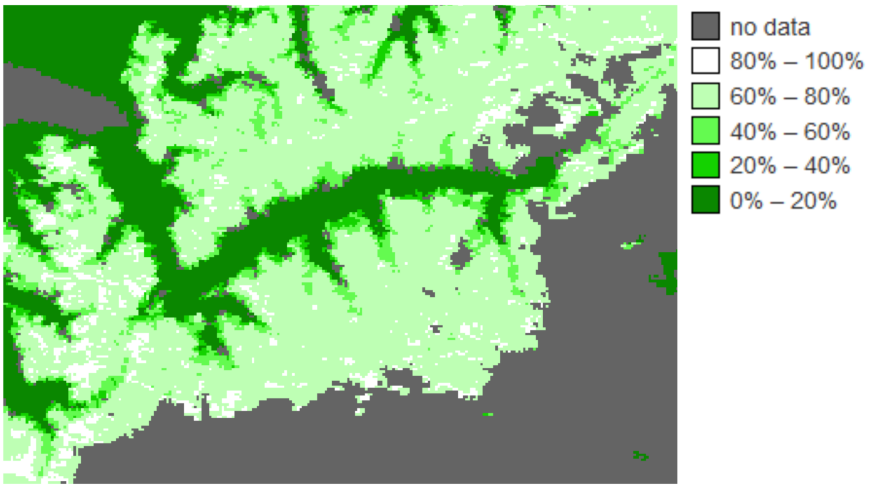

Figure 3.3 – Example of a daily map of NDSI values, resulting from the merging of the Terra and Aqua data.

nates are given in Table B.4, in Appendix D.

The SWE is measured by snow coring. Due to the destructive aspect of the method, the exact location of the measurement changes between the different dates. For each measurement, the average density is computed and the final SWE is estimated as the product of this density with the snow depth measured at a reference fix-mounted snow depth pole. To ensure robust data, the selected 11 sites only include locations with a slope lower than 20°.

Observations are generally performed every two weeks and more measurements are available during the accumulation rather than the melting phase. Over the studied period (October 2012 - September 2018), 469 observations are available over the 11 sites (Table 3.2). For the analysed period and over the 11 pixels containing the SWE observation sites, the percentage of days with an available NDSI data (NDSI data coverage) varies from 37.0% to 50.5% (Table 3.2).

3.3 Methodology

This section is organized in five parts. In the first two parts, the snow model and its calibration are presented. Third, the different QPE products are listed and detailed. Fourth, the performance assessment of the QPE products is explained, followed by implementation details.

3.3.1 The Snow-SD model

Snow modelling is done with the Snow-SD model (Snow model with a Seasonal Degree-day factor) implemented in the RS MINERVE software [Foehn et al., 2019a, García Hernández et al.,

Table 3.2 – SWE observation sites and NDSI data coverage.

Short name	Full name	Elevation [m a.s.l.]	Available measures	Period	NDSI data coverage [%]
1MI	Morgins	1320	41	12.2012-04.2018	45.1
4BP	Bourg St-Pierre	1670	40	11.2012-03.2018	49.4
4CR	Marécottes La Creusaz	1720	44	12.2012-04.2018	42.7
4EG	Egginer	2645	69	12.2012-04.2018	51.0
4FY	Fionnay	1500	43	12.2012-04.2018	46.2
4KU	Fiescheralp-Kuhboden	2210	55	12.2012-04.2018	37.0
4MS	Münster	1410	36	12.2012-04.2018	42.7
4SF	Saas-Fee	1791-1795	21	02.2013-04.2018	44.3
4UL	Ulrichen	1350	42	01.2013-04.2018	46.6
4WI	Wiler	1450	37	12.2012-04.2018	46.3
4ZE	Zermatt	1600	41	11.2012-04.2018	50.5

2019] at an hourly time step. The Snow-SD model is an improved version of the snow model proposed by Schaefli et al. [2005] and Hamdi et al. [2005], composed of two reservoirs, one for the solid fraction and one the liquid fraction of the snow pack to simulate the evolution of the snow pack and the melt water outflow as a function of snow pack saturation [e.g. Schaefli et al., 2014].

In a first step, the precipitation is divided into liquid and solid precipitation as a function of air temperature, using a linear increase of the liquid fraction between a minimum and maximum critical temperature for phase change [e.g. Jennings and Molotch, 2019].

To account for seasonal variation of the melt factor [Rango and Martinec, 1995], a temporal evolution of the degree-day factor S is considered [Slater and Clark, 2006, Griessinger et al., 2016, Magnusson et al., 2014] :

$$S(t) = \max\left(S_{min}; S_r + \frac{\Delta}{2}\sin\left(2\pi\frac{n - S_{ph}}{365}\right)\right) \tag{3.1}$$

where $S(t)$ is the time-varying degree-day factor, S_{min} is the minimal time-varying degree-day factor value, S_r is the reference (mean) degree-day factor, Δ is the degree-day factor variation interval, n is the day of the year since January 1^{st} and S_{ph} is the horizontal phase shift of the sinusoidal function with respect to the first day of the year. See Table 3.6 for all variables of the chapter.

The variation of the water equivalent of the solid fraction of snow, $H(t)$, is given by:

$$\frac{dH(t)}{dt} = P_s(t) - M(t) \tag{3.2}$$

where t is the time step, $P_s(t)$ is the solid precipitation rate and $M(t)$ is the melting or freezing rate of snow, given by:

$$\begin{cases} M(t) = S(t)\big(1 + b_p P_l(t)\big)\big(T(t) - T_{cf}\big) & \text{if} \quad T(t) > T_{cf} \\ M(t) = S(t)\left(T(t) - T_{cf}\right) & \text{if} \quad T(t) \leq T_{cf} \end{cases} \tag{3.3}$$

where b_p is the melting coefficient due to precipitation, $P_l(t)$ is the liquid precipitation rate and T_{cf} is the critical snow melt temperature. The initial condition of the water equivalent of the solid fraction of the snow pack $H(0)$ is given by the model value at the first time step.

The variation of the water depth of the liquid fraction of the snow pack, W(t), is given by:

$$\frac{dW(t)}{dt} = P_l(t) + M(t) - P_{eq}(t) \tag{3.4}$$

where $W(t)$ is the water depth of the liquid fraction of the snow and $P_{eq}(t)$ is the equivalent precipitation rate produced by the Snow-SD model, defined as:

$$\begin{cases} P_{eq}(t) = P_l(t) + \frac{dW(t)}{dt} & \text{if} \quad H(t) = 0 \\ P_{eq}(t) = 0 & \text{if} \quad H(t) > 0\,,\, \theta(t) \leq \theta_c \\ P_{eq}(t) = (\theta(t) - \theta_c)\frac{dH(t)}{dt} & \text{if} \quad H(t) > 0\,,\, \theta(t) > \theta_c \end{cases} \tag{3.5}$$

where θ_c is the critical relative water content in the snow pack before water outflow starts and $\theta(t)$ is the relative water content in the snow pack, given by:

$$\theta(t) = \frac{W(t)}{H(t)} \tag{3.6}$$

The initial condition of the water depth of the liquid fraction of the snow pack $W(0)$ is given by the model value at the first time step.

Finally, the Snow Water Equivalent (SWE), in [mm], is given by:

$$\text{SWE(t)} = H(t) + W(t) \tag{3.7}$$

where SWE is the total amount of solid and liquid water contained in the snow pack.

3.3.2 Parameter calibration

The calibration of the model aims at estimating the snow melting parameters, i.e. parameters S_r (reference degree-day factor) and Δ (degree-day factor variation interval) so that the simulated SWE reproduces the snow-covered area provided by the MODIS data. As this reference data only provides an information on the snow-covered area and not on the amount of SWE, the calibration is done on a Snow/No snow comparison basis for each pixel, for which ground observations are available.

It is noteworthy that temperature-index type snow models were initially not recommended for such small scales (nor for small time steps) [Rango and Martinec, 1995], but applications at the pixel scale have yielded "results reasonably consistent with observations" [Pistocchi et al., 2017] in the recent past.

Both the simulated SWE and the NDSI (from MODIS) data are transformed into a binary variable with 0 being "no snow" and 1 being "with snow". Threshold values were fixed based on the values defined by Parajka and Blöschl [2008b], for which the error was considered as unbiased, i.e. snow overestimation and underestimation errors were similar:

$$\begin{cases} \text{NDSI}_{bin} = 0 \quad \text{if} \quad \text{NDSI} < 25 \\ \text{NDSI}_{bin} = 1 \quad \text{if} \quad \text{NDSI} \geq 25 \end{cases} \tag{3.8}$$

$$\begin{cases} \text{SWEsim}_{bin} = 0 \quad \text{if} \quad \text{SWEsim} = 0 \\ \text{SWEsim}_{bin} = 1 \quad \text{if} \quad \text{SWEsim} > 0 \end{cases} \tag{3.9}$$

It must be noted that these threshold values were computed on an earlier version of the MODIS data and might not be the best for the new version of the MODIS product. Future investigations might explore other threshold values to improve the results.

The calibration considers for the computation only the days with an available daily value of the pixel, i.e. with data at least from one of both satellites over the pixel (see Section D.1 in Appendix D for more information). The optimization is done within the RS MINERVE software with the Shuffled Complex Evolution – University of Arizona (SCE-UA) algorithm [Duan et al., 1993]. The objective function is composed of the Overall Accuracy performance indicator alone [Parajka and Blöschl, 2008a], derived from a confusion matrix (Table 3.3) with two dimensions opposing predicted and actual values where each category (cell) represents the corresponding number of days. The Overall Accuracy is given by:

$$\text{Overall Accuracy (OA)} := \frac{T_P + T_N}{T_P + T_N + F_P + F_N} \tag{3.10}$$

where T_P is the number of True Positive cases, T_N of True Negative, F_P of False Positive and F_N of False Negative. The indicator varies from 0 to 1 and indicates the percentage of days correctly estimated in terms of presence or absence of snow with respect to the defined thresholds.

Table 3.3 – Confusion matrix defining the terms used for the Overall Accuracy computation.

Number of days	**Snow-covered (NDSI)**	**No snow (NDSI)**
Snow-covered (Sim)	T_P	F_P
No snow (Sim)	F_N	T_N

In the calibration of the snow melting factors, seasonal variation of the factor is also studied. Three different fixed variation intervals (Δ=0, Δ=1 and Δ=2 [mm °C^{-1} d^{-1}]) are explored, as well as a calibration of the optimal variation interval for each SWE measurement site (Δ=calib).

3.3.3 QPE Design

Four different QPE products are used for comparison within this study. Whereas the first product is provided by MeteoSwiss, the 3 others have been computed for the present study.

Product QPE1

The first QPE product, hereafter referred to as QPE1, is the operational QPE product of MeteoSwiss computed over entire Switzerland and known as *CombiPrecip*. Rain gauges from the automatic monitoring network SwissMetNet (SMN) of MeteoSwiss are combined with the radar data (see Subsection 3.2.1) using data from the time step of computation as well as from the preceding time step (as secondary variable) in a co-kriging with external drift approach [Sideris et al., 2014a].

Data are delivered as hourly sum of precipitation at a 1-km spatial resolution. Over the studied period, data were missing for 268 hours (no available hourly raster), representing on average over the entire period 0.5% of the data. For these times steps, a precipitation of 0 mm/h over the entire domain was considered.

Product QPE2

The second QPE product, hereafter referred to as QPE2, is the spatially distributed precipitation product RCK presented in Chapter 2 [Foehn et al., 2018]. The interpolation is carried out using a regression co-kriging applied to the radar data provided by MeteoSwiss combined to two non-collocated networks of rain gauges: the SMN network of MeteoSwiss and the network of the private company MeteoGroup Switzerland AG (MG). The integration of 23 MG stations located within the basin provides for the computation an information on areas less covered by the SMN stations. However, as demonstrated in Chapter 2, due to the installed equipment, the MG stations tend to underestimate the precipitation up to more than 20%. The use of a regression co-kriging approach allows benefiting from the local information provided by these stations while accounting for their underestimation with an hourly analysis of the correlation between the SMN and MG networks. In the very final interpolation step (local correction), data from stations of the networks of the Canton of Bern, Météo-France, Électricité de France, Regione Autonoma Valle d'Aosta and ARPA Piemonte are also used when available (see Chapter 1).

The computation is done over the studied basin and data are computed as hourly sums of precipitation at a 1-km spatial resolution. For the hourly time steps without radar data

(42 hours over the studied period), Inverse distance weighting was applied to the gauge precipitation data (see Chapter 1). Thereby, QPE2 does not contain time steps with missing data.

Products QPE2-120 and QPE2-130

To explore the correction of the solid precipitation undercatch by rain gauges, two modified versions of the QPE2 product have been computed for the study. The observed precipitation at rain gauges is modified according to the observed temperature before the spatial interpolation computation:

$$\begin{aligned} P(t) &= P_m(t) \quad \text{if } T(t) \geq 2^\circ\text{C} \\ P(t) &= \beta P_m(t) \quad \text{if } T(t) < 2^\circ\text{C} \end{aligned} \tag{3.11}$$

where $P(t)$ is the corrected precipitation rate at the station, $P_m(t)$ is the measured precipitation rate at the station, $T(t)$ is the air temperature measured at the station and β is the correction factor.

When no temperature data is available for a given station and a given hour (due to the absence of a temperature sensor or to a temporary breakdown of the sensor), the temperature of the spatial temperature product presented in Subsection 3.2.2 is used, by considering the pixel containing the rain gauge.

Two values of the parameter β are explored in this study: 1.2 for the product QPE2-120 and 1.3 for the product QPE2-130. Data from both SMN and MG stations are corrected with Eq.(3.11).

3.3.4 QPE performance assessment

The performance of the different QPEs is compared as follows:

First, the Overall Accuracy (OA), used for model calibration, is considered to evaluate the capacity of the different QPEs to reproduce the presence/absence of snow.

A graphical representation of the temporal evolution of observed and simulated SWE at each location is then given to provide better understanding of the relation between simulation results and observations and insights into the snow cover evolution at the different SWE observation locations.

Biases induced by the different QPEs are highlighted with linear regressions between simulated and observed points, which gives a global comparison between all simulated and observed SWE values.

To give more weights to higher values of SWE in the evaluation, comparisons are completed separately for different SWE intervals.

The final evaluation is done using the Mean absolute error (MAE) of the SWE simulations computed for each QPE for each studied Δ value. The case with the lower MAE is then selected as the optimal QPE product (in combination with an optimal Δ value).

3.3.5 Implementation

The retained model parameter values as well as search ranges for calibration are summarized in Table 3.4.

Table 3.4 – Parameter values for the Snow-SD model

Fixed parameters	Value	Remark
θ_c	0.1 (10%)	-
S_{ph}	80 (March 21^{st})	-
T_{cp1}	0°C	[He et al., 2014]
T_{cp2}	2.5°C	[He et al., 2014]
S_{min}	0.5 [mm °C^{-1} d^{-1}]	-
b_p	0.0125 [d mm^{-1}]	[Foehn et al., 2019a]
Calibrated parameters	**Range**	**Remark**
S_r	0-20 [mm °C^{-1} d^{-1}]	-
Δ	0-4 [mm °C^{-1} d^{-1}]	For Δ=calib

All computations are completed in the R language and environment for statistical computing [R Core Team, 2018]. Used packages are *gstat* for the spatial interpolation [Pebesma, 2004, Gräler et al., 2016], the package *parallel* for parallel computation [R Core Team, 2018], the package *lubridate* for dates and times formatting [Grolemund and Wickham, 2011], the package *openxlsx* for Excel file handling [Walker, 2018], the package *ggplot2* for the plots [Wickham, 2016], as well as *raster* [Hijmans, 2017], *gridExtra* [Auguie, 2017] and *httr* [Wickham, 2018].

The snow modelling computation has been done with the software RS MINERVE[2] through its command tasks functionality. The successive operations (model opening, dataset loading, model calibration, results exportation, etc.) are defined in VBScripts and launched as external process from the R language.

3.4 Results

This section first presents the pre-treatment of the data explaining why some stations have been partly or completely excluded from the analysis, followed by the model calibration and a detailed analysis of the QPE performance. Finally, the selection of the optimal product is presented.

[2] Software version RS MINERVE 2.7.6

3.4.1 Pre-treatment

Simulated SWE followed the observed SWE relatively well for most of the points when looking in particular at the results with the QPE2-120 and QPE2-130 products (see Figure D.2 in Appendix D). However, two locations tended to strongly underestimate the snow quantity: 4EG (Egginer) and 1MI (Morgins). These two locations have therefore been investigated.

Regarding the 4EG station, the analysis revealed a clear reduction in the simulated SWE over the four last winters as compared to the first two ones (Figure 3.4, left). Over the two first winters, the simulated SWE follows closely the observed values. As from the winter 2014-2015, the simulation strongly underestimates the observations. The same is observed, though less evident, for station 4SF (Saas-Fee, see Figure 3.4, right), located about 3 km more downstream in the same valley.

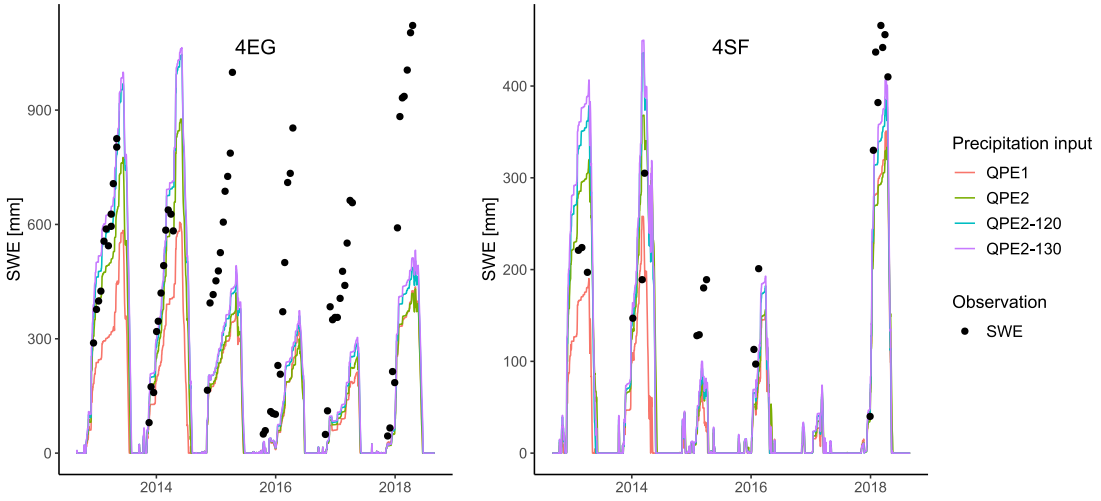

Figure 3.4 – Observed and simulated SWE with the 4 different QPE products for the stations Egginer (4EG), left, and Saas-Fee (4SF), right.

The moment of appearance of the performance switch coincides with the entry into service of the new weather radar of Pointe de la Plaine Morte (PPM) in June 2014. The radar data provided by MeteoSwiss have been extracted for the 3 pixels containing respectively the SWE observation sites 4EG and 4SF as well as the SMN station Saas Balen (VSSAB), the nearest SMN station. The cumulative radar precipitation has been computed over these 3 pixels from September 1, 2012 to August 31, 2018. The difference between the cumulative precipitation at the SWE observation sites with the cumulative precipitation at the SMN station is given in Figure 3.5. Before June 2014, the precipitation given by the radar pixel containing the VSSAB station reported less precipitation than the two pixels containing the SWE observation sites (increasing differences in Figure 3.5 for both curves). After the entry into service of the new weather radar, the tendency was clearly reversed with more precipitation observed over the pixel containing the VSSAB station.

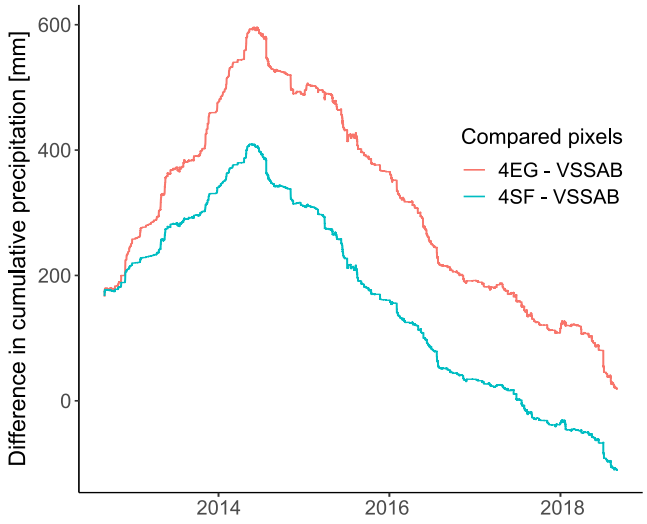

Figure 3.5 – Difference between the cumulative radar precipitation estimation over the pixels containing the SWE observation sites 4EG and 4SF and the pixel containing the SMN station VSSAB.

The entry into service of the new radar at Pointe de la Plaine Morte has modified differently the visibility over the concerned pixels. Whereas it has increased considerably over the pixel containing the VSSAB station, the visibility has not increased much over the two other pixels (based on the analysis of the visibility maps of the radar composite products, not shown here). The analysis showed that the Scatter [Germann et al., 2006] over the VSSAB pixel has reduced from 3.67 to 3.24 dB when comparing the two years before and the two years after the entry into service of the PPM radar, which is a lot. This different increase in visibility has a direct effect in the QPE products computation. Indeed, in the co-kriging with external drift (QPE1 approach) or the regression co-kriging (QPE2 approaches), the difference between the gauge observation and the radar value defines the local correction brought in the final step of the interpolation. If the pixel over which the comparison is done (in that case over VSSAB) implies a lower correction (due to good visibility) as compared to what surrounding pixels would need (due to lower visibility), the surrounding pixels might suffer from an underestimation in the interpolation result. Further investigation will be necessary to clarify the observed issue. Based on this analysis, data for the locations 4EG and 4SF over the four last winters have been excluded from the analysis.

The second station on which strong underestimation in the simulated SWE is observed is the 1MI station (Figure 3.6). The analysis revealed that the problem of SWE underestimation at this station already occurred before June 2014 and was in that case not related to the precipitation but to the temperature. Indeed, the precipitation over the winter allowed to reproduce the observed SWE with the simulation much better when applying a reduction of the temperature of about 3 to 5 degrees.

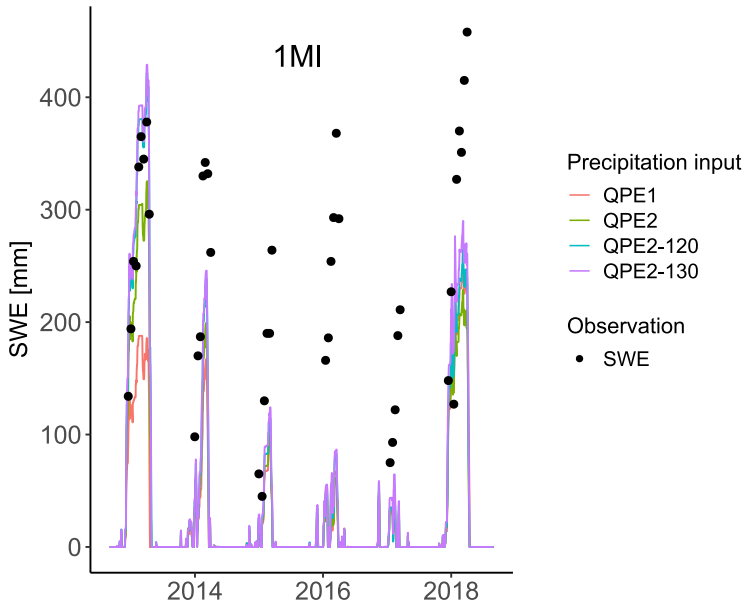

Figure 3.6 – Observed and simulated SWE with the 4 different QPE products for the station Morgins (1MI).

The observed melting events in the simulation allowed to identify episodes during which the temperature at many stations in the vicinity of the 1MI observation site reported temperatures clearly above the ones observed at other stations in the basin with similar elevation (Figure 3.7). Differences in temperature are mostly observed at elevations up to 1000 m a.s.l. The observed phenomena results from the presence of a cold-air pool installed in the central part of the studied basin (far from 1MI station). The warmer air blowing from the west overflies the cold air mass and affects only stations located at an elevations higher than 1000 to 1500 m a.s.l. In the interpolation of the spatial product of temperature used in this work, this phenomena tends to increase locally the temperature in the vicinity of stations reporting temperatures higher than the average temperature at this elevation. The temperature vs. elevation relation being computed over all stations, local corrections can thereby be affected by the inadequacy of the mentioned relation. This is probably what happens to the Morgins SWE measurement site, located at 1320 m a.s.l. and on which the 3 of 4 resulting excess degrees are sufficient to affect the simulated SWE.

Further work will be necessary on the temperature data to obtain a robust hourly spatial product. The local aspect of the observed phenomena will, however, certainly represent a real challenge. Based on this analysis, the station 1MI was completely excluded for the analysis.

After the partial exclusion of the observation sites 4EG and 4SF and the complete exclusion of the site 1MI, 367 SWE observations remain available for the analysis.

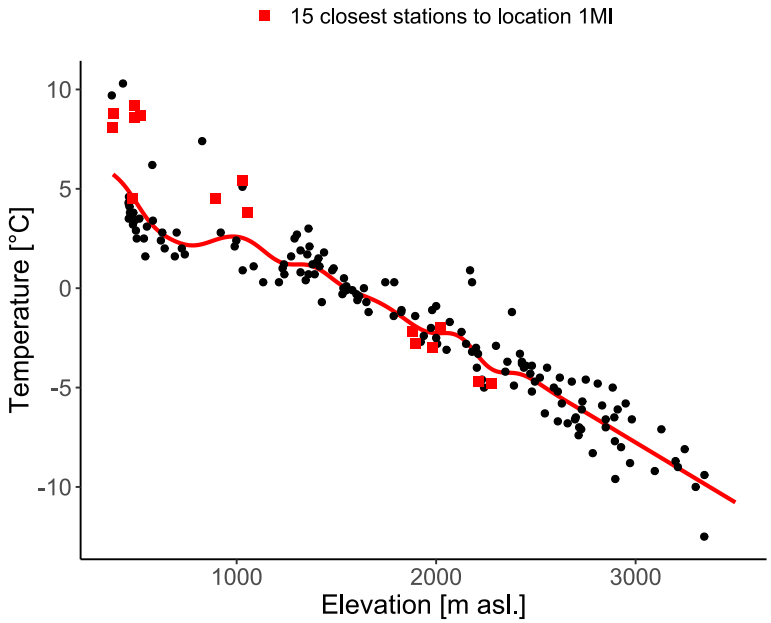

Figure 3.7 – Hourly averaged temperatures observed over the entire basin on 2016-01-11T12:00:00Z. The red points highlight the 15 temperature gauges closest to location 1MI used in the interpolation.

3.4.2 Model calibration results

Figure 3.8 illustrates the behaviour of the binarized simulated SWE (red line) and the binarized NDSI data (black points). The presence and absence of snow is well reproduced, even though some isolated MODIS observations are not reproduced with the simulation and some appearances of snow in the simulation are not confirmed by the observations.

In terms of DDF values, Figure 3.9 gives the obtained values for three key dates marking the seasons, December 21 (where $S(t) = S_r\text{-}0.5\Delta$), March 21 ($S(t) = S_r$) and June 21 ($S(t) = S_r\text{+}0.5\Delta$). The increase of melting rates over the winter is well visible for variation intervals different from 0. For the values obtained for December 21, the fixed minimum value of 0.5 [mm °C^{-1} d^{-1}] is reached at some locations with Δ=2 and Δ=calib. For the case with calibrated Δ values, obtained values using QPE2 as input varied between 1.6 and 3.7 [mm °C^{-1} d^{-1}]. The results also show that a higher DDF variation interval increases the amount of SWE (see Figures D.3 and D.4 in Appendix D). Using for example the product QPE2-120 as precipitation input, the linear regression value of 0.96 obtained with $\Delta = 0$ increases to 1.01 with a calibration of Δ.

This increase was expected as a higher variation interval not only increases the melting at the end of the winter, but also reduces the melting over the first winter months, thereby potentially increasing the SWE accumulation over the first part of the winter. The differences in terms of simulated SWE are mostly occurring over the first winter months (Figure D.5 in Appendix D).

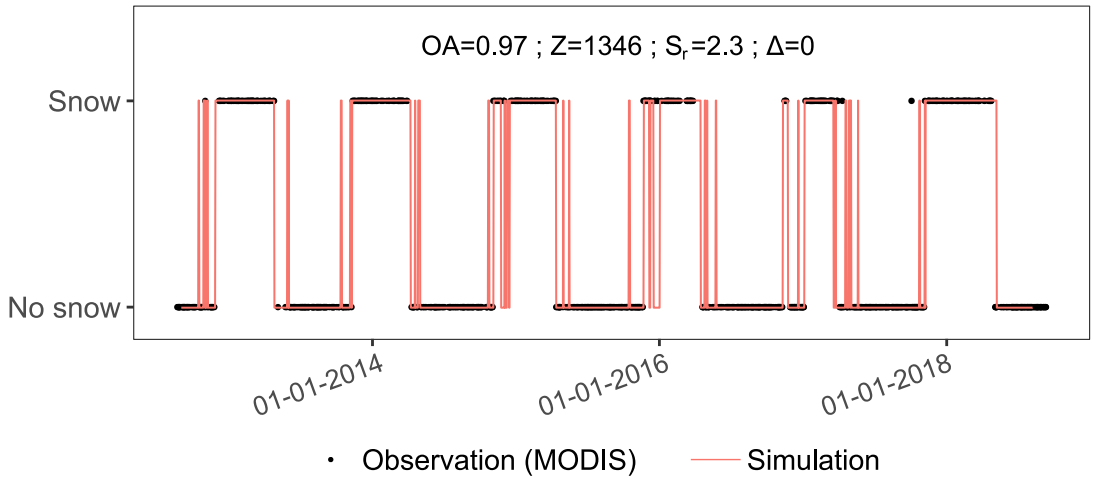

Figure 3.8 – Example of a binarized series of simulated SWE and the corresponding binarized NDSI observations at location 4UL (Ulrichen) . Computation realized with the QPE1 product. OA refers to Overall Accuracy and Z to elevation.

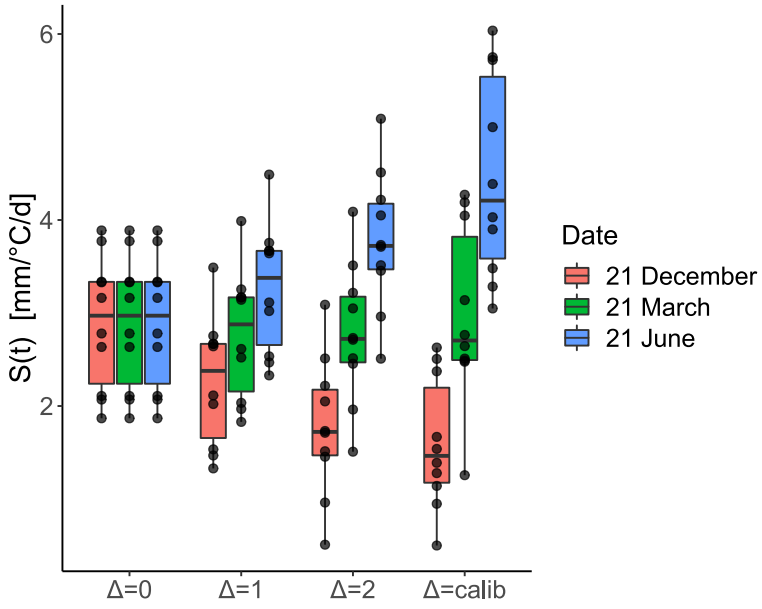

Figure 3.9 – Time-varying degree-day factor (S_t) values obtained with the QPE2-120 precipitation input. Minimum (21 December), mean (21 March) and Maximum (21 June) values are given for the 10 SWE measurement locations. The boxplots show the median (bold horizontal line) and the 25 and 75 quantiles (hinges). The upper (respectively lower) whisker extend from the hinge to the largest (lowest) value no further than 1.5 times the inter-quartile range. Further values would be shown as outliers.

The Overall Accuracy (OA) tends to increase with increasing Δ (Figure 3.10), indicating a better snow-covered area reproduction with a higher freedom on the snow melt variation interval.

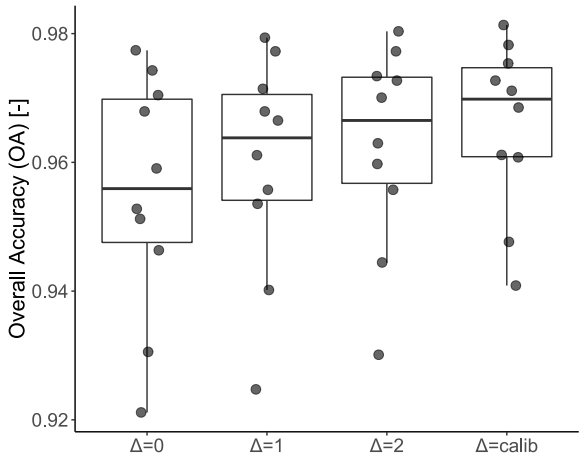

Figure 3.10 – Overall Accuracy values obtained in the reproduction of the snow-covered area with the different values of DDF variation interval, using the QPE2-120 product. Horizontal shifting of points is only for visibility.

3.4.3 Difference between QPEs

Results show that an increase of precipitation at stations measuring snow (with QPE2-120 and QPE2-130) tends to increase the value of the calibrated degree-day factors (Figure 3.11). With a deeper snow pack, but the same snow-covered period (given by the MODIS data), the model needs to melt the snow faster.

Interestingly, the OA values show only little difference between the precipitation products (Figure 3.12). QPE1 provides a slightly better median value than the others (based on the 10 points corresponding to the 10 SWE observation sites). This small difference between the QPE products suggests that the tested QPEs and namely the associated snowfall corrections have almost no impact on the presence or absence of snow. This is particularly true for the three versions of the QPE2 products, with almost no difference between QPE2, QPE2-120 and QPE2-130.

In terms of reproducing the observed SWE temporal evolution, the simulation reproduces globally well the observed quantities (Figure 3.13). For some locations, the model performs even very well, for example at the location 4CR (Marécottes-La Creusaz). However, results for station 4WI (Wiler) tend to highly overestimate observed SWE values with QPE2-120 and QPE2-130 over the first and last winters. No particular explanation could be found in that case. Correspondence of simulations with observations is also variable for example for locations 4BP and 4ZE.

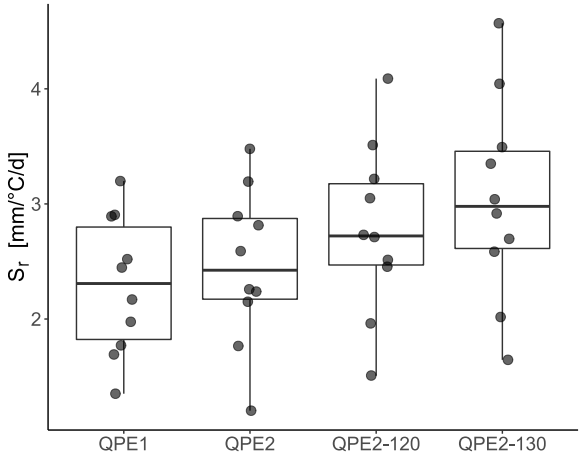

Figure 3.11 – Reference degree-day factor (S_r) values obtained with the four QPE products for the 10 analysed SWE measurement locations ($\Delta = 2$).

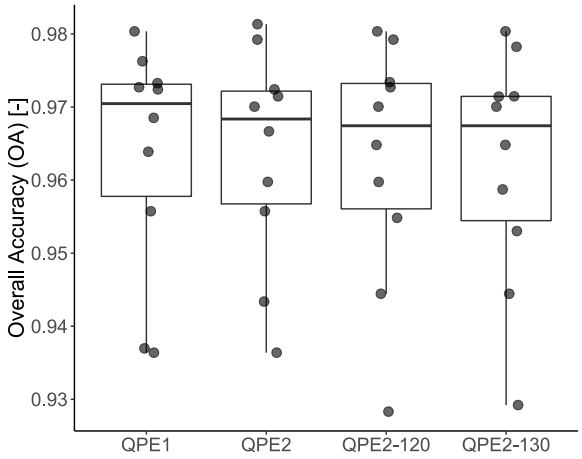

Figure 3.12 – Overall Accuracy values obtained in the reproduction of the snow-covered area using the different QPE products and calibrating S_r at each location with a fixed DDF variation interval ($\Delta = 2$).

To highlight potential biases, Figure 3.14 presents a scatter plot of the simulated and observed SWE using the four QPE products. The obtained results show that a correction of observed precipitation when temperature is lower than 2°C yields only small biases: For QPE2-120 and QPE2-130, the slope of the linear regression is close to 1 (0.96 for QPE2-120 and 1.02 for QPE2-130), whereas in the absence of precipitation correction, the simulations show a strong underestimation (with a slope of 0.67 for QPE1 and of 0.81 for QPE2).

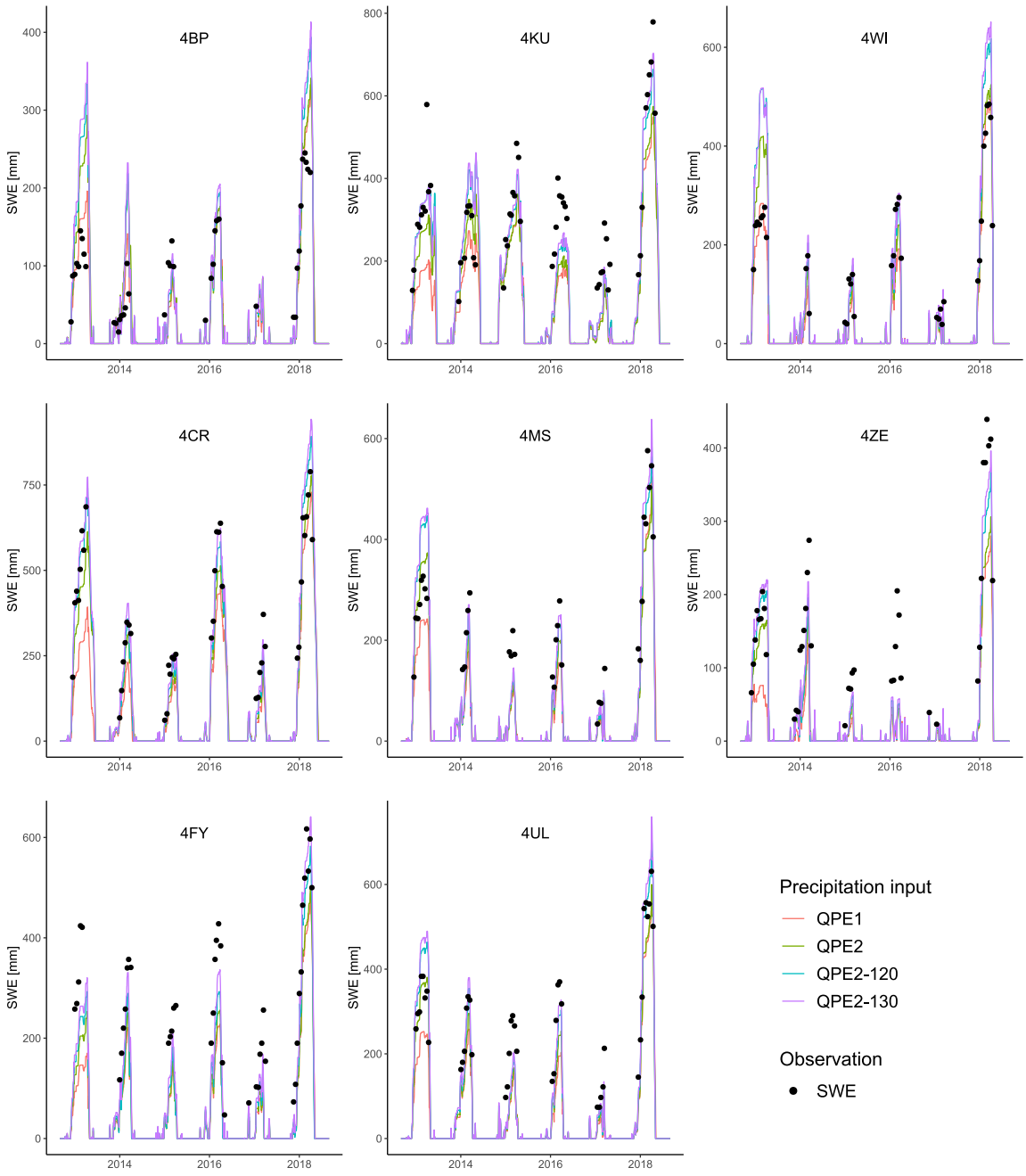

Figure 3.13 – Simulated SWE with the 4 QPE products versus observed SWE at the 8 SWE observation sites for which all the data have been used for the analysis (with $\Delta = 0$).

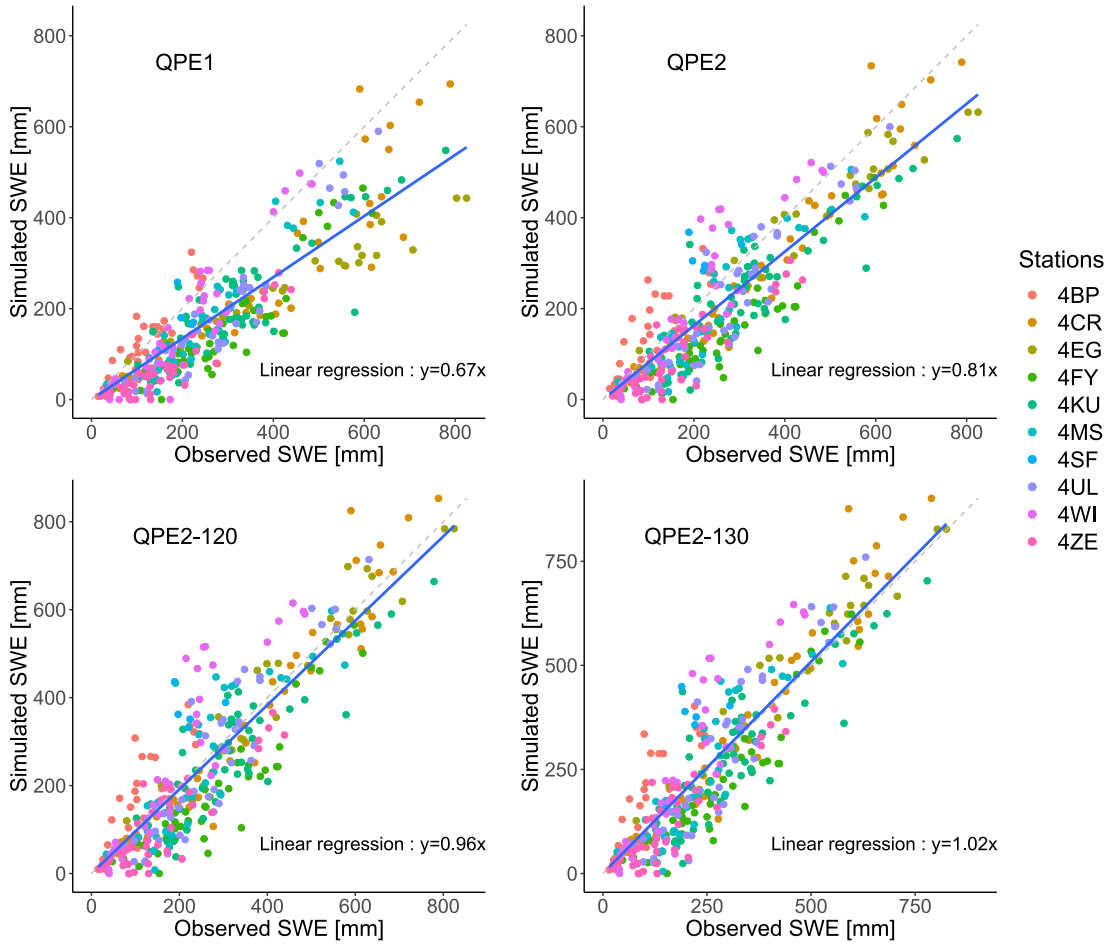

Figure 3.14 – Simulated vs. observed SWE for the four QPE products ($\Delta = 0$). The grey dashed line indicates a slope of 1. Number of points: 367.

3.4.4 QPE performance assessment

Figure 3.15 proposes a more detailed analysis with a computation of the confusion matrices considering four different SWE threshold values (100, 200, 400 and 600 mm). For the 100 mm threshold, for which there is the highest number of available observations, QPE2-130 yields the best Overall Accuracy (0.87), followed by QPE2-120, QPE2 and QPE1. This order changes for the different thresholds (Figure 3.15), with QPE1 showing consistently lower OA values than the other QPEs. For the 600 mm threshold (only 22 observations), all QPEs show almost the same performance.

In that last case, QPE2-130 reproduces much better the 22 observations overrunning the threshold (17 out of 22), but the number of false overrun passes from 1 for QPE1 to 11 for QPE2-130. Indeed, with an increase of the solid precipitation, the number of False Negative (bottom left), demonstrating an underestimation by the model, tends to reduce in favour of

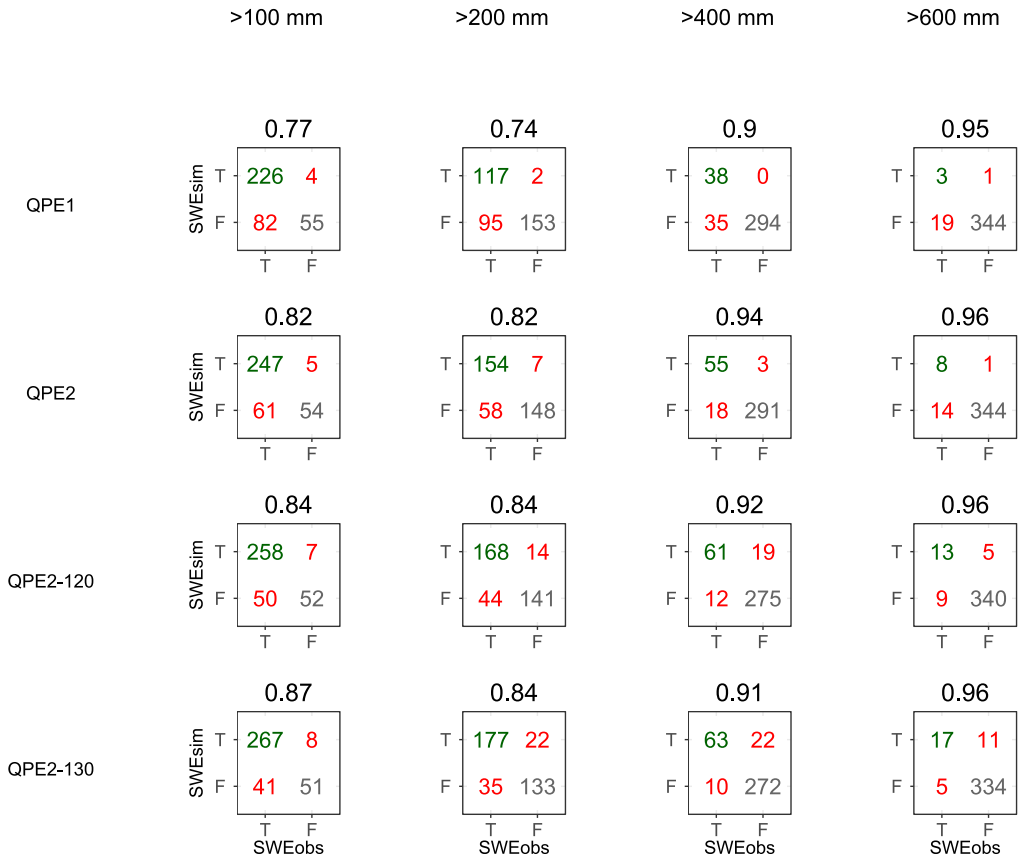

Figure 3.15 – Confusion matrices and Overall Accuracy values obtained with the four QPE products ($\Delta = 0$) to reproduce the observed SWE values when applying SWE thresholds of 100, 200, 400 and 600 mm. T (TRUE) refers to threshold overrun (=Snow) whereas F (FALSE) indicates cases without threshold overrun (=NoSnow).

True Positive cases (upper left). This is due to the fact that the sum of True Positive and False Negative remains constant as it corresponds to the (fixed) number of observations above the studied threshold. At the same time, the number of False Positive (upper right), sign of an overestimation by the model, tends to increase as a result of the increased precipitation.

Depending on the analysed threshold, this interaction can have a different impact on the obtained OA values. This probably explains why the analysis with the four thresholds does not clearly identify one QPE that outperforms the others for all four thresholds. However, overall, QPE2-130 provides the best results for lower threshold values.

Figure 3.16 provides a graphical comparison for the four SWE thresholds and the four explored DDF variation intervals. The conclusions from Figure 3.15, computed with Δ=0, remain globally valid for all Δ values. Only for the 400 mm threshold, the QPE1 performance overpasses the one of QPE2-120 and QPE2-130 with increasing flexibility on the DDF variation interval. The confusion matrices corresponding to Figure 3.16 are given in Figures D.6 to D.9.

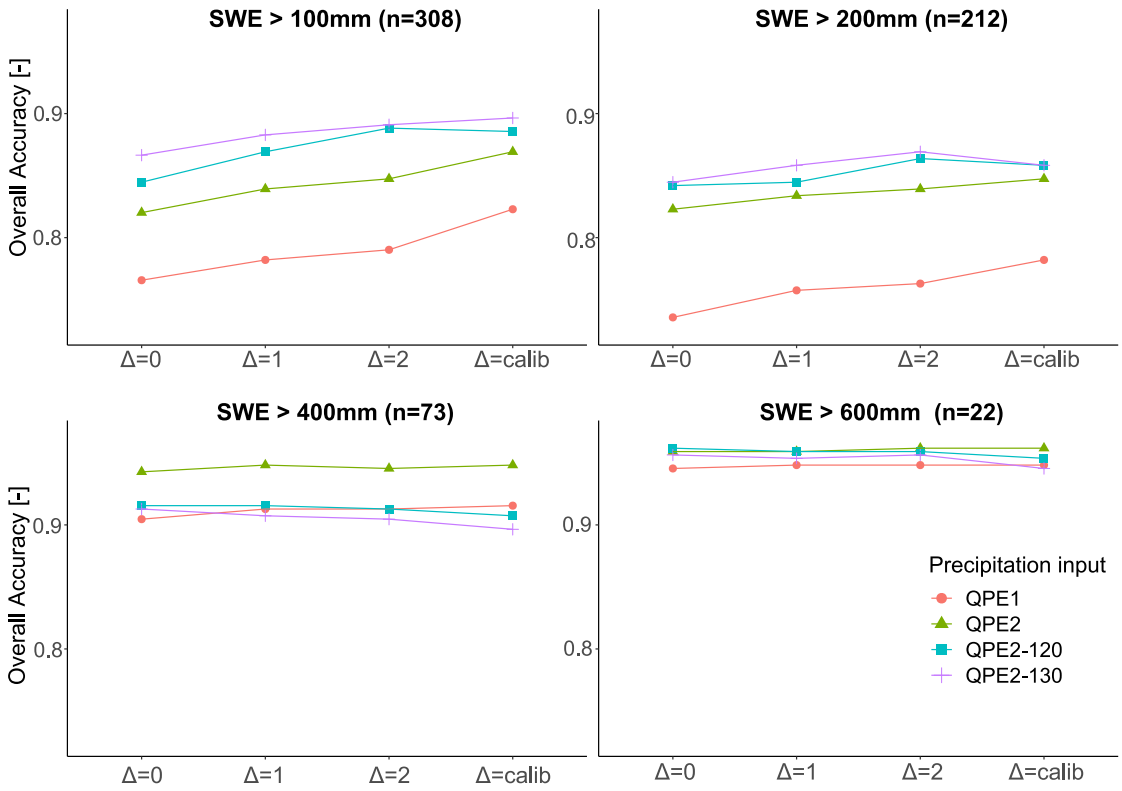

Figure 3.16 – Overall Accuracy values obtained with the four QPE products and the four variation intervals over the four analysed SWE threshold values. *n* indicates the number of observations overrunning the threshold.

Finally, the estimation errors for each SWE observation were computed for the four different QPE products and for the four studied variation intervals (Figure 3.17).

The clear underestimation with QPE1 and QPE2 is well visible with negative errors for most of the points, in particular for QPE1. For the two variation intervals Δ=2 and the calibrated Δ, the median of the errors is just below 0 for QPE2-120 and just above 0 for QPE2-130, which confirms the better performance of these two products. In addition, this result suggests that the ideal constant correction factor value is probably situated between 1.2 and 1.3.

The Mean Absolute Errors (MAEs) have been computed for the 16 configurations. The lowest error value is obtained with QPE2-120 and Δ=2 (Table 3.5). This configuration is therefore retained as the best combination considering the available input data.

Table 3.5 – Mean Absolute Errors (MAE) obtained with the different QPE products and the different degree-day factor variation intervals (Δ, expressed in [mm °C^{-1} d^{-1}]). Units of MAE values are [mm].

Variation interval	**QPE1**	**QPE2**	**QPE2-120**	**QPE2-130**
$\Delta = 0$	98.2	74.2	66.6	66.1
$\Delta = 1$	92.9	70.0	64.1	65.0
$\Delta = 2$	91.2	66.7	**61.6**	63.4
$\Delta = calib$	85.0	62.4	62.0	66.1

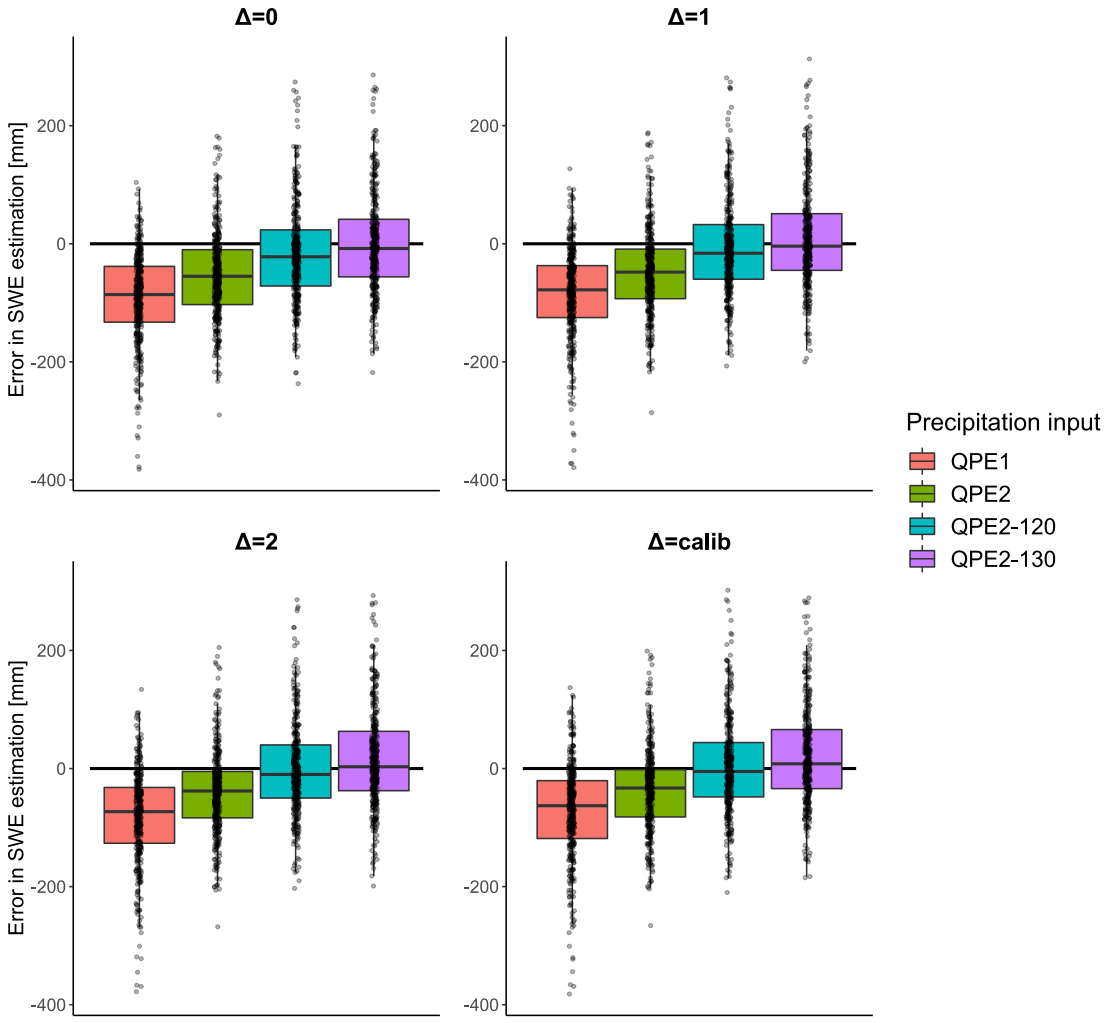

Figure 3.17 – Estimation errors for the 367 SWE measurements considering the different QPE products and the different DDF variation intervals.

3.5 Discussion

3.5.1 Methodological choices

Considering the methodology presented in this chapter, a few points are worth further discussion. First, the OA values are computed over the entire simulation period, rather than only over the accumulation phase. The present choice might a priori seem questionable since including the melting phase in the analysis might result in a compensation effect between the degree-day factors and the accumulated SWE, therefore reducing the relevance of the comparison between QPE products. However, the use of MODIS data, not providing information on the quantity of snow but only on its presence or absence, requires considering the entire period for the evaluation, as disappearance of snow is required for comparison (and calibration) purposes.

Second, the QPE1 and QPE2 products were not used in combination with multiplicative precipitation correction factors, i.e. there is no correction of the precipitation values after spatial interpolation. Such an approach could arguably be considered as being the simplest possible approach to account for snow undercatch QPEs. This choice was motivated by the wider hydrological context of the underlying research project, which involves the need of producing a precipitation input over the entire year. In this context, the use of a multiplicative factor over the entire year is not a viable option.

Finally, improvements in the modelling methodology are also possible. For example, fine tuning of the threshold used in the binarization of MODIS data and simulated SWEs could be investigated, as values from literature have been used in the present study. Another source of uncertainty within the model comes from the minimum and maximum critical temperature for liquid precipitation. Modification of these values could positively affect the simulation results and might be further investigated in future research.

3.5.2 Advantage of fixing the variation interval

The obtained results clearly suggest that retaining a fixed DDF variation interval value (Δ=2) yields very good performances as compared to site-specific calibrated values when using the two QPE products integrating a correction of solid precipitation. This is an important added value in the perspective of later calibrating the melt factors for all pixels over a catchment (in chapter 4), with possibly much higher variability between the pixels due for example to the presence of forest or higher slopes (the SWE observation locations used here are on flat and clear terrain). Fixing the DDF variation interval reduces the risk of excessive spatial variability of the parametrization. In addition, considering a fixed DDF variation interval will also facilitate the comparison between the DDF values obtained over the catchments.

3.5.3 Input products

An interesting observation is the difference in the temporal evolution between the simulated SWE values obtained with QPE1 and QPE2 over the winters, although both products are based on the same radar data. Whereas differences are relatively high over the first analysed winter (2012-2013), differences become much smaller or even disappear over the last winter (2017-2018), as for example well illustrated for the Zermatt (4ZE) station (see Figure 3.13). The reason of this evolution cannot be explained at this stage. Among the possible reasons, one can mention an evolution of the algorithm underlying the computation of QPE1 over time (QPE2 and its modified versions were computed at once; see Subsection 3.3.3). Another explanation could be the evolution of the automatic meteorological network, affecting differently QPE1 and QPE2, with the first being computed over entire Switzerland and the second only over the studied basin.

Future work should probably investigate finer correction of the precipitation values instead of applying temporally-constant multiplier factors, in particular by accounting for wind speed. The use of "transfer functions" [Kochendorfer et al., 2017] to relate correction factors to wind speed seems particularly promising in this context. One can expect that with finer correction, the final QPE product will be closer to the real precipitation, in particular in windy areas, thereby allowing also better snow modelling. However, a new challenge will arise from the fact that many rain gauges are not combined with a wind gauge.

Such a finer correction would also benefit from improved air temperature interpolations. The highlighted cold-air pool phenomena issue during the presence of a stable cold air mass in the centre of the Valley should be further analysed to develop a more robust product of temperature.

Furthermore, the non-continuity in precipitation of radar data after the introduction of the new weather radar of Pointe de la Plaine Morte probably also explains part of the differences between simulated and observed SWE values over the studied basin. Future improvements in the complex aggregation of radar data will certainly allow a gain for snow and hydrological modelling. Recomputation of the radar historical data with improved algorithms could be very interesting in that perspective.

3.6 Conclusions

In this chapter, a methodology has been proposed to compute quantitative precipitation estimates (QPEs) for snow hydrological modelling, based on an existing product obtained from radar data and ground station merging. Four different QPE products are tested in combination with a temperature-index snow model. Two of the QPE products include a correction for snow undercatch. This correction is obtained by applying a multiplicative correction factor to observed solid precipitation before spatial interpolation of the data, where solid precipitation is supposed to occur for air temperatures below 2°C.

The snow model includes a time-varying degree-day factor (DDF) to account for the increasing sun radiation from December to June; it is calibrated based on the reproduction of the presence or absence of snow given by the snow-covered area MODIS data. The QPE assessment is based on a detailed comparison of snow water equivalent (SWE) simulations to SWE measurements at up to 11 ground stations in the 5351 km^2 Upper Rhône River basin, Switzerland. After detailed data pre-treatment, a total of 367 ground-based SWE measurements were available for QPE performance assessment for a 6 years period.

The simulations with the two QPE products accounting for solid precipitation undercatch clearly yield a better reproduction of the observed SWE values, in terms of biases and simulation errors obtained from a classical confusion matrix. The best performance in terms of mean absolute error is obtained with the QPE product integrating a correction factor for solid precipitation equal to 1.2, in combination with a DDF variation interval of 2 [mm $°C^{-1}$ d^{-1}].

The results presented are specific for the used temperature-index snow model, which is widely used for hydrological modelling. The comparison of different QPEs in combination with this model allows the following conclusions:

- The integration of a seasonal variation of the DDF values allows a better reproduction of the presence of snow (snow-covered area). In addition, this seasonal DDF variation slightly increases the accumulated SWE by reducing the effect of short melting episodes in the early winter, which emphasizes the importance of time-variable DDFs in the context of snow undercatch studies for hydrological modelling.
- Best QPEs accounting for snow undercatch can be identified despite of the interaction between calibrated snow model parameters (namely the degree-day factor) and precipitation correction. Calibration on snow-cover duration (spatial information), along with detailed analyses of point SWE observations might however be a pre-condition for successful QPE construction for snow hydrological modelling.
- Studies of snow undercatch correction require a careful choice of performance assessment criteria, including namely a detailed analysis of different SWE thresholds.

Finally, it should be emphasized that the obtained results show that even a simple temperature-index snow model can show very good modelling performances. However, the quality of the results is strongly dependent on the quality of the input. Future investigations should thus focus on further improving the precipitation and temperature products, for example by correcting the precipitation using wind speed data.

Acknowledgments

Dr. Marco Gabella, Dr. Ioannis Sideris and Dr. Yves-Alain Roulet from MeteoSwiss are acknowledged for their input and feedback.

Table of variables

Table 3.6 – Table of variables for Chapter 3

Variable	Units	Description
b_p	[d mm^{-1}]	Melting coefficient due to precipitation
dt	[d]	Time step
H	[mm]	Water equivalent of the solid fraction of the snow
M	[mm d^{-1}]	Snowmelt or snow freezing rate
n	[-]	N^{th} day of the year
P	[mm d^{-1}]	Corrected precipitation rate at the station
P_m	[mm d^{-1}]	Measured precipitation rate at the station
P_{eq}	[mm d^{-1}]	Equivalent precipitation rate
P_s	[mm d^{-1}]	Solid precipitation rate
P_l	[mm d^{-1}]	Liquid precipitation rate
S_r	[mm °C^{-1} d^{-1}]	Reference (mean) degree-day factor (DDF)
S	[mm °C^{-1} d^{-1}]	Time-varying degree-day factor (DDF)
S_{min}	[mm °C^{-1} d^{-1}]	Minimal time-varying degree-day factor (DDF) value
S_{ph}	[d]	Horizontal phase shift of the sinusoidal function with respect to the first day of the year
SWE	[mm]	Snow Water Equivalent
T	[°C]	Measured temperature
T_{cf}	[°C]	Critical snowmelt temperature
T_{cp1}	[°C]	Minimum critical temperature for liquid precipitation
T_{cp2}	[°C]	Maximum critical temperature for liquid precipitation
W	[mm]	Water depth of the liquid fraction of the snow
β	[-]	Precipiation correction factor
Δ	[mm °C^{-1} d^{-1}]	Degree-day factor variation interval
θ	[-]	Relative water content in the snow pack
θ_c	[-]	Critical relative water content in the snow pack

4 Multi-approach hydrological calibration with multiple precipitation inputs

4.1 Introduction

The quality of hydrological forecasts is highly dependent on the quality of the model used for the computation and its calibration. In addition, in Alpine catchments like the Upper Rhône River (URR) basin, snow hydrology plays a major role through water sequestration during winter followed by snow melt in spring and summer. Therefore, improving the calibration of the snow-melt model at the catchment scale can be expected to lead to better forecasts during the snow-melting period. Parajka and Blöschl [2008a] have suggested that using spatial data of snow cover from the Moderate-Resolution Imaging Spectroradiometer (MODIS), respectively produced by the satellites Aqua and Terra [Hall et al., 2016a,b], allows an improvement of snow modelling for hydrological purposes. He et al. [2014] proposed a methodology for degree-day factors estimation without calibration using MODIS data and ground-based snow depth measurements. Pistocchi et al. [2017] also obtained good results working with daily values of temperature and precipitation in combination with MODIS data.

In Chapter 3, snow modelling has been explored pointwise over locations of snow monitoring sites. As suggested, this is particularly interesting to understand for example the interaction between precipitation estimates and the evolution of snow water equivalent (SWE) and showed that the approach allows a good reproduction of the SWE values observed on the ground. However, in the context of flood forecasting, modelling has to be applied at the catchment scale. In this chapter, a decoupling of the hydrological model calibration is therefore explored. First the snow-melt degree-day factors are calibrated using MODIS data, by extending the pointwise methodology to entire basins. The proposed snow model calibration methodology is based on MODIS data and does not include snow depth measurements (contrary to He et al. [2014]). In addition, a major difference with Pistocchi et al. [2017] is the consideration of hourly values of precipitation and temperature instead of daily values. Second, the remaining parameters of the hydrological model are calibrated based on discharge data. To evaluate

the possible gain resulting from the 2-phase calibration, the performance is compared with a model entirely calibrated on discharge data, hereafter named conventional calibration.

For the hydrological modelling part, the present chapter builds on previous work achieved within the MINERVE project [Jordan, 2007a, García Hernández, 2011a, García Hernández et al., 2014], the objective being to improve the existing model over the Upper Rhône River (URR) basin. The semi-distributed GSM (Glacier and SnowMelt) and SOCONT (Soil CONTribution) models [Schaefli et al., 2005, Hamdi et al., 2005] are therefore used for the rainfall-runoff modelling and the computation is performed using the hydrological-hydraulic modelling software RS MINERVE [Foehn et al., 2019a, García Hernández et al., 2019]. It is worth mentioning here that the URR basin is largely constrained by the many large hydropower schemes and reservoirs present in the basin. In that context, the currently implemented semi-distributed GSM and SOCONT conceptual models are already a very useful tool, with a computation time well adapted to an operational flood forecasting system. Regarding the calibration, optimization is done with the Shuffled Complex Evolution (SCE-UA) optimization algorithm looking for the global optimum of a given objective function by evolving cluster samples in the parameter space [Duan et al., 1993, Rahnamay Naeini et al., 2019].

In the approach presented in this chapter, except for the snow-melting parameters calibrated with spatial data, the remaining parameters are calibrated with discharge data. This approach is known to possibly result in pseudo-accurate model parametrization, with simulated discharge somehow reproducing the observed discharge, but through incorrect internal watershed process representation. This idea of equifinality [Beven, 2012] suggests that considering both limitations of the model structure and the data used for calibration, different representations of a catchment may result in similar performance in reproducing the observed data. As a consequence, remotely sensed estimates of water balance components such as surface soil moisture [Li et al., 2018] or actual evapotranspiration [Immerzeel and Droogers, 2008] are increasingly used as spatially distributed information for multi-scale, multi-objective calibration of hydrological models.

Pistocchi et al. [2017] highlighted the importance of precipitation and temperature data reliability for hydrological modelling. Andres et al. [2016] evaluated the application to a transnational river basin in southern Switzerland and northern Italy of a hydrological-hydraulic model chain by using different inputs datasets, including rain gauge measurements, quantitative radar estimates and the operational rain gauge-radar merging product *CombiPrecip* of MeteoSwiss. In their study, the best discharge simulation results were obtained with rain gauge data, mainly because these had been used for the model calibration. Sikorska and Seibert [2018] investigated the value of three precipitation datasets for flood predictions in an alpine catchment in Switzerland. Comparing radar-based precipitation to station network precipitation and interpolated grid precipitation, Sikorska and Seibert [2018] concluded that the radar-based precipitation was the most useful dataset. To investigate the impact of different precipitation input datasets from a hydrological point of view, the hydrological model is here calibrated using three different QPE products and rain gauges data for comparison purposes.

4.2 Studied basins and input data

4.2.1 Studied basins

In the present chapter, three sub-catchments of the Upper Rhône River basin are investigated, the one of the Saltina River, the one of the Lonza River and the one of the Grande-Eau River (Figure 4.1). All three sub-catchments have at their outlet an official stream gauge from the Swiss Federal Office for the Environment (FOEN) and the selection aimed at covering different scenarios of weather radar visibility after the installation of the new weather radar of Pointe de la Plaine Morte (in June 2014). Over the Saltina catchment, the visibility is good without any major topographical obstacle between the weather radar and the catchment. The visibility over the Lonza and Grande-Eau catchments is lower due to the topography. In the case of the Grande-Eau, part of the basin is even very poorly covered due to the presence of the Wildhorn peak (3250 m a.s.l.) in between. Another particularity of the Grande-Eau catchment is its better coverage than the two other studied catchments by the weather radar of La Dôle (available already before 2014; see Figure 2.1), again for topographical reasons. These characteristics will be considered in the results analysis for the validation period (2012-2014).The characteristics of the catchments are given in Table 4.1.

Table 4.1 – Characteristics of the studied sub-catchments. The yearly average discharge corresponds to the period 1935-2017. Data: FOEN [2017b].

River	Saltina	Lonza	Grande-Eau
Area [km^2]	76.5	77.4	132
Mean elevation of catchment [m a.s.l.]	2014	2624	1562
Hydrometric station elevation [m a.s.l.]	677	1520	414
Glaciation [%]	2.5	24.7	0.8
Yearly average discharge [m^3/s]	2.3	4.7	4.9

The Saltina and Grande-Eau rivers are equipped with a small run-of-river hydropower plant. The capacity of the installation on the Saltina is 1.5 [m^3/s]. The equipped discharge over the Grande-Eau was 2.5 m^3/s until 2015 and is 6.5 m^3/s since April 2016. In both cases, no storage capacity is available. However, the Grande-Eau catchment receives in addition water diverted from the Lac d'Arnon, a reservoir with a capacity of 11 million m^3 located in a nearby catchment. When the natural discharge in the Grande-Eau River is below the installed capacity of the two successive run-of-river hydropower plants, the water from the external reservoir is turbined at a hydropower plant located in Les Diablerets, upstream of the run-of-river scheme, with a capacity of 1.75 m^3/s. The operating data of the scheme were not available for the present study. However, this contribution must be considered when analysing the calibration performance over the basin, in particular in terms of volume bias. Indeed, the external contribution is estimated to about 5 to 10% of the natural volume of the Grande-Eau, based on estimations data of yearly turbined discharges at the Les Diablerets power plant, provided by Romande Energie, owner of the hydropower scheme.

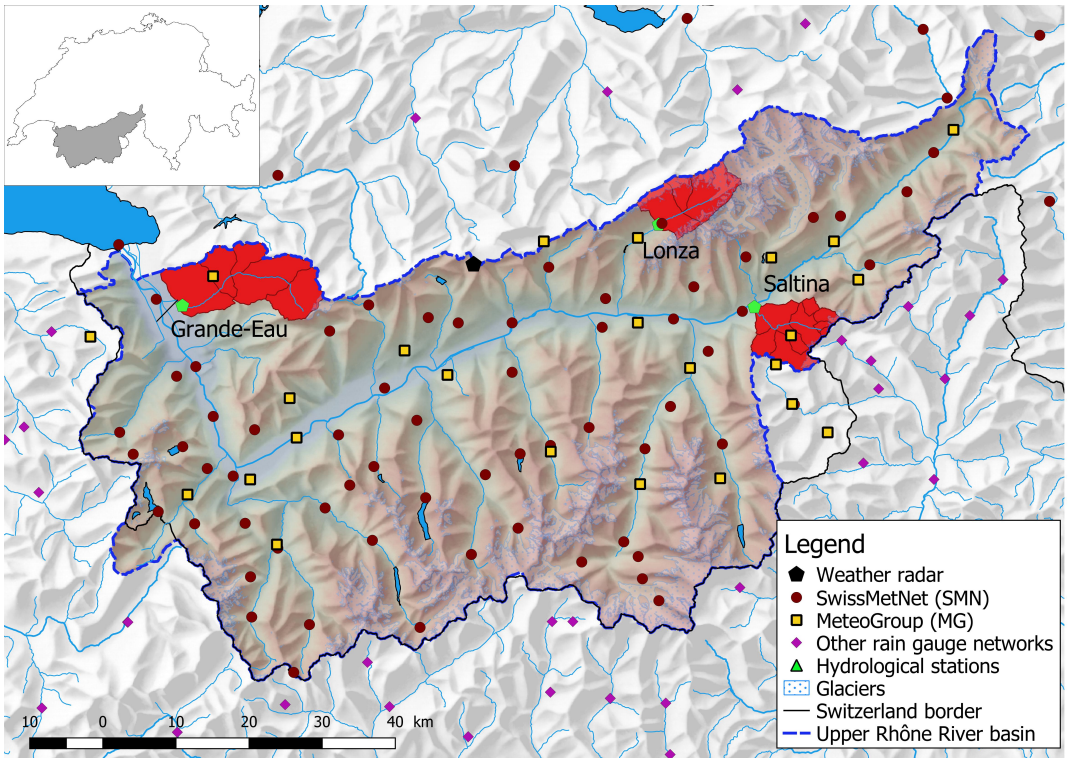

Figure 4.1 – Upper Rhône River basin upstream of Lake Geneva and the Saltina, Lonza and Grande-Eau subcatchments. Data source: Swisstopo [2017b] for the rivers and lakes, Swisstopo [2013] for the glaciers (with modifications), Swisstopo [2005] for the digital elevation model, Swisstopo [2012] for the hillshade and Swisstopo [2017a] for the national border.

Precipitation data

Different precipitation inputs are considered for the analysis. Station data are seen as the base scenario. First, only data from the SwissMetNet (SMN) network of MeteoSwiss are considered. Only the Lonza catchment has a SMN station (*Blatten, Lötschental*) within the basin, near its outlet, but providing data at hourly resolution only since May 31st 2013 (see Table B.1 in Appendix B). Second, the data of the SMN network are combined with the data of the network of the private company MeteoGroup Switzerland AG (MG). Thereby, the number of stations in the basins is increased, the Saltina and Grande-Eau basins having a MeteoGroup station more or less in their centre with data available for the entire studied period (1.9.2012 - 31.8.2018) but no SMN station within the basin. However, as demonstrated in Chapter 2, the MG stations tend to report less precipitation and can thereby result in negative biases.

In addition to the station data, three of the QPE products presented in Subsection 3.3.3 are used as input (Table 4.2). The first product (hereafter refereed as QPE1), is the hourly operational QPE product of MeteoSwiss, known as *CombiPrecip* [Sideris et al., 2014a]. The second (QPE2) is the product developed in Chapter 2, whereas the third (QPE2-120) is the QPE product

developed in Chapter 3 which corresponds to QPE2 with a correction of solid precipitation measured at rain gauges by a multiplicative correction factor of 1.2 (see Subsection 3.2.2). All the products have a spatial resolution of 1 km and an hourly temporal resolution. It must be mentioned that QPE1 contains 268 missing values (i.e. about 0.5% of the data) over the studied period, with 122 missing values occurring in 2013 (1.4% of yearly data). A value of 0 mm/h has been considered for hours without data.

Table 4.2 – QPE products used for the analysis.

Precipitation input	Precipitation data	References
SMN	SMN	-
SMN+MG	SMN+MG	-
QPE1	radar + SMN	Sideris et al. [2014a]
QPE2	radar + SMN+MG	Chapter 2, Foehn et al. [2018]
QPE2-120	radar + SMN+MG with correction	Chapter 3

4.2.2 Temperature data

Two different inputs of temperature are considered. First, the spatial product of temperature presented in Subsection 3.2.2 is used. However, further analysis of the product has revealed that the product suffers from border anomalies at high elevation. Due to the very limited number of stations above 3000 m a.s.l., the performed Kriging with external drift (KED) can result over pixels with high elevation in incoherent daily variation (colder during the day, hotter during the night). This seems to result from the linear regression computed in the KED, used to compute the trend of temperature (a 2D surface of a priori computed temperature, on which local correction is applied after interpolation of the residuals). If no station is available in the vicinity of a pixel, the temperature value is highly based on the regression, which can result in incoherent values out of the observed value's elevation range. Based on this analysis, the study also explores the use of station temperature data alternatively to the spatialized product of temperature, to evaluate the impact on the hydrological model performance.

4.2.3 Discharge data

Hourly discharge data based on water level observations at official gauge stations of the Swiss Federal Office for the Environment [FOEN, 2017a], located at the outlet of the three studied sub-catchments, are used as reference data for the calibration.

4.3 Snow and hydrological modelling

The snow modelling is performed with the Snow-SD model presented in Subsection 3.3.1, based on a degree-day factor (DDF) approach. The hydrological modelling is performed using the rainfall-runoff semi-distributed conceptual GSM and SOCONT models [Schaefli et al., 2005, Hamdi et al., 2005, García Hernández et al., 2019], illustrated in Figure 4.2. The GSM

model is used for the glacial parts of the basin and the SOCONT model for the non-glacial parts. The main parameters of the models are given in Table 4.3.

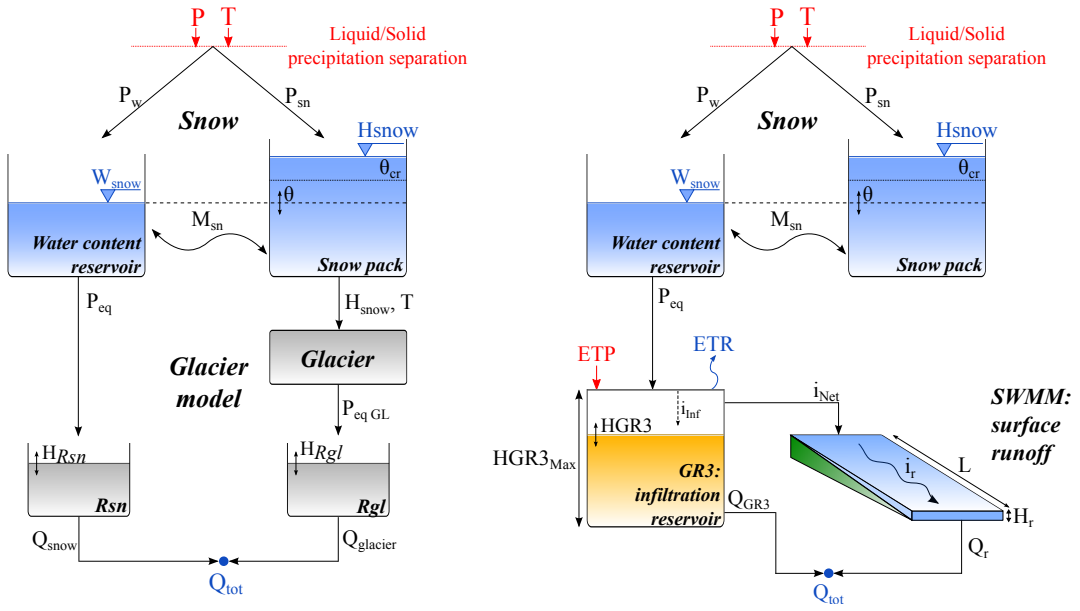

Figure 4.2 – Structure of the GSM and SOCONT models (Source García Hernández et al. [2019]).

Table 4.3 – Main parameters of the SOCONT and GSM models.

Parameter	Units	SOCONT
S_r	mm/°C/d	Reference degree-day snowmelt coefficient
Δ	mm/°C/d	Degree-day snowmelt interval
H_{GR3Max}	m	Maximum height of infiltration reservoir
K_{GR3}	1/s	Release coefficient of infiltration reservoir
K_r	$m^{1/3}/s$	Strickler coefficient of surface runoff
Parameter	**Units**	**GSM**
S_r	mm/°C/d	Reference degree-day snowmelt coefficient
Δ	mm/°C/d	Degree-day snowmelt interval
G	mm/°C/d	Degree-day glacier melt coefficient
K_{sn}	1/d	Release coefficient of snow melt reservoir
K_{gl}	1/d	Release coefficient of glacier melt reservoir

Studied catchments are divided into elevation bands with an elevation range not exceeding 500 m. This allows in particular accounting for the vertical evolution of temperature. For the GSM model, snow melt and ice melt do not occur simultaneously over an elevation band. As long as snow is present, snow-melting takes place. When the surface is free of snow, glacial melting is considered based on the glacier melt coefficient and the temperature. The amount of ice to melt is not limited in the GSM model. For the SOCONT model, the generated discharge at the outlet of the basin is controlled by the maximum height of the infiltration reservoir, the release coefficient of the infiltration reservoir as well as the roughness (Strickler coefficient) of

the surface runoff surface. The division in elevation bands used in the operational system has been considered for the computation.

4.3.1 Calibration and validation of the model

Two approaches are considered for the calibration. The first approach consists in a conventional calibration using only discharge data as reference to calibrate all parameters. The second approach decouples the calibration by first evaluating the DDFs based on spatial satellite data, before calibrating the remaining parameters in the second phase similarly to the conventional calibration. The Shuffled Complex Evolution (SCE-UA) global optimization algorithm is used for the calibration [Duan et al., 1993]. Table 4.4 summarizes the parameters calibrated in each phase.

Table 4.4 – Calibrated parameters for the two calibration approaches.

-	Conventional calibration	2-phases calibration
SOCONT - Phase 1	-	S_r, Δ
SOCONT - Phase 2	H_{GR3Max}, K_{GR3}, K_r, S_r, Δ	H_{GR3Max}, K_{GR3}, K_r
GSM - Phase 1	-	-
GSM - Phase 2	S_r, Δ, G, K_{sn}, K_{gl}	S_r, Δ, G, K_{sn}, K_{gl}

In the 2-phase approach, the DDFs are estimated using the same model calibration methodology as presented in Subsection 3.3.2. The S_r parameters are calibrated such that the model reproduces best the presence or absence of snow on the ground given by the snow-covered area information provided by the spectroradiometer MODIS. Fixed parameters given in Table 3.4 are used and a seasonal variation of 2 [mm $^\circ C^{-1}$ d^{-1}], corresponding to $\pm$1mm $^\circ C^{-1}$ d^{-1} around the reference degree-day snowmelt coefficient value, is considered for all pixels (see Subsection 3.4.4). The calibration of the S_r parameters is performed over the six years of radar data availability (1.9.2012-1.9.2018). The performance metric used is the Overall Accuracy (OA), presented in Equation 3.10. The analysis is performed for each pixel of the non-glacial elevation bands ; the presence of ice does not allow the identification of the snow presence period over glacial elevation bands, not allowing calibration over these bands with the 2-phase approach. Once all the pixels computed, the values are aggregated through averaging over each elevation band considering the pixels for which the performance has been evaluated as sufficient, based on the criteria given in Table 4.5. These criteria were defined based on initial tests and considering a tendency to reducing OA values with increasing snow coverage over the year, as well as the tendency of low elevation pixels with only very few days with snow to provide S_r values extremely high, up to 20 [mm $^\circ C^{-1}$ d^{-1}]. In addition, a minimum of five valid pixels has been fixed to perform the aggregation over a given elevation band, to avoid aggregated values computed only over 1 or 2 pixels. If this condition is not satisfied, the value of the nearest elevation band containing at least five pixels with valid data is considered.

Table 4.5 – Minimum Overall Accuracy required at pixel scale for considering the pixel in the aggregation. The number of days with snow is estimated based on NDSI data analysis considering the average number over the studied period.

Number of days per year with snow	Minimum OA value
<10	0.995
<25	0.99
<50	0.97
≥50	0.95

For the discharge-based calibration, the Kling-Gupta Efficiency (KGE) performance metric [Gupta et al., 2009] is used in its modified form proposed by Kling et al. [2012]:

$$\mathrm{KGE} = 1 - \sqrt{(r-1)^2 + (\beta-1)^2 + (\gamma-1)^2} \tag{4.1}$$

$$\beta = \frac{\mu_s}{\mu_0}$$

$$\gamma = \frac{CV_s}{CV_o} = \frac{\sigma_s/\mu_s}{\sigma_o/\mu_o}$$

where r is the correlation coefficient between simulated and observed runoff (dimensionless), β is the bias ratio (dimensionless), γ is the variability ratio (dimensionless), μ is the mean discharge in m^3/s, CV is the coefficient of variation (dimensionless), σ is the standard deviation of discharge in m^3/s, and the indices s and o indicate respectively simulated and observed runoff values. The value of KGE varies from 0 to 1 with 1 representing the best possible performance. The choice of KGE was motivated by the conclusions of Mizukami et al. [2018], who demonstrated that the use of KGE results in better annual peak flow estimates than from the commonly used Nash-Sutcliffe efficiency (NS) [Nash and Sutcliffe, 1970].

The performed spatial analysis allows a spatial variability of the aggregated S_r parameter values. For all other parameters, calibrated in the conventional approach or in the second phase, a unique value over the entire catchment is defined. Ranges used for the calibration are given in Table 4.6.

Table 4.6 – Parameters calibrated and corresponding ranges (min and max values).

Model	Parameter	Unit	Minimum	Maximum
GSM	S_r	$[mm°C^{-1}d^{-1}]$	0.5	12
GSM	Δ	$[mm°C^{-1}d^{-1}]$	0	5
GSM	G	$[mm°C^{-1}d^{-1}]$	0.5	12
GSM	K_{sn}	[1/d]	0.2	20
GSM	K_{gl}	[1/d]	0.2	20
SOCONT	S_r	$[mm°C^{-1}d^{-1}]$	0.5	12
SOCONT	Δ	$[mm°C^{-1}d^{-1}]$	0	5
SOCONT	H_{GR3Max}	[m]	0.1	2
SOCONT	K_{GR3}	[1/s]	0.00001	0.1
SOCONT	K_r	$[m^{1/3}/s]$	0.001	3
Kinematic Wave	K	$[m^{1/3}/s]$	10	90

For the hydrological calibration and validation, periods given in Table 4.7 are considered. The calibration period corresponds to the four complete hydrological year after the installation of the new weather radar of Pointe de la Plaine Morte (see Subsection 2.2.3), whereas the validation corresponds to the two preceding years. This division was motivated by the hypothesis of the high influence of the new weather radar on the hydrological performances.

Table 4.7 – Periods used for calibration and validation of the hydrological models.

-	Period
Calibration	01.09.2014-31.8.2018
Validation	01.09.2012-31.8.2014

In the performance evaluation, KGE is used in combination with Nash-Sutcliffe efficiency (NS), the Relative Volume Bias (RVB) and the Nash-Sutcliffe efficiency for logarithm values (NS-ln) [Krause et al., 2005], as defined hereafter:

$$\mathrm{NS} = 1 - \frac{\sum_{t=1}^{n}(x_{s,t} - x_{o,t})^2}{\sum_{t=1}^{n}(x_{o,t} - \mu_o)^2} \tag{4.2}$$

where n is the total number of time-steps, $x_{s,t}$ is the simulated discharge at time-step t, $x_{o,t}$ is the observed discharge at time-step t, and μ_t is the mean of the observed discharge. NS varies from -∞ to 1 with 1 representing the best possible performance;

$$\text{NS-ln} = 1 - \frac{\sum_{t=1}^{n}(ln(x_{s,t}) - ln(x_{o,t}))^2}{\sum_{t=1}^{n}(ln(x_{o,t}) - ln(\mu_o))^2} \tag{4.3}$$

NS-ln varies from -∞ to 1 with 1 representing the best possible performance. Ns-ln is used to assess the hydrological models performance for low flow values;

$$\mathrm{RVB} = \frac{\sum_{t=1}^{n}(x_{s,t} - x_{o,t})}{\sum_{t=1}^{n} x_{o,t}} \tag{4.4}$$

RVB varies from -∞ to ∞ with an optimal value of 0.

Considering the different input data as well as the different calibration approaches, 11 configuration combinations were explored for each basin (Table 4.8).

It is worth mentioning that one of the objectives of the presented methodology being the performance comparison obtained using different QPEs, no correction is brought to the input data within the simulation (i.e. no multiplicative correction was considered for precipitation data within the hydrological modelling approach).

Table 4.8 – Calibration configurations used for the analysis.

Method names	Precipitation data	Temperature data	Calibration approach
Hydro_STA-SMN	Stations (SMN)	Stations (SMN)	Conventional
Hydro_STA-SMN+MG	Stations (SMN+MG)	Stations (SMN+MG)	Conventional
Hydro_QPE1-Tsta	QPE1	Stations (SMN+MG)	Conventional
Hydro_QPE2-Tsta	QPE2	Stations (SMN+MG)	Conventional
Hydro_QPE2-120-Tsta	QPE2-120	Stations (SMN+MG)	Conventional
Snow-Hydro_QPE1-Tsta	QPE1	Stations (SMN+MG)	2-phases
Snow-Hydro_QPE2-Tsta	QPE2	Stations (SMN+MG)	2-phases
Snow-Hydro_QPE2-120-Tsta	QPE2-120	Stations (SMN+MG)	2-phases
Snow-Hydro_QPE1-Tspa	QPE1	Spat. Temperature	2-phases
Snow-Hydro_QPE2-Tspa	QPE2	Spat. Temperature	2-phases
Snow-Hydro_QPE2-120-Tspa	QPE2-120	Spat. Temperature	2-phases

4.3.2 Implementation

The modelling computation were performed using the RS MINERVE[1] software [Foehn et al., 2019a, García Hernández et al., 2019], based on the object-oriented programming concept and allowing the computation of hydrological and hydraulic modelling with a semi-distributed approach. In addition to simulate hydrological processes such as surface and subsurface runoff or snow and ice melt, the software enables an easy integration of hydraulic structures such as reservoirs, spillways, derivations, turbines or pumps. At each elevation band of the semi-distributed model, the meteorological data (precipitation and temperature) are interpolated from the provided data. Considering that only precipitation and temperature inputs are used in the MINERVE system, the empirical method proposed by Turc [1961], which requires only temperature data and has been verified in many countries [Liang, 1982, Karpouzos et al., 2011], is used for evapotranspiration computation. Future consideration of for example radiation data could improve the modelling of the evapotranspiration process within the modelling framework. Furthermore, it is worth mentioning here that no sublimation is considered in the used snow model.

The presented methodology has been implemented in the R language and environment for statistical computing [R Core Team, 2018]. This includes the data acquisition as well as the interactions with RS MINERVE launched trough VBScripts defining the tasks to be performed by the modelling software (open model, open database, run calibration, etc.). This has enabled a complete automation of the computation implementation presented here. Used R Packages include ggplot2 [Wickham, 2016], httr [Wickham, 2018], OpenStreetMap [Fellows and using the JMapViewer library by Jan Peter Stotz, 2016], openxlsx [Walker, 2018], parallel [R Core Team, 2018] and raster [Hijmans, 2017].

Data files were also prepared using the R language and environment for statistical computing. For configurations using stations data, values were interpolated at the centre of gravity of elevation bands using an inverse distance weighting method. For each hour, data from

[1] Software version RS MINERVE 2.7.6

available nearby stations were considered (including stations having been installed during the studied period). For spatial products, values are aggregated over elevation bands at exportation from the spatial database and attributed to the coordinates of the centre of gravity of the elevation band.

For the hydrological calibration, a single dataset of initial conditions were first computed based on a simulation over the year preceding the calibration period using SMN data. A first calibration with 1500 iterations was then performed for each configuration, before computing individual datasets of IC over the same preceding year with the pre-calibrated models. The final calibration, with a maximum of 3000 iterations, was then realized for each configuration.

4.4 Results

This section is divided into two parts. First, the snow modelling results are presented with the DDFs computation and the aggregation over elevation bands. The second part presents and discusses the results from a hydrological perspective with the discharge-based calibration of the model.

4.4.1 Calibration of degree-day factors

The DDF values were calibrated for all the pixels contained in the three studied sub-catchments. Figures 4.3 to 4.5 present the values obtained at the pixel scale and after aggregation for the studied sub-catchments. Only pixels for which the Overall Accuracy (OA) was considered as sufficiently high (see Table 4.5) are displayed and used for the aggregation.

For both Saltina and Grande-Eau basins, the lower part of the basin is very poorly covered by satisfying pixels. On the contrary, in the Lonza basin, located at higher elevation, the lower part of the basin is well covered and the upper part much less. The absence of satisfying pixels in the lower elevation of Saltina and Grande-Eau as well as in the upper part of the Lonza catchment is clearly the result of the thresholds defined in Table 4.5. Figures E.1, E.2 and E.3 in Appendix E provide the OA values obtained by all the pixels without threshold-based filtering. When looking for example at results obtained for Saltina (Figure E.1), OA values of 0.995 for pixels with less than 10 days (or 3% of the year) with snow and 0.99 for pixels with less than 25 days (or 7%) with snow seem to be too restrictive. Future investigation might explore lowering the threshold values to include more pixels, with the possible drawback of including pixels with less coherent parametrization.

To better understand the relation between the obtained DDF values (parameter S_r) and the physical characteristics of the basins, Figures 4.6 to 4.8 present boxplots of the S_r parameter versus orientation (with respect to North and clockwise rotation) and elevation. The correlation with the orientation is relatively strong over the Grande-Eau catchment (Figure 4.8), with the highest median S_r values obtained around 180° (South exposition). This relation is still

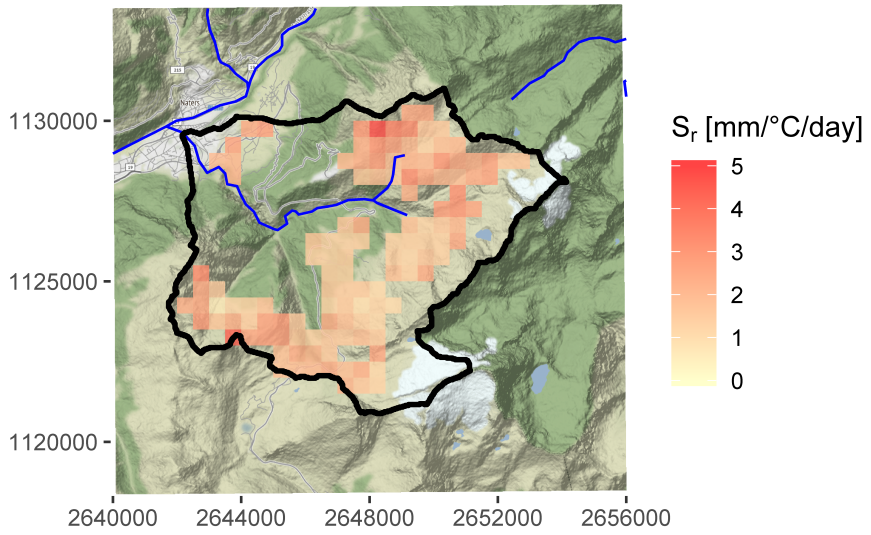

(a) Values obtained for the S_r parameter at pixel scale. Only values of pixels with sufficiently high OA values are displayed.

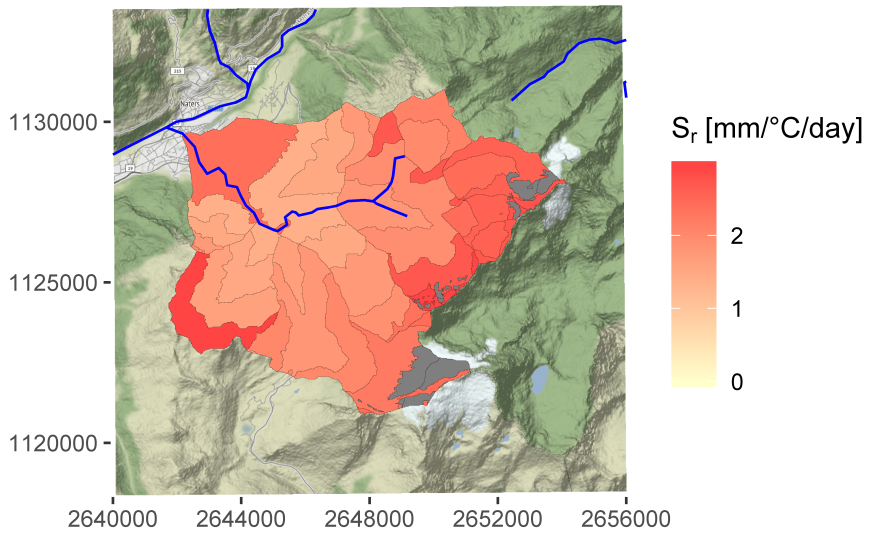

(b) Values obtained for the S_r parameter after aggregation over elevation bands using values shown in a). Bands in grey correspond to the glacial elevation bands. Colour scale is different between a) and b).

Figure 4.3 – Calibration of the parameter S_r for the Saltina basin, using product QPE2. Background data: map tiles by Stamen Design, under CC BY 3.0. Data by OpenStreetMap, under ODbL.

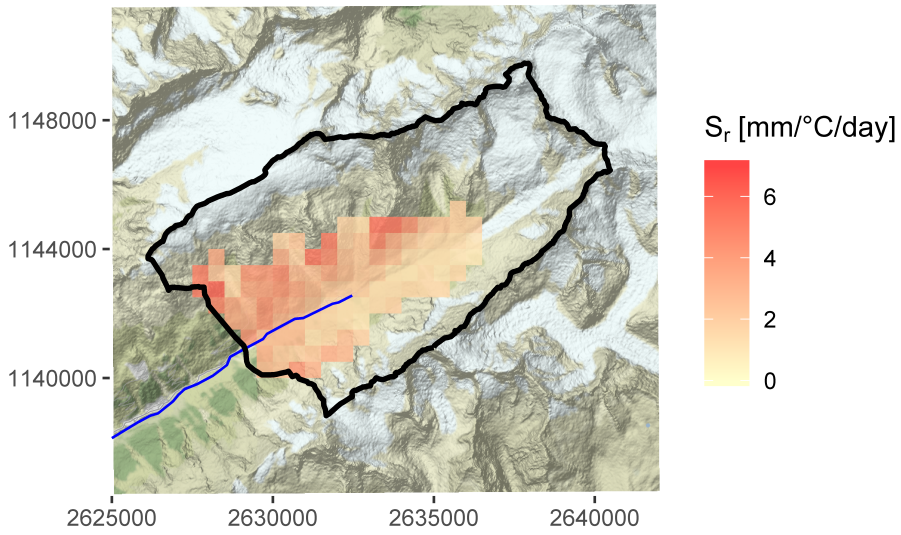

(a) Values obtained for the S_r parameter at pixel scale. Only values of pixels with sufficiently high OA values are displayed.

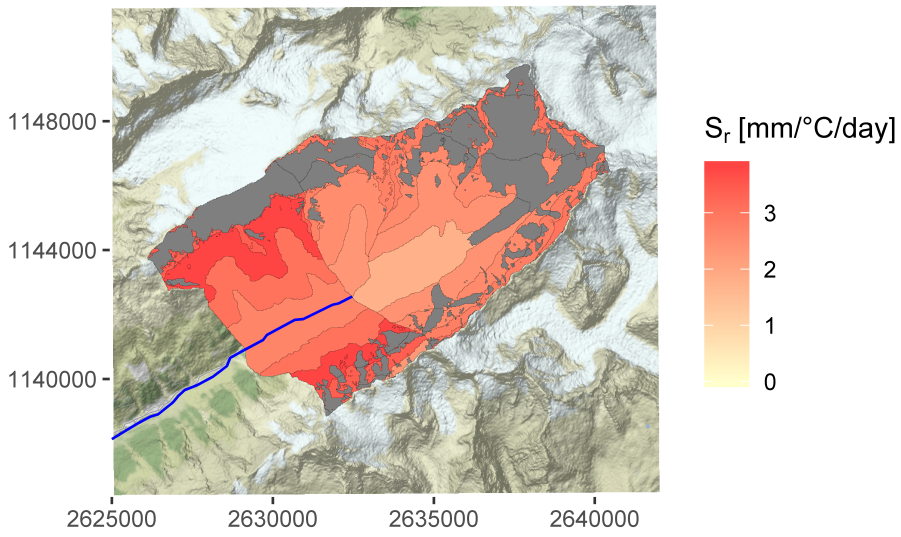

(b) Values obtained for the S_r parameter after aggregation over elevation bands using values shown in a). Bands in grey correspond to the glacial elevation bands. Colour scale is different between a) and b).

Figure 4.4 – Calibration of the parameter S_r for the Lonza basin, using product QPE2. Background data: map tiles by Stamen Design, under CC BY 3.0. Data by OpenStreetMap, under ODbL.

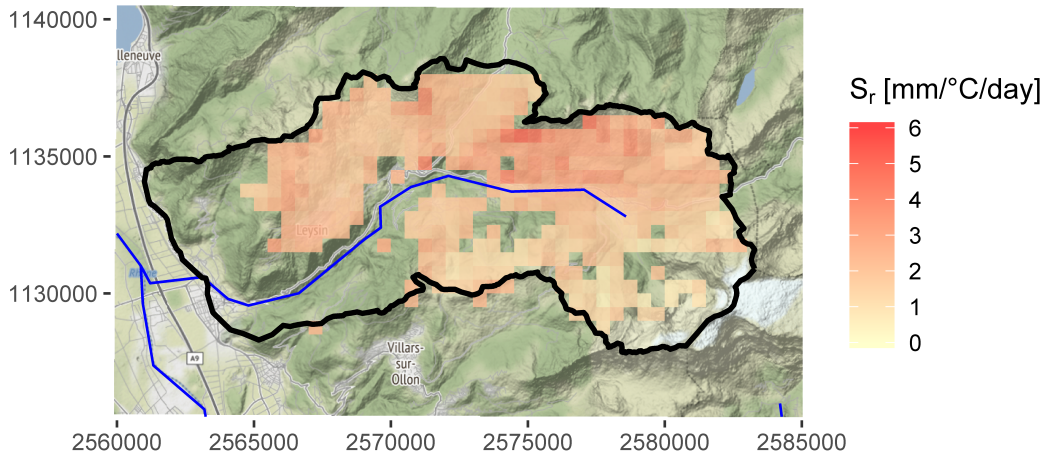

(a) Values obtained for the S_r parameter at pixel scale. Only values of pixels with sufficiently high OA values are displayed.

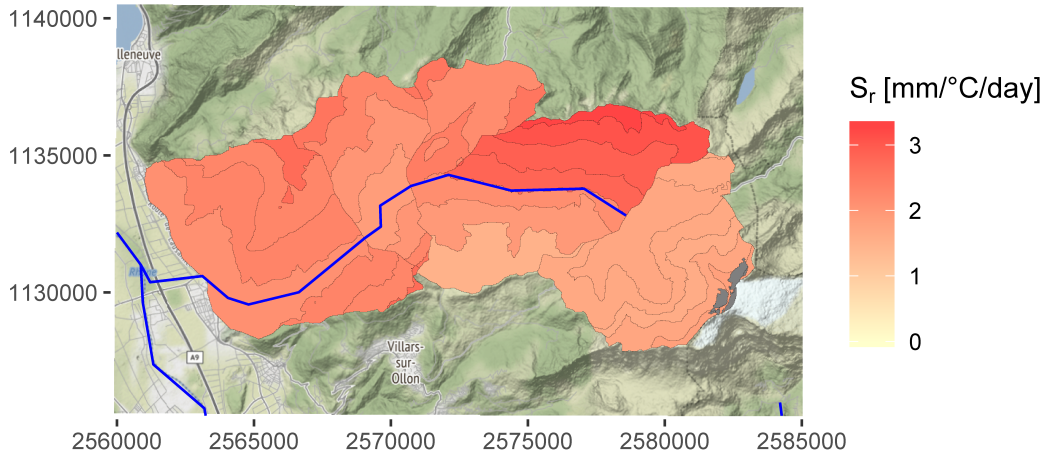

(b) Values obtained for the S_r parameter after aggregation over elevation bands using values shown in a). Bands in grey correspond to the glacial elevation bands. Colour scale is different between a) and b).

Figure 4.5 – Calibration of the parameter S_r for the Grande-Eau basin, using product QPE2. Background data: map tiles by Stamen Design, under CC BY 3.0. Data by OpenStreetMap, under ODbL.

visible for Saltina, though less clear. It however disappears for Lonza, where no clear tendency can be identified.

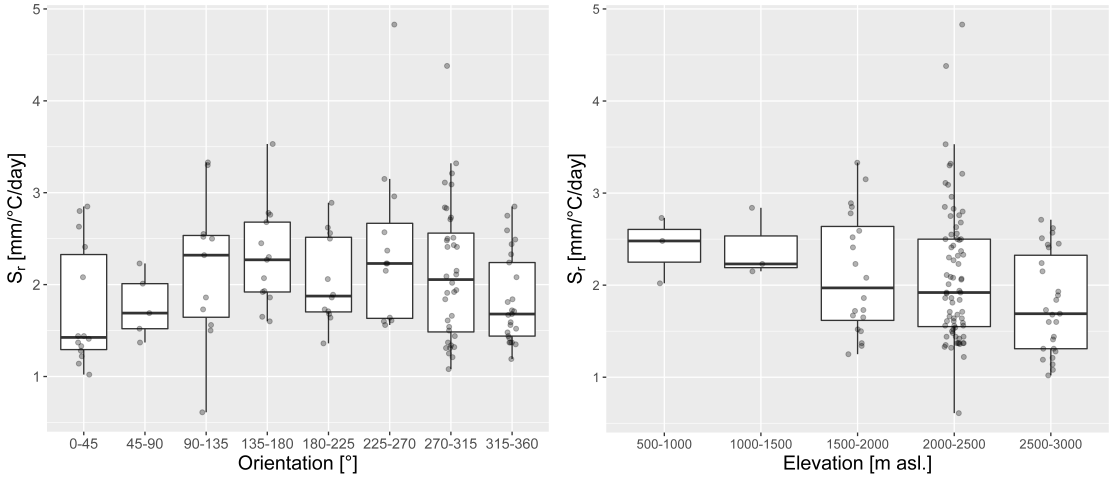

Figure 4.6 – S_r distribution versus orientation (left) and elevation (right) for the Saltina catchment. Each point corresponds to a pixel. Only pixels with OA value higher than thresholds given in Table 4.5 are displayed.

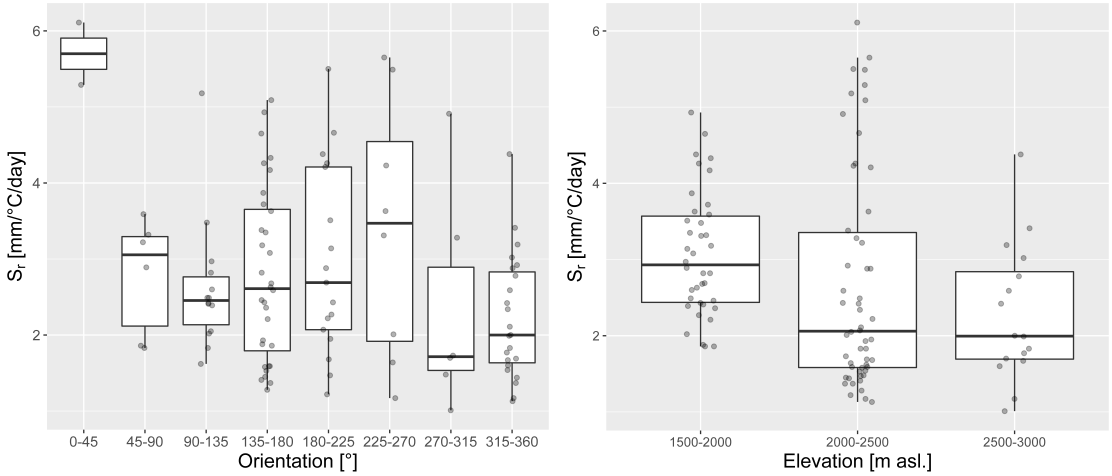

Figure 4.7 – S_r distribution versus orientation (left) and elevation (right) for the Lonza catchment. Each point corresponds to a pixel. Only pixels with OA value higher than thresholds given in Table 4.5 are displayed.

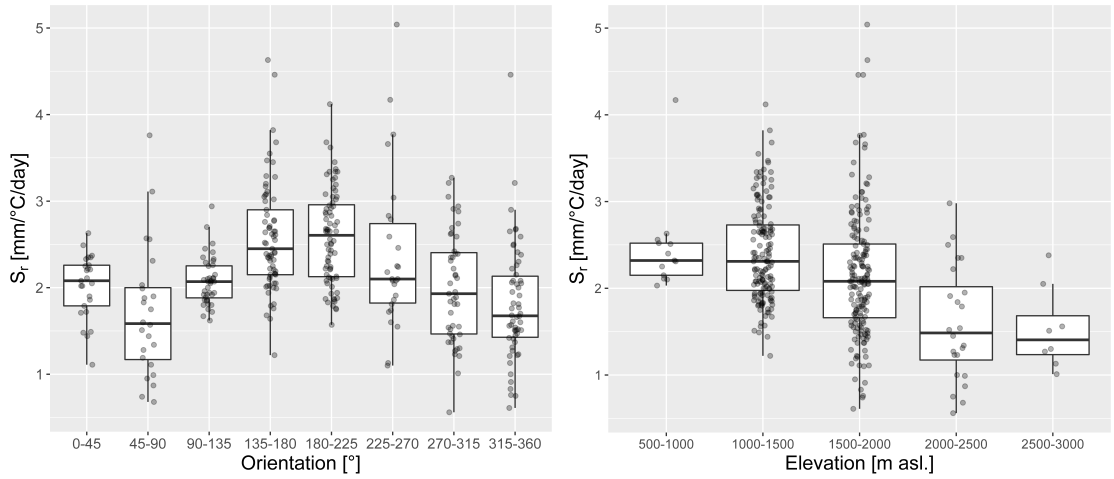

Figure 4.8 – S_r distribution versus orientation (left) and elevation (right) for the Grande-Eau catchment. Each point corresponds to a pixel. Only pixels with OA value higher than thresholds given in Table 4.5 are displayed.

Regarding elevation, S_r values tend to decrease with increasing elevation. However, it must be emphasized that only the reference degree-day factor (S_r) values are displayed here, and not the seasonal varying degree-day factor values. When not considering a seasonal variation (not shown here), the S_r tended to increase with elevation. With pixels in higher elevation melting later in the season, the degree-day factor values during melting occurrence can thereby be higher with increasing elevation.

4.4.2 Hydrological model calibration

The calibration of the other parameters has been performed, either for the conventional calibration or for the second phase of the 2-phase calibration (see Table 4.4). Results are presented hereafter. For each catchment, a table first summarizes the yearly average precipitation for the different inputs, computed as the average of the precipitation received by all elevation bands in the catchment. For each product, the percentage compared to the SMN stations base scenario is given. Another table with the performance metrics is given both for calibration (2014-2018) and validation (2012-2014) periods for each catchment in combination with a table presenting the obtained parameter values.

For the Saltina catchment, Table 4.9 presents the yearly average precipitation over the catchment for the different precipitation datasets. Results show that the combination of the MeteoGroup (MG) stations with the SMN stations (SMN+MG dataset) impacts the precipitation by reducing it both on calibration (-5.6%) and validation (-7.9%).

Table 4.9 – Estimated average precipitation over the Saltina basin with the different precipitation datasets. For the comparison in %, the SMN stations are used as reference.

	Calibration (2014-2018)		Validation (2012-2014)	
Dataset	Average rain [mm]	% of SMN	Average rain [mm]	% of SMN
SMN	891	100.0	982	100.0
SMN+MG	841	94.4	904	92.1
QPE1	918	103.0	980	99.8
QPE2	952	106.8	1239	126.2
QPE2-120	1021	114.6	1461	148.9

Over the calibration period, only little difference is reported between QPE1 and QPE2, both products reporting slightly more precipitation than the SMN data (+3 and +7%). QPE2-120 results in 7% more precipitation as compared to QPE2, which is reasonable with the 1.2 factor being applied only for solid precipitation. Looking at the validation period (during which the radar of Pointe de la Plaine Morte was not yet installed), differences between QPE products are considerably higher, with QPE1 reporting 99.8% of the SMN stations precipitation, whereas values for QPE2 and QPE2-120 are respectively 126.2% and 148.9%. Due to the low visibility of the Swiss weather radar network before 2014 over the URR basin, the radar data tended to underestimate the precipitation. The bias correction applied over entire Switzerland (in QPE1) applies a country-wide correction factor lower than the one computed only on stations located in the URR basin (in QPE2 and QPE2-120), more correcting the local negative bias of the radar data over the studied basin. The solid precipitation correction by a factor 1.2, in the product QPE2-120, further increases this bias correction. Looking only at Table 4.9, it is not possible to say which of the product is more correct. The hydrological application discussed hereafter will answer this question.

Looking at the performance metrics (Table 4.10), the best KGE calibration performance is obtained with a conventional calibration using the QPE2-120 product (Hydro_QPE2-120_Tsta). This configuration leads also to the best performance with the three other performance metrics. Over the validation, the 2-phase approach with the same inputs gives the best KGE and NS performance.

Simulated and observed discharge for the period March 1 to October 1 2016 are shown in Figure 4.9 for the configuration with best calibration performance. In addition to failing reproduction of some peaks, the model also struggles to reproduce the variability associated to ice melting. The corresponding hydrograph for the entire studied period (calibration and validation) is given in Figure 4.10, whereas Figure 4.11 is a variant considering the logarithmic values of the discharge, highlighting differences in low discharge values. The effect of the hydropower operations is well visible in Figure 4.11 with the high variability of the observed discharge during the low flow season.

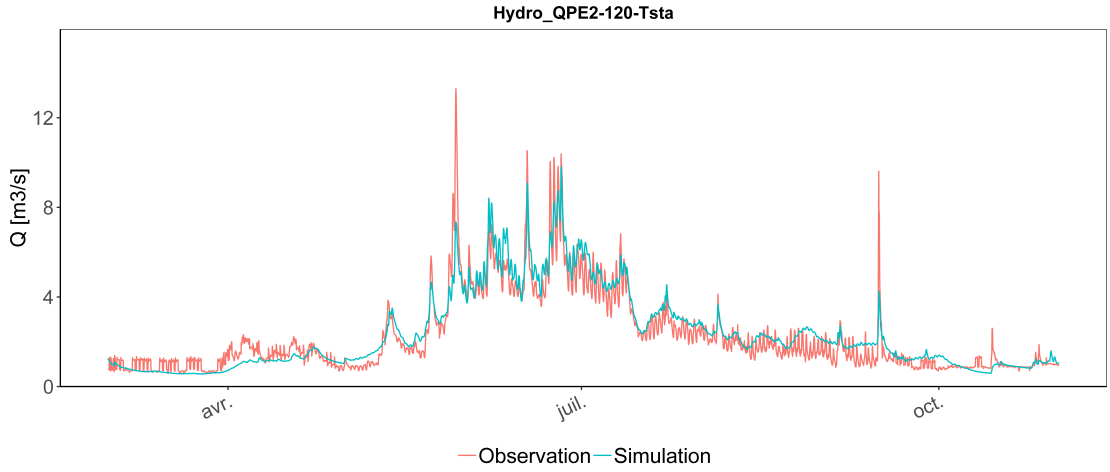

Figure 4.9 – Hydrograph with hourly values for the Saltina catchment over the period March 1, 2016 to October 31 (Configuration: Hydro_QPE2-120-Tsta)).

Over the validation period, QPE2 outperforms clearly QPE1 for all explored configurations. This is particularly true for the RVB performance metric. The high differences between spatial precipitation inputs over the validation period discussed earlier are well visible with the obtained RVB values. Looking at the conventional calibration configurations, a RVB of -25% results from using QPE1, reduced to -11% with QPE2 and reaching -2% with QPE2-120. The two other configurations based on QPE2-120 (using the 2-phase calibration approach) resulted in RVB values of 1 and 0%, suggesting a good adequacy of the correction factor value. This improvement is also confirmed by the other performance metrics over the catchment.

The two configurations using SMN and SMN with MG data result in much lower RVB values (-16% and -19%) than during calibration (-1% for both datasets). This difference likely results from the station configuration evolution between the two periods. Two of the closest stations

Table 4.10 – Performance metrics obtained over the Saltina catchment. Best values are given in bold.

	Calibration				Validation			
Configuration	KGE	RVB	NS	NS-ln	KGE	RVB	NS	NS-ln
Hydro_STA-SMN	0.91	-0.01	0.83	0.52	0.80	-0.16	0.76	0.25
Hydro_STA-SMN+MG	0.91	-0.01	0.82	0.40	0.78	-0.19	0.77	-0.20
Hydro_QPE1-Tsta	0.93	**0.00**	0.87	0.63	0.73	-0.25	0.71	0.17
Hydro_QPE2-Tsta	0.93	-0.01	0.86	0.57	0.85	-0.11	0.79	0.19
Hydro_QPE2-120-Tsta	**0.94**	**0.00**	**0.89**	**0.79**	0.90	-0.02	0.82	**0.67**
Snow-Hydro_QPE1-Tsta	0.90	-0.01	0.81	0.57	0.71	-0.25	0.67	-0.05
Snow-Hydro_QPE2-Tsta	0.88	**0.00**	0.77	0.67	0.86	-0.11	0.82	0.47
Snow-Hydro_QPE2-120-Tsta	0.88	**0.00**	0.78	0.70	**0.91**	0.01	**0.83**	0.54
Snow-Hydro_QPE1-Tspa	0.87	-0.02	0.76	0.50	0.69	-0.25	0.60	-0.35
Snow-Hydro_QPE2-Tspa	0.83	-0.02	0.71	0.60	0.83	-0.12	0.78	0.29
Snow-Hydro_QPE2-120-Tspa	0.85	-0.01	0.74	0.68	0.90	**0.00**	0.81	0.46

used for calibration deliver only data respectively since October 16^{th} 2013 for the SMN station *Brig*, located near the outlet of the catchment, and January 17^{th} 2014 for the SMN station *Binn*. This last station being subject to heavy precipitation coming from the South, like the Saltina catchment, and having data for the station over the calibration but only over the 8 last months for the 2-years validation period, this difference can significantly impact the performance. This is probably what happens here.

Looking at the RVB values over the calibration period, differences observed between the SMN and SMN+MG (94.4% of SMN) configurations about the average precipitation (Table 4.9) are not visible anymore in the performance metrics (Table 4.10). The explanation of this finding can be given with the obtained model parametrization (Table 4.11). The snow melt degree-day factor for the GSM models (parameter S_r with a seasonal variation of $\pm 0.5 \cdot \Delta$) is higher with the SMN+MG configuration (6.8 ± 1.3 mm °C^{-1} d^{-1}) than when using only SMN stations (5.3 ± 2.5 mm °C^{-1} d^{-1}). The same is true for the ice melt degree-day factor (parameter GSM - G), with 7.4 mm °C^{-1} d^{-1} for SMN+MG and 6.2 mm °C^{-1} d^{-1} for SMN. With a slightly faster snow melt over ice followed by a more intense ice melt, the SMN+MG configuration generates more flow from ice melt, compensating thereby a possible lack of precipitation.

This analysis shows how the type of model used here can compensate some errors with the parametrization of the mode. These examples illustrate how the interaction between parameters can complicate the analysis of the results.

Furthermore, it must be mentioned that all configurations with the 2-phase approach resulted here in lower performance than the conventional approach and that they led to degree-day snowmelt interval for GSM elevation bands (parameter GSM - Δ) of 5 mm °C^{-1} d^{-1}, which

corresponds to the upper range limit given for the calibration of the parameter. These high values suggest that the model tries to generate discharge from snow melt over glaciers more at the end of the snow melt season. With the conventional calibration, Δ values were much more variable. No clear explanation could be found. However, considering the limitations of the 2-phase approach discussed earlier, this was not further investigated.

Table 4.11 – Parameter values obtained for the different configuration over the Saltina catchment.

	GSM				
-	S_r	Δ	G	K_{sn}	K_{gl}
Configuration	$[\frac{mm}{°C \cdot d}]$	$[\frac{mm}{°C \cdot d}]$	$[\frac{mm}{°C \cdot d}]$	$[\frac{1}{d}]$	$[\frac{1}{d}]$
Hydro_STA-SMN	5.3	4.9	6.2	0.5	0.4
Hydro_STA-SMN+MG	6.8	2.5	7.4	14.5	0.3
Hydro_QPE1-Tsta	4.5	4.7	6.1	1.1	0.5
Hydro_QPE2-Tsta	5.2	0.0	5.0	14.9	0.6
Hydro_QPE2-120-Tsta	3.6	3.2	4.9	9.6	0.4
Snow-Hydro_QPE1-Tsta	3.0	5.0	5.2	9.0	3.1
Snow-Hydro_QPE2-Tsta	2.9	5.0	5.3	11.8	11.9
Snow-Hydro_QPE2-120-Tsta	2.0	5.0	2.8	10.2	10.5
Snow-Hydro_QPE1-Tspa	2.2	5.0	4.3	13.7	17.5
Snow-Hydro_QPE2-Tspa	2.0	5.0	4.1	5.5	8.3
Snow-Hydro_QPE2-120-Tspa	2.0	5.0	2.1	9.3	19.9

	SOCONT				
-	S_r	Δ	H_{GR3Max}	K_{GR3}	K_r
Configuration	$[\frac{mm}{°C \cdot d}]$	$[\frac{mm}{°C \cdot d}]$	[m]	$[\frac{1}{s}]$	$[\frac{m^{1/3}}{s}]$
Hydro_STA-SMN	1.4	1.1	0.33	0.00119	2.76
Hydro_STA-SMN+MG	0.6	3.0	0.31	0.00109	0.11
Hydro_QPE1-Tsta	1.7	0.1	0.25	0.00116	0.19
Hydro_QPE2-Tsta	0.6	3.7	0.44	0.00093	0.20
Hydro_QPE2-120-Tsta	1.5	0.6	0.30	0.00063	0.08
Snow-Hydro_QPE1-Tsta	-	-	0.53	0.00107	2.00
Snow-Hydro_QPE2-Tsta	-	-	0.40	0.00082	1.43
Snow-Hydro_QPE2-120-Tsta	-	-	0.59	0.00094	2.84
Snow-Hydro_QPE1-Tspa	-	-	0.50	0.00122	2.48
Snow-Hydro_QPE2-Tspa	-	-	0.39	0.00094	1.11
Snow-Hydro_QPE2-120-Tspa	-	-	0.56	0.00100	2.67

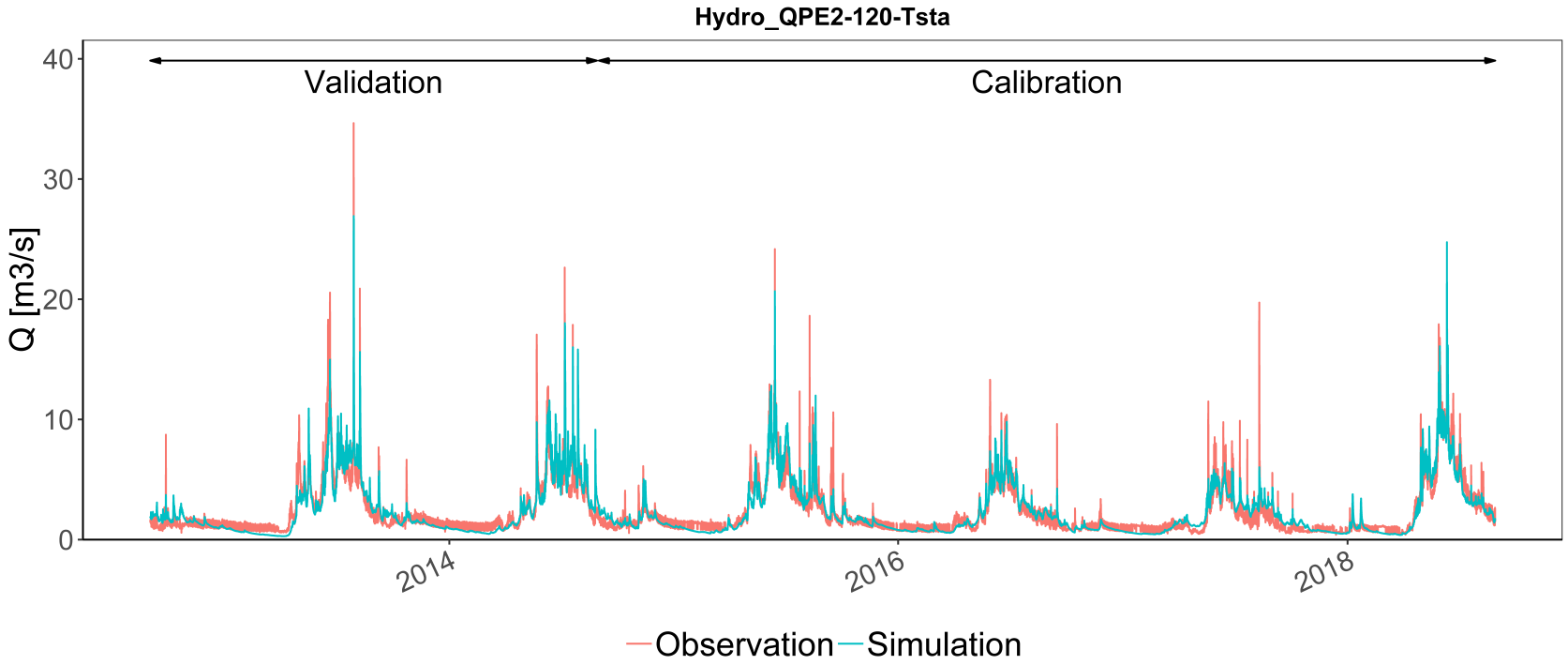

Figure 4.10 – Hydrograph for the Saltina catchment (Configuration: Hydro_QPE2-120-Tsta)).

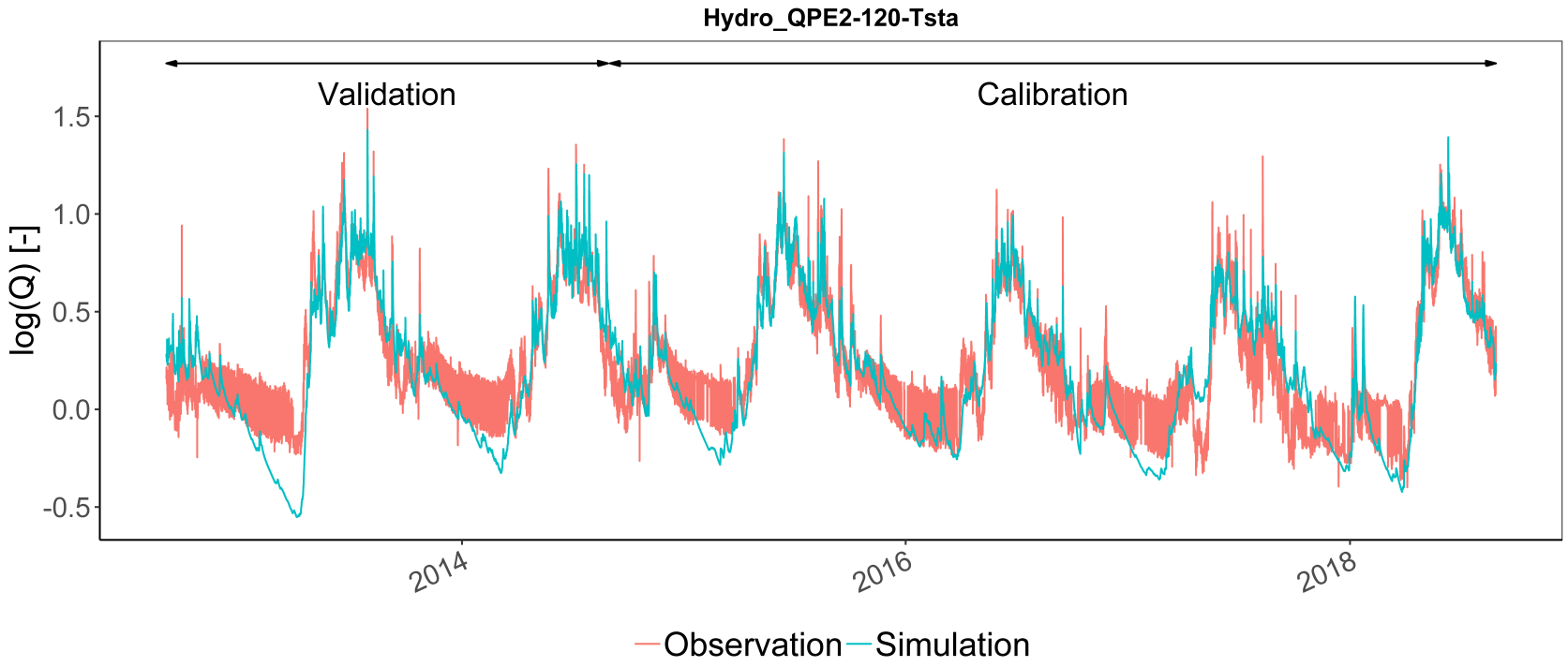

Figure 4.11 – Log of discharge versus time for the Saltina catchment (Configuration: Hydro_QPE2-120-Tsta)).

Over the Lonza catchment, the combination of MG stations with SMN stations also resulted in a reduction of the average precipitation with about -6% over both the calibration and validation periods (Table 4.12). Over the calibration period, the difference between QPE1 and QPE2 is smaller than over Saltina, with QPE2 reporting in that case less precipitation. However, both products report much less precipitation than the SMN stations, with about 10% less volume as compared to SMN. Even the QPE2-120 product with the solid undercatch correction by a factor 1.2 does not reach 100% of the SMN dataset. Whereas the SMN input could also be overestimating the real precipitation, these lower values of all products integrating radar data suggest that some parts of the basin might not well be seen by the weather radar of Pointe de la Plaine Morte (which is known to be the case due to the topography). In the vicinity of the SMN station, this will be corrected in the QPE computation, but for the remaining part of the basin, the information will be mostly taken from the drift computed from the radar data, possibly underestimating the real precipitation.

Table 4.12 – Estimated average precipitation over the Lonza basin with the different precipitation datasets. For the comparison in %, the SMN stations are used as reference.

	Calibration (2014-2018)		Validation (2012-2014)	
Dataset	Average rain [mm]	% of SMN	Average rain [mm]	% of SMN
SMN	995	100.0	1017	100.0
SMN+MG	936	94.1	954	93.8
QPE1	912	91.7	983	96.7
QPE2	897	90.1	1212	119.2
QPE2-120	977	98.2	1352	132.9

From the hydrological performance perspective (Table 4.13), the best calibration KGE performance is obtained with the conventional calibration and with two different precipitation datasets: the SMN station data and QPE2-120. The hydrograph for the second one is given in Figure 4.12, again with a variant of the log of the discharge in Figure 4.13. The poor reproduction of the low flow is well visible on Figure 4.13, with differences between simulation and observation increasing over the low flow season. The simulation also shows to suffer well reproducing the peaks, underestimating most of the high flow events. Over the validation period, the best performance is shared between two configurations using respectively QPE2 and QPE2-120.

For the NS-ln values, the best performance is obtained using the QPE1 product, with the 2-phase approach over calibration and the conventional calibration over validation. However, several configurations led to NS-ln almost as good. The worst NS-ln values are obtained with the two configurations using QPE2-120 in the 2-phase approach.

Over the validation period, RVB values obtained with QPE1 are also lower than the one obtained with QPE2 and QPE2-120, though with smaller variations than over Saltina. Part

Table 4.13 – Performance metrics obtained over the Lonza catchment. Best values are given in bold.

	Calibration				Validation			
Configuration	KGE	RVB	NS	NS-ln	KGE	RVB	NS	NS-ln
Hydro_STA-SMN	**0.95**	**0.00**	0.89	0.59	0.88	-0.08	0.85	0.73
Hydro_STA-SMN+MG	0.94	**0.00**	0.89	0.70	0.87	-0.10	0.85	0.80
Hydro_QPE1-Tsta	0.94	**0.00**	0.89	0.65	0.89	-0.08	0.86	**0.83**
Hydro_QPE2-Tsta	0.94	**0.00**	0.89	0.43	**0.93**	0.01	0.88	0.62
Hydro_QPE2-120-Tsta	**0.95**	**0.00**	**0.90**	0.66	0.92	0.01	**0.89**	0.74
Snow-Hydro_QPE1-Tsta	0.93	**0.00**	0.85	**0.77**	0.88	-0.08	0.83	0.77
Snow-Hydro_QPE2-Tsta	0.93	**0.00**	0.86	0.75	0.91	0.03	0.82	0.78
Snow-Hydro_QPE2-120-Tsta	0.92	**0.00**	0.86	-3.03	**0.93**	**0.00**	0.86	-4.31
Snow-Hydro_QPE1-Tspa	0.90	-0.01	0.81	-0.50	0.85	-0.09	0.76	-1.78
Snow-Hydro_QPE2-Tspa	0.91	**0.00**	0.82	-0.05	0.86	0.02	0.72	-0.80
Snow-Hydro_QPE2-120-Tspa	0.91	-0.01	0.85	-3.52	0.87	-0.04	0.80	-8.82

of this smaller difference probably takes its origin in the different glaciation over the two catchments (2.5% for Saltina, 24.7% for Lonza, see Table 4.1). In the present case, it is not so much the parametrization which explains the difference, the snow melt degree-day factors for GSM models being 4.7 ± 1.5 mm $^{\circ}C^{-1}$ d^{-1} for QPE1 and 4.6 ± 1.5 mm $^{\circ}C^{-1}$ d^{-1} for QPE2. But with a higher contribution from glacier, the difference of more than 22% between the datasets when looking at the precipitation volume appears less large (9%) over the year when including the ice melt. Nevertheless, it should be further investigated if ice melt contribution alone can explain the difference between these two values.

Table 4.14 – Parameter values obtained for the different configuration over the Lonza catchment.

	GSM				
-	S_r	Δ	G	K_{sn}	K_{gl}
Configuration	$[\frac{mm}{°C \cdot d}]$	$[\frac{mm}{°C \cdot d}]$	$[\frac{mm}{°C \cdot d}]$	$[\frac{1}{d}]$	$[\frac{1}{d}]$
Hydro_STA-SMN	5.1	0.0	4.9	2.2	0.5
Hydro_STA-SMN+MG	3.7	3.3	4.9	1.9	0.5
Hydro_QPE1-Tsta	4.7	3.0	5.0	1.9	0.5
Hydro_QPE2-Tsta	4.6	3.0	5.1	2.0	0.4
Hydro_QPE2-120-Tsta	3.8	2.7	5.0	2.7	0.5
Snow-Hydro_QPE1-Tsta	10.4	0.8	4.5	0.4	0.6
Snow-Hydro_QPE2-Tsta	10.0	0.3	4.6	0.5	0.5
Snow-Hydro_QPE2-120-Tsta	4.2	0.0	5.1	1.2	0.2
Snow-Hydro_QPE1-Tspa	12.0	3.4	5.3	0.2	0.2
Snow-Hydro_QPE2-Tspa	10.6	0.3	5.6	0.2	0.2
Snow-Hydro_QPE2-120-Tspa	4.6	0.0	6.2	5.9	0.2

	SOCONT				
-	S_r	Δ	H_{GR3Max}	K_{GR3}	K_r
Configuration	$[\frac{mm}{°C \cdot d}]$	$[\frac{mm}{°C \cdot d}]$	[m]	$[\frac{1}{s}]$	$[\frac{m^{1/3}}{s}]$
Hydro_STA-SMN	10.1	2.7	1.40	0.00138	1.86
Hydro_STA-SMN+MG	10.0	1.1	1.42	0.00127	2.42
Hydro_QPE1-Tsta	12.0	1.1	1.63	0.00142	1.69
Hydro_QPE2-Tsta	9.3	2.0	1.99	0.00158	1.33
Hydro_QPE2-120-Tsta	10.7	3.0	1.57	0.00130	2.34
Snow-Hydro_QPE1-Tsta	-	-	1.67	0.00074	2.70
Snow-Hydro_QPE2-Tsta	-	-	1.99	0.00077	1.66
Snow-Hydro_QPE2-120-Tsta	-	-	1.54	0.00269	1.42
Snow-Hydro_QPE1-Tspa	-	-	1.43	0.00208	1.30
Snow-Hydro_QPE2-Tspa	-	-	0.98	0.00300	0.00
Snow-Hydro_QPE2-120-Tspa	-	-	1.64	0.00422	2.98

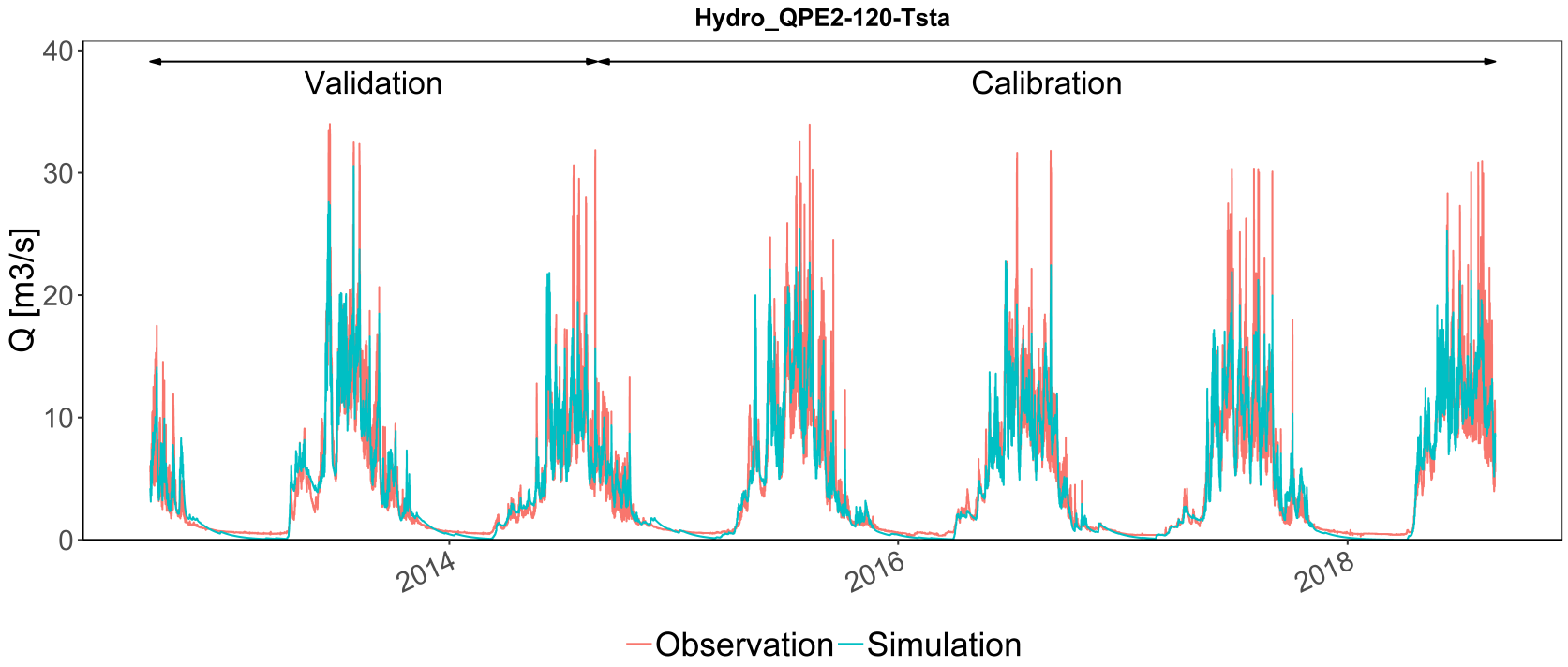

Figure 4.12 – Hydrograph for the Lonza catchment (Configuration: Hydro_QPE2-120-Tsta).

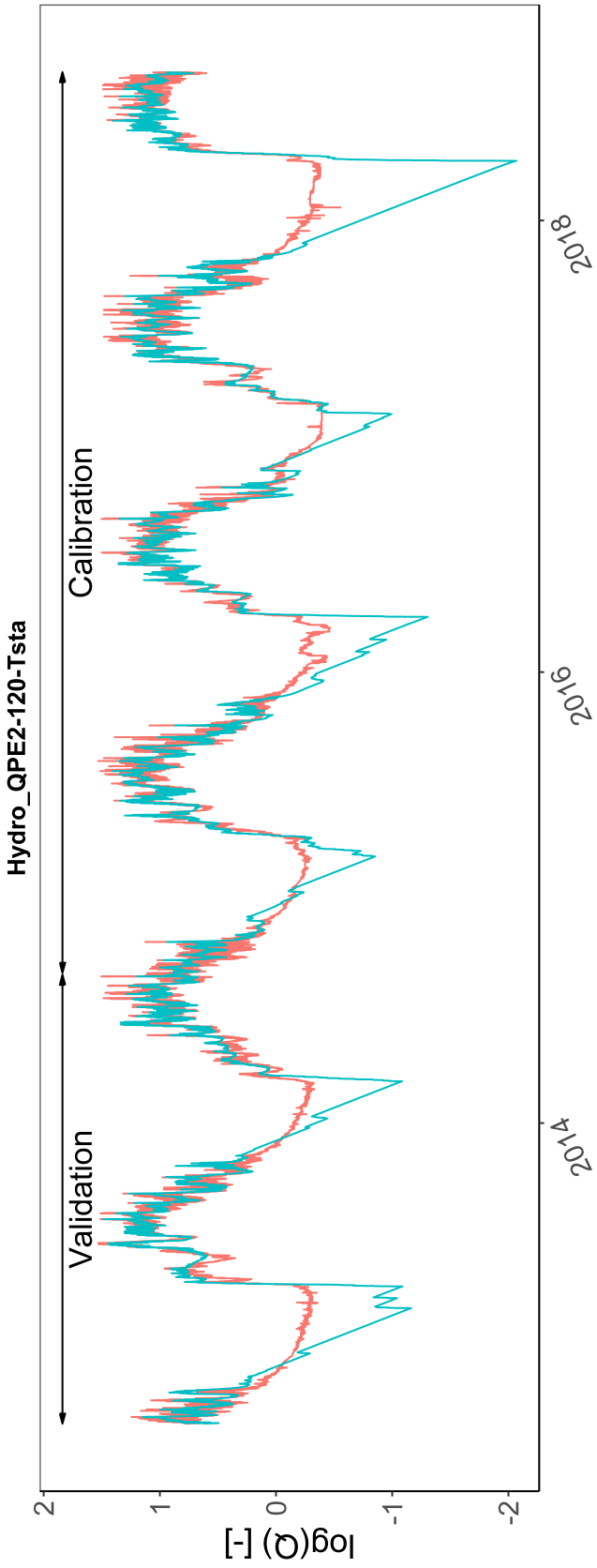

Figure 4.13 – Log of discharge versus time for the Lonza catchment (Configuration: Hydro_QPE2-120-Tsta).

Over the Grande-Eau catchment, the analysis of yearly rain accumulation (Table 4.15) shows that in terms of percentage, the behaviour over the calibration period looks like the one of Lonza, with all QPE reporting less precipitation than the SMN reference dataset. Differences are even stronger, with QPE1 and QPE2 reporting about 11% less than the SMN input. Over the validation period, QPE1 reports only 84.3% of the precipitation computed using the SMN stations, whereas QPE2 gives 105.2%.

Table 4.15 – Estimated average precipitation over the Grande-Eau basin with the different precipitation datasets. For the comparison in %, the SMN stations are used as reference.

	Calibration (2014-2018)		Validation (2012-2014)	
Dataset	Average rain [mm]	% of SMN	Average rain [mm]	% of SMN
SMN	1248	100.0	1455	100.0
SMN+MG	1212	97.1	1406	96.7
QPE1	1106	88.6	1226	84.3
QPE2	1113	89.1	1532	105.3
QPE2-120	1179	94.5	1708	117.4

The best KGE and NS performance (Table 4.16) is here obtained with the configuration using data from the SMN stations (Hydro_STA-MCH), followed by the one using SMN and MG together (Hydro_STA-MCHMG), for both the calibration and validation periods. The lower performance of the radar-based QPE products as compared to data from stations is probably explained over the calibration period by the low visibility of the weather radar of Pointe de la Plaine Morte over the Grande-Eau basin, mainly due to the presence of the Wildhorn peak (3250 m a.s.l.) (see Subsection 4.2.1).

Looking at the hydrograph Figure 4.14 and the log values of the discharge versus time Figure 4.15, difficulties to well reproduce the base flow during winter are again well visible.

The observation done for Saltina about the increasing RVB values obtained in the validation period when using respectively QPE1, QPE2 and QPE2-120 is also well observed for the Grande-Eau basin. However, the two second QPE products result in that case in positive RVB values (i.e. an overestimation): QPE1 generates RVB of about -13%, QPE2 of +8% and QPE2-120 of +11 to +14%. The higher bias correction for QPE2 and QPE2-120 over the entire URR basin, discussed for Saltina, is here also valid. However, due to its location, the Grande-Eau basin was probably somehow better covered by the La Dôle weather radar than the rest of the URR basin and the URR-based bias correction is therefore probably too high. This effect is obviously further strengthened in the case of QPE2-120 with the correction factor for solid precipitation. The above described overestimation is clearly not desired, as RVB should rather be lower than 0 in the case of the Grande-Eau catchment, due to the external inputs of the Lac d'Arnon (see Subsection 4.2.1), not taken into account in the simulation. This is also why no value is given in bold for the RVB performance metric in Table 4.16.

Table 4.16 – Performance metrics obtained over the Grande-Eau catchment. Best values are given in bold. For the RVB, no values are given in bold, as the ideal value is here not 0, the observed discharge being perturbed by the external input of the Lac d'Arnon.

	Calibration				Validation			
Configuration	KGE	RVB	NS	NS-ln	KGE	RVB	NS	NS-ln
Hydro_STA-SMN	**0.87**	-0.03	**0.76**	-0.20	**0.66**	-0.09	0.55	-1.35
Hydro_STA-SMN+MG	0.83	-0.11	0.75	**0.13**	0.65	-0.15	**0.61**	**-0.41**
Hydro_QPE1-Tsta	0.78	-0.05	0.58	-1.03	0.61	-0.13	0.49	-2.76
Hydro_QPE2-Tsta	0.78	-0.05	0.58	-1.28	0.59	0.08	0.19	-3.56
Hydro_QPE2-120-Tsta	0.81	-0.06	0.64	-0.99	0.56	0.14	0.03	-3.13
Snow-Hydro_QPE1-Tsta	0.77	-0.05	0.57	-1.05	0.62	-0.13	0.48	-2.59
Snow-Hydro_QPE2-Tsta	0.77	-0.04	0.56	-1.10	0.61	0.08	0.22	-2.64
Snow-Hydro_QPE2-120-Tsta	0.80	-0.08	0.65	-0.28	0.59	0.12	0.17	-0.97
Snow-Hydro_QPE1-Tspa	0.77	-0.04	0.57	-0.86	0.58	-0.13	0.44	-2.54
Snow-Hydro_QPE2-Tspa	0.76	-0.04	0.55	-0.83	0.59	0.08	0.19	-2.36
Snow-Hydro_QPE2-120-Tspa	0.79	-0.08	0.63	-0.04	0.57	0.11	0.15	-0.73

Analysing the parameter values obtained for Grande-Eau (Table 4.17), the reader might be surprised by the high S_r values obtained for the GSM model for all configurations using QPE1 and QPE2 (the value of 12 [mm °C^{-1} d^{-1}] for the parameter S_r corresponds to the calibration range upper limit). As for the other catchments, this is again a compensation of the model to the lack of precipitation. Even though the glacial surface is very small (0.8%), the model removes the snow as fast as possible over glacial elevation bands to start earlier the ice melt.

Comparing the results obtained with the conventional and 2-phase calibration approaches, no clear conclusion can be made. Best KGE values were obtained for calibration over the three catchments with the conventional approach. However, over the validation period, the 2-phase approach led to the best KGE values over Saltina and Lonza.

Finally, looking at results obtained with the 2-phase approach, configurations considering temperature data from stations provided in general better results compared to the ones using the spatial product of temperature. This confirms that improvements will be necessary in this spatialized product of temperature to get a robust estimation of temperature over the entire basin and for the entire catchments elevation range.

Table 4.17 – Parameter values obtained for the different configuration over the Grande-Eau catchment.

	GSM				
-	S_r	Δ	G	K_{sn}	K_{gl}
Configuration	$[\frac{mm}{°C \cdot d}]$	$[\frac{mm}{°C \cdot d}]$	$[\frac{mm}{°C \cdot d}]$	$[\frac{1}{d}]$	$[\frac{1}{d}]$
Hydro_STA-SMN	6.3	2.0	9.0	19.7	8.7
Hydro_STA-SMN+MG	5.7	0.6	6.7	4.3	15.4
Hydro_QPE1-Tsta	11.9	0.1	8.9	9.9	8.1
Hydro_QPE2-Tsta	12.0	5.0	9.6	4.4	12.5
Hydro_QPE2-120-Tsta	12.0	3.1	9.2	10.0	6.5
Snow-Hydro_QPE1-Tsta	12.0	5.0	10.0	6.0	2.9
Snow-Hydro_QPE2-Tsta	12.0	4.3	10.8	6.6	2.6
Snow-Hydro_QPE2-120-Tsta	12.0	0.2	12.0	20.0	13.9
Snow-Hydro_QPE1-Tspa	12.0	1.8	9.8	9.7	2.9
Snow-Hydro_QPE2-Tspa	11.9	4.9	10.1	9.3	2.6
Snow-Hydro_QPE2-120-Tspa	11.8	2.2	12.0	13.4	3.3

	SOCONT				
-	S_r	Δ	H_{GR3Max}	K_{GR3}	K_r
Configuration	$[\frac{mm}{°C \cdot d}]$	$[\frac{mm}{°C \cdot d}]$	[m]	$[\frac{1}{s}]$	$[\frac{m^{1/3}}{s}]$
Hydro_STA-SMN	2.6	0.0	0.17	0.00406	2.96
Hydro_STA-SMN+MG	3.0	1.7	0.12	0.00465	1.20
Hydro_QPE1-Tsta	1.9	1.3	2.00	0.00996	2.08
Hydro_QPE2-Tsta	1.4	1.2	1.92	0.00959	2.50
Hydro_QPE2-120-Tsta	1.5	1.0	0.20	0.00921	1.99
Snow-Hydro_QPE1-Tsta	-	-	2.00	0.00944	1.38
Snow-Hydro_QPE2-Tsta	-	-	2.00	0.00936	0.55
Snow-Hydro_QPE2-120-Tsta	-	-	0.16	0.00590	2.98
Snow-Hydro_QPE1-Tspa	-	-	2.00	0.00948	2.17
Snow-Hydro_QPE2-Tspa	-	-	1.98	0.00926	0.03
Snow-Hydro_QPE2-120-Tspa	-	-	0.16	0.00530	2.97

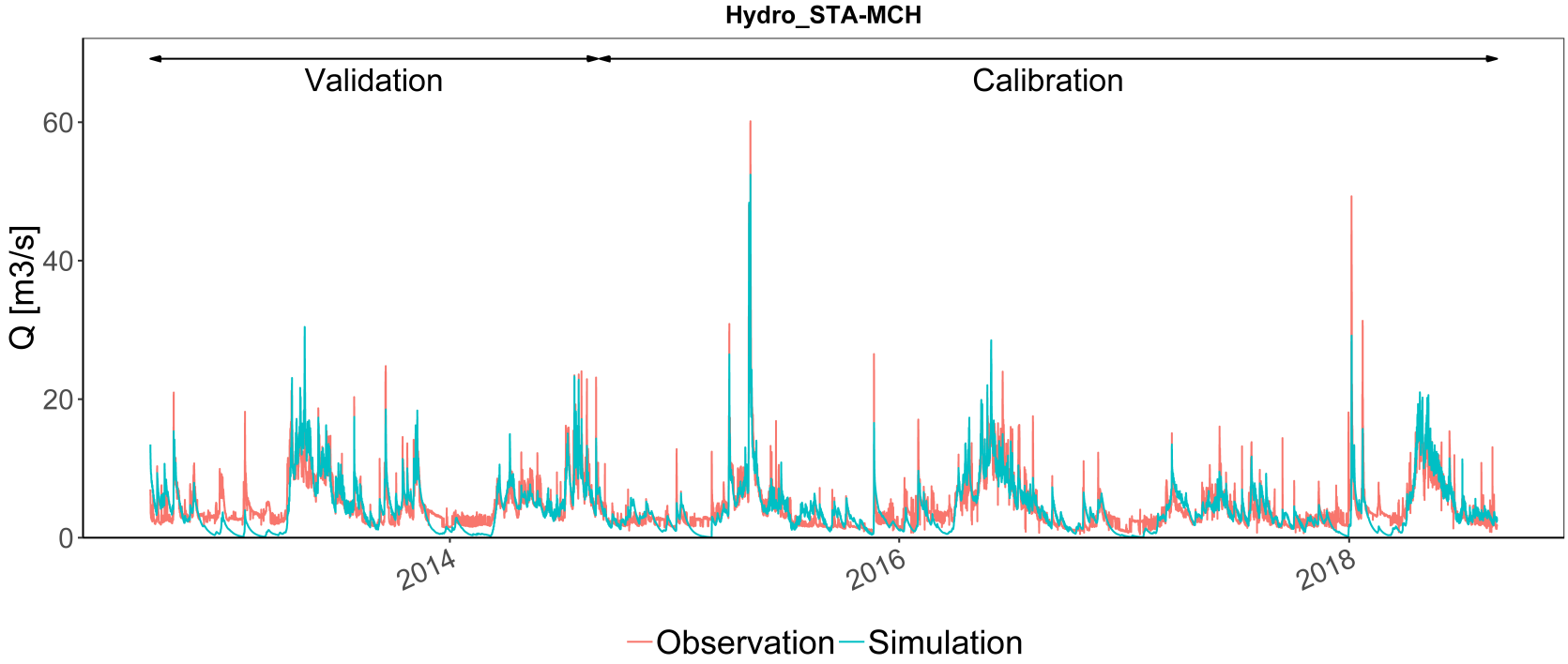

Figure 4.14 – Hydrograph for the Grande-eau catchment (Configuration: Hydro_STA-MCH).

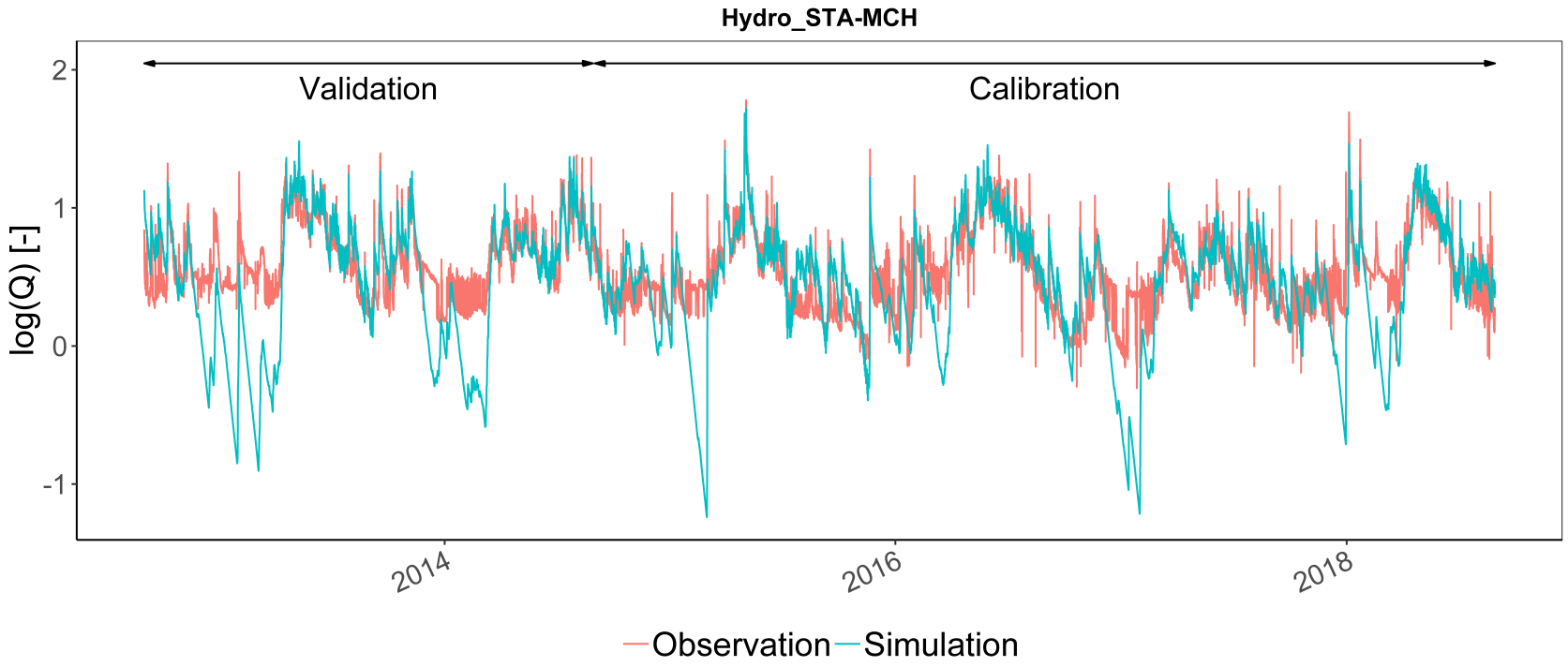

Figure 4.15 – Log of discharge versus time for the Grande-eau catchment (Configuration: Hydro_STA-MCH).

4.5 Discussion

The proposed methodology is based on a complete automatic calibration of the hydrological models. This automation was necessary to avoid manual calibration that could have biased the analysis. However, it must be pointed out that manual calibration could further improve the calibration of the model, in particular in terms of peak flows. This is particularly true if temporal shifts, even small, exist between the simulation and the observation. In that case, simulated peaks might be strongly lower than observed ones, resulting from the error minimisation of the calibration process. The same observation is true for daily discharge variability associated to ice melt. As shown for Saltina, the simulated discharge failed to reproduce with the automatic calibration the amplitude of the daily variations. Manual calibration tests showed that increasing reactivity resulted in temporal shifting of the maximum and minimum values as compared to the observed discharge, explaining why the automatic calibration tends to smooth the simulated discharge to minimize the error. Future developments might therefore explore implementing in RS MINERVE performance metrics enabling good maximum peak flow reproduction even if small temporal shifts exist.

But temporal shifts between simulated and observed discharge might also suggest inadequacy of the model to the complexity of the catchment. The ice melt release reservoir of the GSM model, for example, contains only a unique reservoir. This might not be sufficient to reproduce well the amplitude of the system with an adequate timing. The same is true for the SOCONT model, where increased complexity of the model could allow better reproduction of the observed flow. The river objects used for discharge transfer might also be further investigated. Indeed, improving the hydrology without properly modelling the hydraulics of the system will not lead to good results.

A more complete revision of the MINERVE model might even be necessary in the near future. To reduce for example the problem of equifinality, implementing a distributed model for the MINERVE catchment would allow to move the calibration to a multi-objective approach, considering not only discharge data. This was not the objective of the present dissertation, where the focus was rather given to the input and the snow modelling, but should be considered in future developments of the MINERVE project, with time-variant and spatially explicit components. Precipitation correction in the parametrization, intentionally not explored in this chapter, will certainly also have to be investigated, radar-based quantitative precipitation estimates having shown to suffer from beam shielding in complex topography of the Upper Rhône River basin.

Regarding the snow-melt degree-day factors calibrated with MODIS data, an important difference between the applications done over single pixels in Chapter 3 and the one done over all pixels in the present chapter is the ideal configuration of the pixels used in Chapter 3. The SWE measurement sites used in Chapter 3 correspond to surfaces without trees and with slopes lower than 20°. When applying the method over all pixels in a catchment, these conditions are not satisfied anymore for a large fraction of the pixels, in particular in Alpine catchments like

the ones studied here, complicating the application of the methodology.

In addition, as already discussed in the results section, the definition of thresholds selecting the pixels considered in the aggregation over elevation bands plays a major role in the estimation of degree-day factors in the 2-phase approach. This will need further investigation and will probably allow an improvement in the performance of the configurations considering the 2-phase approach for the calibration. Alternatives to the Overall Accuracy performance metric could also be investigated. As demonstrated, obtained OA values depend on the yearly snow coverage period, which implies the above-discussed thresholds definition. Performance metrics resulting in comparable values over the entire elevation range (i.e. for all snow coverage periods) would facilitate the analysis by avoiding using variable thresholds.

4.6 Conclusion

This chapter explores different input datasets of precipitation for calibrating three catchments of the Upper Rhône River basin using the GSM and SOCONT models. The base scenario is given by precipitation data measured at rain gauges of the SwissMetNet (SMN) network of MeteoSwiss. Alternatively, three quantitative precipitation estimate (QPE) products are used: (1) the operational rain gauge-radar merging product *CombiPrecip* of MeteoSwiss, referred as QPE1; (2) the rain gauge-radar merging developed in Chapter 2, referred as QPE2; and (3) the QPE product presented in Chapter 3 corresponding to QPE2 with a correction of solid precipitation by a factor 1.2, referred as QPE2-120. In addition, a combination of the SMN data with data from the network of the company MeteoGroup Switzerland AG (MG) is explored. For the temperature, both data from stations and the spatial product of temperature presented in Chapter 3 are used for comparison purpose between the two temperature datasets.

This chapter proposes an application of the degree-day factors (DDF) values estimation methodology presented in Chapter 3 at the catchment scale. The DDFs are estimated for each pixel using the snow-covered area information given by the satellite-based Moderate-Resolution Imaging Spectroradiometer (MODIS) as reference data to define the presence or absence of snow. The Overall Accuracy (OA) performance metric is used as objective function. The values of the pixels for which the calibration resulted in sufficiently high OA values are then aggregated over elevation bands. The remaining parameters of the hydrological model are finally calibrated on discharge data. The performance is compared to a conventional calibration in which all the parameters are calibrated on discharge data.

The hydrological calibration of the model, using the Kling-Gupta Efficiency (KGE) performance metric, was realized over the four hydrological years for which data were available for the new weather radar of Pointe de la Plaine Morte. The validation is done over the two preceding hydrological years.

The three studied sub-catchments are all equipped at their outlet with an official stream gauge from the Swiss Federal Office for the Environment (FOEN). In addition, they correspond to

different scenarios of visibility for the new weather radar of Pointe de la Plaine Morte: Saltina is well covered, Lonza a bit more hidden by topography and Grande-Eau suffers from the presence of the Wildhorn peak (3250 m a.s.l.) between the radar and the catchment.

Over the Saltina and Lonza catchments, the configuration considering a conventional calibration using the QPE2-120 product provided the best calibration performance. In the case of Lonza, similar calibration performance was however obtained using only data from the SMN network of MeteoSwiss. Over the validation period, the best KGE value for these two catchments is obtained with the QPE-120 precipitation input but with the 2-phase calibration approach using temperature data at stations. For the Grande-Eau catchment, with the weakest studied radar coverage, best performance is obtained almost for all performance metrics by the conventional calibration using the SMN data.

The analysis showed that the different precipitation inputs result in relatively high difference in yearly precipitation inputs, in particular over the validation periods, where differences between datasets exceeded 55% over Saltina when comparing the combination of SMN and MG data as compared to the QPE2-120 product. Looking at the hydrological performance metrics allows to compare the different products: with a volume input difference of 48% between the QPE2-120 product and the dataset based only on SMN stations, the obtained RVB values of the first product is 0% for QPE2-120 and -15% for SMN, suggesting a better volume of the spatial product.

Considering the fact that the QPE2-120 product resulted in the best performance for the two catchments with best radar visibility, the results suggest that the proposed rain gauge-radar merging methodology accounting for solid precipitation undercatch offers a robust precipitation interpolation over the URR basin in the case of reliable radar data. The equally good performance with SMN stations data over Lonza, known to suffer from an already weaker radar visibility, consolidates this hypothesis. This should however be confirmed by applying the methodology to more sub-catchments. To do so, a map of radar data quality would be extremely helpful. Indeed, the assumptions used in this research about radar visibility over catchments was based only on topographical analysis to define the weather radar installation's visibility over the studied catchments. A scientifically more robust map should be generated as a supporting-tool for future investigations. Furthermore, changes in the station's network configuration over time can also complicate the results analysis.

Decoupling the calibration in two phases was expected to improve the performance of the model by enabling a better spatial coverage of the snow-melting parameters. This assumption was based on the idea that more data leads to better performance. In the obtained results, the 2-phase approach did not allow outperforming the conventional approach over the calibration period. Nevertheless, over the validation period, for the Saltina and Lonza catchments, best KGE performance was obtained with the decoupled approach, maybe suggesting a higher robustness of the calibration in case of important changes in the input. As mentioned in the discussion, thresholds used to select pixels for aggregation based on their calibration

performance were shown to exclude a large portion of pixels, in particular for low and high elevations. The thresholds' definition was based on preliminary investigations to exclude pixels resulting in DDF values considered as too high. Further investigations should explore lowering these thresholds. In addition, proposing another performance metric than the Overall Accuracy used for pixel calibration (e.g. the Heidke Skill Score [Heidke, 1926]) has also been identified as a necessary improvement.

The comparison of results using the spatial product of temperature and the data at stations showed that better performance was obtained with the station data. This was expected from observations realized during the methodology implementation that revealed issues with the spatial product of temperature at high elevations, due to border effects in the elevation range without measuring stations. Here also, further development might result in performance improvements with a more robust spatial product of temperature.

Finally, the analysis also suggests how the parametrization can compensate for example a lack of precipitation by a faster snow melt over glacial parts to start earlier the ice melt, as well as higher ice melt factors to increase the ice melt contribution. This is clearly a limitation of the approach and agrees with the concept of equifinality mentioned in the introduction, in which different parametrizations can lead to identical performance by modelling differently the processes. Such complex parametrization can render results difficult to analyse and interpret. In future developments of the MINERVE system, a revisitation of the hydrological approach might be necessary, by moving for example to a distributed model to benefit from the possibilities of remotely sensed data or at least complexifying the GSM and SOCONT models on some aspects.

5 Implementation of an ensemble Kalman filter for flood forecasting

5.1 Introduction

Despite efforts on the calibration of any hydrological model, discharge forecasts at the closure of an alpine catchment are subject to a number of uncertainties [Srikanthan et al., 2008]. First, meteorological inputs suffer from uncertainties both on the meteorological measurements and forecasts. This is true for both precipitation and temperature data, which can be difficult to estimate accurately in Alpine catchments. Second, the model inevitably represents a simplification of the real system and is subject to an imperfect calibration, which implies errors in the simulated discharges. Consequently, discrepancy between the model state and the true system state occurs. If these model conditions are used for hydrologic forecasting, the discrepancy will inevitably impact the performance of the forecast.

Data assimilation (DA) techniques are mathematical tools developed to update the model state using the newly available system observations and taking into account explicitly the different sources of uncertainty. This includes also uncertainty in the discharge measurements that suffer from various possible errors, which depend on the particular hydraulic conditions of the control section. Different methods have been used in hydrology and the main techniques are summarized hereafter [Liu and Gupta, 2007, Liu, 2012].

The Kalman-type filters [Sun et al., 2016] are the most commonly used data assimilation techniques in hydrology. The original formulation of the Kalman filter (KF), developed in 1960 by Rudolph Emil Kalman, is based on a recursive implementation of a "prediction step", during which the model is advanced in time, and an "update step", in which the newly available observation(s) is used to update the model. The update is based on the so-called Kalman gain computed from relative magnitudes of the state error covariance and the observation error covariance and acts as a weighting factor in the update process. The Kalman filter is optimal for linear models, which is not the case of most hydrological models. Many extensions of the Kalman filter have therefore been proposed to support nonlinear processes. One of them is the extended Kalman filter (EKF) [Jazwinski, 1970], in which models are linearized beforehand. In case of strong model nonlinearities, the EKF showed to be unstable. Another

extension of the KF is the ensemble Kalman filter (EnKF) in which the linearization of the model is replaced by an ensemble of model realisations, each member representing an equally-plausible representation of the real-world [Evensen, 1994]. The relatively easy implementation of the EnKF and the fact that model error covariances must not be specified, as it is computed from the members, made EnKF to find favour in hydrology [Abaza et al., 2015a, Clark et al., 2008, Moradkhani et al., 2005b, Srikanthan et al., 2008]. One of the limitations of EnKF is to consider only the latest available observation value. To better consider issues associated to the time of concentration of the catchment, McMillan et al. [2013] proposed a recursive ensemble Kalman filter (REnKF) in which model states are updated through iterative application of the EnKF over a period corresponding to the maximum lag time of the catchment and found that REnKF overcomes instabilities of the EnKF associated with this time of concentration.

Another approach also relying on an ensemble of model realizations (like EnKF) are particle filters (PF) [Moradkhani et al., 2005a]. The true system state is represented by a weighting of the particles, each having an associated weight. Particles are propagated in time and when a new observation is available, the respective weights are updated. The state variables themselves are not modified in the updating step. One major limitation of PF is that a high number of particles is generally required. Furthermore, particle filters are subject to filter impoverishment, also referred to as filter degeneracy: after several assimilation steps, the weight of one particle tends to become increasingly large and the ensemble is effectively described by this single particle. To prevent filter degeneracy, resampling algorithms are used to reduce the variance in the weights. Weerts and El Serafy [2006] compared the EnKF with Particle filtering and showed that EnKF was more robust and outperformed the two other analysed filters. Recently, particle filters are becoming increasingly popular, in particular with new resampling algorithms [Abbaszadeh et al., 2019, Berg et al., 2019].

Yet another approach for hydrological data assimilation is variational methods [Seo et al., 2003]. The basic idea of variational methods is to update states or inputs variables over a predetermined window of time in order to optimize the initial state of the model [Abaza et al., 2015b]. The need of an adjoint model, to compute the gradient of the optimization cost function, has made variational approaches less common in hydrology [McMillan et al., 2013]. Nevertheless, they have the potential of being much less computationally expensive than Kalman filters for complex systems [McMillan et al., 2013]. Abaza et al. [2015b] compared EnKF and variational data assimilation over two dissimilar watersheds in Canada and Germany. Their study showed that the EnKF approach outperformed the variational technique for all forecast horizons over the 10 days of forecast.

In this chapter, an implementation of an ensemble Kalman filter with updating of state variables is explored [Foehn et al., 2019b] using the GSM (Glacier and SnowMelt) and SOCONT (Soil CONTribution) semi-distributed conceptual models [Schaefli et al., 2005, Hamdi et al., 2005]. The objective is to propose a framework to improve the updating of initial conditions in the MINERVE operational flood forecasting system [Jordan, 2007a, García Hernández, 2011a, García Hernández et al., 2014] and to present the results of a first implementation as well

as identifying the next steps of development. The performance gain is evaluated over two flood events concerning two different rivers located within the Upper Rhône River basin in Switzerland (Chapter 1).

5.2 Material and Methods

5.2.1 Watersheds and data

The analysis concerns the simulation of the streamflow at the outlet of two sub-catchments of the Upper Rhône River basin. The sub-catchments selection considered the availability of streamflow measurements at the outlet and only a limited perturbation of the discharge due to hydropower operations. In addition, the sub-catchments had to have experienced a high flow event (return periods equal to or larger than 10 years) over the period of data availability for the weather radar of Pointe de la Plaine Morte, the use of radar data being expected to better reproduce the spatial distribution of the precipitation generating the event. These constraints led to selecting the Grande-Eau (high flow event in May 2015) and the Rhône River upstream of Reckingen (event in June 2019). The characteristics of the sub-catchments are given in Table 5.1.

Table 5.1 – Main characteristics of the catchments and studied peak flow events. Data source: FOEN [2017b].

Station	Reckingen	Aigle
River	Rhône	Grande-Eau
Area [km^2]	214	132
Catchment mean elevation [m asl.]	2305	1562
Glaciation [%]	11.8	0.8
Hourly peak flow [m^3/s]	127.7	60.1
Estimated return period of the studied event [years]	14	10

Both rivers are equipped with a small run-of-river hydropower plant. The one over the Rhône (Reckingen basin) has an equipped discharge of 5.7 m^3/s (2018 yearly average observed discharge at Reckingen: 10.6 m^3/s). The equipped discharge over the Grande-Eau was 2.5 m^3/s in 2015 (2015 yearly average observed discharge at Aigle: 4.02 m^3/s). The Grande-Eau catchment receives in addition water diverted from the Lac d'Arnon, a reservoir located in a nearby catchment with a capacity of 11 million m^3. When the natural discharge in the Grande-Eau River is below the installed capacity of the two successive run-of-river hydropower plants, the water from the external reservoir is turbined at a third more upstream hydropower plant located in Les Diablerets, with a capacity of 1.75 m^3/s. The operating data of the scheme were not available for the present study.

Precipitation data are taken from the spatial product of precipitation following the regression co-kriging (RCK) approach presented in Chapter 2, in which radar data are combined with two networks of ground stations data into a 1km x 1km gridded data with a one hour temporal

resolution. Temperature data are interpolated from the values observed at the meteorological stations using an inverse distance weighting interpolation and considering a constant vertical lapse rate of -5.5°C/1000m.

In order to evaluate the performance of the data assimilation method, observed data of precipitation and temperature are both used for the assimilation and forecast simulations; i.e. no weather forecast data are considered in the present analysis. This was mainly based on the limited temporal coverage of historical weather forecasts data. Furthermore, working with observed value can be seen as introducing less uncertainty than with weather forecasts. Nevertheless, it must be mentioned that the two basins studied in this chapter are not well covered by the SwissMetNet automatic monitoring network of the Swiss Federal Office of Meteorology and Climatology (MeteoSwiss). Nor are they well covered by the Swiss weather radar network, due to the complex topography of the Upper Rhône River basin. The radar data are therefore locally subject to possible underestimation of the precipitation.

To account for these underestimations, the spatial product of precipitation is multiplied in the simulation over the Grande-Eau catchment by a correction factor resulting from a manual calibration with values between 1.15 and 1.4. Spatial variation in the factors is justified by varying visibility of the weather radar data over the basin, with the Wildhorn peak (3250 m a.s.l.) considerably reducing the visibility over the basin from the closest weather radar, the one at Pointe de la Plaine Morte, located at only 2926 m a.s.l.

5.2.2 The GSM and SOCONT hydrological models

Simulations are performed with the rainfall-runoff semi-distributed conceptual GSM and SOCONT models [Schaefli et al., 2005, García Hernández et al., 2019], illustrated in Figure 4.2. The main parameters of the model are given in Table 4.3.

The GSM model is used for glacial elevation bands and the SOCONT model for non-glacial elevation bands. For both models, the snowmelt rate is controlled by the snowmelt coefficient (degree-day factors). For the GSM model, when the surface is free of snow, glacial melting is considered based on the glacier melt coefficient and the temperature. For the SOCONT model, the generated discharge at the outlet of the basin is controlled by the absorption capacity of the soil, the release coefficient of the infiltration reservoir as well as the roughness of the surface runoff surface.

The model for the Grande-Eau catchment is taken from the calibration performed in Chapter 4. For the Reckingen model, the one of the MINERVE system is considered.

5.2.3 Data assimilation techniques

Two data assimilation techniques are explored in this work to improve the values of the system state variables at the beginning of each forecast. The first method is based on a

comparison between simulated and observed discharges volumes over the past 24 hours including the latest available data [Hamdi et al., 2006, Jordan, 2007a]. This method has been used operationally since 2017 in the MINERVE system. The second method consists in an ensemble Kalman filter, where an ensemble of possible model trajectories are corrected by assimilating the latest available hourly discharge observation.

The objective of the data assimilation is reducing the discrepancy between the simulated state variables and the actual state of the system as measured in real-time. This step would improve the performance of the model during the forecast. To do so, the state variables of the model are updated using the available system observations, namely the discharge. The state variables that need to be updated are given in Table 5.2. They are evaluated at each spatial node of the model. The variable names indicated in Table 5.2 correspond to the variable names in RS MINERVE. The water level in the glacial melt and snow melt reservoirs is expressed in terms of corresponding flow ($Q_{glacier}$ and Q_{snow}), but is effectively related to the initial height in the reservoirs.

Table 5.2 – State variables to update for the SOCONT and GSM models.

Parameter	Units	SOCONT
H_{GR3}	m	Water level in infiltration reservoir
H_r	m	Runoff water level downstream of the surface
SWE	m	Snow water equivalent height
Parameter	Units	GSM
SWE	m	Snow water equivalent height
$Q_{glacier}$	m^3/s	Outflow of linear snow reservoir
Q_{snow}	m^3/s	Outflow of linear glacier reservoir

In the following, $\boldsymbol{x}_t$ will indicate the system state vector of dimension n_{state}=6×n_{nodes}, which elements are the SOCONT state variables H_{GR3}, H_r and SWE and GSM state variables SWE, $Q_{glacier}$ and Q_{snow} in all modelled nodes. The temporal evolution of the state vector obtained with the GSM and SOCONT models is formally represented by the following dynamical model:

$$\boldsymbol{x}_{t+1} = f(\boldsymbol{x}_t, \boldsymbol{u}_t, \boldsymbol{w}_t) \tag{5.1}$$

where the function f is the set of equations linking the state of the system from time t to t+1, $\boldsymbol{u}_t$ represents the vector of model inputs (here, spatial maps of temperature and precipitation), $\boldsymbol{w}_t$ is the possible occurrence of system noise (not directly considered in this analysis).

The assimilation procedure is performed using real measurements of the system given by discharge data based on water level observations at the outlet of the watershed, provided by the Swiss Federal Office for the Environment (FOEN). To do so, the discharge of the (kinematic wave) river reaches (Q_{kw}) of the model are also considered as state variables. Observations are indicated with the vector $\boldsymbol{y}_t$ of dimension n_{obs} (here n_{obs}=1, since the observation is the discharge at time t at a unique gauging station). The link between the state variables $\boldsymbol{x}_t$ and

the observations, $\boldsymbol{y}_t$, is provided by the observation operator:

$$\boldsymbol{y}_t = \boldsymbol{H}\boldsymbol{x}_t + \boldsymbol{v}_t \tag{5.2}$$

where **H** is a projection matrix (dimension $n_{obs} \times n_{state}$), and $\boldsymbol{v}_t$ represents possible measurement errors (see Subsection 5.3.1). Matrix **H** is constructed with a value of 1 in correspondence of the state variable being observed, and 0 elsewhere [Clark et al., 2008].

The two assimilation procedures considered in this chapter to produce forecasts of discharge as well as the reference scenario without data assimilation are described hereafter.

Control simulation (Control)

The reference scenario is computed by running the model (Eq. 5.1) without any perturbation of the input data (i.e., $\boldsymbol{u}_t$ corresponds to the nominal values of precipitation and temperature) and without considering the discharge measurements during the simulation (no data assimilation). This simulation corresponds to what is frequently called the open-loop scenario.

For each forecast, the model is first run over the preceding 24 hours using observed meteorological data. For this simulation, initial conditions used for the forecast done 24 hours earlier are used to initialize the model. The state variables obtained at the end of the 24 hours control simulation are then used as initial conditions for the new forecast.

Volume-based update (VBU)

The first data assimilation approach is the volume-based update (VBU), which is based on the comparison between the volumes of the observed and the simulated hydrographs. The implemented approach is based on the methodology developed within the MINERVE project [Hamdi et al., 2006]. The only updated state variable is the soil water content (H_{GR3}) of the SOCONT models and used operationally in the MINERVE system since 2017.

The value of the corresponding H_{GR3} at the start of the VBU simulation (24 hours before the beginning of the hydrological forecast) is iteratively changed so that the simulated volume throughout the simulation is as close as possible to the observed one. At each iteration, a correction factor Ψ is computed based on the observed and simulated volumes:

$$\Psi = \begin{cases} 2.5 & \text{if } \nu \leq -0.6\,, \\ \frac{1}{\nu+1} & \text{if } -0.6 < \nu < 4\,, \\ 0.2 & \text{if } \nu \geq 4\,. \end{cases} \tag{5.3}$$

with

$$\nu = \frac{V_{obs} - V_{sim}}{V_{sim}} \tag{5.4}$$

where V_{sim} is the volume corresponding to the simulated discharge over the 24 preceding hours and V_{obs} the corresponding volume for the observed discharge. The choice of 24 hours satisfies the minimum of 12 hours recommended in [Jordan, 2007a] to exceed the catchment transit time and doing the analysis over one day is convenient for practical reason in the operational system.

Once the correction factor Ψ computed for iteration n, the new water level in the infiltration reservoir, for each elevation band i, is given for the next iteration $n+1$ by:

$$H_{GR3_{i,n+1}} = \Psi \cdot H_{GR3_{i,n}} \tag{5.5}$$

The iterative approach is interrupted if $|\nu_t - \nu_{t-1}| < 0.01$, if $\nu_t < 0.05$ or after a maximum of 10 iterations.

In addition, the implemented approach limits the saturation at the start of the VBU simulation to 75% of the maximum water content in the soil, in order to avoid a too much reactive results. This value has been defined in the implementation of the VBU method where higher values of threshold resulted in some cases in large overestimation of the observed discharge du to the update. Note that VBU does not take into consideration the uncertainties in the inputs, model, or observations. Similarly to the control simulation, VBU provides as output only one model trajectory.

Ensemble Kalman filter (EnKF)

The second data assimilation approach is an implementation of the ensemble Kalman filter (EnKF), which allows updating all state variables taking into consideration model and measurements uncertainties. EnKF is an adaptation of the Kalman filter in which the covariance matrix is replaced by the sample covariance computed from an ensemble of possible state vectors. EnKF is based on the sequential repetition of two steps: the prediction step and the analysis (or assimilation) step. In the prediction step, the different members of the ensemble are independently advanced in time by running the model (Eq.(5.1)) using different random samples of the uncertain forcing terms [Srikanthan et al., 2008, Abaza et al., 2015a]:

$$\boldsymbol{x}_{t+1}^{i,p} = f(\boldsymbol{x}_t^{i,a}, \boldsymbol{u}_t^i, \boldsymbol{w}_t), i = 1, \ldots, n_{ens} \tag{5.6}$$

where $\boldsymbol{x}_{t+1}^{i,p}$ is the ith member predicted state at time t+1, $\boldsymbol{x}_t^{i,a}$ is the ith updated member state at time t, $\boldsymbol{u}_t^i$ represents a possible occurrence of the model and/or input uncertainties (here, a perturbation of temperature and precipitation, see Subsection 5.3.1) and n$_{ens}$ is the number of ensemble members. The index "p" indicates the prediction and the index "a" the analysis.

In the assimilation step, the predicted state variables $\boldsymbol{x}_{t+1}^{i,p}$ are updated using the newly available observation, $\boldsymbol{y}_{t+1}$. The n$_{ens}$ members are combined into the n$_{state}$ × n$_{ens}$ model state

matrix, that is:

$$\boldsymbol{X}_{t+1}^{p} = \left(\boldsymbol{x}_{t+1}^{1,p}, \boldsymbol{x}_{t+1}^{2,p}, \ldots, \boldsymbol{x}_{t+1}^{n_{ens},p}\right) \tag{5.7}$$

where n_{state} is the number of state variables. The ensemble mean is given by:

$$\overline{\boldsymbol{x}}_{t+1}^{p} = \frac{1}{n_{ens}} \sum_{i=1}^{n_{ens}} \boldsymbol{x}_{t+1}^{i,p} \tag{5.8}$$

and it is used to compute the ensemble of anomalies:

$$\boldsymbol{E}_{t+1}^{p} = \left(\boldsymbol{x}_{t+1}^{1,p} - \overline{\boldsymbol{x}}_{t+1}^{p}, \boldsymbol{x}_{t+1}^{2,p} - \overline{\boldsymbol{x}}_{t+1}^{p}, \ldots, \boldsymbol{x}_{t+1}^{n_{ens},p} - \overline{\boldsymbol{x}}_{t+1}^{p}\right) \tag{5.9}$$

The ensemble model covariance matrix ($n_{state} \times n_{state}$) can then be defined as follows:

$$\boldsymbol{P}_{t+1}^{p} = \frac{1}{n_{ens}-1} \boldsymbol{E}_{t+1}^{p} \boldsymbol{E}_{t+1}^{p^{T}} \tag{5.10}$$

In order for the EnKF to maintain sufficient spread in the ensemble and prevent filter divergence [Burgers et al., 1998], observations are perturbed in accordance with the measurement error to create a $n_{obs} \times n_{ens}$ vector of observations $\boldsymbol{Y}_{t+1}$.The analysis equation is then given by the EnKF update, which is optimal in the case of errors with a Gaussian distribution:

$$\boldsymbol{X}_{t+1}^{a} = \boldsymbol{X}_{t+1}^{p} + \boldsymbol{K}_{t+1}\left(\boldsymbol{Y}_{t+1} - \boldsymbol{H}_{t+1}\boldsymbol{X}_{t+1}^{p}\right) \tag{5.11}$$

where the matrix $\boldsymbol{K}_{t+1}$ ($n_{state} \times n_{obs}$) is called the Kalman gain:

$$\boldsymbol{K}_{t+1} = \boldsymbol{P}_{t+1}^{p} \boldsymbol{H}_{t+1}^{T}\left(\boldsymbol{H}_{t+1}\boldsymbol{P}_{t+1}^{p}\boldsymbol{H}_{t+1}^{T} + \boldsymbol{R}_{t+1}\right)^{-1} \tag{5.12}$$

and where $\boldsymbol{R}_{t+1}$ is the $n_{obs} \times n_{obs}$ observation error covariance matrix.

Note that each ensemble member is updated separately; this update is different for each member, as it is function of the predicated state variable values of the member. Moreover, the forecast computed after an EnKF update consists of an ensemble of model trajectories in which the same perturbation of precipitation and temperature are considered, trajectories from which it is possible to quantify the uncertainty associated to the forecast. Furthermore, the constraint of maximum 75% of soil saturation used in the VBU is not applied in the implementation of the EnKF. This choice was motivated by the hypothesis that the higher sophistication of the EnKF using the ensemble approach does not requires this limitation. Nevertheless, EnKF can also result in oversaturation in case of large differences between simulated and observed discharges.

5.3 Experimental set-up

5.3.1 Uncertainties in input and output

Model uncertainties are quantified by the ensemble Kalman filter through the empirical probabilistic distribution of the ensemble members. Input forcing data (precipitation and temperature in this study) are perturbed to provide each member a different input and thereby ensures spread in the ensemble. Members are initialized with a perturbation of the main state variables of the model.

Precipitation uncertainty

Precipitation is perturbed following a lognormal distribution with a temporal correlation. During the prediction step of EnKF, the nominal value of precipitation is multiplied by a coefficient as follows:

$$\begin{cases} P_t^i = P_t e_t^i, \\ e_t^i = \exp(z_t^i) \sim \text{logN}(m_e, \sigma_e^2). \end{cases} \tag{5.13}$$

where P_t is the measured precipitation at time t, e_t^i is the multiplier coefficient for the ith member at time t and P_t^i is the perturbed precipitation for the ith member at time t.

At time t=0, z_o^i is sampled from:

$$z_0^i \sim \text{N}(0, \theta^2) \tag{5.14}$$

with a mean equal to 0 so that the median of $\exp(z_0^i)$ equals 1 and a standard deviation θ fixed to 0.3 for Grande-Eau and 0.5 for Reckingen on which a higher precipitation uncertainty is considered (a θ of 0.5 corresponds to perturbation factor e_t^i with quantiles 5, 25, 50, 75 and 95% of respectively 0.44, 0.71, 1.00, 1,40 and 2.18).

At time t>0, in order to ensure a temporal correlation of the perturbation in a given member, the time evolution of precipitation errors is simulated as follows:

$$\begin{cases} z_t^i = \rho z_{t-1}^i + \sqrt{1-\rho^2}\omega_t^i, \\ \omega_t^i \sim \text{N}(0, \theta^2), \\ \rho = 1 - \frac{\Delta T}{\tau}. \end{cases} \tag{5.15}$$

where ω_t^i is the sample white noise, ρ is the temporal persistence parameter, ΔT is the temporal resolution of precipitation data and τ the decorrelation time step. In the present study, ΔT is one hour and τ is fixed to 24 hours (following Clark et al. [2008]).

In addition to the temporal correlation, the spatial correlation of the perturbation is considered by modifying for a given member all pixels with the same correction.

Temperature uncertainty

Temperature is perturbed using an additive term following a normal distribution:

$$T_t^i = T_t + s_t^i \tag{5.16}$$

where T_t is the measured temperature at time t, s_t^i is the additive coefficient for the ith member at time t and T_t^i is the perturbed temperature for the ith member at time t.

At time t=0, the perturbation of the ith member is given by:

$$s_0^i \sim \mathrm{N}(0, \sigma_s^2) \tag{5.17}$$

where the standard deviation σ_s is fixed to 2°C. At time t>0, a temporal correlation of the perturbation is considered following Eq. 5.15 using the normal distribution given in Eq. 5.17 and a decorrelation time fixed to 12 hours. Similarly to the precipitation, a spatially constant correction is considered for each member.

Measurement uncertainty

Errors in the streamflow measurements can result from both errors in the level measurement and uncertainties in the rating curve used to transform water level into discharge data. The perturbed discharges are consequently computed with an additive term as following:

$$\begin{cases} y_t^i = y_t + \beta_t^i - \gamma\,, \\ \beta_t^i \sim \mathrm{N}(0, \sigma_\beta^2)\,, \\ \sigma_\beta = \epsilon_y y_t\,. \end{cases} \tag{5.18}$$

where ϵ_y is a hyper-parameter allowing to define the perturbation proportionally to the discharge values, fixed to 10%, γ corresponds to a correction for possible external discharge contributions to the basin, like in the case of the Grande-Eau (1.75 m^3/s from the Lac d'Arnon located outside of the basin). The γ correction is randomly considered by using a uniform random variable (i.e. discharge values for 50% of the members are reduced by the defined external discharge, 50% are not modified).

Members initialization

Before the first assimilation, initial conditions of the state variables are also perturbed. The original initial values are computed with a one year warm-up simulation using the same

precipitation and temperature data as the one used for the data assimilation. State variables are then perturbed using a normal distribution with mean 0 and a standard deviation corresponding to 40% of the original state variable values.

5.3.2 Performance evaluation

Two precipitation events are analysed and VBU and EnKF are used to assimilate streamflow measurements. After each assimilation, a new streamflow forecast of 3 days is produced using observed perturbed precipitation and temperature data. The performances of the control scenario, VBU and EnKF are evaluated by computing the Root Mean Squared Error (RMSE) between the forecasted and measured streamflow values at different hourly forecast horizons as follow [Srikanthan et al., 2008, Abaza et al., 2015a]:

$$\mathrm{RMSE}_t = \sqrt{\frac{\sum_{j=1}^{n} \left\{ Q_{t,j}^{f} - Q_{t,j}^{obs} \right\}^2}{n}} \tag{5.19}$$

where n is the number of forecasts produced over the studied flood event, $Q_{t,j}^{f}$ is the member median at forecast horizon t for the jth forecast, $Q_{t,j}^{obs}$ the observed discharge at forecast horizon t for the jth forecast. For the forecasts based on Control and VBU, $Q_{t,j}^{f}$ corresponds to the forecasted discharge at forecast horizon t for the jth forecast.

In addition to the RMSE, the Kling-Gupta efficiency (KGE), used in Chapter 4 for model calibration, is used for comparing the two assimilation approaches and the reference scenario. The KGE values are computed over three time intervals: 1-24h, 25-48h, 49-72h.

Note that the first 4 forecasts are not considered in the computation of RMSE and KGE, to allow the EnKF approach to adapt to the high uncertainty given in the initialization of the first forecast. For both events, forecast simulations were performed over a period so that the discharge increase is not yet visible on the end of the first forecast and to stop few hours after the event. The exact periods covered by the analysis are given in Table F.1 in Appendix F.

5.3.3 Code implementation

The methodology has been implemented in the R language and environment [R Core Team, 2018], in particular with the packages parallel for parallel computation [R Core Team, 2018], ggplot2 for the plots [Wickham, 2016] and httr for the data acquisition [Wickham, 2018].

The implemented code has been developed based on the existing operational MINERVE forecasting system (see Chapter 1), in particular for the data acquisition. This constraint was imposed by the intention of operationally using the EnKF approach, once finalized, for the operational system.

The hydrological modelling is done with the RS MINERVE[1] software [García Hernández et al., 2019]. The information transfer between the R language and RS MINERVE is done through text files. This includes for example initial conditions for each forecast time, perturbed precipitation and temperature data, as well as simulation results from RS MINERVE. These data being different for each member, n_{ens} files are generated for each forecast time and each phase of the EnKF approach requiring an information transfer between R and RS MINERVE or the other way around.

5.3.4 Methodology application

In the EnKF implementation realized in this study, an update of the state variables followed by a hydrological forecast is performed every 4 hours for the Reckingen catchment and every 2 hours for the Grande-Eau catchment. The longer time between forecasts for the Reckingen catchment is justified by its larger catchment area. It is important to consider sufficiently long propagation time for them to be longer than the concentration time of the catchments. If the concentration time is longer than the propagation time, modifications brought by the EnKF in the most upstream parts of the catchment might not have arrived to the outlet of the catchment, negatively impacting the updating process.

Based on preliminary tests, 100 members have been considered for the EnKF approach.

5.4 Results

Simulations have been run for the two events presented in Table 5.1 and the results are presented hereafter.

5.4.1 Results over the Reckingen catchment

Figure 5.1 shows the forecasted flow about 24 hours before the peak flow for the high flow event at station Reckingen (Rhône River). For the EnKF approach, lines corresponding to all the members (light red) as well as the median (red) and the mean (brown) are shown. Over the assimilation period, these lines exist only over the four hours preceding the forecast time (given by the vertical dashed line). For the analysis presented hereafter, EnKF refers to EnKF-median.

The forecast RMSE values obtained for the event are presented in Figure 5.2. The EnKF clearly provides the best average performance for all forecast horizons over the studied event, followed by the VBU approach for the first day of forecast. For the second day of forecast, Control outperforms VBU and the two methods provide similar results over the third day of forecast.

[1] Software version RS MINERVE 2.7.6

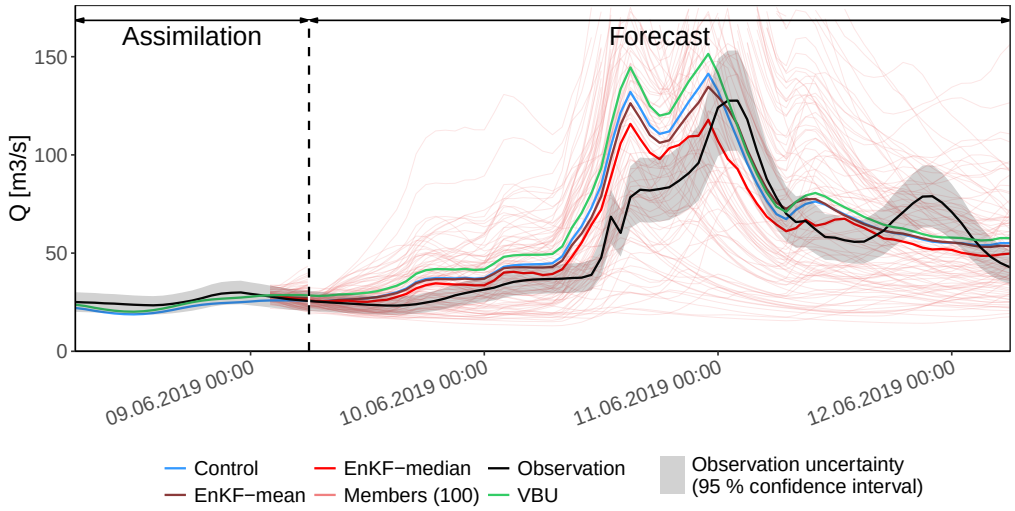

Figure 5.1 – Forecasted discharges for the three different approaches at the Reckingen station on the Rhône River. The dashed line corresponds to 2019-06-09T06+01:00. The grey zone around observed discharge data corresponds to a 95% confidence interval based on the hyperparameter defined in Eq. 5.18.

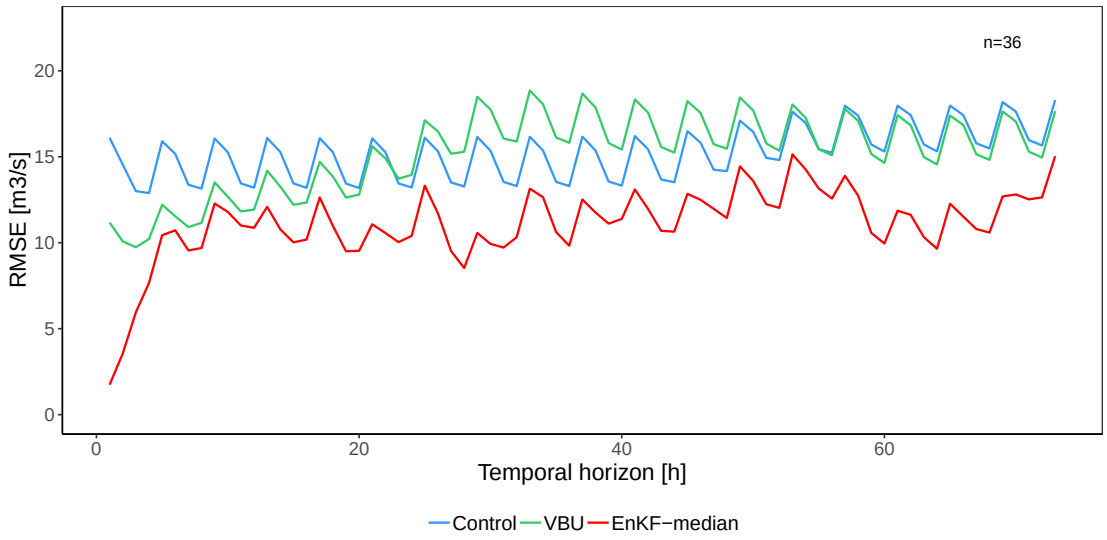

Figure 5.2 – RMSE values obtained for the three approaches for the high flow event at the Reckingen station on the Rhône River. The n value indicates the number of forecasts considered in the computation of the RMSE value for each forecast horizon.

The Kling-Gupta efficiency for the three methods has been computed over the 3 days of forecast (Figure 5.3). Each point of the figure corresponds to the KGE value obtained over one forecast for the concerned period of 24 hours. Results obtained with EnKF-median outperform the two other methods over all three time intervals, in particular in terms of median values. However, EnKF also shows some points with weak KGE values.

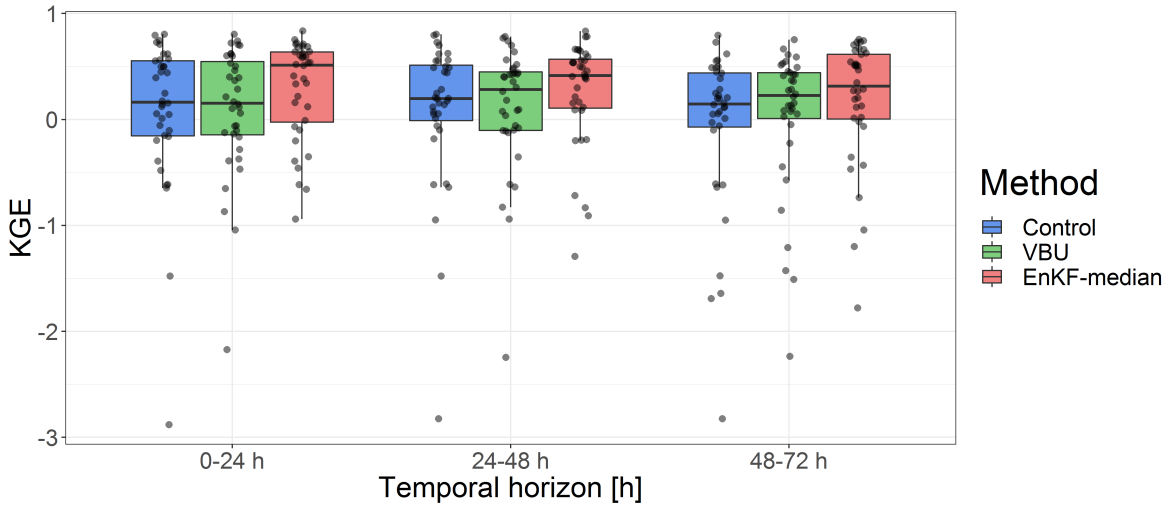

Figure 5.3 – KGE values obtained for the three approaches for the high flow event at the Reckingen station on the Rhône River. Each point corresponds to the KGE value obtained over the studied period (1-24,25-48,49-72h).

One limitation of the implemented EnKF solution is the high variability of the assimilated initial conditions resulting from the assimilation being based only on the unique last available discharge data. If the model does not reproduce adequately the timing of the observed flood evolution, undesired updating can be generated. This is for example the case at the beginning of the studied event, where a sudden reduction in the observed discharge results in a reduction of the foreseen discharge (Figure 5.4). To remedy this over-reactiveness of the methodology, an adaptation of the implemented solution to consider more than one value could be explored, for example with a recursive ensemble Kalman filter [McMillan et al., 2013]. Furthermore, for the sake of transparency, the performance over the 4 days preceding the studied event is analysed in the three following figures (run *Reckingen before* in Table F.1 in Appendix F). Indeed, the performance of the implemented EnKF method has appeared to be less effective when applied to base flow. Figure 5.5 gives an example where the model is unable to well reproduce the daily variation amplitude of the observed discharge. The state variables update performed by the EnKF results in an underestimation of the observed discharge for a good part of the forecast.

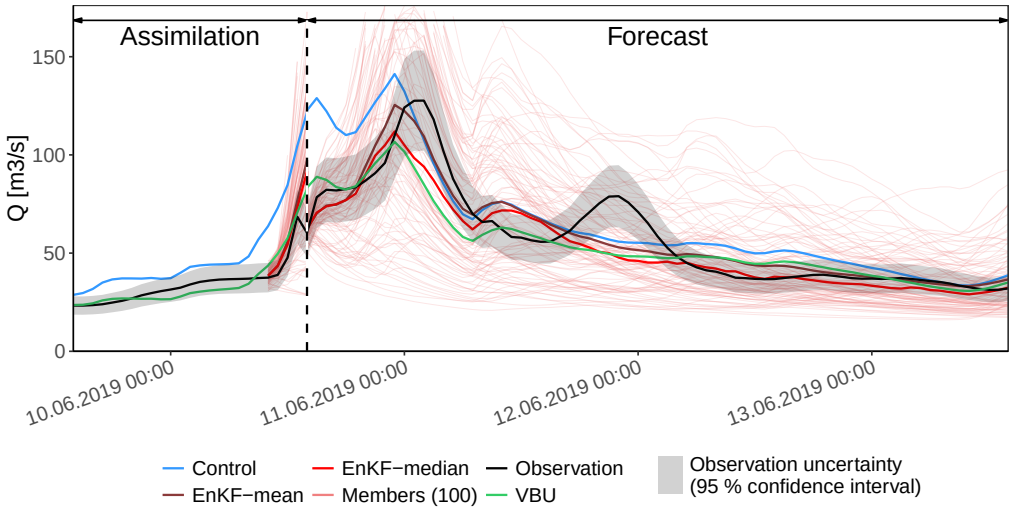

Figure 5.4 – Forecasted discharges for the three different approaches at the Reckingen station on the Rhône River. The dashed line corresponds to 2019-06-10T14+01:00.

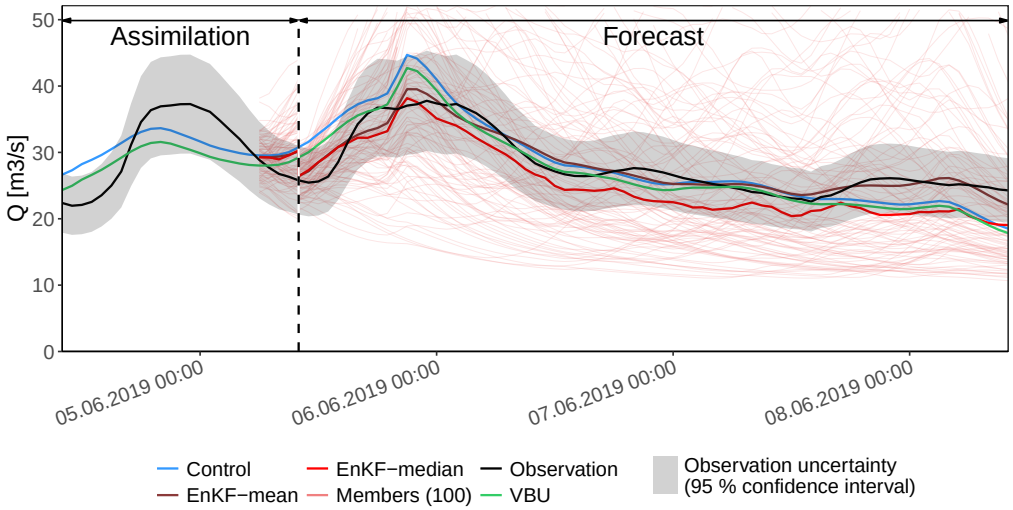

Figure 5.5 – Forecasted discharges for the three different approaches at the Reckingen station on the Rhône River. The dashed line corresponds to 2019-06-05T10+01:00.

Figure 5.6 and Figure 5.7 provide the RMSE and KGE figures over the same 4 days preceding the high flow event. Performances of the EnKF are in that case much more discutable, except over the first 10 hours of forecast for RMSE where it provides best performance.

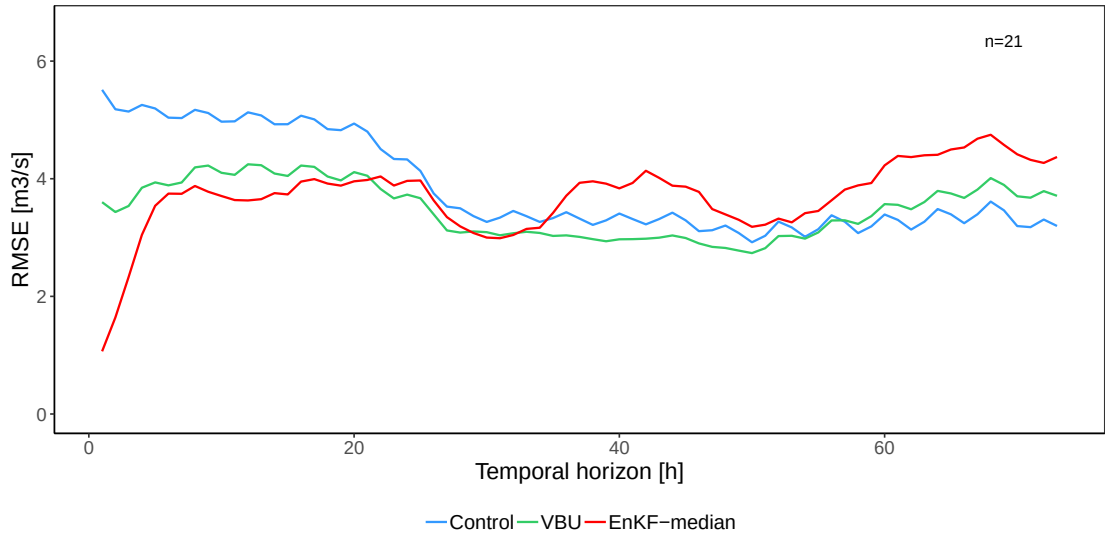

Figure 5.6 – RMSE values obtained for the three approaches over the 4 days preceding the high flow event at the Reckingen station on the Rhône River. The n value indicates the number of forecasts considered in the computation of the RMSE value for each forecast horizon.

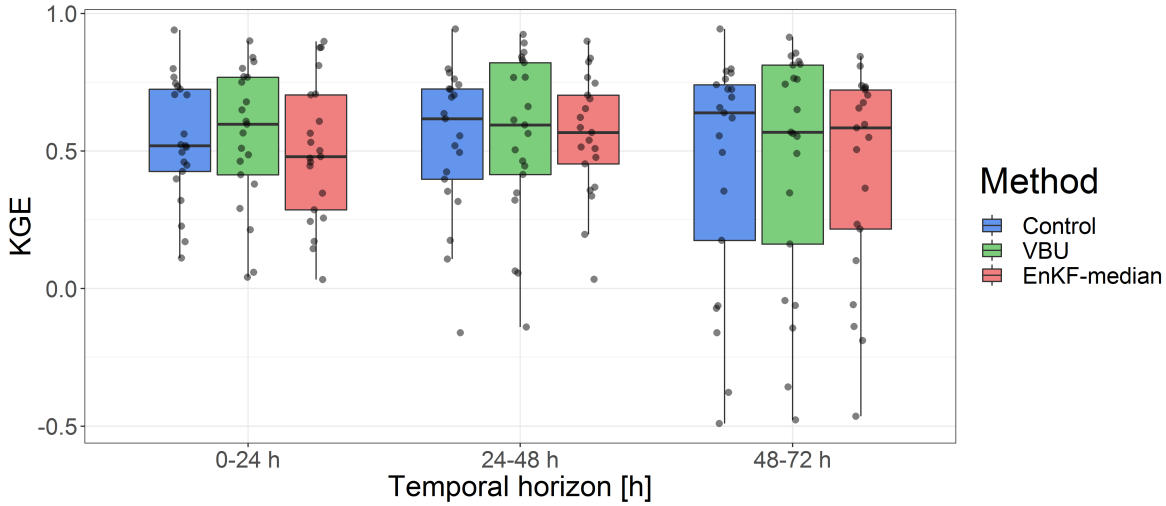

Figure 5.7 – KGE values obtained for the three approaches over the 4 days preceding the high flow event at the Reckingen station on the Rhône River. Each point corresponds to the KGE value obtained over the studied period (1-24,25-48,49-72h).

These results show the importance of the model calibration. Without a high-quality model calibration, updating model state variables can result in undesired correction and worse forecast performances for forecast horizons higher than a few hours. In the case of Reckingen, daily variations of the discharge linked to snow and ice melt should be particularly improved in the model. Alternatively, updating the model parameters within the EnKF, not explored in this research, could also be investigated.

5.4.2 Results over the Grande-Eau catchment

Over the second studied high flow event, over the Grande-Eau basin, both the VBU and EnKF approaches provide performance similarly good to the Control simulation during the event (Figure 5.8).

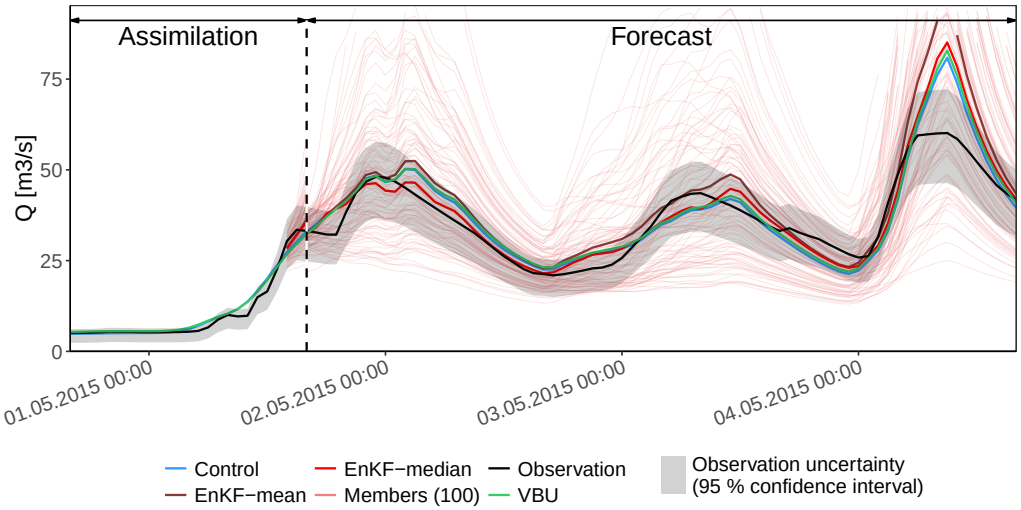

Figure 5.8 – Forecasted discharges for the three different approaches at the Aigle station on the Grande-Eau River. The dashed line corresponds to 2015-05-01T16+01:00.

However, when looking at the performance over the entire event (i.e. including the forecasts generated during the three days preceding the event), the Control simulation performs best for forecast horizons higher than 20 hours (Figure 5.9), followed by EnKF and finally VBU. Over the first 20 hours of forecast, EnKF performs slightly better than Control. Similar conclusions can be inferred from the KGE performance obtained over the three days of forecast (Figure 5.10). The good performance of the Control simulation results from the good capacity of the model without any correction to reproduce the observed discharge over the studied event. In that context, improving the performance or at least avoiding decreasing it with data assimilation methods is a real challenge.

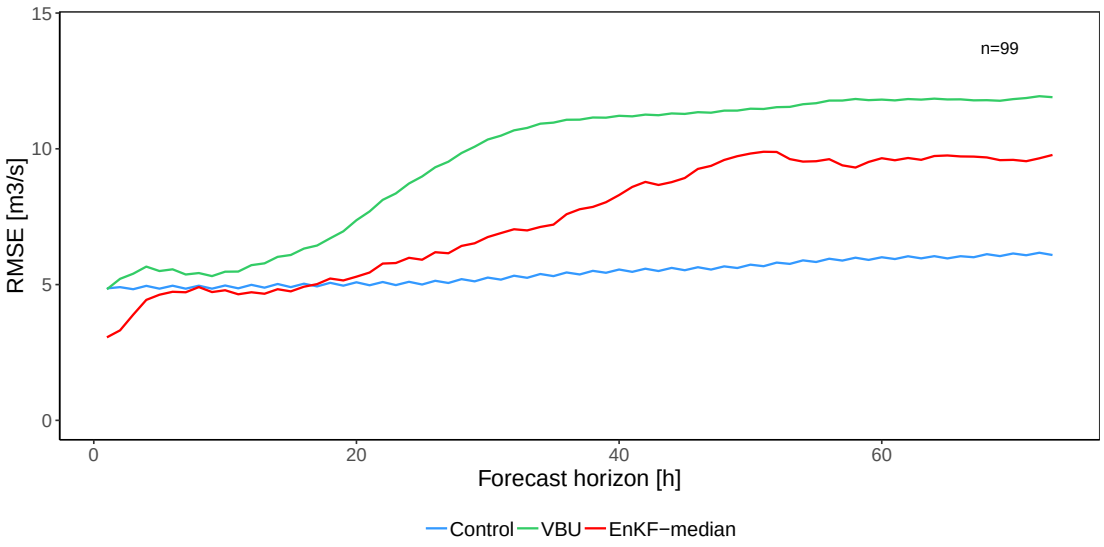

Figure 5.9 – RMSE values obtained for the three approaches for the high flow event at the Aigle station on the Grande-Eau River (assimilation was performed from 2015-04-28T20+01:00 to 2015-05-06T06+01:00). The n value indicates the number of forecasts considered in the computation of the RMSE value for each forecast horizon.

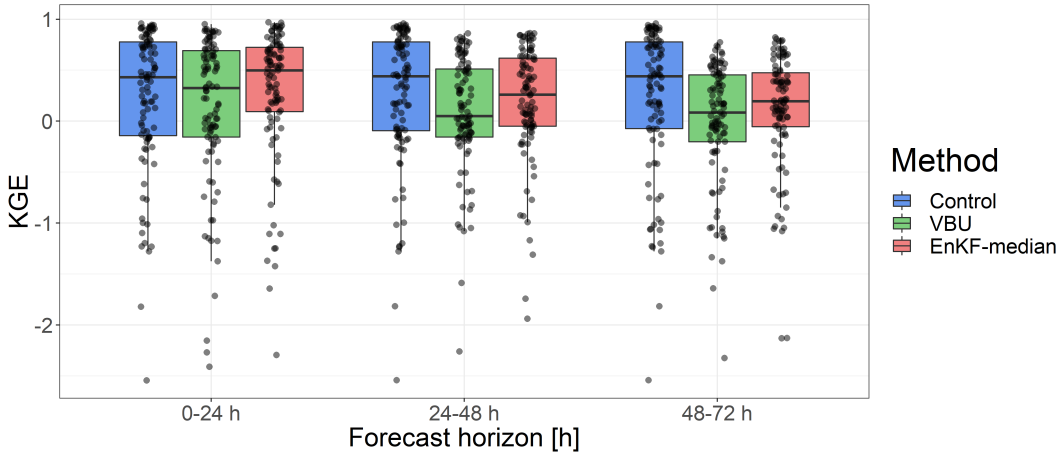

Figure 5.10 – KGE values obtained for the three approaches for the high flow event at the Aigle station on the Grande-Eau River. Each point corresponds to the KGE value obtained over the studied period (1-24,25-48,49-72h).

The lower performance of the VBU and EnKF methods as compared to the Control results from the fact that when applying the data assimilation methods on the base flow, both VBU and EnKF methods fail in well forecasting the discharge increase during the high flow event by highly overestimating the discharge (Figure 5.11). This overestimation is here mainly linked to the external water (from the Lac d'Arnon) turbined in the upstream part of the basin. Exclu-

sively operated during low flow periods to increase the available discharge for the downstream turbines, the relative impact on the base flow is considerable. Over the studied event, the external input results in an increase of the observed discharge from 6.2 m^3/s to 9.8 m^3/s (+3.6 m^3/s), which represents an artificial increase of the natural discharge of 58%. Other rapid increases and decreases over the days preceding the event vary between 3 and 4 m^3/s. No clear explanation could be found for the intensity of these discharge variations, as the official release capacity at Les Diablerets is 1.75 m^3/s and the uncertainty on the observed discharge estimated to less than 5% (E. Lehmann, Swiss Federal Office For the Environment, personal communication, June 17, 2019). This will need to be better analysed and will have to be considered for future development of the above presented EnKF methodology implementation.

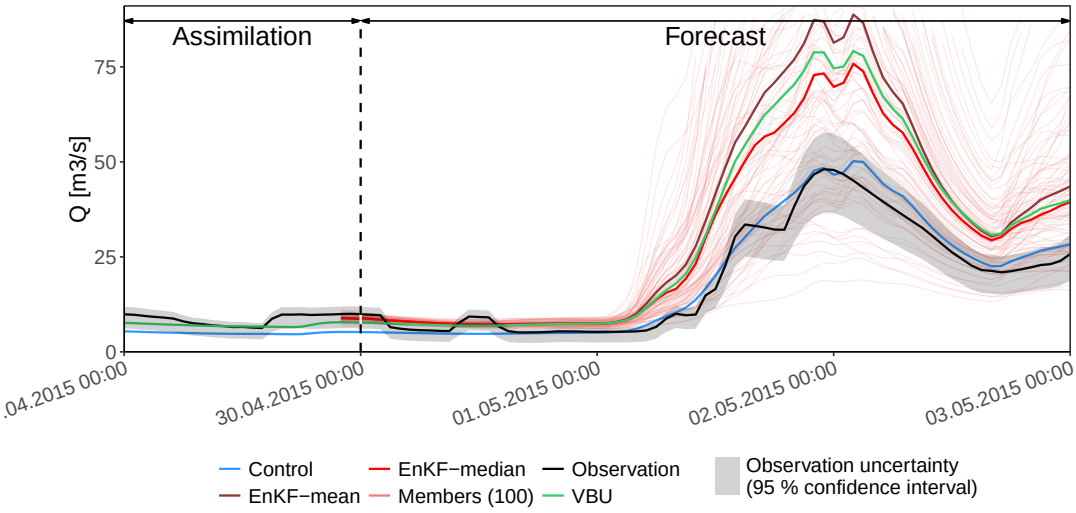

Figure 5.11 – Forecasted discharges for the three different approaches at the Aigle station on the Grande-Eau River. The dashed line corresponds to 2015-04-30T00+01:00. The variations of the observed discharge (black line) are due to hydropower water releases.

For the VBU approach, the external water discharge implies an increase in the soil water content to try to reproduce the observed discharge through a higher water release from the infiltration reservoir. The longer the operation of the turbine over the last 24 hours, the more VBU will tend to increase the soil saturation. For the EnKF approach, the model reaction slightly differs, mostly due to the consideration of the external input in the approach, by modifying the observed discharges with the turbine capacity for 50% of the members. When the observed discharge includes external turbined water, an overestimation is also observed in the forecasted discharge, even though it tends to be less extreme than the one of VBU (see Figure 5.11). On the contrary, when the turbine is not operating (i.e. the observed discharge corresponds to the natural discharge), the scheme tends to underestimate the observed discharge in the forecast, due to the discharge correction.

Considering the above observations, the computation has been run again starting the assimilation after the last hydropower perturbation of the base flow preceding the high flow event (run *Grande-Eau short* in Table F.1 in Appendix F). For this run, no discharge correction for hydropower contribution was considered (γ of Equation 5.18 equals 0 m^3/s). Figure 5.12 gives the RMSE values over this shorter period of analysis. EnKF performs best over the few first hours. Then Control again gives best results up to about 30 hours of forecast. For higher forecast horizons, Control and EnKF lead to similar errors. VBU leads to the weakest performance over the entire event, mainly because over the first forecasts, VBU still suffers from the overestimation resulting from the external hydropower inputs, as the analysis period if much longer (24h) for the VBU than for the EnKF (2h).

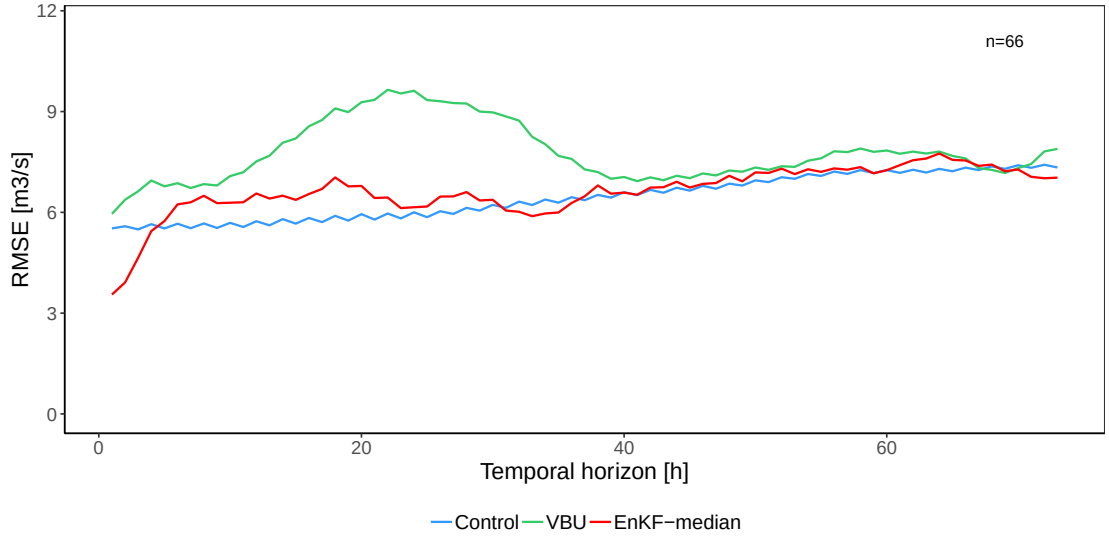

Figure 5.12 – RMSE values obtained for the three approaches for the high flow event at the Aigle station on the Grande-Eau River considering forecasts only during the event (the first forecast is done after the latest hydropower input from the external reservoir). The n value indicates the number of forecasts considered in the computation of the RMSE value for each forecast horizon.

5.5 Discussion

Results show that the implemented solution to account for hydropower perturbations with a modification of the observed discharge for 50% of the members is not efficient. This issue will need more investigation to come to a robust solution. Ideally, real data from the turbine injecting the external water would be integrated directly in the model at the location of the hydropower plant to reduce this high source of uncertainty. Thereby, the forecasting performance would certainly be higher.

Furthermore, the importance of correct base flow discharges is also true for the simulation. If the model is not able to well reproduce the base flow, correction by the EnKF model might result in large over- or underestimation of the high flow events as a result of an inadequate correction of the soil water content and other state variables. Implementation of the presented methodology should therefore be considered only on basins with a robust calibration. Structural changes in the hydrological model used in the MINERVE system might also be necessary to reach a level of robustness sufficiently high for safe application of an ensemble Kalman filter.

In addition, the performance related to the update of the SWE variable for both GSM and SOCONT models, not addressed here, remains an open question. The relation between SWE and discharge existing only during snow melt occurrence, it is not clear how the EnKF will perform during the snow melting season and even more importantly at its end. However, with a precipitation input perturbed over the different members, the snow amount within the members can largely differ. Thereby, the variable will have to be updated in some way.

Finally, the methodology should be applied to other events and on other catchments to analyse the results on a larger sample as well as larger scale. Future investigations might also explore other configuration parameter values for the a priori values used in the present study, for example about the number of members, the intensity of initial conditions perturbation before the first assimilation, the intensity of precipitation, temperature and discharge perturbation as well as the time interval between assimilation.

5.6 Conclusions

Two data assimilation methods are explored in this study to improve the initial conditions of the model state variables with the objective of improving the quality of hydrological forecasts. They are compared with the reference scenario working without data assimilation (Control). The first method updates the soil saturation based on a volume-based update (VBU) over the 24 hours preceding the forecast. The second is an implementation of an ensemble Kalman filter (EnKF). The semi-distributed conceptual hydrological models GSM and SOCONT are used for the simulations.

The methods are applied to two high flow events having occurred over two different catchments of the Upper Rhône River basin in Switzerland. Spatially interpolated precipitation data in combination with temperature data observed at stations are used both for the assimilation and forecast parts. The performance is evaluated with the Root Mean Square Error (RMSE) at hourly forecast horizon up to 72 hours and the Kling-Gupta efficiency over three periods of 24 hours.

The results differ over the two basins. Over one basin, the EnKF provides on average clearly the best RMSE performance over the entire forecast horizon (72 h). Up to one day of forecast, the VBU outperforms the Control approach. For higher forecast horizons, Control and VBU

perform somehow similarly.

Over the second basin, the results are relatively different. The best performance is obtained with the Control simulation, owing to a good reproduction of the observed discharge by the simulation without any correction. The low performance of the data assimilation approaches is explained by the impact of the water injection through a turbine from a reservoir external to the basin, considerably impacting the observed base flow with changes exceeding 50% of the natural base flow and thereby directly affecting the data assimilation methods. The effective turbine operation data not being available to the system, the data assimilation techniques fail to adequately forecast the flow during the studied event by highly overestimating it. When starting the analysis just few hours before the event with a natural observed discharge (no external inputs), the EnKF approach performs similarly to the Control and even outperforms it for the few first hours. This case highlights the importance of having access to timing of operations and transferred water volumes by hydropower schemes for discharge forecasts in strongly managed watersheds.

As demonstrated over the first event, the analysis revealed the EnKF tends to be somehow too reactive, particularly due to the analysis based only on the last available discharge data. This can be a problem in the case of temporal shifts, even small, between the simulation and the observation, in which case inappropriate corrections of the model can occur. Further developments might explore considering more than a single value for the assimilation, in a concern of robustness. Adapting the implemented solution for example to a recursive ensemble Kalman filter (REnKF), as presented by McMillan et al. [2013], could be explored.

We also showed that when applying EnKF on base flow periods with a model for example not able to well reproduce the daily melt amplitude, updating performances tend to be lower. This finding supports that state variables updating with EnKF should be applied only to catchments with a model able to well reproduce the different hydrological processes. In that perspective, a reassessment of the hydrological model used within the MINERVE system will probably have to be undertaken in a next step of development to investigate structural changes of the model with possible changes in the approach.

Finally, the different issues revealed in this chapter in relation to the implementation of an ensemble Kalman filter for the MINERVE operational system also show that this task is not easy. With the discharge in most of the rivers in the Upper Rhône River basin being modified by hydropower schemes (to a larger extent than the two catchments presented here), the implementation over the entire basin will consist a big, but exciting challenge. And this will not only require further development by engineers, but as shown above, also a larger access to hydropower operation data to feed the system. In the interest of population and infrastructure security.

Acknowledgments

I would like to thank Charles de Broglie and Anne Schwob, who contributed in the development of the data assimilation code used in this work during their internship and Master thesis at the Laboratory of Hydraulic Constructions. My thanks also go to Dr. Damiano Pasetto, from the Laboratory of ecohydrology, for his support in the theoretical development of this chapter. I would like to thank also Hélène Monnard and Eugène Lehmann, from the Swiss Federal Office for the Environment - Hydrology Division, for their answers to my questions about the hydrometric stations. Finally, Andy Kaufmann, from Romande Energie, is also acknowledged for having answered my questions about the Grande-Eau hydropower scheme and for the information provided about monthly estimated turbined volumes.

6 Conclusions and Outlook

6.1 Overview

This dissertation focuses on meteorological and hydrological processes taking place in Alpine environments. The study is based on the work having been achieved within the MINERVE project, initiated in 1999, which aimed at developing a flood forecasting system for the Upper Rhône River (URR) basin upstream of Lake Geneva, in Switzerland. One of the main output of the MINERVE project has been the implementation, in 2013, of an operational flood forecasting and management system for the Canton of Valais. Based on the experience of this system and the challenges faced in its application, three main research axes have been identified and investigated in the present thesis.

In Chapter 2, the combination of weather radar data with multiple rain gauge networks is investigated to propose a high-quality spatial product of precipitation over the basin. The installation of a new weather radar within the URR basin, at Pointe de la Plaine Morte in June 2014, half a year before the start of the present project, represents a new source of data and offers a terrain for exploration. The proposed regression co-kriging methodology enables the consideration of data from two non-collocated rain gauge networks composed of sensors of different quality, in combination with weather radar data. The SwissMetNet (SMN) network of MeteoSwiss is used as primary network and the network of the private company MeteoGroup Switzerland AG (MG) as secondary network. It even allows integration of data from additional networks, the interpolation being decomposed in three successive steps: (a) computation of a linear regression between the hourly radar data and the data from stations to define a spatially-constant multiplying correction factor to be applied to the radar data to get the so-called drift; (b) the computation of the linear model of co-regionalisation (variograms); c) the computation before interpolation of the residuals, given by the difference between the drift and values at stations. For each step, the networks to be considered can be different, enabling the integration of additional networks in combination with one of the two main networks. The results of the interpolation suggested that regression co-kriging considering data from the SMN and MG networks provided the best quantitative precipitation estimates (QPE) for

the study area when compared to a series of well-established precipitation interpolation methods. The study showed that not considering the quality difference between the two networks resulted in problems of negative bias in the interpolated precipitation fields. This finding implies that incorporation of additional data from a network with different equipment can contribute to improve precipitation estimates, but requires an adequate interpolation method.

In Chapter 3, the focus is given to solid precipitation undercatch by rain gauges. Indeed, the integration of the QPE developed in Chapter 2 in a temperature-index snow model revealed a lack of precipitation as compared to ground-based snow water equivalent (SWE) measurements. This issue being notoriously known, it is however only rarely considered before QPE computation. A transferable methodology to account for solid precipitation undercatch by rain gauges in QPE computation is therefore proposed. Four different QPE products are tested as input to a temperature-index snow model. These include: (1) the operational rain gauge-radar merging *CombiPrecip* product of MeteoSwiss; (2) the output of the rain gauge-radar merging co-kriging regression methodology presented in Chapter 2; for (3) and (4) the same QPE product as in (2) has been computed with a correction of solid precipitation by a factor of respectively 1.2 and 1.3, applied before the interpolation. Temperature data is taken from a spatial product computed with a kriging with external drift (KED) using elevation as drift. The degree-day factor (DDF) parameters of the snow model are calibrated based on the reproduction of the presence or absence of snow given by a snow-covered area product provided by the satellite-based spectroradiometer MODIS; thereby, the model is calibrated without using ground-based snow observations, making it applicable at catchment scale. Ground-based SWE observations from 11 snow-monitoring sites are used only after calibration for performance assessment. The results revealed that the simulations with the two QPE products accounting for solid precipitation undercatch clearly yield a better reproduction of the ground-based observed SWE values. The lowest absolute error was obtained with the QPE including a correction factor of 1.2. Another important conclusion is that the integration of a seasonal variation of the DDF values allows a better reproduction of the presence or absence of snow over the year. Another interesting finding is that for two snow-monitoring sites, the entry in operation of the weather radar of Pointe de la Plaine Morte resulted in a considerable reduction of the computed precipitation over the pixels containing the sites. This undesired reduction results from the negative effect of the spatially heterogeneous visibility of the new weather radar in the spatial interpolation computation.

Different precipitation datasets are explored in Chapter 4 as input for calibrating the hydrological model of three sub-catchments of the URR basin. Considering precipitation at rain gauges as the base scenario, three QPE products are used: (1) the *CombiPrecip* product of MeteoSwiss, (2) the QPE product based on the developed co-kriging regression and (3) the QPE product with a solid precipitation correction by a factor 1.2. For the temperature, two different datasets are used: (a) measurements at the stations used with an inverse distance weighting method and a constant vertical lapse rate and (b) the spatial product based on KED, preliminary analyses having revealed possible issues with the spatial product at high

elevations. A decoupling of the model calibration is also explored, with a 2-phase approach: snow-melting parameters (DDF) are first estimated with the MODIS-based methodology presented in Chapter 3, before calibrating the other parameters based on discharge data. Results are compared to a conventional calibration exclusively based on discharge data. Estimated volumes over the catchments for the precipitation datasets revealed differences exceeding 10% over the calibration period (2014-2018, including the Pointe de la Plaine Morte radar data) and exceeding 35% over the validation period (2012-2014), highlighting the difference between the datasets. Results for the 11 explored configurations suggest that the proposed QPE product accounting for solid precipitation undercatch leads to the best performance in case of good radar visibility over the catchment. In case of lower radar visibility, using station data provided equal or better performances. This finding suggests that current weather radar estimates are an excellent tool for identifying zones receiving precipitation, but that the quantitative estimation in complex topography is not yet sufficient for hydrological applications, even after radar-rain gauge merging. Regarding the 2-phase approach, the currently-obtained performances tend to be better with the conventional approach. However, identified limitations in the implementation leave space for improvements that could increase the performance of the 2-phase approach. Finally, the parallel considerations of two temperature inputs confirmed a probable issue with the spatial product of temperature, better results having been obtained with the configurations using values reported by stations. The analysis also showed how the parametrization can compensate for possible lack of precipitation by a faster snow melt over glacial elevation bands to start earlier the ice melt, as well as higher ice melt factors to increase the ice melt contribution. Such compensation by the parametrization can render results difficult to analyse and interpret.

In Chapter 5, the implementation of a data assimilation approach to improve the flood forecasting performance by updating the initial conditions used for the forecast is presented. The implemented solution is an ensemble Kalman filter (EnKF), in which an ensemble of model trajectories are analysed to update the initial conditions before each hydrological forecast. Performances are compared to the scenario working without data assimilation and a data assimilation approach operational since 2017 in the MINERVE system, based on a volume comparison over the 24 hours preceding the forecast. The application is done over two subcatchments of the URR basin, the second having the particularity of receiving water through a turbine from a reservoir external to the catchment. Forecasting errors are evaluated with the root mean square error for each hour up to 72 hours of forecast and the Kling-Gupta efficiency over three periods of 24 hours. Over the first event, having occurred in June 2019 over the Reckingen catchment, EnKF leads to the best performance over the entire forecasting horizon. However, the implemented solution is shown to be somehow too reactive as a result of updating the IC only on the unique latest discharge observation. Furthermore, when comparing the performance of the three methods over the 4 days preceding the event, EnKF outperforms the two other methods only over the first 24 hours of forecast. For higher forecast horizons, it results in the poorest performance. With the model not being able to well reproduce the daily streamflow variation amplitude, this finding shows the necessity of the model calibration

to be able to well reproduce the different hydrological processes. Over the second event, having occurred in 2015 over the Grande-Eau catchment, results show that application of the methodology on perturbed discharges is not straightforward and can result in inappropriate update of the IC, generating large over- or underestimation of the observed discharge during high flow events. This finding underlines the need for the operational forecasting system to have access to near real-time hydropower operation data to feed the system, in order to increase the reliability of the generated forecasts.

6.2 From station data to spatial data: a real challenge

As a result of the project objectives, the present research made the MINERVE system evolve to move from using data at meteorological stations to spatialized products with quantitative precipitation estimates as well as a spatialized product of temperature. This represented a challenge for many reasons. First, the quantity of data to store and manage increases substantially. This implies the set-up of an adequate database. Second, the simulations having been applied over many years with hourly data, the amount of data to extract and to combine into input files was in some cases considerable, with extraction by basin taking up to several hours despite the optimization efforts. Adequate extraction functions had to be developed, to take into account also the limiting capacity of the server hosting the database. These questions must not be underestimated when setting-up a project like the one presented in this dissertation.

Furthermore, working over a basin like the URR basin, with a complex topography and a large number of hydropower schemes, implies that the ideal catchment with a discharge free of any hydropower perturbation and with an excellent radar visibility does not exist. Mostly the beam shielding issue for radar data makes the analysis complex in such environments. The analysis work performed about the precipitation data offers the MINERVE system a better understanding of the available weather radar data and the implications of the new weather radar of Pointe de la Plaine Morte on the radar data quality over the Upper Rhône River basin. In addition, the performed data analysis also allowed to identify issues with missing data in the MeteoSwiss database, enhancing the data availability for the corresponding data user community.

6.3 Outlook

One strength of the present project has been the hydrological application for comparison purpose of different state-of-the-art quantitative precipitation estimates. In the Swiss context, such type of applications remain limited. Combining meteorology and hydrology is for example particularly important for the rain gauge undercatch issue, that needs coupling of both to properly analyse the problem. More projects should tackle in the future meteorology and hydrology together.

The most interesting research axes for future developments identified during the project are listed and detailed hereafter.

- The spatial product of temperature developed in the project received much less attention than the spatial interpolation of precipitation. The application to hydrological models of the developed spatial product of temperature revealed that spatial interpolation of temperature in Alpine catchments is not straightforward. Further development is necessary to get a robust product of temperature valid for the entire URR basin elevation. Application of cross-validation will allow to quantify errors associated to the interpolated temperatures, not yet available for the current product.

- In the use of radar-rain gauge merging over Switzerland, the highest improvement potential seems to exist mainly in the correction of the weather radar estimates in particular for correcting beam shielding effects. In that perspective, a map of radar data quality would help to identify zones not well covered by the Swiss weather radar network.

  In terms of rain gauges, a promising supplementary source of data could be the recomputed precipitation time series at monitoring stations from the Intercantonal Measurement and Information System (IMIS), equipped with unheated rain gauges. Using the SNOWPACK [Bartelt and Lehning, 2002] model and measurements from the different sensors of IMIS stations including snow height, series of precipitation accounting for liquid and solid precipitation can be computed. If the quality of the series is high enough, this would provide precipitation measurements at elevation today very poorly covered in Switzerland (up to more than 3300 m a.s.l.).

- The solid precipitation undercatch correction proposed in this study considers fixed correction factors, though undercatch is well known to be highly influenced by wind speed. Future developments might explore considering the wind-speed at rain gauges to propose a finer correction of the undercatch with an hourly analysis by station, for example by using recently developed "transfer functions" [Kochendorfer et al., 2017]. This could have a significant effect in particular for wind-exposed meteorological stations. However, not all meteorological stations used in this study being equipped with a wind-speed sensor, this application will not be straightforward.

- Using these enhanced products of precipitation and temperature, further efforts will be necessary on the model calibration:

  – The degree-day factors calibration based on MODIS data should be further investigated. One of the main highlighted limitation was the use of the overall accuracy as performance metric, which results in varying performance depending on the elevation range. Exploration of performance metrics less-dependent on the snow-covered period could help for the application at catchment scale of the approach. Alternative to the MODIS product could also be explored. The Swiss Institute

for Snow and Avalanche Research SLF generates for example a map of SWE over entire Switzerland, named *Operationellen schneehydrologischen Dienst*, based on a combination of measurements and simulation. This product was not used for the present research mainly because it is based on a different precipitation product (RhiresD) of MeteoSwiss, which would have highly complicated the analysis due to high differences between RhiresD and QPE based on radar data, including *CombiPrecip*.

- The entire MINERVE hydrological model should also be recalibrated. Indeed, a change in the input requires an adaptation of the hydrological model's calibration. The following prerequisites could help to obtain a more robust calibration:
  - Turbine operation data: With most of the main subcatchments of the URR basin being affected by hydropower operations, access to turbine operation data for the calibration of the model is important. Conventions with the main stakeholders should be signed to formalize this data exchange.
  - GSM and SOCONT models enhancement: The calibration work performed during the project revealed some probable limitations in the GSM and SOCONT model structures. In particular for the GSM model, reproducing the snow and ice melt with both correct timing and daily variation amplitude proved to be very difficult. Complexifying the structure of the models, with additional reservoirs, could possibly help to better reproduce the observed discharge.
  - Ice melt quantification: The ice melt contribution should be quantified. In the present work, the volume of precipitation for each input dataset is quantified, enabling a comparison between the different precipitation inputs. Quantitative estimation of ice melt resulting from the calibration of the different configurations would allow, in combination also to a quantification of the volume corresponding to evapotranspiration, a complete picture for the water mass balance over the catchments.
  - New performance metrics: Developments remain also possible in terms of performance metrics. In Chapter 4, the need in RS MINERVE of an indicator looking for similar peak flow values between the simulation and observations accepting for short temporal shifts was for example mentioned.
- More fundamental changes might also be investigated in the future for the MINERVE system, to make the system evolve to more up-to-date modelling tools, for example to benefit from the increasing available remotely sensed data for the calibration.

- The EnKF methodology implementation presented in this dissertation aimed at developing a first version of the future MINERVE updating method. Several aspects will have to be further developed. This includes:
  - Performing a sensitivity analysis to propose a more robust configuration of the EnKF method. The ideal number of ensemble members to consider, as well as the the intensity of precipitation and temperature perturbation should be explored. The time interval between forecasts, corresponding to the propagation time between two analysis time steps, should also be clarified.
  - The performance of data assimilation approaches has been shown to be dependent on the calibration of the model. A possible alternative would be to update within the EnKF also the parameters, not explored here. Similarly to state variables update, parameters can be updated in the assimilation step (see for example Srikanthan et al. [2008]).
  - With the example of the Grande-Eau catchment and its external input issue, the ensemble Kalman filter as currently implemented showed to be unsuitable for application to perturbed observed discharges. If a real improvement in terms of hydrological flood forecasts over the URR basin is desired, conventions to be signed with hydropower stakeholders should also lead to near real-time delivery of turbining operation data.
  - A question that remains open concerns the performance of the implemented data assimilation methodology in relation to snow-melting. The relation between SWE and discharge being less straightforward than between soil saturation and discharge due to its temperature-dependence, more investigations will be needed to ensure robustness also at the end of the melting season.
  - Finally, the overractiveness of the currently implement methodology, resulting from the analysis being based only on the unique latest available value, should be further addressed. A possible solution mentioned earlier would be the adaptation of the code to a recursive ensemble Kalman filter [McMillan et al., 2013], in which more than one observation is considered.

A Acknowledgement to data providers

The meteorological data used within the project come from the SwissMetNet network of MeteoSwiss, as well as the networks of the private company MeteoGroup Switzerland AG, the Intercantonal Measurement and Informmation System (IMIS) from the Institute for Snow and Avalanche Research (SLF), Agrometeo, the Canton of Bern, Météo-France, Électricité de France, the Regione Autonoma Valle d'Aosta and the ARPA Piemonte. The radar data have been provided by MeteoSwiss. The SWE measurements were provided by the SLF. The MODIS data were downloaded from the National Snow and Ice Center website. The discharge data were provided by the Swiss Federal Office for the Environment. We thank all the different data providers.

B List of stations with coordinates

B.1 SwissMetNet meteorological stations

Table B.1 – SwissMetNet (SMN) stations within the basin used for the analysis. Elevation is given in m asl.

Station name	In the basin	Equipment	Data since	X Coord	Y Coord	Elevation
Aigle	Yes	Lambrecht	01.01.1981	560401	130713	381
Anzère	Yes	Ott	04.10.2010	597607	128205	1614
Arolla	Yes	Ott	05.10.2011	603504	95835	2000
Baltschiedertal	Yes	Ott	06.10.2010	633928	132421	1318
Barrage Grande Dixence	Yes	Ott	30.09.2011	597251	103584	2150
Bex	Yes	Ott	19.12.2012	565806	121511	402
Binn	Yes	Lambrecht	17.01.2014	657996	135422	1479
Blatten, Lötschental	Yes	Lambrecht	31.05.2013	629564	141078	1538
Blinnen	Yes	Ott	25.09.2013	663085	145404	1530
Bourg-St-Pierre	Yes	Ott	14.11.2013	581350	86251	1826
Bricola	Yes	Ott	05.10.2011	609887	99430	2440
Brig	Yes	Ott	16.10.2013	640567	129069	665
Bruchji	Yes	Ott	11.10.2012	641050	136500	2300
Champéry	Yes	Ott	27.10.2010	555392	112526	1055
Choëx	Yes	Ott	14.11.2013	563181	120189	896
Clusanfe	Yes	Ott	16.11.2011	557243	109534	1899
Derborence	Yes	Ott	11.10.2012	584115	126364	1380
Durnand	Yes	Ott	30.10.2012	572558	100091	1212
Emosson	Yes	Ott	17.11.2011	560664	101691	1923
Ergisch	Yes	Ott	16.10.2013	621396	126882	1133
Evionnaz	Yes	Lambrecht	06.12.2013	568190	114700	480
Evolène	Yes	Lambrecht	23.09.1986	605415	106740	1825
Fieschertal	Yes	Ott	09.02.2016	653990	142082	1175
Findelen	Yes	Ott	12.10.2011	626317	95547	2170
Fionnay	Yes	Ott	04.09.2013	589960	97765	1500
Grächen	Yes	Lambrecht	31.05.2013	630736	116062	1605
Grand-St-Bernard	Yes	Lambrecht	08.10.1981	579200	79720	2472

Grimsel Hospiz	Yes	Lambrecht	26.04.1989	668583	158215	1980
Isérables	Yes	Ott	11.10.2012	585332	112179	1237
Jeizinen	Yes	Ott	06.10.2010	621858	130808	1550
La Fouly	Yes	Ott	17.11.2011	573453	87284	1550
Les Collons	Yes	Ott	12.11.2013	596041	114169	1787
Les Marécottes/Salvan	Yes	Lambrecht	25.08.2015	567375	107577	990
Leukerbad	Yes	Ott	04.09.2013	614083	135090	1286
Mattsand	Yes	Ott	06.10.2010	627250	110279	1230
Moiry	Yes	Ott	29.09.2011	610169	109590	2127
Montagnier-Bagnes	Yes	Lambrecht	19.01.2017	583492	102189	839
Montana	Yes	Lambrecht	17.02.1981	601706	127482	1427
Mottec	Yes	Lambrecht	12.10.2015	614325	110730	1580
Nendaz Praz Mounet	Yes	Ott	11.10.2012	590166	107852	1938
Orsières	Yes	Ott	21.12.2012	577022	96695	929
Otemma	Yes	Ott	12.11.2015	596477	85864	2357
Saas Balen	Yes	Ott	06.10.2010	637837	110929	1535
Salanfe	Yes	Ott	16.11.2011	564020	110569	1880
Saleina	Yes	Ott	14.10.2010	573291	92777	1600
Sierre	Yes	Ott	12.11.2013	609073	127492	535
Simplon-Dorf	Yes	Lambrecht	28.10.2016	647683	116340	1465
Sion	Yes	Lambrecht	01.01.1981	591630	118575	482
Sorniot/Fully	Yes	Ott	30.10.2012	573849	112885	2005
Stafel	Yes	Ott	12.10.2011	618596	94805	2180
Trient	Yes	Ott	05.03.2013	565652	100027	1290
Tsanfleuron	Yes	Ott	11.10.2012	589461	129932	2052
Turtmann	Yes	Ott	29.09.2011	619600	113183	2180
Ulrichen	Yes	Lambrecht	17.02.1981	666740	150760	1346
Vercorin	Yes	Ott	07.10.2010	609075	120732	1650
Visp	Yes	Lambrecht	01.01.1981	631149	128020	639
Visperterminen	Yes	Ott	25.09.2013	635896	123602	1360
Zermatt	Yes	Lambrecht	02.12.1981	624350	97566	1638

Table B.2 – SwissMetNet (SMN) stations around the basin used for the analysis. Elevation is given in m asl.

Station name	In the basin	Equipment	Data since	X Coord	Y Coord	Elevation
Adelboden	No	Lambrecht	24.11.1983	609400	148975	1320
Airolo	No	Ott	20.12.2013	688910	153400	1139
Andermatt	No	Lambrecht	19.11.2013	687442	165034	1438
Château-d'Oex	No	Lambrecht	08.02.2012	577042	147645	1029
Göscheneralp	No	Lambrecht	16.10.2013	681250	166790	1745
Guttannen	No	Ott	16.01.2014	665296	167601	1055
Interlaken	No	Lambrecht	31.12.1980	633019	169093	577
Le Moléson	No	Lambrecht	21.09.1982	567723	155072	1974
Oron	No	Lambrecht	12.01.2012	555502	158048	827
Pully	No	Lambrecht	31.12.1980	540811	151514	456
Robiei	No	Lambrecht	20.12.1990	682588	144091	1895

B.2 MeteoGroup meteorological stations

Table B.3 – MeteoGroup (MG) stations used for the analysis. Elevation is given in m asl.

Station name	In the basin	Equipment	Data since	X Coord	Y Coord	Elevation
Binn	Yes	Davis	29.05.2009	656432	133389	1410
Eischoll	Yes	Davis	17.10.2008	626269	127515	1239
Fiesch	Yes	Davis	18.05.2007	653098	138628	1030
Finhaut	Yes	Davis	28.06.2008	564674	104020	1354
Gemmipass	Yes	Davis	13.01.2013	613411	138628	2347
Leysin	Yes	Davis	19.09.2007	568167	133865	1302
Martigny	Yes	Davis	19.09.2007	573247	106084	460
Nax	Yes	Davis	18.07.2008	600234	120372	1273
Oberwald	Yes	Davis	28.11.2012	669449	153868	1365
Orsières	Yes	Davis	05.12.2007	576898	97194	920
Ovronnaz	Yes	Davis	27.11.2009	578644	117197	1391
Randa	Yes	Davis	22.02.2008	626587	105449	1401
Riederalp	Yes	Davis	17.10.2008	644526	136405	2068
Saas Fee	Yes	Davis	06.11.2009	637541	106243	1790
Saviese	Yes	Davis	17.10.2007	594361	123705	998
Saxon	Yes	Davis	19.09.2007	579597	111799	465
Simplon Dorf	Yes	Davis	03.12.2009	647383	116403	1486
Simplonpass	Yes	Davis	19.11.2012	645161	121800	2000
Stalden, Ackersand	Yes	Davis	11.07.2008	633413	121324	699
Wasenalp, Simplon	Yes	Davis	03.06.2011	647224	125769	1960
Wiler, Lötschen	Yes	Davis	10.11.2008	626269	139104	1415
Zinal	Yes	Davis	28.11.2008	614363	109894	1661
Zwischbergen	Yes	Davis	06.06.2008	652241	112512	1360
La Chapelle-d'Abondance	No	Davis	20.11.2009	551393	125594	1027

B.3 SLF observation locations

Table B.4 – Coordinates of the SLF SWE observation sites in Swiss coordinates (CH1903 / LV03).

Short name	X Coordinate	Y Coordinate
1MI	555350	120700
4BP	582150	88300
4CR	565820	107630
4EG	636860	103090
4FY	589968	97778
4KU	651200	140610
4MS	663350	149125
4SF	637730	105951
4UL	666750	150765
4WI	626550	139340
4ZE	624200	96950

C Appendix to chapter 2

C.1 Events results for high precipitation events

This appendix provides additional results for the events studied in Chapter 2.

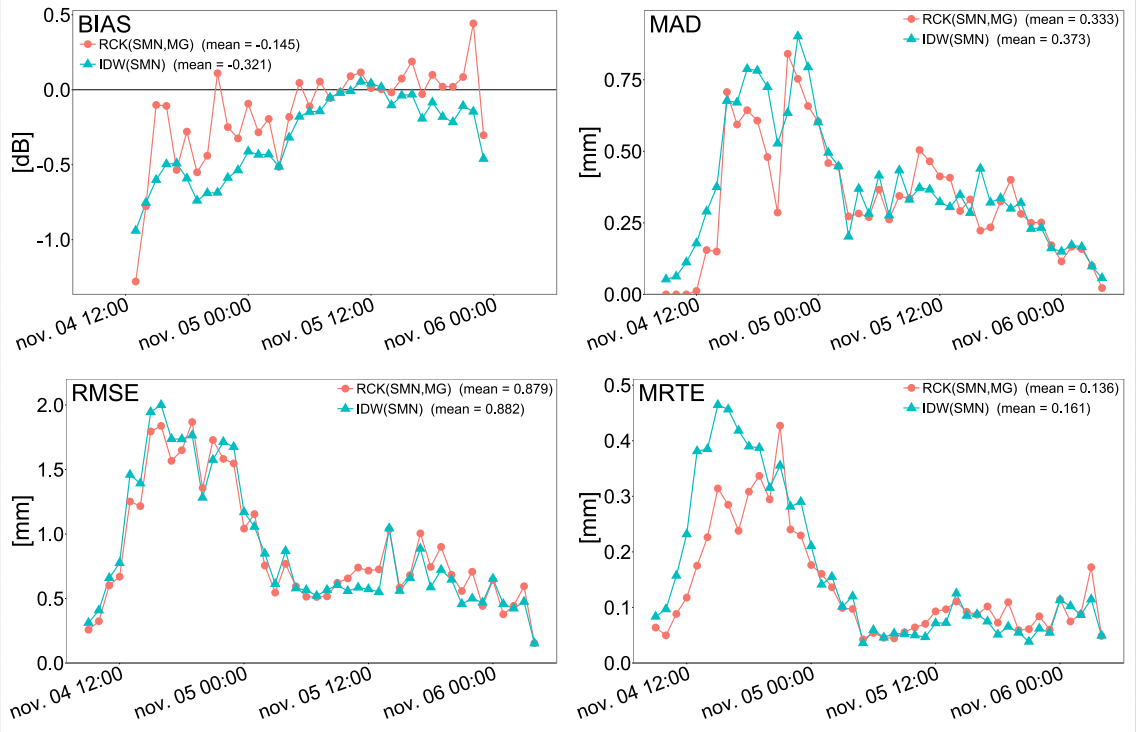

Figure C.1 – Hourly values of performance indicators for event 1 (November 2014).

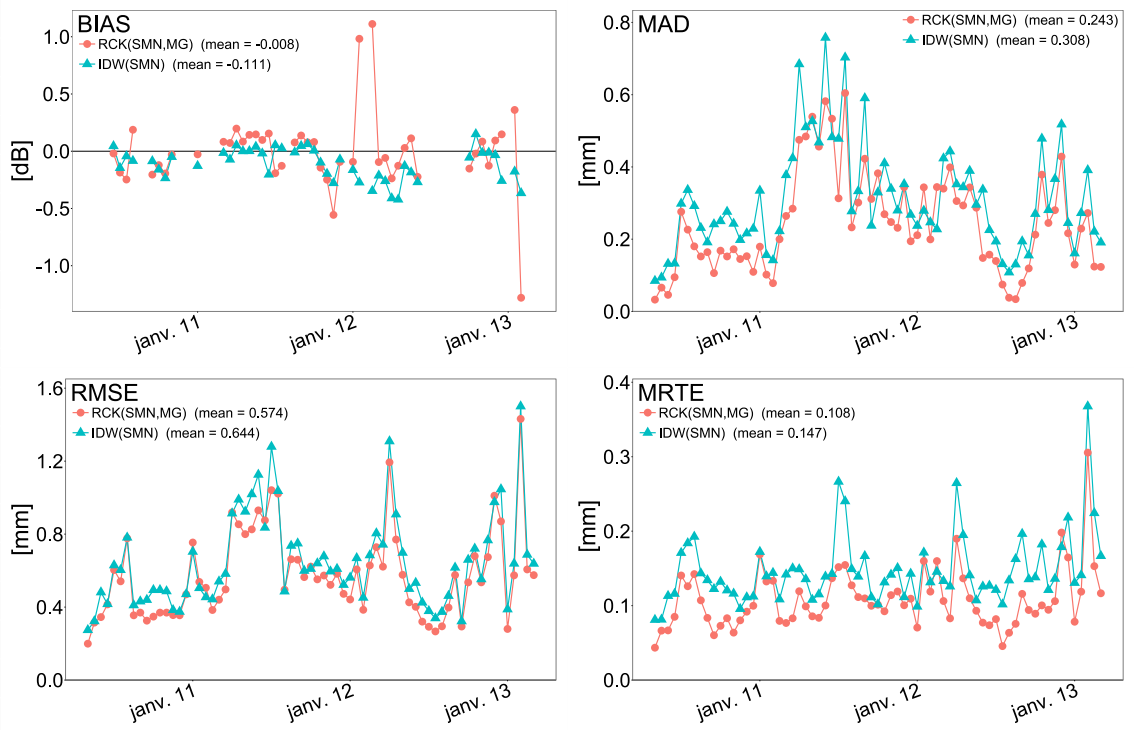

Figure C.2 – Hourly values of performance indicators for event 3 (January 2016).

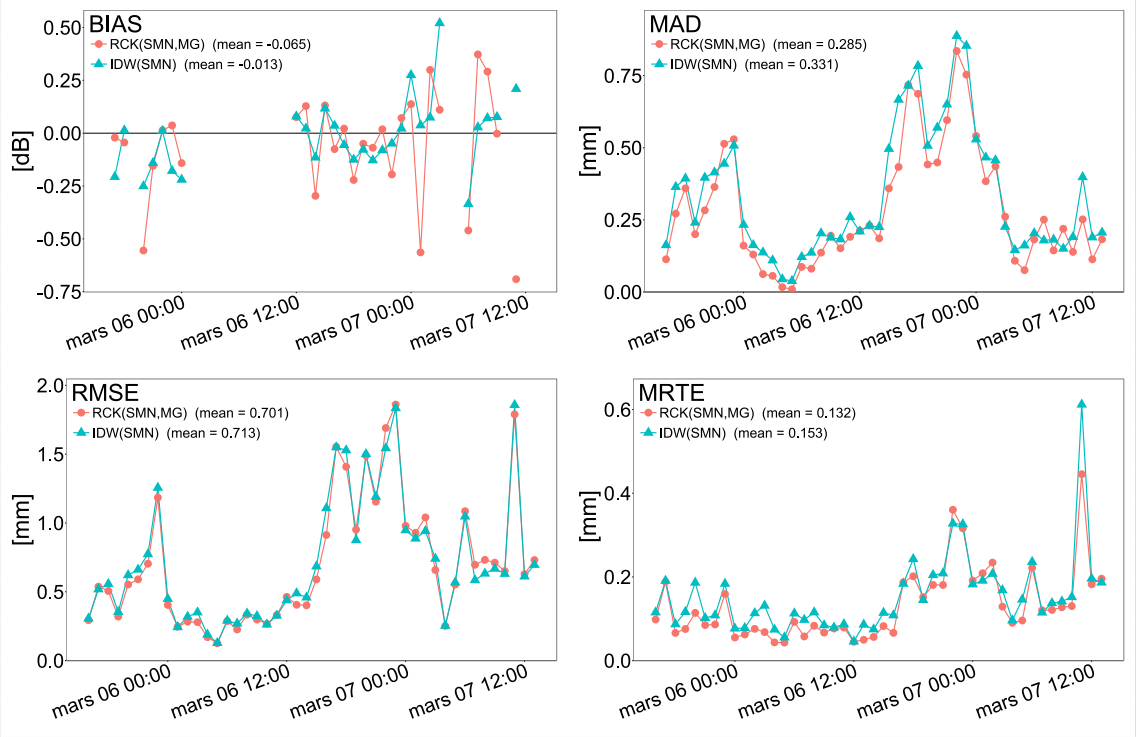

Figure C.3 – Hourly values of performance indicators for event 4 (March 2017).

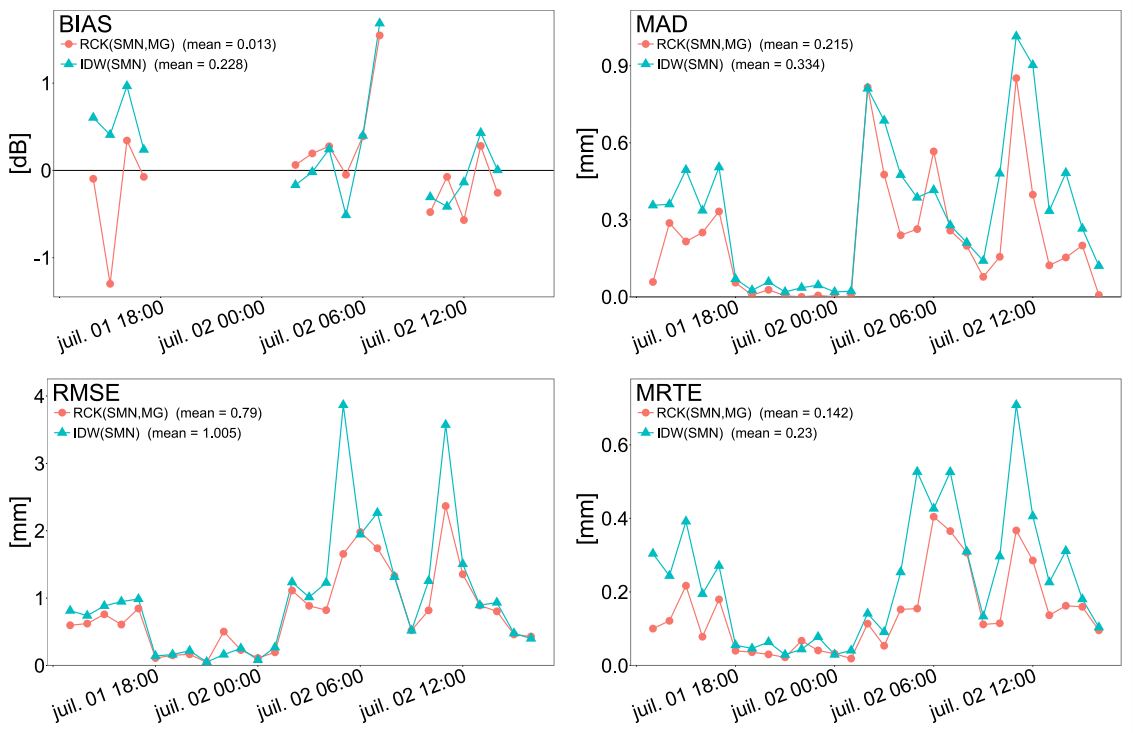

Figure C.4 – Hourly values of performance indicators for event A (July 2012).

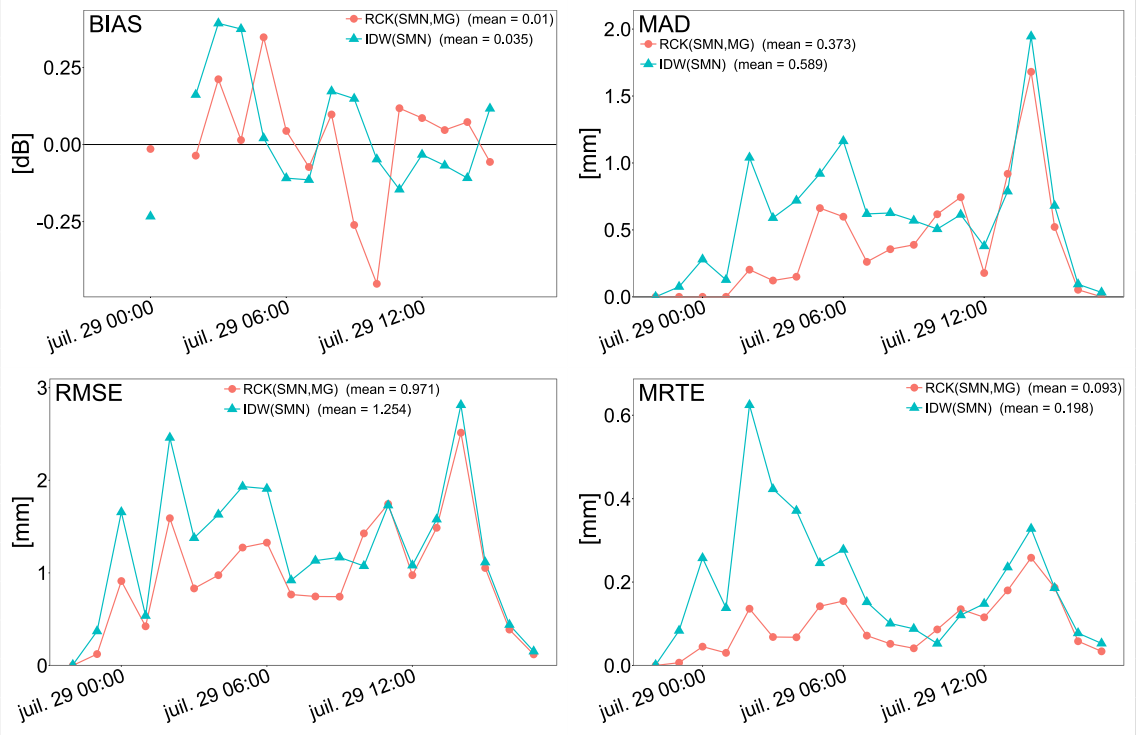

Figure C.5 – Hourly values of performance indicators for event B (July 2013).

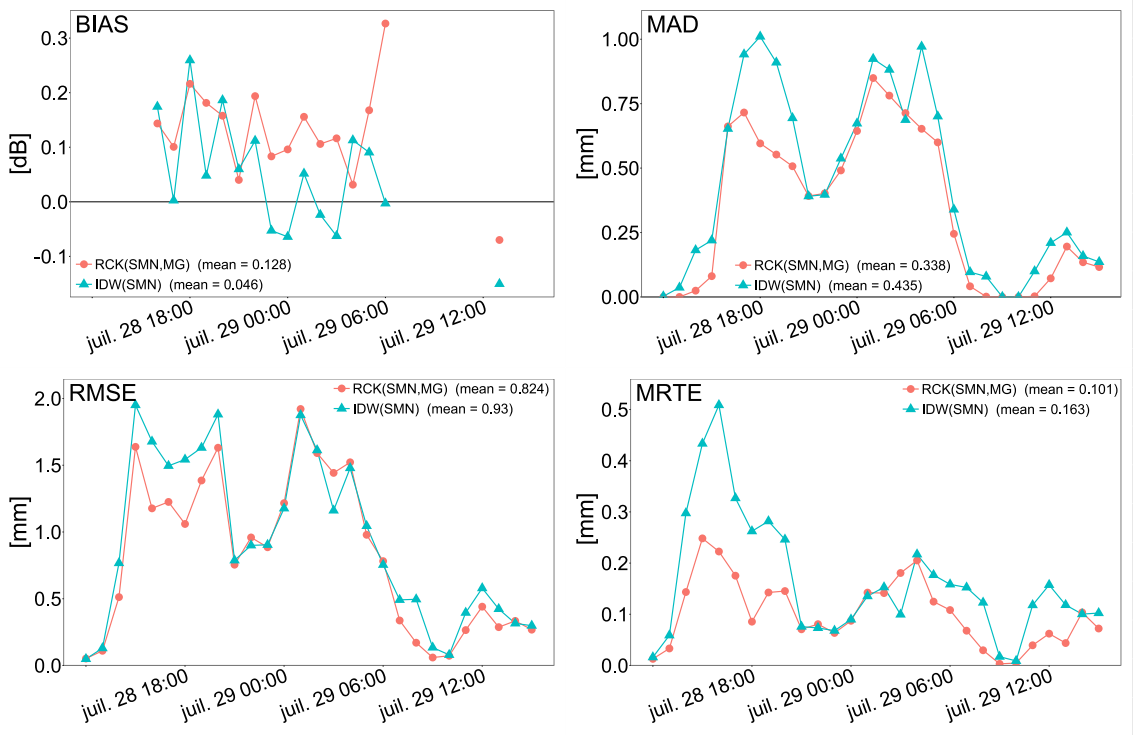

Figure C.6 – Hourly values of performance indicators for event C (July 2014).

D Appendix to chapter 3

D.1 Precision about the calibration

In the article, the calibration is presented as being computed only on time steps with available MODIS data. In reality, the software RS MINERVE computes the indicator on a regular time series. To do so, the observations are interpolated between the known data (observations). In order to compute the indicator only on the really available observed MODIS values, the values are modified before importation by applying a value of -1 to all the missing time steps. During the calibration process, using the object Planner in RS MINERVE, the same value is applied to the simulated values for the time steps without an observed MODIS data. In this manner, simulated and observed values of time steps without observed MODIS data are always transformed to 0 in the binarization and not affecting the calibration. Figure D.1 in Appendix D gives an illustration of the model. Finally, the Overall Accuracy values are recomputed in R after the calibration, based only on the time steps with MODIS data. These values are used in the figures presented in the paper.

D.2 Data management

The above presented work is based on several spatial products delivered as raster data. Working at the scale of a pixel requires the possibility of easily extracting time series for the pixel. All used data have been stored in a PostgreSQL database [PostgreSQL Global Development Group, 2018]. Extraction functions have been implemented with a Swagger API [SmartBear Software, 2018].

D.3 Supplementary figures

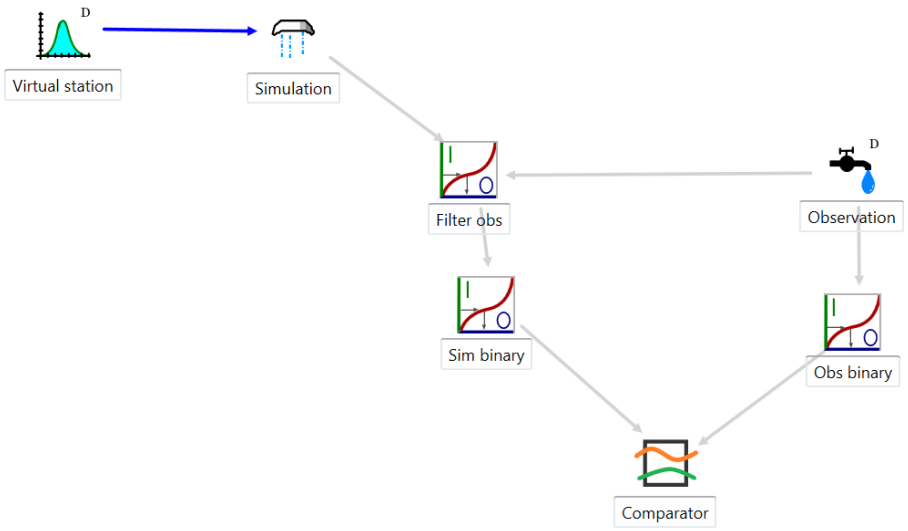

Figure D.1 – Illustration of the model used in RS MINERVE. The virtual (weather) station computes the temperature and ETP based on data available in the database. Using pre-processed observation data in which missing time steps were tagged as -1 (object 'Observation'), simulated values of corresponding time steps are replaced by -1 values (object 'Filter obs'). Observed values and filtered simulated values are then binarized by the objects 'Obs binary' and 'Sim binary'. During each simulation of the calibration process, the performance indicators are computed by the Comparator object.

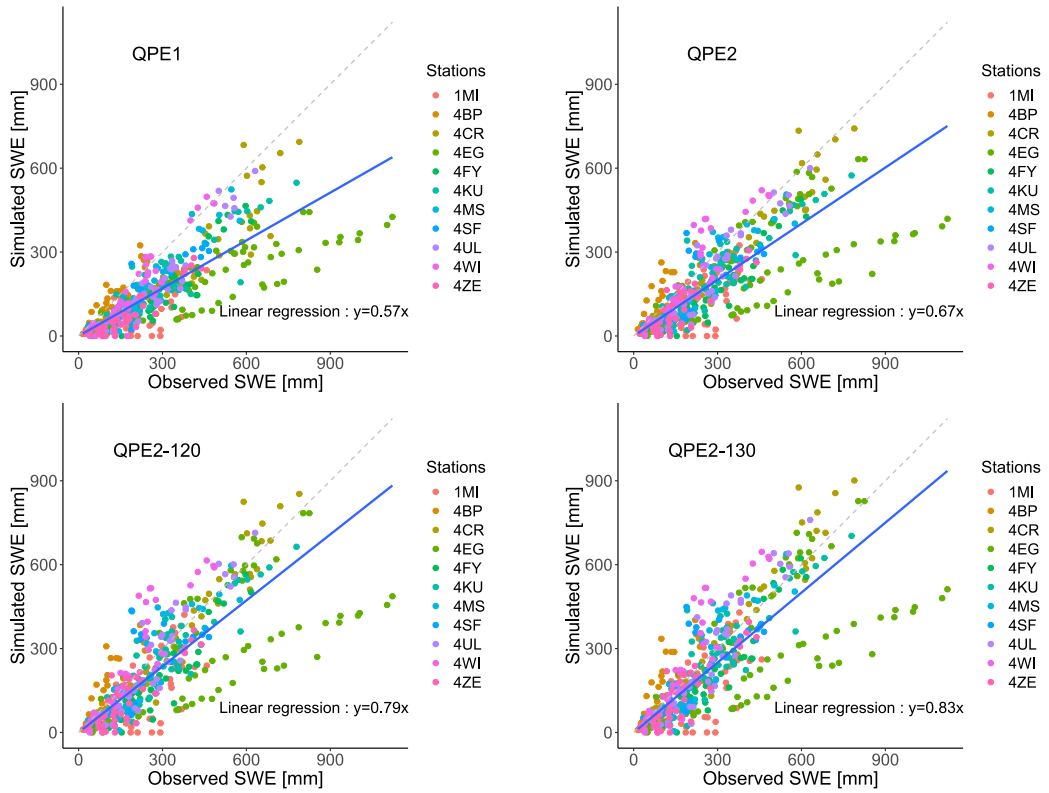

Figure D.2 – Simulated vs. observed SWE at the 11 locations for the four different QPE products ($\Delta = 2$). The grey dashed line indicates a slope of 1. Number of points: 469.

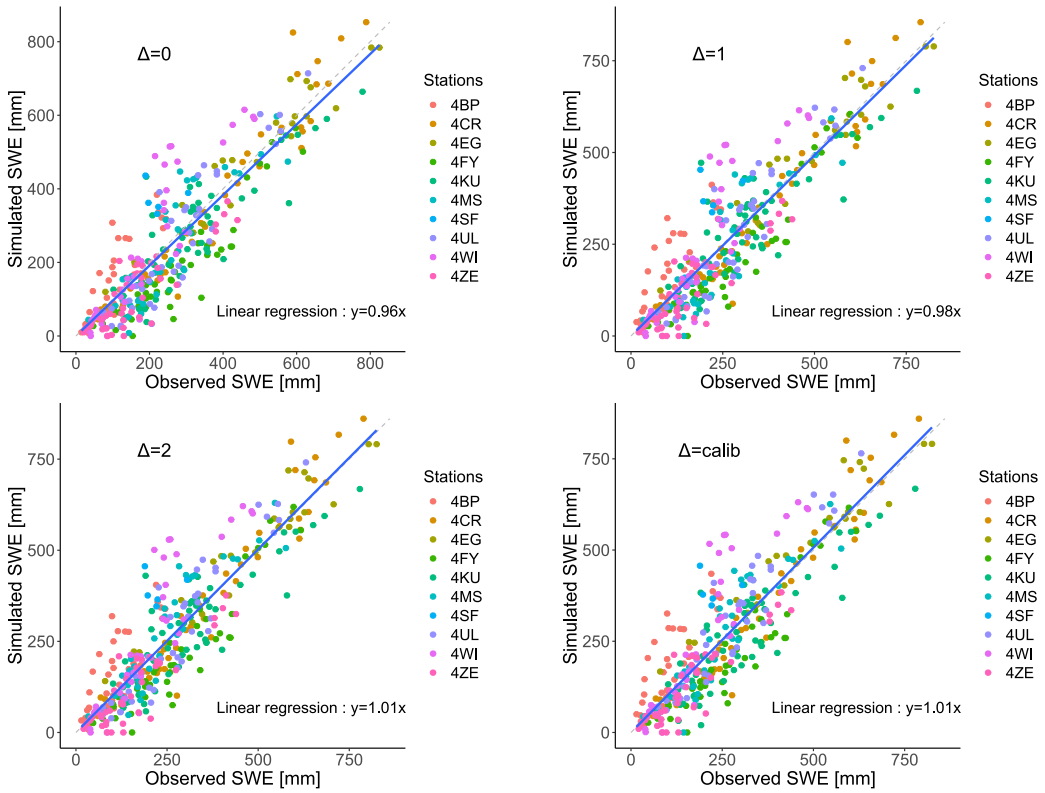

Figure D.3 – Simulated vs. observed SWE for the four different DDF variation interval using the QPE2-120 product. The grey dashed line indicates a slope of 1. Number of points: 367.

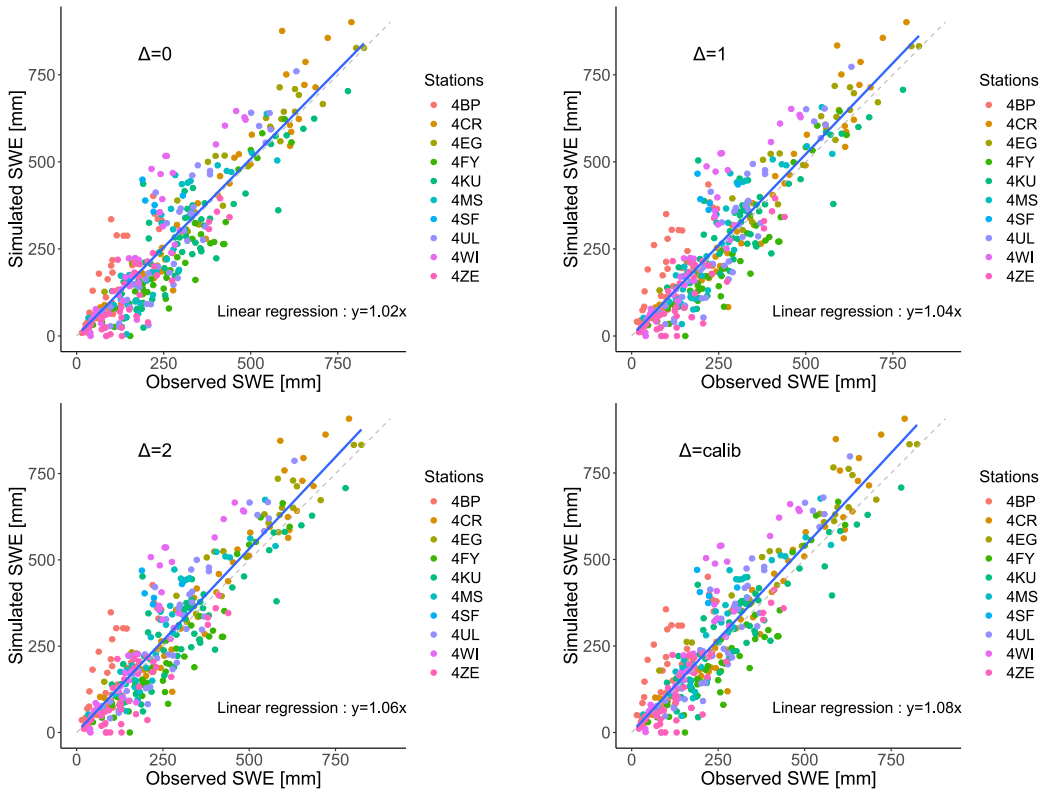

Figure D.4 – Simulated vs. observed SWE for the four different DDF variation interval using the QPE2-130 product . The grey dashed line indicates a slope of 1. Number of points: 367.

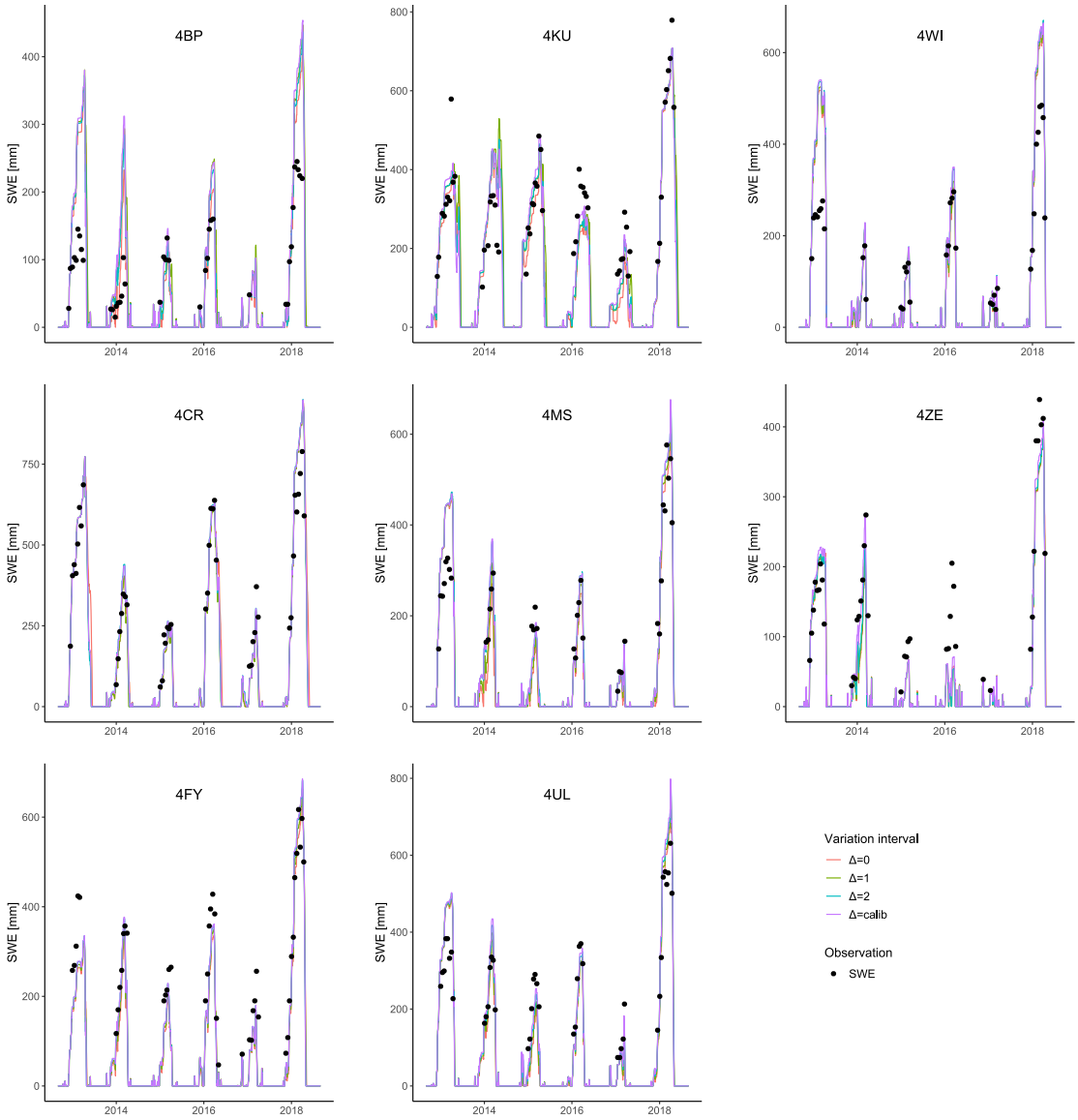

Figure D.5 – Simulated SWE for the 4 variation intervals versus observed SWE at the 8 SWE observation sites for which all the data have been used for the analysis. Simulation run with the QPE2-130 product.

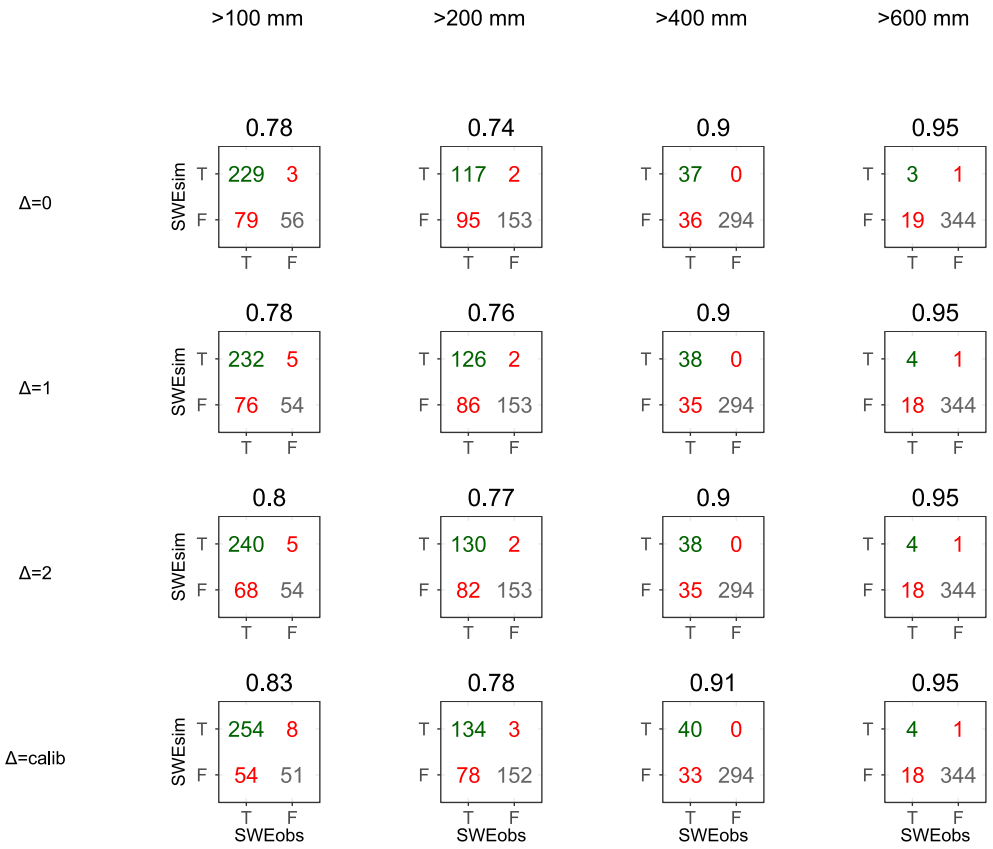

Figure D.6 – Confusion matrices and Overall Accuracy values obtained with the product QPE1 and the four variation interval configurations to reproduce the SWE quantity when applying SWE thresholds of 100, 200, 400 and 600 mm. T (TRUE) refers to threshold overrun (=Snow) whereas F (FALSE) indicates cases without threshold overrun (=NoSnow).

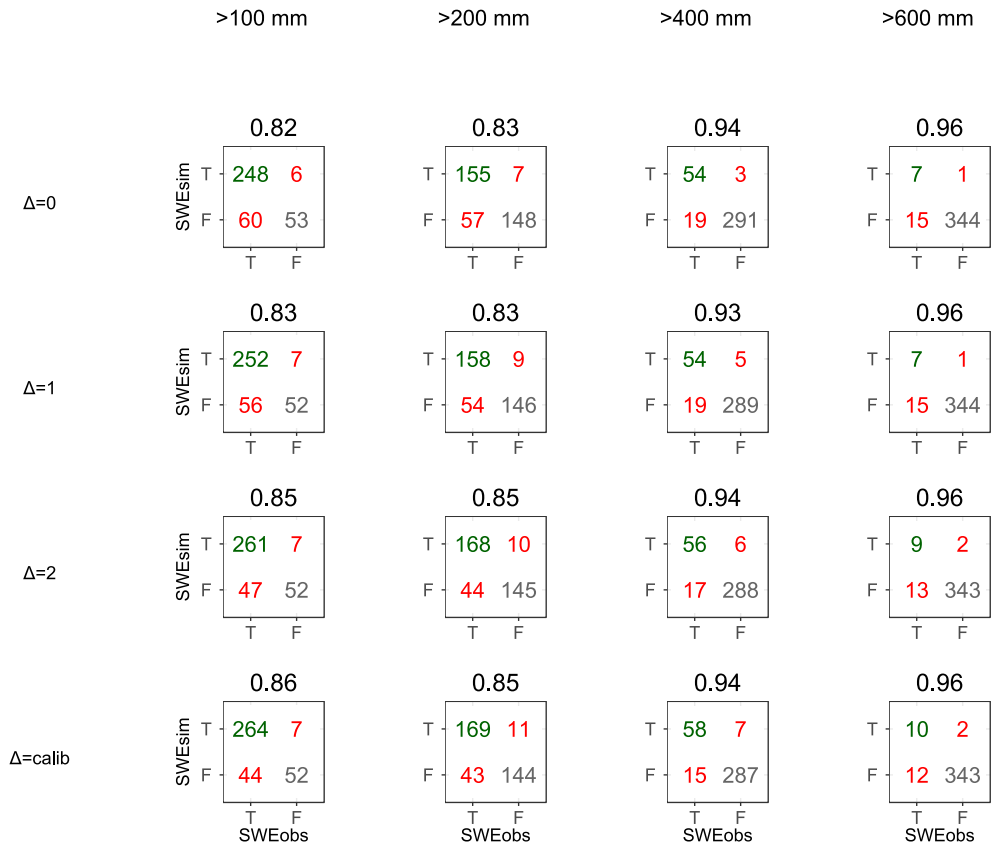

Figure D.7 – Confusion matrices and Overall Accuracy values obtained with the product QPE2 and the four variation interval configurations to reproduce the SWE quantity when applying SWE thresholds of 100, 200, 400 and 600 mm. T (TRUE) refers to threshold overrun (=Snow) whereas F (FALSE) indicates cases without threshold overrun (=NoSnow).

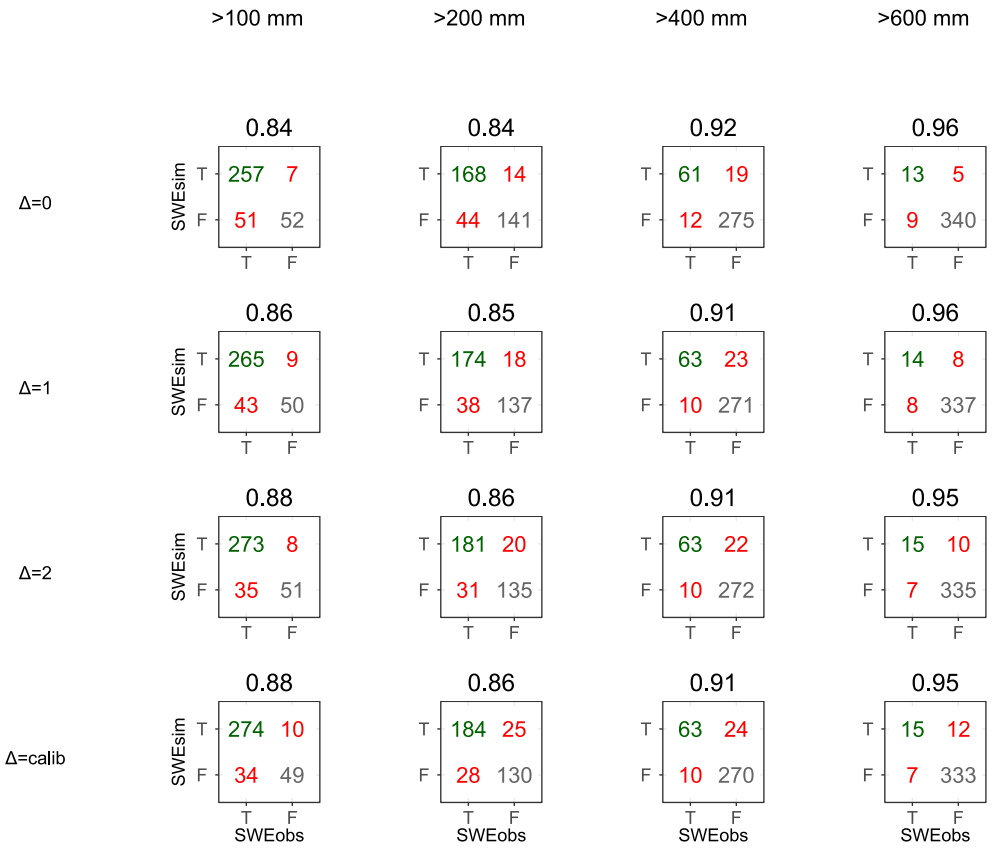

Figure D.8 – Confusion matrices and Overall Accuracy values obtained with the product QPE2-120 and the four variation interval configurations to reproduce the SWE quantity when applying SWE thresholds of 100, 200, 400 and 600 mm. T (TRUE) refers to threshold overrun (=Snow) whereas F (FALSE) indicates cases without threshold overrun (=NoSnow).

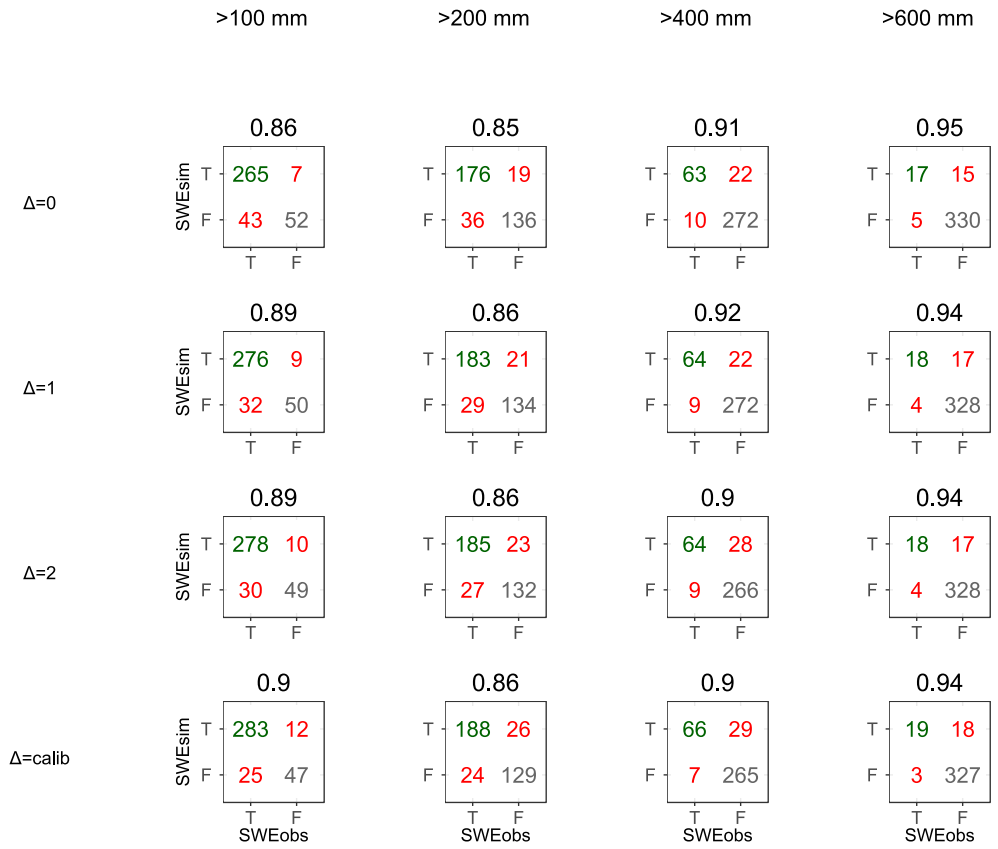

Figure D.9 – Confusion matrices and Overall Accuracy values obtained with the product QPE2-130 and the four variation interval configurations to reproduce the SWE quantity when applying SWE thresholds of 100, 200, 400 and 600 mm. T (TRUE) refers to threshold overrun (=Snow) whereas F (FALSE) indicates cases without threshold overrun (=NoSnow).

E Appendix to chapter 4

E.1 Supplementary figures

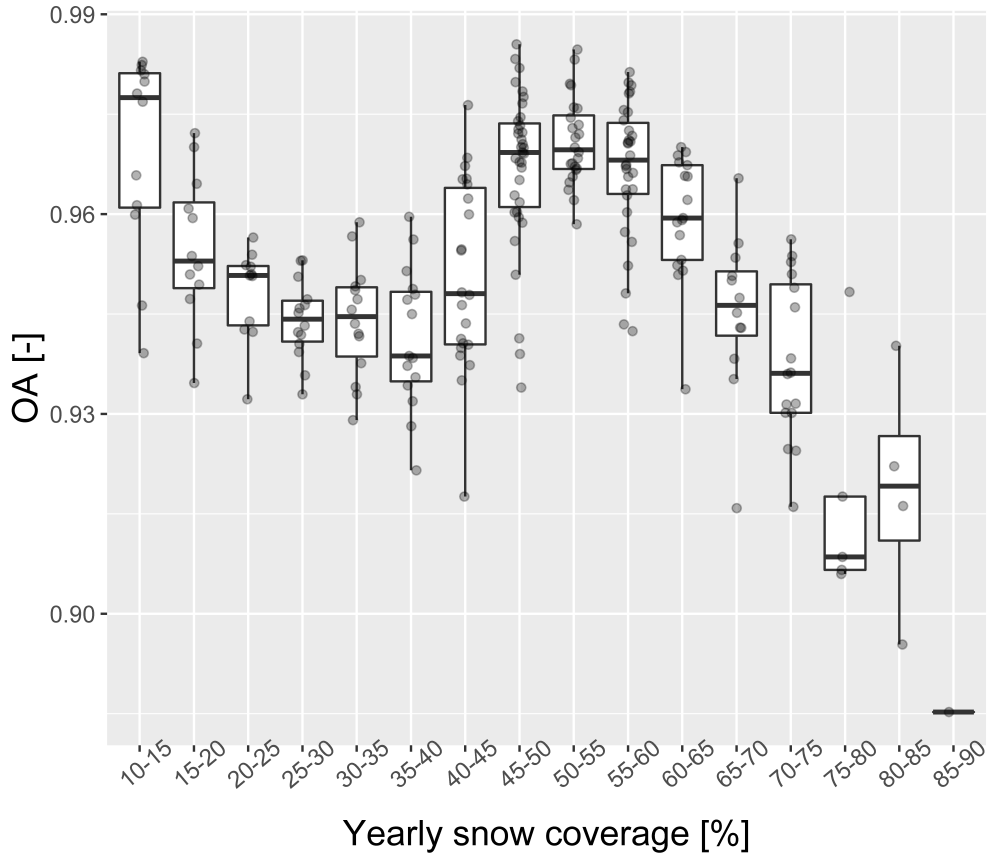

Figure E.1 – Overall accuracy (OA) versus the percentage of yearly snow coverage, by pixel, for the Saltina catchment. Precipitation product: EQP2.

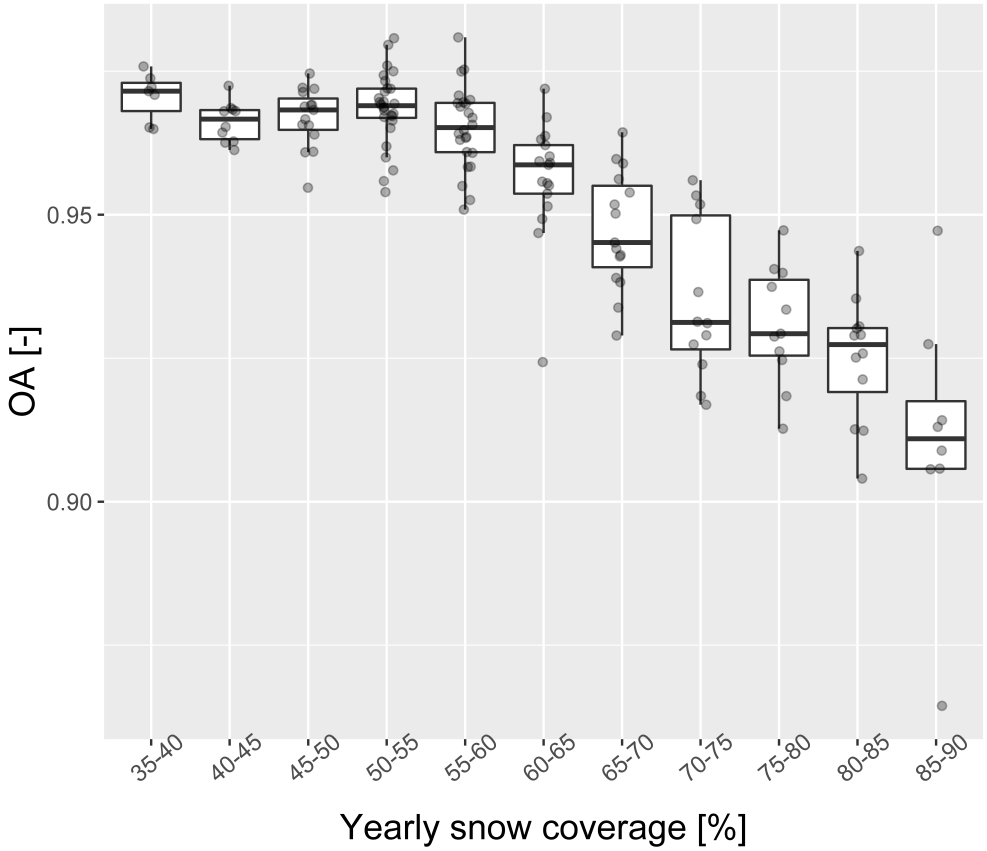

Figure E.2 – Overall accuracy (OA) versus the percentage of yearly snow coverage, by pixel, for the Lonza catchment. Precipitation product: EQP2.

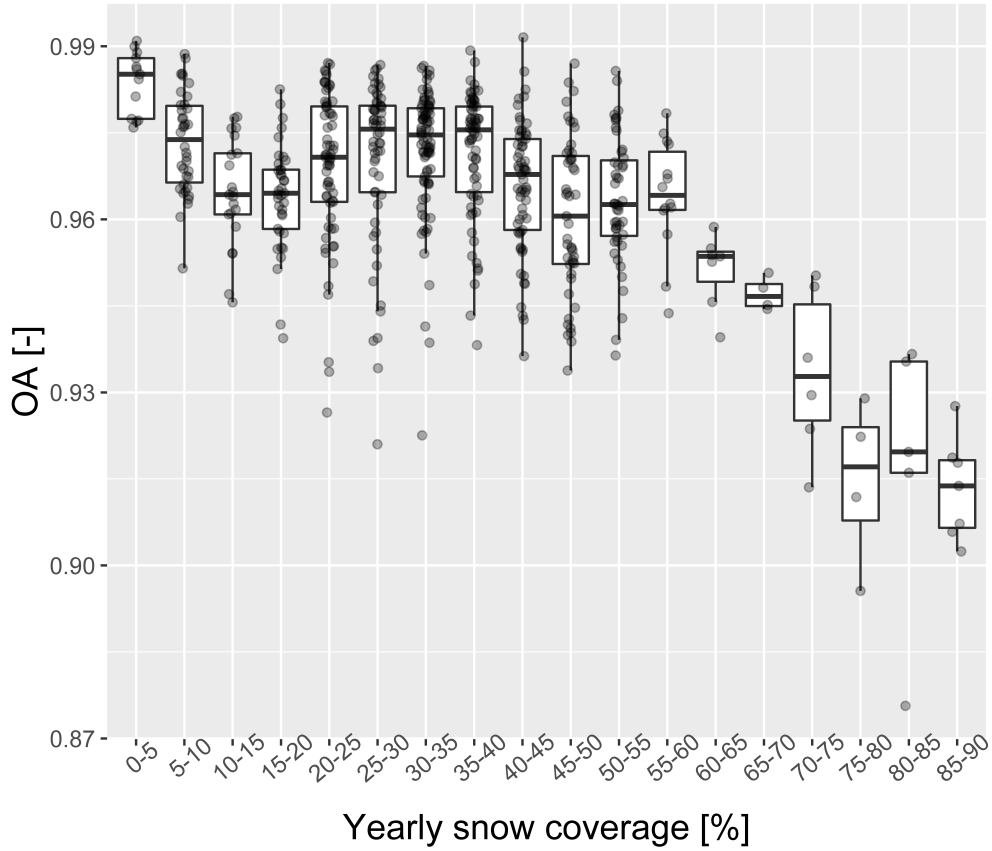

Figure E.3 – Overall accuracy (OA) versus the percentage of yearly snow coverage, by pixel, for the Grande-Eau catchment. Precipitation product: EQP2.

F Appendix to chapter 5

F.1 Supplementary table

Table F.1 – Periods considered for the different runs.

Catchment	Run name	Start	End
Reckingen	*Reckingen*	2019-06-06T02+00:01	2019-06-12T12+00:01
Reckingem	*Reckingen before*	2019-06-02T02+00:01	2019-06-06T02+00:01
Grande-Eau	*Grande-Eau complete*	2015-04-27T18+00:01	2015-05-06T06+00:01
Grande-Eau	*Grande-Eau short*	2015-04-30T20+00:01	2015-05-06T06+00:01

Bibliography

M. Abaza, F. Anctil, V. Fortin, and R. Turcotte. Exploration of sequential streamflow assimilation in snow dominated watersheds. *Advances in Water Resources*, 80:79–89, 2015a. ISSN 03091708. doi: 10.1016/j.advwatres.2015.03.011.

M. Abaza, C. Garneau, and F. Anctil. Comparison of sequential and variational streamflow assimilation techniques for short-term hydrological forecasting. *Journal of Hydrologic Engineering*, 20(2):04014042, 2015b. ISSN 1084-0699, 1943-5584. doi: 10.1061/(ASCE)HE.1943-5584.0001013.

P. Abbaszadeh, H. Moradkhani, and D. N. Daescu. The quest for model uncertainty quantification: A hybrid ensemble and variational data assimilation framework. *Water Resources Research*, 55(3):2407–2431, 2019. ISSN 0043-1397, 1944-7973. doi: 10.1029/2018WR023629.

T. E. Adams and T. C. Pagano. *Flood Forecasting*. Elsevier, 2016. ISBN 978-0-12-801884-2. doi: 10.1016/C2014-0-01361-5.

Agroscope. Agrometeo - Prévision et gestion des risques pour l'agriculture, 2017. [Available online at www.agrometeo.ch].

S. Ahmed and G. De Marsily. Comparison of geostatistical methods for estimating transmissivity using data on transmissivity and specific capacity. *Water Resources Research*, 23(9):1717–1737, 1987. doi: 10.1029/WR023i009p01717.

L. Alfieri, L. Feyen, F. Dottori, and A. Bianchi. Ensemble flood risk assessment in europe under high end climate scenarios. *Global Environmental Change*, 35:199–212, 2015. ISSN 09593780. doi: 10.1016/j.gloenvcha.2015.09.004.

H. Alsamamra, J. A. Ruiz-Arias, D. Pozo-Vázquez, and J. Tovar-Pescador. A comparative study of ordinary and residual kriging techniques for mapping global solar radiation over southern Spain. *Agricultural and Forest Meteorology*, 149(8):1343–1357, 2009. doi: 10.1016/j.agrformet.2009.03.005.

K. M. Andreadis and D. P. Lettenmaier. Assimilating remotely sensed snow observations into a macroscale hydrology model. *Advances in Water Resources*, 29(6):872–886, 2006. ISSN 03091708. doi: 10.1016/j.advwatres.2005.08.004.

N. Andres and A. Badoux. Hochwasserschäden: Entwicklung und trends. In *Forum für Wissen 2019. Lernen aus Extremereignissen*. WSL Berichte Heft 78, 2019a.

N. Andres and A. Badoux. Unwetterschäden in der Schweiz im Jahre 2018 - Rutschungen, Murgänge, Hochwasser und Sturzereignisse. *Wasser Energie Luft*, 111. Jahrgang (Heft 1), 2019b.

N. Andres, G. Lieberherr, I. V. Sideris, F. Jordan, and M. Zappa. From calibration to real-time operations: an assessment of three precipitation benchmarks for a swiss river system: From calibration to real-time operations. *Meteorological Applications*, 23(3):448–461, 2016. ISSN 13504827. doi: 10.1002/met.1569.

N. Andres, A. Badoux, F. Techel, and C. Hegg. Todesfälle durch Naturgefahrenprozesse in der Schweiz von 1946 bis 2015. *Wasser Energie Luft*, 109. Jahrgang (Heft 2), 2017.

S. Attinger and J. Fallot. Fréquence des intempéries et des précipitations abondantes en Valais (Alpes Suisses Occidentales) durant le 20ème siècle. *Association Int. de Climatol*, 15:253–259, 2003.

B. Auguie. *gridExtra: Miscellaneous Functions for Grid Graphics*, 2017. URL https://CRAN.R-project.org/package=gridExtra. R package version 2.3.

T. P. Barnett, J. C. Adam, and D. P. Lettenmaier. Potential impacts of a warming climate on water availability in snow-dominated regions. *Nature*, 438(7066):303–309, 2005. ISSN 0028-0836, 1476-4687. doi: 10.1038/nature04141.

P. Bartelt and M. Lehning. A physical SNOWPACK model for the swiss avalanche warning: Part i: numerical model. *Cold Regions Science and Technology*, 35(3):123–145, 2002. ISSN 0165232X. doi: 10.1016/S0165-232X(02)00074-5.

D. Berg, H. H. Bauser, and K. Roth. Covariance resampling for particle filter – state and parameter estimation for soil hydrology. *Hydrology and Earth System Sciences*, 23(2):1163–1178, 2019. ISSN 1607-7938. doi: 10.5194/hess-23-1163-2019.

S. Bergström. Development and application of a conceptual runoff model for Scandinavian catchments. Technical Report RHO 7, Swedish Meteorological and Hydrological Institute (SMHI), 1976.

S. Bergström. Recent developments in snowmelt-runoff simulation. In *Proc. Symp. Cold Regions Hydrology, Tech. Publ. Ser. TPS-86-1*, pages 461–468, Fairbanks, AK, 1986. American Water Resources Association.

C. Berndt, E. Rabiei, and U. Haberlandt. Geostatistical merging of rain gauge and radar data for high temporal resolutions and various station density scenarios. *Journal of Hydrology*, 508:88–101, 2014. doi: 10.1016/j.jhydrol.2013.10.028.

A. Berne and W. F. Krajewski. Radar for hydrology: Unfulfilled promise or unrecognized potential? *Advances in Water Resources*, 51:357–366, 2013. doi: 10.1016/j.advwatres.2012.05.005.

N. Besic, G. Vasile, F. Gottardi, J. Gailhard, A. Girard, and G. d'Urso. Calibration of a distributed SWE model using MODIS snow cover maps and in situ measurements. *Remote Sensing Letters*, 5(3):230–239, 2014. ISSN 2150-704X, 2150-7058. doi: 10.1080/2150704X.2014.897399.

K. J. Beven. *Rainfall-runoff modelling: the primer*. Wiley-Blackwell, 2nd edition, 2012. ISBN 978-0-470-71459-1.

K. J. Bormann, J. P. Evans, and M. F. McCabe. Constraining snowmelt in a temperature-index model using simulated snow densities. *Journal of Hydrology*, 517:652–667, 2014. ISSN 00221694. doi: 10.1016/j.jhydrol.2014.05.073.

F. Bosello, A. Iglesias, M. Termansen, A. Jeuken, H. Winsemius, E. De Cian, A. Chiabai, and L. Garrote. Economy-wide impacts of climate mitigation and adaptation strategies across european regions. In *Adapting to Climate Change in Europe*, pages 245–271. Elsevier, 2018. ISBN 978-0-12-849887-3. doi: 10.1016/B978-0-12-849887-3.00005-8.

A. Bárdossy and G. Pegram. Interpolation of precipitation under topographic influence at different time scales. *Water Resources Research*, 49(8):4545–4565, 2013. doi: 10.1002/wrcr.20307.

D. Bérod. Estimation et prévision des crues en Valais. Technical report, Swiss Hydrological Commission (CHy), Bern, 2013.

G. Burgers, P. Jan van Leeuwen, and G. Evensen. Analysis scheme in the ensemble Kalman filter. *Monthly Weather Review*, 126(6):1719–1724, 1998. ISSN 0027-0644, 1520-0493. doi: 10.1175/1520-0493(1998)126<1719:ASITEK>2.0.CO;2.

R. J. C. Burnash, R. L. Ferral, and R. A. McGuire. *A generalized streamflow simulation system – Conceptual modelling for digital computers*. US Department of Commerce, National Weather Service and State of California, Department of Water Resources, 1973.

P. Cantet. Mapping the mean monthly precipitation of a small island using kriging with external drifts. *Theoretical and Applied Climatology*, 127(1-2):31–44, 2017. doi: 10.1007/s00704-015-1610-z.

A. Castellarin and A. Pistocchi. An analysis of change in alpine annual maximum discharges: implications for the selection of design discharges. *Hydrological Processes*, 26(10):1517–1526, 2012. ISSN 08856087. doi: 10.1002/hyp.8249.

F. Cecinati, M. Moreno Ródenas, and M. A. Rico-Ramirez. Integration of rain gauge errors in radar-rain gauge merging techniques. In *10th World Congress on Water Resources and Environment*, pages 279 – 285, Athens, 2017a.

F. Cecinati, O. Wani, and M. A. Rico-Ramirez. Comparing approaches to deal with non-gaussianity of rainfall data in kriging-based radar-gauge rainfall merging. *Water Resources Research*, 53(11):8999–9018, 2017b. ISSN 00431397. doi: 10.1002/2016WR020330.

G. J. Ciach and W. F. Krajewski. On the estimation of radar rainfall error variance. *Advances in Water Resources*, 22(6):585–595, 1999. doi: 10.1016/S0309-1708(98)00043-8.

M. P. Clark, A. G. Slater, A. P. Barrett, L. E. Hay, G. J. McCabe, B. Rajagopalan, and G. H. Leavesley. Assimilation of snow covered area information into hydrologic and land-surface models. *Advances in Water Resources*, 29(8):1209–1221, 2006. doi: 10.1016/j.advwatres.2005.10.001.

M. P. Clark, D. E. Rupp, R. A. Woods, X. Zheng, R. P. Ibbitt, A. G. Slater, J. Schmidt, and M. J. Uddstrom. Hydrological data assimilation with the ensemble Kalman filter: Use of streamflow observations to update states in a distributed hydrological model. *Advances in Water Resources*, 31(10):1309–1324, 2008. ISSN 03091708. doi: 10.1016/j.advwatres.2008.06.005.

M. P. Clark, J. Hendrikx, A. G. Slater, D. Kavetski, B. Anderson, N. J. Cullen, T. Kerr, E. O. Hreinsson, and R. A. Woods. Representing spatial variability of snow water equivalent in hydrologic and land-surface models: A review. *Water Resources Research*, 47, 2011. doi: 10.1029/2011wr010745.

J. D. Creutin, G. Delrieu, and T. Lebel. Rain measurement by raingage-radar combination: a geostatistical approach. *Journal of Atmospheric and Oceanic Technology*, 5(1):102–115, 1988. doi: 10.1175/1520-0426(1988)005<0102:RMBRRC>2.0.CO;2.

S. F. Daly, R. Davis, E. Ochs, and T. Pangburn. An approach to spatially distributed snow modelling of the Sacramento and San Joaquin basins, California. *Hydrological Processes*, 14 (18):3257–3271, 2000. ISSN 0885-6087, 1099-1085. doi: 10.1002/1099-1085(20001230)14:18<3257::AID-HYP199>3.0.CO;2-Z.

J. Delhomme. Kriging in the hydrosciences. *Advances in Water Resources*, 1(5):251–266, 1978. doi: 10.1016/0309-1708(78)90039-8.

A. Di Piazza, F. L. Conti, L. Noto, F. Viola, and G. La Loggia. Comparative analysis of different techniques for spatial interpolation of rainfall data to create a serially complete monthly time series of precipitation for Sicily, Italy. *International Journal of Applied Earth Observation and Geoinformation*, 13(3):396–408, 2011. doi: 10.1016/j.jag.2011.01.005.

S. J. Déry, V. V. Salomonson, M. Stieglitz, D. K. Hall, and I. Appel. An approach to using snow areal depletion curves inferred from MODIS and its application to land surface modelling in Alaska. *Hydrological Processes*, 19(14):2755–2774, 2005. ISSN 0885-6087, 1099-1085. doi: 10.1002/hyp.5784.

Q. Y. Duan, V. K. Gupta, and S. Sorooshian. Shuffled complex evolution approach for effective and efficient global minimization. *Journal of Optimization Theory and Applications*, 76(3): 501–521, 1993. ISSN 0022-3239, 1573-2878. doi: 10.1007/BF00939380.

L. Egli, T. Jonas, and R. Meister. Comparison of different automatic methods for estimating snow water equivalent. *Cold Regions Science and Technology*, 57(2-3):107–115, 2009. ISSN 0165232X. doi: 10.1016/j.coldregions.2009.02.008.

U. Ehret. *Rainfall and flood nowcasting in small catchments using weather radar*. Number Heft 121 in Mitteilungen des Instituts für Wasserbau. Universität Stuttgart, Stuttgart, 2003. ISBN 978-3-933761-24-8.

M. Engel, C. Notarnicola, S. Endrizzi, and G. Bertoldi. Snow model sensitivity analysis to understand spatial and temporal snow dynamics in a high-elevation catchment. *Hydrological Processes*, 31(23):4151–4168, 2017. ISSN 08856087. doi: 10.1002/hyp.11314.

R. Erdin, C. Frei, and H. R. Künsch. Data transformation and uncertainty in geostatistical combination of radar and rain gauges. *Journal of Hydrometeorology*, 13(4):1332–1346, 2012. doi: 10.1175/JHM-D-11-096.1.

G. Evensen. Sequential data assimilation with a nonlinear quasi-geostrophic model using Monte Carlo methods to forecast error statistics. *Journal of Geophysical Research*, 99:10143, 1994. ISSN 0148-0227. doi: 10.1029/94JC00572.

I. Fellows and using the JMapViewer library by Jan Peter Stotz. *OpenStreetMap: Access to Open Street Map Raster Images*, 2016. URL https://CRAN.R-project.org/package=OpenStreetMap. R package version 0.3.3.

C. Fierz, P. Riber, E. Adams, A. Curran, P. Föhn, M. Lehning, and C. Plüss. Evaluation of snow-surface energy balance models in alpine terrain. *Journal of Hydrology*, 282(1-4):76–94, 2003. ISSN 00221694. doi: 10.1016/S0022-1694(03)00255-5.

M. Fischer, M. Huss, and M. Hoelzle. Surface elevation and mass changes of all Swiss glaciers 1980–2010. *The Cryosphere*, 9(2):525–540, 2015. doi: 10.5194/tc-9-525-2015.

A. Foehn, J. García Hernández, S. Alesina, A. J. Schleiss, and J. Fluixá-Sanmartín. Los desafíos de la modelización hidrológica y la previsión de crecidas en tiempo real en alta montaña. In *XXVII Congreso latinoamericano de hydráulica LADHI*. International Association of Hydraulic Engineering and Research, IAHR, 2016a.

A. Foehn, J. García Hernández, B. Schaefli, G. De Cesare, and A. J. Schleiss. Spatialization of precipitation data for flood forecasting applied to the Upper Rhone River basin. In *International Conference Hydro 2016*, Montreux, 2016b.

A. Foehn, J. García Hernández, B. Schaefli, and G. De Cesare. Spatial interpolation of precipitation from multiple rain gauge networks and weather radar data for operational applications in Alpine catchments. *Journal of Hydrology*, 563:1092–1110, 2018. ISSN 00221694. doi: 10.1016/j.jhydrol.2018.05.027.

A. Foehn, J. García Hernández, B. Roquier, J. Fluixá-Sanmartín, J. Paredes Arquiola, and G. De Cesare. RS MINERVE – User manual, v2.13. Ed. CREALP, Switzerland. 2019a. ISSN 2673-2653.

A. Foehn, D. Pasetto, J. García Hernández, and G. De Cesare. Application of an ensemble Kalman filter to a semi-distributed hydrological flood forecasting system in Alpine catchments. In *SimHydro 2019*, Sophia Antipolis, France, 2019b.

FOEN. Federal Office for the Environment, 10 minutes average discharge data, 2017a.

FOEN. Federal Office for the Environment, Hydrological data and forecasts, 2017b. [Available online at http://hydrodaten.admin.ch].

C. Frei and F. A. Isotta. Ensemble spatial precipitation analysis from rain gauge data: Methodology and application in the European Alps. *Journal of Geophysical Research: Atmospheres*, 2019. ISSN 2169-897X, 2169-8996. doi: 10.1029/2018JD030004.

M. Gabella, E. Morin, and R. Notarpietro. Using TRMM spaceborne radar as a reference for compensating ground-based radar range degradation: Methodology verification based on rain gauges in Israel. *Journal of Geophysical Research*, 116:D02114, 2011a. ISSN 0148-0227. doi: 10.1029/2010JD014496.

M. Gabella, I. Sideris, and U. Germann. NCCR Climate III – sub-project CombiPrecip – Milestone2010.11, version 1.0: Comparison between radar-gage data at various time scales, 2011b.

M. Gabella, P. Speirs, U. Hamann, U. Germann, and A. Berne. Measurement of precipitation in the Alps using dual-polarization C-band ground-based radars, the GPM spaceborne Ku-band radar, and rain gauges. *Remote Sensing*, 9(11), 2017. ISSN 2072-4292. doi: 10.3390/rs9111147.

J. García Hernández. *Flood management in a complex river basin with a real-time decision support system based on hydrological forecasts*. Communication 48 du Laboratoire de Constructions Hydrauliques. Ed. A. Schleiss, EPFL, Lausanne, 2011a.

J. García Hernández. *Flood management in a complex river basin with a real-time decision support system based on hydrological forecasts*. PhD Thesis N° 5093, Ecole Polytechnique Fédérale de Lausanne, Lausanne, 2011b.

J. García Hernández, F. Jordan, J. Dubois, and J.-L. Boillat. *Routing System II - Modélisation d'écoulements dans des systèmes hydrauliques*. Communication 32 du Laboratoire de Constructions Hydrauliques. Ed. A. Schleiss, EPFL, Lausanne, 2007.

J. García Hernández, J.-L. Boillat, F. Jordan, and B. Hingray. La prévision hydrométéorologique sur le bassin versant du Rhône en amont du Léman. *La Houille Blanche*, (5):61–70, 2009a. doi: 10.1051/lhb/2009057.

J. García Hernández, P. Horton, C. Tobin, and J. Boillat. MINERVE 2010 : Prévision hydrométéorologique et gestion des crues sur le Rhône alpin. *Wasser Energie Luft*, (4):297–302, 2009b.

J. García Hernández, A. Claude, J. Paredes Arquiola, B. Roquier, and J.-L. Boillat. Integrated flood forecasting and management system in a complex catchment area in the Alps - implementation of the MINERVE project in the Canton of Valais. In A. Schleiss, J. Speerli, and R. Pfammatter, editors, *Swiss Competences in River Engineering and Restoration*, pages 87–97. CRC Press, 2014. ISBN 978-1-138-02676-6 et 978-1-4987-0443-4.

J. García Hernández, A. Foehn, J. Fluixá-Sanmartín, B. Roquier, J. Paredes Arquiola, and G. De Cesare. RS MINERVE – Technical manual, v2.22. Ed. CREALP, Switzerland. 2019. ISSN 2673-2661.

U. Germann and J. Joss. Mesobeta profiles to extrapolate radar precipitation measurements above the Alps to the ground level. *Journal of Applied Meteorology*, 41(5):542–557, 2002. ISSN 0894-8763, 1520-0450. doi: 10.1175/1520-0450(2002)041<0542:MPTERP>2.0.CO;2.

U. Germann, G. Galli, M. Boscacci, and M. Bolliger. Radar precipitation measurement in a mountainous region. *Quarterly Journal of the Royal Meteorological Society*, 132(618): 1669–1692, 2006. doi: 10.1256/qj.05.190.

U. Germann, M. Berenguer, D. Sempere-Torres, and M. Zappa. REAL-Ensemble radar precipitation estimation for hydrology in a mountainous region. *Quarterly Journal of the Royal Meteorological Society*, 135(639):445–456, 2009. doi: 10.1002/qj.375.

U. Germann, M. Boscacci, M. Gabella, and M. Sartori. Peak Performance - Radar design for prediction in the Swiss Alps - The latest fourth-generation MeteoSwiss weather radar network is called Rad4Alp. *Meteorological Technology International*, pages 42–45, 2015.

P. Goovaerts. *Geostatistics for natural resources evaluation*. Applied geostatistics series. Oxford University Press, New York, 1997. ISBN 978-0-19-511538-3.

P. Goovaerts. Geostatistical approaches for incorporating elevation into the spatial interpolation of rainfall. *Journal of Hydrology*, 228(1–2):113–129, 2000. doi: 10.1016/S0022-1694(00)00144-X.

E. Goudenhoofdt and L. Delobbe. Evaluation of radar-gauge merging methods for quantitative precipitation estimates. *Hydrology and Earth System Sciences*, 13(2):195–203, 2009. doi: 10.5194/hess-13-195-2009.

J. Grazioli, D. Tuia, and A. Berne. Hydrometeor classification from polarimetric radar measurements: a clustering approach. *Atmospheric Measurement Techniques*, 8(1):149–170, 2015. doi: 10.5194/amt-8-149-2015.

N. Griessinger, J. Seibert, J. Magnusson, and T. Jonas. Assessing the benefit of snow data assimilation for runoff modeling in Alpine catchments. *Hydrology and Earth System Sciences*, 20(9):3895–3905, 2016. ISSN 1607-7938. doi: 10.5194/hess-20-3895-2016.

B. Gräler, E. Pebesma, and G. Heuvelink. Spatio-Temporal Interpolation using gstat. *The R Journal*, 8:204–218, 2016. URL https://journal.r-project.org/archive/2016-1/na-pebesma-heuvelink.pdf.

G. Grolemund and H. Wickham. Dates and times made easy with lubridate. *Journal of Statistical Software*, 40(3):1–25, 2011. URL http://www.jstatsoft.org/v40/i03/.

H. V. Gupta, H. Kling, K. K. Yilmaz, and G. F. Martinez. Decomposition of the mean squared error and NSE performance criteria: Implications for improving hydrological modelling. *Journal of Hydrology*, 377(1):80–91, 2009. ISSN 00221694. doi: 10.1016/j.jhydrol.2009.08.003.

U. Haberlandt. Geostatistical interpolation of hourly precipitation from rain gauges and radar for a large-scale extreme rainfall event. *Journal of Hydrology*, 332(1-2):144–157, 2007. doi: 10.1016/j.jhydrol.2006.06.028.

D. Hall, V. Salomonson, and G. Riggs. MODIS/Aqua Snow Cover Daily L3 Global 500m Grid, Version 6. 2016a. URL https://nsidc.org/data/MYD10A1/versions/6.

D. Hall, V. Salomonson, and G. Riggs. MODIS/Terra Snow Cover Daily L3 Global 500m Grid, Version 6. 2016b. URL https://nsidc.org/data/MOD10A1/versions/6.

D. K. Hall, G. A. Riggs, V. V. Salomonson, N. E. DiGirolamo, and K. J. Bayr. MODIS snow-cover products. *Remote Sensing of Environment*, 83(1-2):181–194, 2002. ISSN 00344257. doi: 10.1016/S0034-4257(02)00095-0.

Y. Hamdi, B. Hingray, and A. Musy. Un modèle de prévision hydro-météorologique pour les crues du Rhône supérieur en Suisse. *Eau, energie, air*, 97(11):325–332, 2005.

Y. Hamdi, B. Hingray, and A. Musy. Projet MINERVE - modèle de prévision et de gestion des crues : Rapport intermédiaire n°4 - volet b : Modélisation hydrologique : Rapport final [unpublished], 2006.

Z. H. He, J. Parajka, F. Q. Tian, and G. Blöschl. Estimating degree-day factors from MODIS for snowmelt runoff modeling. *Hydrology and Earth System Sciences*, 18(12):4773–4789, 2014. ISSN 1607-7938. doi: 10.5194/hess-18-4773-2014.

P. Heidke. Berechnung des erfolges und der güte der windstärkevorhersagen im sturmwarnungsdienst. *Geografiska Annaler*, 8(4):301–349, 1926. ISSN 2001-4422. doi: 10.1080/20014422.1926.11881138.

T. Hengl, G. B. Heuvelink, and D. G. Rossiter. About regression-kriging: From equations to case studies. *Computers & Geosciences*, 33(10):1301–1315, 2007. doi: 10.1016/j.cageo.2007.05.001.

R. J. Hijmans. *raster: Geographic data analysis and modeling*, 2017. URL https://CRAN.R-project.org/package=raster. R package version 2.6-7.

B. Hingray, B. Schaefli, A. Mezghani, and Y. Hamdi. Signature-based model calibration for hydrological prediction in mesoscale Alpine catchments. *Hydrological Sciences Journal*, 55(6):1002–1016, 2010. doi: 10.1080/02626667.2010.505572.

R. Hock. Temperature index melt modelling in mountain areas. *Journal of Hydrology*, 282(1-4):104–115, 2003. ISSN 00221694. doi: 10.1016/S0022-1694(03)00257-9.

G. Hudson and H. Wackernagel. Mapping temperature using kriging with external drift: Theory and an example from Scotland. *International Journal of Climatology*, 14(1):77–91, 1994. ISSN 08998418, 10970088. doi: 10.1002/joc.3370140107.

W. Immerzeel and P. Droogers. Calibration of a distributed hydrological model based on satellite evapotranspiration. *Journal of Hydrology*, 349(3):411–424, 2008. ISSN 00221694. doi: 10.1016/j.jhydrol.2007.11.017.

A. H. Jazwinski. *Stochastic processes and filtering theory*. Elsevier, 1970. ISBN 978-0-08-096090-6.

K. S. Jennings and N. P. Molotch. The sensitivity of modeled snow accumulation and melt to precipitation phase methods across a climatic gradient. *Hydrol. Earth Syst. Sci. Discuss.*, 2019:1–33, 2019. doi: 10.5194/hess-2019-82.

K. S. Jennings, T. S. Winchell, B. Livneh, and N. P. Molotch. Spatial variation of the rain–snow temperature threshold across the Northern Hemisphere. *Nature Communications*, 9(1): 1148, 2018. ISSN 2041-1723. doi: 10.1038/s41467-018-03629-7.

S. A. Jewell and N. Gaussiat. An assessment of kriging-based rain-gauge-radar merging techniques: Gauge-radar merging schemes for flood forecasting. *Quarterly Journal of the Royal Meteorological Society*, 141(691):2300–2313, 2015. ISSN 00359009. doi: 10.1002/qj.2522.

F. Jordan. *Modèle de prévision et de gestion des crues : optimisation des opérations des aménagements hydroélectriques à accumulation pour la réduction des débits de crue*. Communication 29 du Laboratoire de Constructions Hydrauliques. Ed. A. Schleiss, EPFL, Lausanne, 2007a.

F. Jordan. *Modèle de prévision et de gestion des crues : optimisation des opérations des aménagements hydroélectriques à accumulation pour la réduction des débits de crue*. PhD Thesis N° 3711, Ecole Polytechnique Fédérale de Lausanne, Lausanne, 2007b.

F. Jordan, J. García Hernández, J. Dubois, J.-L. Boillat, and A. Schleiss. *Minerve - Modélisation des intempéries de nature extrême du Rhône valaisan et de leurs effets*. Communication 38 du Laboratoire de Constructions Hydrauliques. Ed. A. Schleiss, EPFL, 2008.

F. Jordan, J.-L. Boillat, and A. Schleiss. Prévision et gestion des crues du Rhône supérieur par l'exploitation optimale des retenues alpines. *La Houille Blanche*, (5):91–102, 2010. doi: 10.1051/lhb/2010060.

F. M. Jordan, J.-L. Boillat, and A. J. Schleiss. Optimization of the flood protection effect of a hydropower multi-reservoir system. *International Journal of River Basin Management*, 10 (1):65–72, 2012. doi: 10.1080/15715124.2011.650868.

S. Jörg-Hess, N. Griessinger, and M. Zappa. Probabilistic forecasts of snow water equivalent and runoff in mountainous areas. *Journal of Hydrometeorology*, 16(5):2169–2186, 2015. ISSN 1525-755X, 1525-7541. doi: 10.1175/JHM-D-14-0193.1.

D. L. Kane, R. E. Gieck, and L. D. Hinzman. Snowmelt modeling at small Alaskan arctic watershed. *Journal of Hydrologic Engineering*, 2(4):204–210, 1997. ISSN 1084-0699, 1943-5584. doi: 10.1061/(ASCE)1084-0699(1997)2:4(204).

D. K. Karpouzos, E. A. Baltas, S. Kavalieratou, and C. Babajimopoulos. A hydrological investigation using a lumped water balance model: the Aison River Basin case (Greece). *Water and Environment Journal*, 25(3):297–307, 2011. ISSN 17476585. doi: 10.1111/j.1747-6593.2010.00222.x.

A. Klein and A. Barnett. Validation of daily MODIS snow cover maps of the Upper Rio Grande River Basin for the 2000–2001 snow year. *Remote Sensing of Environment*, 86(2):162–176, 2003. ISSN 00344257. doi: 10.1016/S0034-4257(03)00097-X.

H. Kling, M. Fuchs, and M. Paulin. Runoff conditions in the upper Danube basin under an ensemble of climate change scenarios. *Journal of Hydrology*, 424-425:264–277, 2012. ISSN 00221694. doi: 10.1016/j.jhydrol.2012.01.011.

E. J. Klok, K. Jasper, K. P. Roelofsma, J. Gurtz, and A. Badoux. Distributed hydrological modelling of a heavily glaciated Alpine river basin. *Hydrological Sciences Journal*, 46(4):553–570, 2001. ISSN 0262-6667, 2150-3435. doi: 10.1080/02626660109492850.

J. Kochendorfer, R. Nitu, M. Wolff, E. Mekis, R. Rasmussen, B. Baker, M. E. Earle, A. Reverdin, K. Wong, C. D. Smith, D. Yang, Y.-A. Roulet, S. Buisan, T. Laine, G. Lee, J. L. C. Aceituno, J. Alastrué, K. Isaksen, T. Meyers, R. Brækkan, S. Landolt, A. Jachcik, and A. Poikonen. Analysis of single-Alter-shielded and unshielded measurements of mixed and solid precipitation from WMO-SPICE. *Hydrology and Earth System Sciences*, 21(7):3525–3542, 2017. ISSN 1607-7938. doi: 10.5194/hess-21-3525-2017.

P. Krause, D. P. Boyle, and F. Bäse. Comparison of different efficiency criteria for hydrological model assessment. *Advances in Geosciences*, 5:89–97, 2005. ISSN 1680-7359. doi: 10.5194/adgeo-5-89-2005.

L. G. Lanza and E. Vuerich. The WMO field intercomparison of rain intensity gauges. *Atmospheric Research*, 94(4):534–543, 2009. doi: 10.1016/j.atmosres.2009.06.012.

Y. Li, S. Grimaldi, V. R. Pauwels, and J. P. Walker. Hydrologic model calibration using remotely sensed soil moisture and discharge measurements: The impact on predictions at gauged and ungauged locations. *Journal of Hydrology*, 557:897–909, 2018. ISSN 00221694. doi: 10.1016/j.jhydrol.2018.01.013.

G. Liang. Net radiation, potential and actual evapotranspiration in Austria. *Archives for Meteorology, Geophysics, and Bioclimatology Series B*, 31(4):379–390, 1982. ISSN 0066-6424. doi: 10.1007/BF02263442.

Y. Liu. Advancing data assimilation in operational hydrologic forecasting: progresses, challenges, and emerging opportunities. *Hydrology and Earth Systems Sciences*, 16:p. 3863–3887, 2012. doi: 10.5194/hess-16-3863-2012.

Y. Liu and H. V. Gupta. Uncertainty in hydrologic modeling: Toward an integrated data assimilation framework. *Water Resources Research*, 43(7), 2007. ISSN 00431397. doi: 10.1029/2006WR005756.

Y. Luo, J. Arnold, S. Liu, X. Wang, and X. Chen. Inclusion of glacier processes for distributed hydrological modeling at basin scale with application to a watershed in Tianshan Mountains, northwest China. *Journal of Hydrology*, 477:72–85, 2013. ISSN 00221694. doi: 10.1016/j.jhydrol.2012.11.005.

S. Ly, C. Charles, and A. Degré. Geostatistical interpolation of daily rainfall at catchment scale: the use of several variogram models in the Ourthe and Ambleve catchments, Belgium. *Hydrology and Earth System Sciences*, 15(7):2259–2274, 2011. doi: 10.5194/hess-15-2259-2011.

S. Ly, C. Charles, and A. Degre. Different methods for spatial interpolation of rainfall data for operational hydrology and hydrological modeling at watershed scale. A review. *Biotechnol. Agron. Soc. Environ*, (17(2)):392–406, 2013.

J. Magnusson, D. Gustafsson, F. Hüsler, and T. Jonas. Assimilation of point SWE data into a distributed snow cover model comparing two contrasting methods. *Water Resources Research*, 50(10):7816–7835, 2014. ISSN 00431397. doi: 10.1002/2014WR015302.

C. Marty. Regime shift of snow days in Switzerland. *Geophysical Research Letters*, 35(12):1–5, 2008. doi: 10.1029/2008GL033998.

G. Matheron. The theory of regionalized variables and its applications. Technical report, Paris : École Nationale Supérieure des Mines de Paris, 1971.

H. K. McMillan, E. . Hreinsson, M. P. Clark, S. K. Singh, C. Zammit, and M. J. Uddstrom. Operational hydrological data assimilation with the recursive ensemble Kalman filter. *Hydrology and Earth System Sciences*, 17(1):21–38, 2013. ISSN 1607-7938. doi: 10.5194/hess-17-21-2013.

H. Messer, A. Zinevich, and P. Alpert. Environmental monitoring by wireless communication networks. *Science*, 312(5774):713–713, 2006. ISSN 0036-8075, 1095-9203. doi: 10.1126/science.1120034.

MeteoSwiss. Nouveau radar météorologique pour la Suisse alémanique. Press release, 2012. URL http://www.meteosuisse.admin.ch/home/actualite/infos.subpage.html/fr/data/news/2012/4/nouveau-radar-meteorologique-pour-la-suisse-alemanique.html?query=radar&topic=0&dateRange=all&dateFrom=&dateTo=.

MeteoSwiss. De nouveaux radars météorologiques pour la Suisse. Press release, 2014a. URL http://www.meteosuisse.admin.ch/home/actualite/infos.subpage.html/fr/data/news/2014/5/de-nouveaux-radars-meteorologiques-pour-la-suisse.html?query=de+nouveaux+radars&topic=0&dateRange=all&dateFrom=&dateTo=.

MeteoSwiss. Räumliche Daten CombiPrecip, 2014b. [Available online at http://www.meteoswiss.admin.ch/home/search.subpage.html/en/data/products/2014/raeumliche-daten-combiprecip.html].

MeteoSwiss. Measurement instruments. Federal Office of Meteorology and Climatology, 2015. [Available online at http://www.meteoswiss.admin.ch/home/measurement-and-forecasting-systems/land-based-stations/automatisches-messnetz/measurement-instruments.html].

MeteoSwiss. Automatic monitoring network, 2016a. [Available online at http://www.meteoswiss.admin.ch/home/measurement-and-forecasting-systems/land-based-stations/automatisches-messnetz.html].

MeteoSwiss. Extreme value analyses (version 2016) - Standard period 1966 - 2015, 2016b. [Available online at http://www.meteoswiss.admin.ch/home/climate/past/climate-extremes/extreme-value-analyses/standard-period.html?].

MeteoSwiss. Project Rad4Alp - A modern radar network for Switzerland. [Available online at http://www.meteoswiss.admin.ch/content/dam/meteoswiss/en/Mess-Prognosesysteme/doc/Rad4Alp_en.pdf], 2016c.

MeteoSwiss. Le réseau de radars météorologiques de la Suisse est achevé. Press release, 2016. URL http://www.meteosuisse.admin.ch/home/actualite/infos.subpage.html/fr/data/news/2016/2/le-reseau-de-radars-meteorologiques-de-la-suisse-est-acheve.html.

MeteoSwiss. Climate diagrams and normal values per station, 2017. [Available online at http://www.meteoswiss.admin.ch/home/climate/past/climate-normals/climate-diagrams-and-normal-values-per-station.html].

MeteoSwiss. COSMO-7 – the model for western and central Europe, 2017. [Available online at http://www.meteoswiss.admin.ch/home/measurement-and-forecasting-systems/warning-and-forecasting-systems/cosmo-forecasting-system/cosmo-7-the-model-for-western-and-central-europe.html].

N. Mizukami, O. Rakovec, A. Newman, M. Clark, A. Wood, H. Gupta, and R. Kumar. On the choice of calibration metrics for "high flow" estimation using hydrologic models. *Hydrology and Earth System Sciences Discussions*, pages 1–16, 2018. ISSN 1812-2116. doi: 10.5194/hess-2018-391.

H. Moradkhani, K.-L. Hsu, H. Gupta, and S. Sorooshian. Uncertainty assessment of hydrologic model states and parameters: Sequential data assimilation using the particle filter. *Water Resources Research*, 41(5), 2005a. ISSN 00431397. doi: 10.1029/2004WR003604.

H. Moradkhani, S. Sorooshian, H. V. Gupta, and P. R. Houser. Dual state–parameter estimation of hydrological models using ensemble Kalman filter. *Advances in Water Resources*, 28(2): 135–147, 2005b. ISSN 03091708. doi: 10.1016/j.advwatres.2004.09.002.

M. Musa, E. Grüter, M. Abbt, C. Häberli, E. Häller, U. Küng, T. Konzelmann, and R. Dössegger. Quality control tools for meteorological data in the MeteoSwiss Datawarehouse system. Internal report, MeteoSwiss, Zürich, 2003.

D. E. Myers. Matrix formulation of co-kriging. *Journal of the International Association for Mathematical Geology*, 14(3):249–257, 1982. doi: 10.1007/BF01032887.

J. Nash and J. Sutcliffe. River flow forecasting through conceptual models part i — a discussion of principles. *Journal of Hydrology*, 10(3):282–290, 1970. ISSN 00221694. doi: 10.1016/0022-1694(70)90255-6.

V. Nešpor and B. Sevruk. Estimation of wind-induced error of rainfall gauge measurements using a numerical simulation. *Journal of Atmospheric and Oceanic Technology*, 16(4):450–464, 1999. doi: 10.1175/1520-0426(1999)016<0450:EOWIEO>2.0.CO;2.

C. Notarnicola, M. Duguay, N. Moelg, T. Schellenberger, A. Tetzlaff, R. Monsorno, A. Costa, C. Steurer, and M. Zebisch. Snow cover maps from MODIS images at 250 m resolution, Part 1: Algorithm description. *Remote Sensing*, 5(1):110–126, 2013a. ISSN 2072-4292. doi: 10.3390/rs5010110.

C. Notarnicola, M. Duguay, N. Moelg, T. Schellenberger, A. Tetzlaff, R. Monsorno, A. Costa, C. Steurer, and M. Zebisch. Snow cover maps from MODIS images at 250 m resolution, Part 2: Validation. *Remote Sensing*, 5(4):1568–1587, 2013b. ISSN 2072-4292. doi: 10.3390/rs5041568.

I. Odeh, A. McBratney, and D. Chittleborough. Further results on prediction of soil properties from terrain attributes: heterotopic cokriging and regression-kriging. *Geoderma*, 67(3-4):215–226, 1995. doi: 10.1016/0016-7061(95)00007-B.

OFEG. Hochwasser 2000 – Les crues 2000. Rapports de l'OFEG, Série Eaux, Nr. 2, Office Fédéral des Eaux et de la Géologie, 2002.

OFEG. Bericht über die Hochwasserereignisse 2005. Technical Report, Rapport au Conseil fédéral du 21.12.05, Office Fédéral des Eaux et de la Géologie, 2005.

A. Ohmura. Physical basis for the temperature-based melt-index method. *Journal of Applied Meteorology*, 40(4):753–761, 2001. ISSN 0894-8763, 1520-0450. doi: 10.1175/1520-0450(2001)040<0753:PBFTTB>2.0.CO;2.

J. Parajka and G. Blöschl. Spatio-temporal combination of MODIS images - potential for snow cover mapping. *Water Resources Research*, 44(3), 2008a. ISSN 00431397. doi: 10.1029/2007WR006204.

J. Parajka and G. Blöschl. The value of MODIS snow cover data in validating and calibrating conceptual hydrologic models. *Journal of Hydrology*, 358(3-4):240–258, 2008b. ISSN 00221694. doi: 10.1016/j.jhydrol.2008.06.006.

E. Pebesma. Gstat user's manual, 2014. URL http://www.gstat.org/gstat.pdf.

E. Pebesma and B. Graeler. Package 'gstat', version 1.1-3, 2017.

E. J. Pebesma. Multivariable geostatistics in S: the gstat package. *Computers & Geosciences*, 30: 683–691, 2004.

C. Perrin, C. Michel, and V. Andréassian. Improvement of a parsimonious model for streamflow simulation. *Journal of Hydrology*, 279(1):275–289, 2003. ISSN 00221694. doi: 10.1016/S0022-1694(03)00225-7.

D. L. Phillips, J. Dolph, and D. Marks. A comparison of geostatistical procedures for spatial analysis of precipitation in mountainous terrain. *Agricultural and Forest Meteorology*, 58 (1-2):119–141, 1992. doi: 10.1016/0168-1923(92)90114-J.

A. Pistocchi, S. Bagli, M. Callegari, C. Notarnicola, and P. Mazzoli. On the direct calculation of snow water balances using snow cover information. *Water*, 9(11):848, 2017. ISSN 2073-4441. doi: 10.3390/w9110848.

M. D. Pollock, G. O'Donnell, P. Quinn, M. Dutton, A. Black, M. E. Wilkinson, M. Colli, M. Stagnaro, L. G. Lanza, E. Lewis, C. G. Kilsby, and P. E. O'Connell. Quantifying and mitigating wind-induced undercatch in rainfall measurements. *Water Resources Research*, 54(6):3863–3875, 2018. ISSN 00431397. doi: 10.1029/2017WR022421.

PostgreSQL Global Development Group. PostgreSQL. http://www.postgresql.org, 2018.

R Core Team. *R: A Language and Environment for Statistical Computing*. R Foundation for Statistical Computing, Vienna, Austria, 2018. ISBN 3-900051-07-0. URL https://www.R-project.org/.

M. Rahnamay Naeini, B. Analui, H. V. Gupta, Q. Duan, and S. Sorooshian. Three decades of the shuffled complex evolution (SCE-UA) optimization algorithm: Review and application. *Scientia Iranica*, 2019. ISSN 1026-3098. doi: 10.24200/sci.2019.21500.

A. Rango and J. Martinec. Application of a snowmelt-runoff model using Landsat data. *Hydrology Research*, 10(4):225–238, 1979. ISSN 0029-1277, 2224-7955. doi: 10.2166/nh.1979.0006.

A. Rango and J. Martinec. Revisiting the degree-day method for snowmelt computations. *Journal of the American Water Resources Association*, 31(4):657–669, 1995. ISSN 1093-474X, 1752-1688. doi: 10.1111/j.1752-1688.1995.tb03392.x.

G. Rees. *Remote sensing of snow and ice*. Taylor & Francis, Boca Raton, 2006. ISBN 978-0-415-29831-5.

P. Riboust, G. Thirel, N. L. Moine, and P. Ribstein. Revisiting a simple degree-day model for integrating satellite data: implementation of SWE-SCA hystereses. *Journal of Hydrology and Hydromechanics*, 67(1):70–81, 2019. ISSN 0042-790X. doi: 10.2478/johh-2018-0004.

M. Savina, B. Schäppi, P. Molnar, P. Burlando, and B. Sevruk. Comparison of a tipping-bucket and electronic weighing precipitation gage for snowfall. *Atmospheric Research*, 103:45–51, 2012. doi: 10.1016/j.atmosres.2011.06.010.

B. Schaefli, B. Hingray, M. Niggli, and A. Musy. A conceptual glacio-hydrological model for high mountainous catchments. *Hydrology and Earth System Sciences*, 9(1/2):95–109, 2005. ISSN 1607-7938. doi: 10.5194/hess-9-95-2005.

B. Schaefli, L. Nicótina, C. Imfeld, P. Da Ronco, E. Bertuzzo, and A. Rinaldo. SEHR-ECHO v1.0: a Spatially Explicit Hydrologic Response model for ecohydrologic applications. *Geosci. Model Dev.*, 7(6):2733–2746, 2014. doi: 10.5194/gmd-7-2733-2014.

R. Schiemann, R. Erdin, M. Willi, C. Frei, M. Berenguer, and D. Sempere-Torres. Geostatistical radar-raingauge combination with nonparametric correlograms: methodological considerations and application in Switzerland. *Hydrology and Earth System Sciences*, 15(5):1515–1536, 2011. doi: 10.5194/hess-15-1515-2011.

J. Schulla and K. Jasper. Model Description WaSiM-ETH, 2007. URL http://www.wasim.ch/downloads/doku/wasim/wasim_2007_en.pdf.

J. M. Schuurmans, M. F. P. Bierkens, E. J. Pebesma, and R. Uijlenhoet. Automatic prediction of high-resolution daily rainfall fields for multiple extents: the potential of operational radar. *Journal of Hydrometeorology*, 8(6):1204–1224, 2007. doi: 10.1175/2007JHM792.1.

D.-J. Seo, V. Koren, and N. Cajina. Real-time variational assimilation of hydrologic and hydrometeorological data into operational hydrologic forecasting. *Journal of Hydrometeorology*, 4: 627–641, 2003.

D. Shepard. A two-dimensional interpolation function for irregularly-spaced data. In *Proceedings of the 1968 23rd ACM national conference*, pages 517–524. ACM Press, 1968. doi: 10.1145/800186.810616.

I. V. Sideris, M. Gabella, R. Erdin, and U. Germann. Real-time radar-rain-gauge merging using spatio-temporal co-kriging with external drift in the alpine terrain of Switzerland. *Quarterly Journal of the Royal Meteorological Society*, 140(680):1097–1111, 2014a. doi: 10.1002/qj.2188.

I. V. Sideris, M. Gabella, M. Sassi, and U. Germann. The CombiPrecip experience: development and operation of a real-time radar-raingauge combination scheme in Switzerland. In *2014 International Symposium Weather Radar and Hydrology*, Washington DC, 2014b.

A. Sikorska and J. Seibert. Value of different precipitation data for flood prediction in an alpine catchment: A bayesian approach. *Journal of Hydrology*, 556:961–971, 2018. ISSN 00221694. doi: 10.1016/j.jhydrol.2016.06.031.

A. G. Slater and M. P. Clark. Snow data assimilation via an ensemble Kalman filter. *Journal of Hydrometeorology*, 7(3):478–493, 2006. ISSN 1525-755X, 1525-7541. doi: 10.1175/JHM505.1.

SLF. Intercantonal Measurement and Information System (IMIS). WSL Institute for Snow and Avalanche Research SLF, 2017. [Available online at http://www.slf.ch/ueber/organisation/warnung_praevention/warn_informationssysteme/messnetze_daten/imis/index_EN].

SLF. SWE manual measures, 2019. [Available online at https://www.slf.ch/en/avalanche-bulletin-and-snow-situation/measured-values/description-of-manual-measuring-sites.htmle].

SmartBear Software. Swagger. https://swagger.io/, 2018.

G. Smiatek, F. Keis, C. Chwala, B. Fersch, and H. Kunstmann. Potential of commercial microwave link network derived rainfall for river runoff simulations. *Environmental Research Letters*, 12(3), 2017. ISSN 1748-9326. doi: 10.1088/1748-9326/aa5f46.

M. M. Sohrabi, D. Tonina, R. Benjankar, M. Kumar, P. Kormos, and D. Marks. Role of temporal resolution of meteorological inputs for process-based snow modelling. *Hydrological Processes*, 32(19):2976–2989, 2018. doi: doi:10.1002/hyp.13242.

P. Speirs, M. Gabella, and A. Berne. A comparison between the GPM dual-frequency precipitation radar and ground-based radar precipitation rate estimates in the Swiss Alps and plateau. *Journal of Hydrometeorology*, 18(5):1247–1269, 2017. ISSN 1525-755X, 1525-7541. doi: 10.1175/JHM-D-16-0085.1.

R. Srikanthan, G. Amirthanathan, and G. Kuczera. Application of ensemble Kalman filter for flood forecasting in Australian rivers. *Australasian Journal of Water Resources*, 12(3):245–255, 2008. ISSN 1324-1583, 2204-227X. doi: 10.1080/13241583.2008.11465351.

L. Sun, O. Seidou, I. Nistor, and K. Liu. Review of the Kalman-type hydrological data assimilation. *Hydrological Sciences Journal*, 61(13):2348–2366, 2016. ISSN 0262-6667, 2150-3435. doi: 10.1080/02626667.2015.1127376.

Swisstopo. DHM25 - The digital height model of Switzerland, 2005.

Swisstopo. Swiss Map Raster 1000 - National map of switzerland 1:1million, 2012.

Swisstopo. swissTLM3D - large-scale topographical landscape model of Switzerland, 2013.

Swisstopo. swissBOUNDARIES3D - Administrative units of Switzerland, 2017a.

Swisstopo. Vector200 - The small-scale landscape model of Switzerland, 2017b.

A. H. Thiessen. Precipitation averages for large areas. *Monthly Weather Review*, 39(7):1082–1089, 1911. doi: 10.1175/1520-0493(1911)39<1082b:PAFLA>2.0.CO;2.

C. Tobin. *Improving Alpine flood prediction through hydrological process characterization and uncertainty analysis*. PhD Thesis N° 5416, Ecole Polytechnique Fédérale de Lausanne, Lausanne, 2012.

C. Tobin, L. Nicotina, M. B. Parlange, A. Berne, and A. Rinaldo. Improved interpolation of meteorological forcings for hydrologic applications in a Swiss Alpine region. *Journal of Hydrology*, 401(1-2):77–89, 2011. doi: 10.1016/j.jhydrol.2011.02.010.

C. Tobin, B. Schaefli, L. Nicótina, S. Simoni, G. Barrenetxea, R. Smith, M. Parlange, and A. Rinaldo. Improving the degree-day method for sub-daily melt simulations with physically-based diurnal variations. *Advances in Water Resources*, 55:149–164, 2013. ISSN 03091708. doi: 10.1016/j.advwatres.2012.08.008.

L. Turc. Evaluation des besoins en eau d'irrigation, formule climatique simplifiée et mise à jour. *Annales agronomiques, INRA*, (12):13–49, 1961.

G. Upton and A. Rahimi. On-line detection of errors in tipping-bucket raingauges. *Journal of Hydrology*, 278(1-4):197–212, 2003. ISSN 00221694. doi: 10.1016/S0022-1694(03)00142-2.

A. Verdin, B. Rajagopalan, W. Kleiber, and C. Funk. A Bayesian kriging approach for blending satellite and ground precipitation observations. *Water Resources Research*, 51(2):908–921, 2015. doi: 10.1002/2014WR015963.

G. Villarini and W. F. Krajewski. Review of the different sources of uncertainty in single polarization radar-based estimates of rainfall. *Surveys in Geophysics*, 31(1):107–129, 2010. ISSN 0169-3298, 1573-0956. doi: 10.1007/s10712-009-9079-x.

G. Villarini, P. V. Mandapaka, W. F. Krajewski, and R. J. Moore. Rainfall and sampling uncertainties: A rain gauge perspective. *Journal of Geophysical Research*, 113:1–12, 2008. doi: 10.1029/2007JD009214.

S. Vogl, P. Laux, W. Qiu, G. Mao, and H. Kunstmann. Copula-based assimilation of radar and gauge information to derive bias-corrected precipitation fields. *Hydrology and Earth System Sciences*, 16(7):2311–2328, 2012. doi: 10.5194/hess-16-2311-2012.

E. Vuerich, C. Monesi, L. Lanza, L. Stagi, and E. Lanzinger. WMO Field intercomparison of rainfall intensity gauges. Instruments and observing methods Report no. 99, World Meteorological Organization, Vigna di Valle, Italy, 2009.

P. D. Wagner, P. Fiener, F. Wilken, S. Kumar, and K. Schneider. Comparison and evaluation of spatial interpolation schemes for daily rainfall in data scarce regions. *Journal of Hydrology*, 464-465:388–400, 2012. doi: 10.1016/j.jhydrol.2012.07.026.

A. Walker. *openxlsx: Read, write and edit xlsx files*, 2018. URL https://CRAN.R-project.org/package=openxlsx. R package version 4.1.0.

R. Webster and M. A. Oliver. *Geostatistics for environmental scientists*. Statistics in practice. Wiley, Chichester, 2nd edition, 2007. ISBN 978-0-470-02858-2.

A. H. Weerts and G. Y. H. El Serafy. Particle filtering and ensemble Kalman filtering for state updating with hydrological conceptual rainfall-runoff models. *Water Resources Research*, 42 (9), 2006. ISSN 00431397. doi: 10.1029/2005WR004093.

H. Wickham. ggplot2: Elegant graphics for data analysis, 2016. URL http://ggplot2.org.

H. Wickham. *httr: Tools for working with URLs and HTTP*, 2018. URL https://CRAN.R-project.org/package=httr. R package version 1.4.0.

WSL. La banque de données suisse sur les dommages dus aux intempéries. 2019.

X. Xu, J. Li, and B. A. Tolson. Progress in integrating remote sensing data and hydrologic modeling. *Progress in Physical Geography: Earth and Environment*, 38(4):464–498, 2014. ISSN 0309-1333, 1477-0296. doi: 10.1177/0309133314536583.

Alain FOEHN

Hildegardstrasse 7
3097 Liebefeld, Switzerland
alain.foehn@protonmail.ch
Swiss nationality, 08.11.1986

WORK EXPERIENCE

PhD student in EDCE Civil and Environmental Engineering (EPFL) 02/2015 – 09/2019
Laboratoire de Constructions Hydrauliques (LCH)
Swiss Federal Institute of Technology Lausanne
Thesis title: Radar-rain gauge merging and discharge data assimilation for flood forecasting in Alpine catchments
Keywords: hydrology, rain gauge, radar, snow modelling, data assimilation

- Merging of rain gauge and radar data for spatial interpolation of precipitation
- Correction for solid precipitation undercatch correction using ground-based snow measures
- Implementation of an Ensemble Kalman filter to an operational flood forecasting system
- Teaching assistantship in Ouvrages et Aménagements hydrauliques, Réseaux hydrauliques, Hydrologie urbaine, Hydraulique fluviale

Hydrology specialist at CREALP, 04/2014 – 01/2015
Research Center on Alpine Environment, Sion

- Implementation and consolidation of the flood forecasting and management system MINERVE
- Development of the hydrological-hydraulic software RS MINERVE

Internship in the field of meteorology, 04/2013 – 06/2013
Service des routes, transports et cours d'eau, Etat du Valais

- Support in the development of the cantonal hydrometeorological database

Civil service in the field environmental engineering 09/2012 – 03/2013
Research Center on Alpine Environment (CREALP), Sion

- Solid transport estimation (MatErosion project) and flood forecasting

EDUCATION

Master of Science (M.Sc) in Environmental Sciences and Engineering *Sep 2010 – Jul 2012*
Swiss Federal Institute of Technology Lausanne (EPFL)
Majors: Natural Water, Soil and Ecosystems Engineering; with Mention of Excellence
Master project at International Center for Integrated Mountain Development, Kathmandu, NEPAL

Bachelor of Science (B.Sc) in Environmental Sciences and Engineering *Sep 2007 – Jul 2010*
Swiss Federal Institute of Technology Lausanne (EPFL)
One year exchange at Indian Institute of Technology, Chennai, INDIA

LANGUAGES

French and Swiss-German: mother tongues
English: C1 level
German: B2 level
Spanish: A2 level

COMPUTER SKILLS

Programming : R, Matlab/Octave, MySQL, SVN, REST API, JSON, VBScripts
Office suite : Latex, Zotero, OpenOffice, Microsoft Office
GIS and modelling : Quantum GIS, ArcGIS, SAGA GIS, RS MINERVE

OTHERS

- Co-presidency of the Swiss Federation of Youth Parliaments (2007-2008)
- Group leader - Winter level 1 of the Swiss Alpine Club (training in 2018)
- Cycle trips (South America, 6700 km - 8 months; Himalaya, 1500 km - 2 months)

JOURNAL PUBLICATIONS

Foehn, A., García Hernández, J., Schaefli, B., De Cesare, G. (2019). Accounting for solid precipitation gauge undercatch in quantitative precipitation estimates for snow modelling in Alpine catchments. *Journal of Hydrometeorology* [under review].

Foehn, A., García Hernández, J., Schaefli, B., De Cesare, G., (2018). Spatial interpolation of precipitation from multiple rain gauge networks and weather radar data for operational applications in Alpine catchments. *Journal of Hydrology* 563, 1092–1110. DOI: 10.1016/j.jhydrol.2018.05.027

CONFERENCE PAPERS

Foehn, A., Pasetto, D., García Hernández, J., De Cesare, G. (2019). Application of an Ensemble Kalman filter to a semi-distributed hydrological flood forecasting system in alpine catchments, in: *SimHydro 2019*. Sophia Antipolis, France.

Foehn, A., García Hernández, J., De Cesare, G., Fluixá Sanmartín, J. (2018). Amélioration du calage du modèle hydrologique du bassin de la grande-eau en suisse avec des produits spatialisés de précipitation, température et couverture de neige, in: *De la prévision des crues à la gestion de crise*. Société hydrotechnique de France, Avignon, France.

García Hernández, J., **Foehn**, A., Fluixá-Sanmartín, J., Roquier, B., 2018. El sistema minerve para la modelización de crecidas en el canton de valais en suiza: análisis de la cuenca de grande-eau. Presented at the XX Congreso Nacional de ingenería civil, Lima, Peru.

Foehn, A., García Hernández, J., Schaefli, B., De Cesare, G., Schleiss, A.J. (2016). Spatialization of precipitation data for flood forecasting applied to the Upper Rhone River basin, in*: International Conference Hydro 2016*. Montreux.

Foehn, A., García Hernández, J., Alesina, S., Schleiss, A.J., Fluixá-Sanmartín, J. (2016). Los desafíos de la modelización hidrológica y la previsión de crecidas en tiempo real en alta montaña, in: *XXVII Congreso Latinoamericano de Hydráulica*. International Association of Hydraulic Engineering and Research, IAHR, Lima, Peru.

Hernández, J.G., **Foehn**, A., Alesina, S., Fluixá-Sanmartín, J. (2016). El sistema operacional MINERVE para la previsión de crecidas en el Cantón de Valais, Suiza. In*: XXVII Congreso Latinoamericano de Hidráulica*. International Association of Hydraulic Engineering and Research, IAHR, Lima, Peru.

MANUALS

Foehn, A., García Hernández, J., Roquier, B., Fluixá-Sanmartín, J., Paredes Arquiola, J. and De Cesare, G. (2019). RS MINERVE – User manual v2.13. Ed. CREALP, Switzerland. ISSN 2673-2653.

García Hernández, J., **Foehn**, A., Fluixá-Sanmartín, J., Roquier, B., Paredes Arquiola, J. and De Cesare, G. (2019). RS MINERVE – Technical manual, v2.22. Ed. CREALP, Switzerland. ISSN 2673-2661.